
Advanced Polymer Components Volume 1

Dr. John Rusek

OLAC PL/RKS
Phillips Laboratory
Edwards AFB CA 93524

October 1995

Final Report

APPROVED FOR PUBLIC RELEASE; DISTRIBUTION UNLIMITED

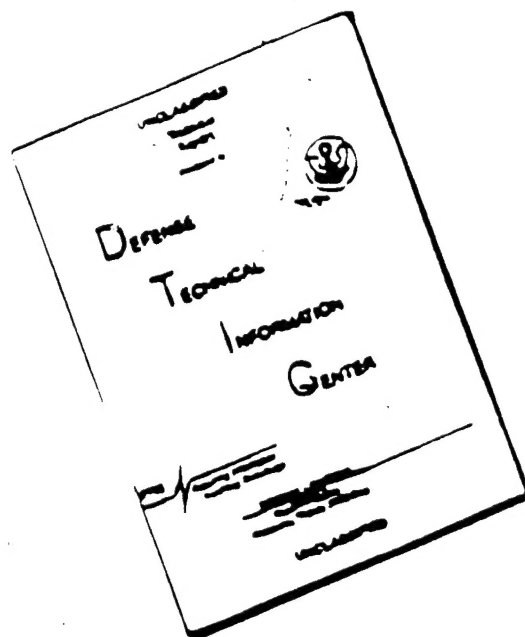
19960227 126



PHILLIPS LABORATORY
Propulsion Directorate
AIR FORCE MATERIEL COMMAND
EDWARDS AIR FORCE BASE CA 93524-7001

19960227 126

DISCLAIMER NOTICE




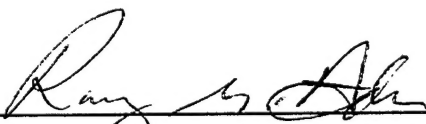
THIS DOCUMENT IS BEST
QUALITY AVAILABLE. THE COPY
FURNISHED TO DTIC CONTAINED
A SIGNIFICANT NUMBER OF
PAGES WHICH DO NOT
REPRODUCE LEGIBLY.


FOREWORD

This in-house final report was prepared by OLAC PL/RKS, Edwards AFB CA, for Operating Location AC, Phillips Laboratory, Edwards AFB CA 93524-7001. Project Manager was Dr. John J. Rusek.

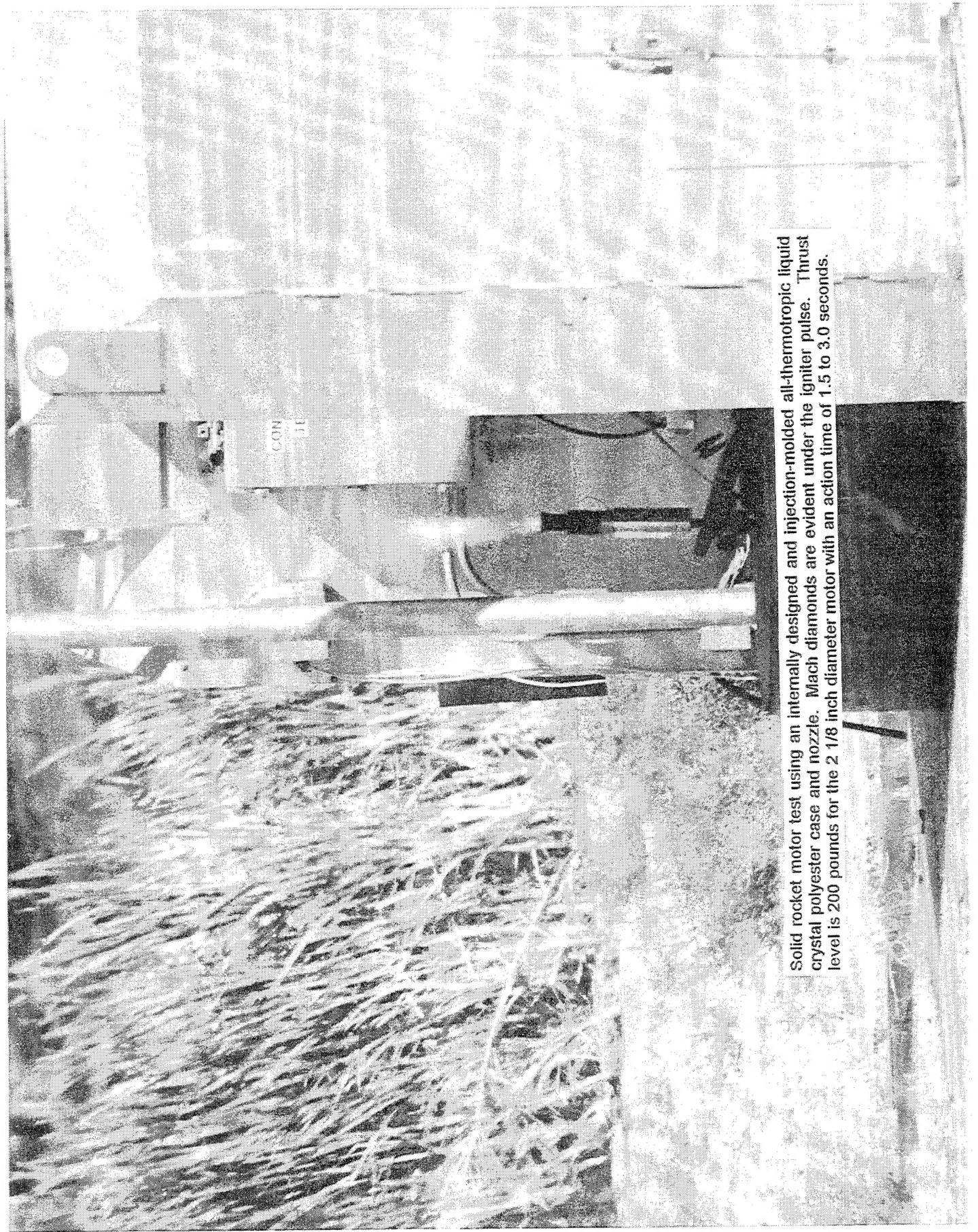
This report has been reviewed and is approved for release and distribution in accordance with the distribution statement on the cover and on the SF Form 298.


DR. JOHN J. RUSEK
Project Manager


RANNEY G. ADAMS 95-1556.
Public Affairs


SCOTT G. WIERSCHKE, Capt, USAF
Deputy Director
Propulsion Sciences Division

REPORT DOCUMENTATION PAGE			Form Approved OMB No 0704-0188	
Public reporting burden for this collection of information is estimated to average 1 hour per response, including the time for reviewing instructions searching existing data sources gathering and maintaining the data needed, and completing and reviewing the collection of information. Send comments regarding this burden estimate or any other aspect of this collection of information, including suggestions for reducing this burden to Washington Headquarters Services, Directorate for Information Operations and Reports, 1215 Jefferson Davis Highway, Suite 1204, Arlington, VA 22202-4302, and to the Office of Management and Budget, Paperwork Reduction Project (0740-0188), Washington DC 20503.				
1. AGENCY USE ONLY (LEAVE BLANK)		2. REPORT DATE October 1995		3. REPORT TYPE AND DATES COVERED Final Report
4. TITLE AND SUBTITLE Advanced Polymer Components Volume 1			5. FUNDING NUMBERS C: In-House PE: PR: 5730 TA: 00R9	
6. AUTHOR(S) Dr. John Rusek				
7. PERFORMING ORGANIZATION NAME(S) AND ADDRESS(ES) OLAC PL/RKS Phillips Laboratory Edwards AFB CA 93524			8. PERFORMING ORGANIZATION REPORT NUMBER	
9. SPONSORING/MONITORING AGENCY NAME(S) AND ADDRESS(ES) OLAC PL/RKS Phillips Laboratory Edwards AFB CA 93524			10. SPONSORING/MONITORING AGENCY REPORT NUMBER PL-TR-95-3002	
11. SUPPLEMENTARY NOTES COSATI CODE(S):				
12a. DISTRIBUTION/AVAILABILITY STATEMENT APPROVED FOR PUBLIC RELEASE; DISTRIBUTION IS UNLIMITED			12b. DISTRIBUTION CODE A	
13. ABSTRACT (MAXIMUM 200 WORDS) The Advanced Polymer Components Initiative began in December 1989. The initial purpose of the program was to explore advanced engineering polymers for use as rocket propulsion components. As research progressed it became apparent that advanced thermoplastics in general were highly dependent on processing and post-processing as well as on chemical composition and morphology. This realization led to a branching of the original objective into an applications research goal and a fundamental research goal. This report, coupled with PL-TR-92-3018, PL-TR-92-3018 Vol. 2 and PL-TR-92-3056, comprise a summary of the entire Advanced Polymer Components Initiative.				
14. SUBJECT TERMS thermotropic liquid crystal polymers; hybrid rocket; advanced polymer components; rocket propulsion; thermotropic resin			15. NUMBER OF PAGES	
			16. PRICE CODE	
17. SECURITY CLASSIFICATION OF REPORT Unclassified	18. SECURITY CLASSIFICATION OF THIS PAGE Unclassified	19. SECURITY CLASSIFICATION OF ABSTRACT Unclassified	20. LIMITATION OF ABSTRACT SAR	



Solid rocket motor test using an internally designed and injection-molded all-thermotropic liquid crystal polyester case and nozzle. Mach diamonds are evident under the igniter pulse. Thrust level is 200 pounds for the 2 1/8 inch diameter motor with an action time of 1.5 to 3.0 seconds.

TABLE OF CONTENTS

Volume 1

Preface	1
Executive Summary	2
Glossary	4
Thermotropic Liquid Crystal Polymers J. Rusek, Phillips Laboratory, Edwards AFB	5
Mechanical Properties of Liquid Crystal Polymers J. Shelley, Phillips Laboratory, Edwards AFB	12
Property Transformation of Thermotropic Liquid Crystal Polymers J. Rusek, K. Chaffee, D. Silver, Phillips Laboratory, Edwards AFB	18
Polyester Synthesis and Analysis B. Lormand, Phillips Laboratory, Edwards AFB	30
1 Kilogram Synthesis of Poly 2-[phenylethyl] para-phenylene terephthalate/Post-synthesis Polymer Cleanup Procedures B. Lormand, Phillips Laboratory, Edwards AFB	48
On the Annealing Question in Liquid Crystal Polymer Systems: Surface and Near Surface Effects J. A. Mann, J. Rusek, Phillips Laboratory, Edwards AFB	53
Synchrotron Radiation Studies of Liquid Crystal Polymers R. W. Hoffman, Phillips Laboratory, Edwards AFB	97
Reduction and Analysis of Synchrotron Spectroscopic Data T. Reed, Phillips Laboratory, Edwards AFB	117
Preparations for Neutron Scattering Investigations of Liquid Crystal Polymers D. Elliot, Arkansas Tech University	129
Initial Irradiation of Liquid Crystal Polymers A. Weeks, McClellan AFB	147

TABLE OF CONTENTS **Volume 1 cont.**

Hardness Test Results of Irradiated Plastic Samples J. Meininger, Advanced Composites	151
The Investigation of Thermotropic Liquid Crystalline Polymeric Fibers at the Micromechanics Level A. Palazotto, Wright Patterson AFB	156
Liquid Crystal Polymer's Suitability for MMH and NTO Turbopump Applications T. R. Hill, Phillips Laboratory, Edwards AFB	225

Volume 2

Cryogenic Testing of Liquid Crystal Polymers J. Phillips, Phillips Laboratory, Edwards AFB	232
USAF Turbopump Plastics Testing: Oxygen Exposure H. D. Beeson, R. Shelley, NASA White Sands Test Facility	241
Tensile Testing of Liquid Crystal Polymers in Liquid Hydrogen T. J. Eisenreich, General Dynamics Space Systems Division	269
Tensile Testing of Liquid Crystal Polymers T. Reed, Phillips Laboratory, Edwards AFB	290
Injection Molded Rocket Motor Case C. L. Frank, USAF Advanced Composites Program Office	295
Hybrid Nozzle Demonstrator E. Schmidt, Phillips Laboratory, Edwards AFB	309
Test Data from the Firings of Two Stainless Steel and Two Liquid Crystal Polymer Case Motors A. Kenney, Phillips Laboratory, Edwards AFB	312
Further Testing of VECTRA 2 x 4 Motor Cases H. T. Nguyen, Phillips Laboratory, Edwards AFB	345
Development and Testing of Liquid Crystal Polymer Solid Rocket Motors T. R. Reed, Phillips Laboratory, Edwards AFB	363

TABLE OF CONTENTS

Volume 2 cont.

Development and Testing of Liquid Crystal Polymer Solid Rocket Motors and Hydrostatic Testing of Liquid Crystal Polymer Rocket Motor Cases T. R. Reed, Phillips Laboratory, Edwards AFB	381
Charred Plastic Tube Specimen Microstructural Evaluation J. Meininger, Phillips Laboratory, Edwards AFB	392
Solid Rocket Propulsion Applications for Advanced Polymers J. Chew, J. Rusek, Phillips Laboratory, Edwards AFB	404
Propulsion Applications for Thermotropic Liquid Crystal Polymers J. Shelley, Phillips Laboratory, Edwards AFB	418
Design of a Blow Molded LCP Pressure Vessel and a Fiber Reinforced Pressure Vessel G. J. Price, Phillips Laboratory, Edwards AFB	421

PREFACE

The Advanced Polymer Components Initiative began in December of 1989. The initial purpose of the program was to explore advanced engineering polymers for use as rocket propulsion components. As research progressed it became apparent that advanced thermoplastics in general were highly dependent on processing and post-processing as well as on chemical composition and morphology. This realization led to a branching of the original objective into an applications research goal and a fundamental research goal.

Within the first year of this effort, thermotropic liquid crystal polymers such as VECTRA, XYDAR and ZENITE were identified as having the most promise for surviving the rigors of the rocket propulsion environment, however, their highly anisotropic nature made fabrication a challenge.

The fundamental and application research goals, as related to thermotropic liquid crystal polymers, are detailed in

PL-TR-92-3018, *Proceedings of the First Annual Advanced Polymer Components Symposium*, July 1992

PL-TR-92-3018 Part 2, Volumes I, II and III, *Proceedings of the Second Annual Advanced Polymer Components Symposium*, December 1994

PL-TR-92-3056, *Physical Properties of Injection Molded Liquid Crystal Polymers and High Temperature Engineering Polymers*, March 1993

This final report, in conjunction with the above reports, details the sum total of the results obtained from the liquid crystal research over the past six years. It is clear that these materials have a significant future in the rocket propulsion community due to their high specific strengths and thermal/chemical compatibility properties.

The United States Air Force is indebted to the exceptional research accomplished by the two dozen Air Force and Navy scientists and engineers, the dozen university faculty and the international scientists which made this project a complete success. With this concerted effort we come ever closer to the stars.



John J. Rusek
Program Manager
Advanced Polymer Components Initiative

EXECUTIVE SUMMARY

The advent of advanced composite materials has led to aerospace articles of high specific strength and modulus. The main drawback to these items is their high fabrication time, lack of consistency and high cost. In contrast, articles produced from commodity thermoplastics yield reproducible, low cost items with very low specific strengths. The discovery of thermotropic liquid crystal polymers over twenty years ago promised articles with the best attributes of both; high reproducibility, lower cost and high performance. The fact that these materials are liquid crystalline in nature and can be quenched to form a molecular composite is both a benefit and a liability. The thermal processing and post-processing become the prime determinant of the ultimate strength of the part. For these reasons, research was initiated and called the Advanced Polymer Components Initiative.

Liquid crystalline materials have been known for over one hundred years. The tobacco mosaic virus and isolated cholesterol were noted to exhibit liquid crystalline behavior in solution. The last thirty years have heralded liquid crystalline polymers, species that exhibit liquid crystalline behavior in solution (lyotropes) and a new class of materials which exhibits this behavior in the molten state (thermotropes). The commercial grades of these are well known as the strongest thermoplastics in existence, have excellent chemical and thermal resistance, and are lightweight.

Three liquid crystalline states have been identified, nematic, smectic and cholesteric. An increase in molecular order occurs from nematic to smectic to cholesteric, however, potential fracture planes become more evident. For structural applications, the nematic phase is the preferred orientation.

Polymeric lyotropes such as KEVLAR form from highly acidic solution. The lyotropes exhibit a nematic crystalline phase, but can only be drawn into fibers or, at best, thin sheets. Polymeric thermotropes such as VECTRA, XYDAR and ZENITE form nematic phases in the melt which can be retained via quenching to yield a highly oriented macroscopic part.

The United States Air Force has been actively pursuing thermally processed liquid crystal polymers under its in-house initiative, Advanced Polymer Components. The targeted application area is structural propulsion components. All propulsion system requirements demand high performance coupled with low weight and cost. The advent of a variety of commercial liquid crystalline materials make the timing ideal for component research.

Initially, commercial thermotropic resins were molded and tested as propulsion test articles at the Phillips Laboratory. The physical properties of the skin region were quite different from those of the interior core. Sectioned specimens were analyzed and found to be different not only in strength, but also in chemical and thermal properties as well.

Post thermal processing (annealing) of the liquid crystalline materials gave as much as a twofold increase in tensile strengths, for certain polymers (ZENITE precursors). This led to a significant fundamental research component directed towards understanding the annealing phenomena.

The work accomplished under the Advanced Polymer Components Initiative has led to the following conclusions:

- 1) Liquid crystal polymers have a viable role in rocket propulsion as advanced ablative, pressure containment and cryogenic storage materials.
- 2) The polymer strengths can be increased further by annealing.
- 3) The chemical resistance of these polymers is excellent, with little degradation in properties by contact with most solvents.
- 4) Chemical resistance with respect to monomethylhydrazine and nitrogen tetroxide can be improved by annealing, however, traditional storable propellant containment is not recommended.
- 5) The mechanical properties remain the same, or improve, with a decrease in temperature, down through liquid hydrogen temperatures. These polymeric materials also have low permeability, hence, liquid hydrogen containment is recommended.
- 6) Reactivity with liquid oxygen is within a factor of three relative to TEFLON, a material classed for oxygen service. Specific applications for liquid oxygen containment should be explored.
- 7) Completely plastic solid rocket motors have been fired successfully. Ablation rates and pressure values have established that the liquid crystalline materials are good candidates for tactical applications.
- 8) Thermotropic liquid crystal polymers have higher strengths in the skin region; thin extruded or blow-molded components have higher specific tensile strengths than thicker injection molded components.

It is clear that thermotropic liquid crystal polymers have a significant role in solid and liquid propulsion. The advent of advanced propulsion concepts, such as hybrid propulsion with non-toxic storable oxidizers, demands extreme materials properties for successful accomplishment. Thermotropic liquid crystal polymers are excellent candidates for these future systems.

It is recommended that a development program be initiated targeted at a storable hybrid tactical variant. It is also recommended that a blow-molding process be coupled with annealing to form a hydrogen peroxide pressure tank and the solid grain combustion chamber. Injection molding can be used to form the nozzle substructure, aerodynamic shell, and airfoils.

Liquid crystal polymers promise rocket propulsion systems that are responsive, flexible and low cost, both in the space-lift and the tactical arenas. These materials, when coupled with advanced propulsion concepts, should enable the next-generation of spacecraft, from large launch to transatmospheric vehicles.

GLOSSARY

AFM-Atomic Force Microscopy
ANSTO-Australian Nuclear Science and Technology Organisation
AP-Ammonium Perchlorate
APC-Advanced Polymer Components
ASTM-American Society for Testing of Materials
BHQ-Bromohydroquinone
BNL-Brookhaven National Laboratory
CHQ-Chlorohydroquinone
CVD-Chemical Vapor Deposition
DESY-Deutsches Elektronen-Synchrotron
DMA-Dynamic Mechanical Analysis
DSC-Differential Scanning Calorimetry
EXAFS-Extended X-ray Absorption Fine Structure
FTIR-Fourier Transform Infrared (Spectroscopy)
HQ-Hydroquinone
LALLS-Low Angle Laser Light Scattering
LB-Langmuir-Blodgett (Film)
LCP-Liquid Crystal Polymer
LH2-Liquid Hydrogen
LN2-Liquid Nitrogen
LOX-Liquid Oxygen
MHQ-Methylhydroquinone
MMH-Monomethylhydrazine
NEMESIS-New Engineering Materials Evaluation/Surface & Interfacial Studies
NMR-Nuclear Magnetic Resonance (Spectroscopy)
NTO-Nitrogen Tetroxide
OTV-Orbit Transfer Vehicle
PAS-Photoacoustic Spectroscopy
PBI-Polybenzimidazole
PEHQ-Phenylethylhydroquinone
PHQ-Phenylhydroquinone
PICNIC-Propellant Insulation Case Nozzle Integrated Component
SANS-Small Angle Neutron Scattering
SAXS-Small Angle X-ray Scattering
SHQ-Styrylhydroquinone
TA-Terephthalic Acid or Terephthalate
TGA-Thermogravimetric Analysis
TIRF-Total Internal Reflection Fluorescence
TMA-Thermal Mechanical Analysis
VATIRF-Variable Angle TIRF
XAFS-X-ray Absorption Fine Structure
XANES-X-ray Absorption Near Edge Structure
XRD-X-ray Diffraction

THERMOTROPIC LIQUID CRYSTAL POLYMERS

John J. Rusek

Phillips Laboratory

OLAC PL/RCP

Edwards AFB, CA 93523

ABSTRACT

The demands of lowering the cost and increasing the reliability of propulsion systems has forced the aerospace industry to investigate new materials and fabrication techniques. Advanced structural plastics, such as thermotropic liquid crystal polymers, may meet these propulsion systems requirements for high strength, high modulus, and low life cycle costs. The Phillips Laboratory at Edwards AFB has initiated an in-house research program to explore such polymers and determine their suitability for these aggressive environments.

INTRODUCTION

Liquid crystalline materials have been known for over one hundred years. The tobacco mosaic virus and isolated cholesterol were both noted to exhibit liquid crystalline behavior in solution as observed by optical anomalies. The last twenty-five years have heralded liquid crystalline polymers, species that exhibit liquid crystalline behavior in solution (lyotropes), as above, and a new class of materials which exhibit this behavior in the molten state (thermotropes).

Both classes of polymers have been commercialized to some degree; prices are in the twenty dollar per pound range for bulk resin. The key issue is the maximization of physical properties by judicious control of processing. Figure 1 shows specific strength plotted as a function of specific modulus. The lower left region shows traditional isotropic materials, including bulk molded polymeric liquid crystals. The same materials, when properly processed to maximize orientation, increase ten-fold in strength and twice in modulus. Further orientation at the molecular level of these thermotropes would place them to the right of the PBX region on the graph, giving a further three-fold increase of specific modulus. Clearly,

these molded articles are very attractive, even when compared to single filament carbon fibers.

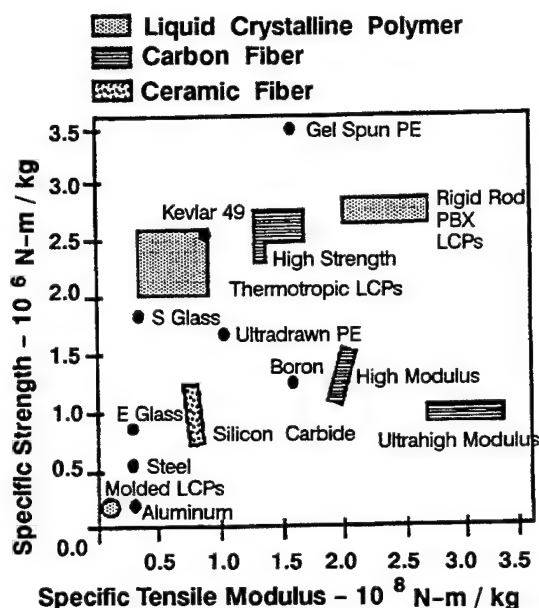


Fig. 1

Specific Strength as a Function of Specific Tensile Modulus for Advanced Materials

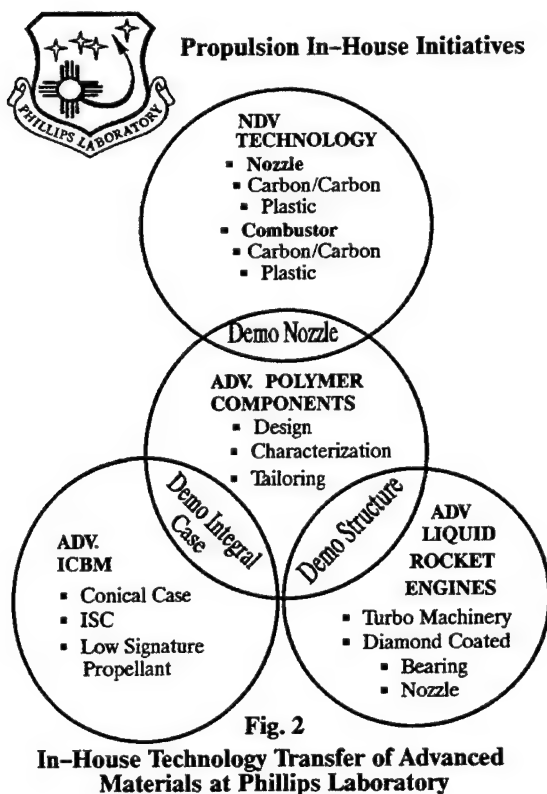
The Air Force has been actively pursuing advanced materials since its inception. Recently, a large in-house effort has been initiated to specifically explore thermotropic systems at the Phillips Laboratory. This program, Advanced Polymer Components, has two primary objectives:

Understand the fundamental mechanisms of liquid crystalline behavior in polymers and predict structure/property relationships to yield fully engineered articles.

Demonstrate the feasibility of thermotropic liquid crystal polymers as system components for both solid and liquid propulsion.

All systems requirements demand high performance coupled with low weight and cost. The advent of commercial lyotropes and thermotropes makes the timing appropriate for system integration.

The ADVANCED POLYMER COMPONENTS (APC) initiative feeds to three other in-house initiatives, two of which are liquid propellant based, and one of which is solid propellant based. The schematic of technology transfer is shown as Figure 2. It is clear from this diagram that advanced polymer components pervade the entire spectrum of propulsion, from tactical components through large launch vehicles as well as orbit transfer devices.



PROPOSITION

The difference between conventional polymers and liquid crystal polymers is shown in schematic as Figure 3. Conventional polymers generally have a high molecular weight that exhibit highly tangled coils that form discrete domains upon gellation. These domains are connected by smaller polymer

fragments which allow some extension or strain capability to the macroscopic part. The domain size and degree of entanglement is critically dependent on the processing shear rate as well as the rate of part cool-down. Thermotropic liquid crystal polymers are significantly different from this, however, in that the intermolecular distances between rigid rods vary with temperature and the polymer rod length is on the order of 100 angstroms (Å). Again, rate of cooling and shear fields determine orientation, but Van der Waals forces predominate for these small polymer rods.

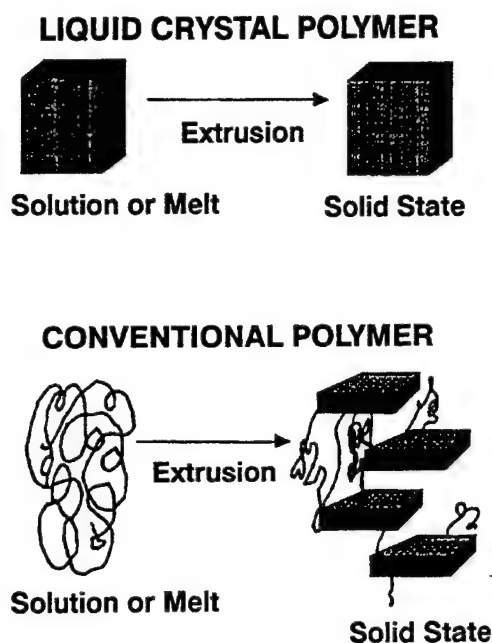


Fig. 3
Schematic Representation of Conventional and Liquid Crystalline Melt Transitions

The macroscopic manifestation of these intermolecular forces is shown as Figure 4. This diagram depicts heat flow as a function of temperature for an idealized thermotropic liquid crystal polymer. Note the transition from crystalline to nematic to isotropic melt, and the corresponding structural changes. Of prime interest is the fact that the viscosity increases from nematic to isotropic, in direct contrast to conventional behavior observed in thermoplastic systems.

Parts derived from thermotropic liquid crystal polymers exhibit a pronounced skin and core effect.

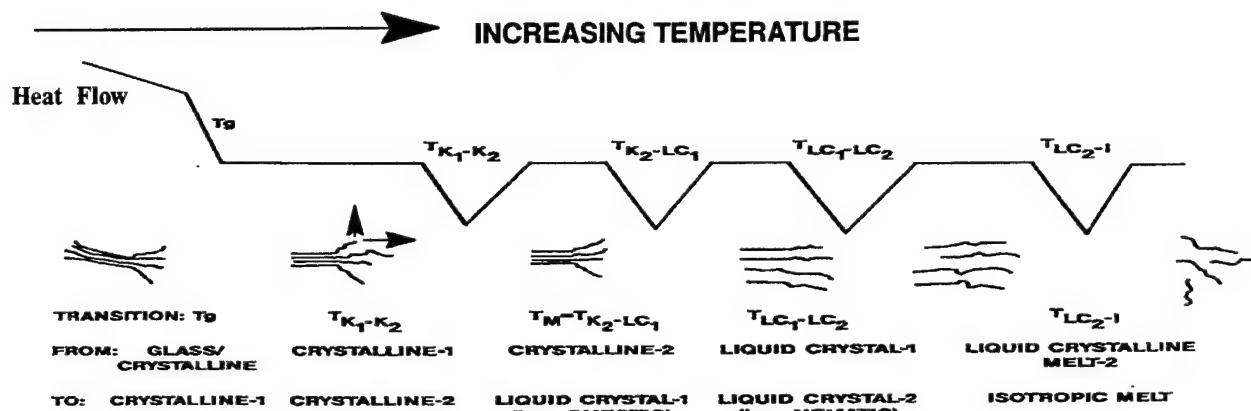


Fig. 4
Heat Flow vs. Temperature for Liquid Crystalline Materials

Figure 5 depicts a representation of the hierarchical morphology of the produced parts. Macrofibrils averaging 5 microns have been noted in all molded structures, as well as microfibrils averaging 0.5 microns diameter. The smallest fibers, consisting of nested rigid rods, have an average diameter of 500 Å. This diagram depicts these three discrete regimes, which are the basis of the high-strength properties manifested in liquid crystal polymers.

Three liquid crystalline phases have been identified: nematic, smectic and cholesteric. Figure 6 depicts the nematic phase. As can be clearly seen, there is only one degree of symmetry with general molecular orientation along a director, depicted by the arrow. Figure 7 shows a representation of the smectic phase. A second order of symmetry is apparent in that not only is there an orientation along the director, but there exists discrete planes of molecules perpendicular to the director. The highest order of symmetry is the cholesteric phase, shown as Figure 8. This structure is essentially a helically-connected system of nematic phases joined on a perpendicular to the mutual directors. All commercial polymeric liquid crystals, whether lyotropic or thermotropic, are nematic in nature.

Polymeric lyotropes form from highly acidic solutions. The lyotropes exhibit a nematic crystalline phase: the lowest symmetry order. Most modern lyotropes need heat to process the polymer, due to the highly polar interactions between the solvent and solute.

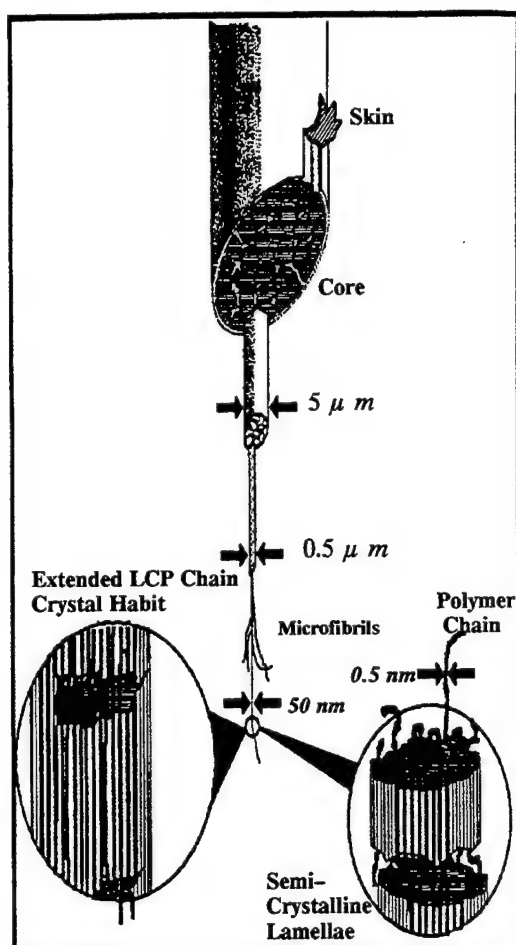


Fig. 5
Hierarchical Morphology of an Idealized Liquid Crystalline Polymer

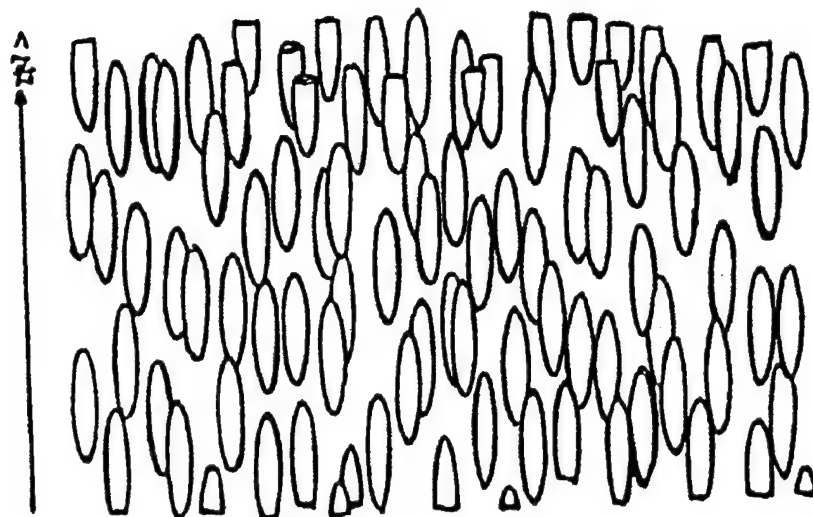


Fig. 6
Representation of Liquid Crystalline Nematic Phase

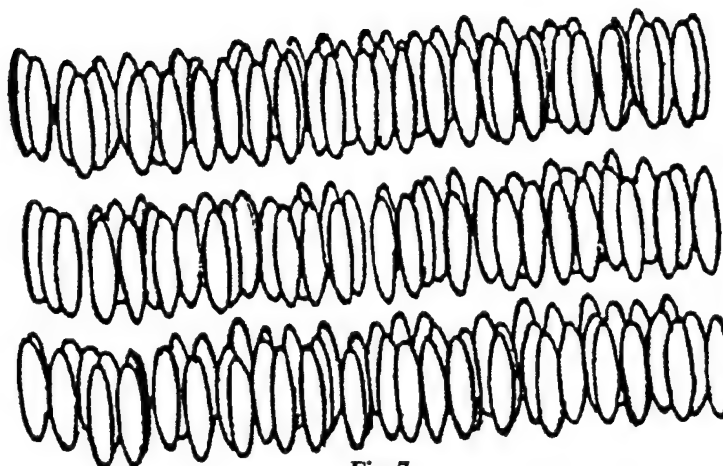


Fig. 7
Representation of Liquid Crystalline Smectic Phase

Polymeric thermotropes exhibit a transition from crystalline to nematic to isotropic liquid with increasing temperature. This follows a trend of decreasing order with temperature. The rheology of the melt phase is highly complex, but in general shows a viscosity lowering from the solid to nematic phase and an increase from nematic to isotropic.

Molecular architecture is the prime determinant in liquid crystalline behavior. Polymeric liquid crystal are rigid rods, usually polyesters, which have a molecular aspect ratio of 30:1. This implies a typical length of 90 Å, and a typical degree of polymerization of 10. Lyotropic polymers have many barriers to rotation,

due to molecular geometry, steric barriers and buried polar moieties.

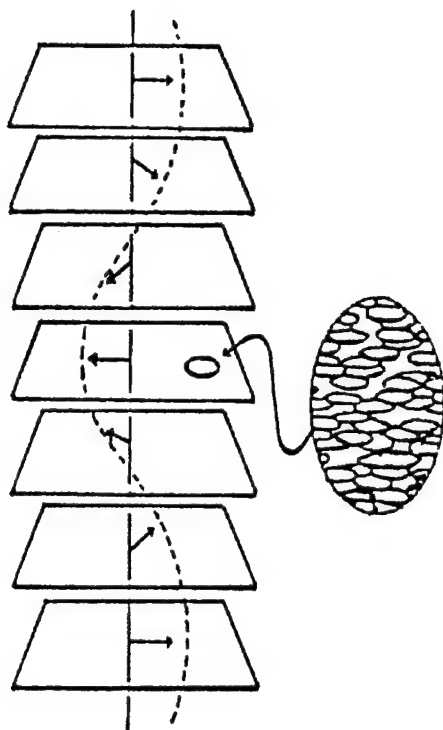


Fig. 8
Representation of Liquid Crystalline
Cholesteric Phase

The most classic example of a lyotropic liquid crystal polymer is depicted as Figure 9. This polymer, commercialized over 20 years ago, is called KEVLAR. The repeating aromatic units are connected by carbonyl and amide linkages, imparting very high strength due to these molecular bonds. This polymer is drawn out of concentrated sulfuric acid and forms fibers quite easily. Unfortunately, no other geometries are obtainable, save some rudimentary biaxial films, because of this complex acid process.

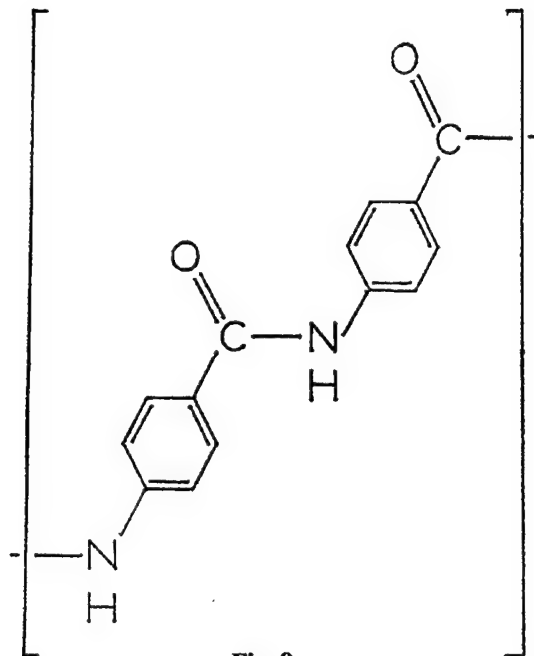


Fig. 9
Molecular Structure of the LyotYPE KEVLAR

More recently, polybenzoxazole has been commercialized (Figure 10). This is a highly compact molecule, and is only free to rotate along the rods semi-major axis. For this reason, heat and a strong acid are needed to form fibers of this material. The polymer is spun from polyphosphoric acid, and is formed into either fibers or biaxial sheets. Again, this imparts a severe limitation on the articles that can be produced.

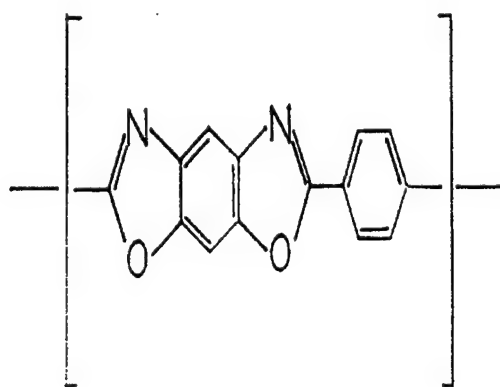


Fig. 10
Molecular Structure of the Lyotropic
Polybenzoxazole

The most recent technology under investigation concerns thermotropic liquid crystal polymers. A typical molecular structure is depicted as Figure 11. This structure is the reaction product of phenylmethyl hydroquinone and terephthaloyl chloride. This polymer is seen to be a polyester and can be made from solution or from the melt. The material behaves as a thermoplastic. A variety of articles can be fabricated by traditional routes such as injection molding or extrusion. The most versatility is seen with these thermotropes; since fibers, sheets, and three-dimensional articles can be fabricated with equal ease.

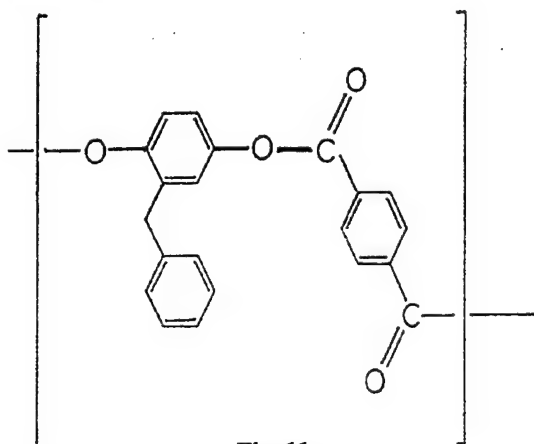


Fig. 11
Molecular Structure of the Thermotropic Reaction. Product of Phenylmethyl Hydroquinone and Terephthalic Acid.

A mysterious phenomena has surfaced during the course of this in-house research. Molded specimens, when subjected to a specified heat-treating cycle, exhibited a phenonema which was termed "physico-chemical annealing". This is defined as the thermotrope losing its thermoplasticity and degrading in the solid state at a temperature well in excess of it original melt transition point. Speculation at this time is that this is not a cross-linking or chain extension sequence of reactions, nor is it a physical annealing phenomena, which is noted in other crystalline materials. It is postulated that a combination of molecular orientation and maximization of intermolecular bonding is occurring, to yield an aggregate of molecules that are tightly locked together when brought below the heat cycle temperature.

Table 1 is a listing of commercially-available liquid crystal polymers. The three lyotropes are currently available as fibers, and can be incorporated into mac-

roscopic structures using traditional composite techniques. These materials are very well characterized in this state, and are readily available. The four thermotropes listed are generally sold admixed with either glass or carbon fibers. The reason they are sold this way is to ensure a good part finish and minimize the anisotropy within the component. As stated previously, part of the charter of this in-house effort is to rationally design propulsion components using the benefit of the laboratory's molecular knowledge to maximize specific strength. The incorporation of the above diluents into the polymer, while yielding an isotropic part, also yields a lower performance part.

Table 1. Commercially Available Liquid Crystal Polymers

<u>Trade Name</u>	<u>Company</u>	<u>Liquid Crystalline Polymer Type</u>
Kevlar 49	Dupont	Lyotrope
Polybenzimidazole	Celanese	Lyotrope
Polybenzoxazole	Dow	Lyotrope
Vectra	Celanese	Thermotrope
Xydar	Amoco	Thermotrope
HX4000	Dupont	Thermotrope
Granlar	Montedison	Thermotrope

This variance between isotropic and anisotropic behavior is best shown by Table 2. This table depicts three different polymers molded in two differing geometries. The transverse tensile strength of VECTRA A950 is 60% of the longitudinal value. The transverse tensile strength of XYDAR SRT500 is 34% of the comparable longitudinal value. XYDAR RC210, a glass-filled resin, has 60% of the tensile properties of the neat resin, when longitudinally molded. It is clear from this table that there exists a great disparity between isotropic and anisotropic values. The focus of future in-house research for this program is to understand the annealing phenomena and to make isotropic space propulsion components.

CONCLUSIONS/FUTURE WORK

The thermotropic liquid crystal polymers can be successfully molded into test articles. These test articles show a high degree of anisotropy, when com-

Table 2. Physical Properties of As-Molded Thermotropic Liquid Crystalline Specimens

Material	Orientation	Tensile Strength (psi)	Tangent Modulus (mpsi)	Admixture
Vectra A950	Transverse	7,470	0.336	Neat
A950	Longitudinal	12,288	1.275	Neat
Xydar SRT 500	Transverse	6,404	0.750	Neat
SRT 500	Longitudinal	19,080	3.130	Neat
Dupont HX4000	Longitudinal	12,001	1.973	Neat
Xydar RC210		11,636	2.304	Glass

pared to glass-filled materials. All domestic base resins have been obtained and are in the process of being molded into test specimens. After tensile testing, propulsion component parts will be fabricated for hot-fire testing. Tensile specimens will be annealed and tested to quantify the increase in structural properties.

The author would like to gratefully acknowledge the following individuals: Chris Frank, McClellan AFB, CA; Rich Griffen, Hill AFB, UT; Jay Shelley, Edwards AFB, CA; and Stephen Osborn, Edwards AFB, CA. This paper would not have been possible without their dedicated effort.

MECHANICAL PROPERTIES OF LIQUID CRYSTAL POLYMERS

J. Shelley
Phillips Laboratory (AFSC)
OLAC PL/RKCCA
Edwards AFB, CA 93523

Abstract:

The solid rocket motor community is constantly striving to develop lower cost, lighter weight components with improved performance. One type of material which shows promise for use in low cost, high performance motor components is Liquid Crystal Polymers (LCP's). These polymers may be able to be exploited for their high strength to weight ratio, good chemical resistance, and high temperature properties. Thermotropic LCP's are relatively new on the market and a suitable database of material properties does not yet exist. Before these new materials can be properly applied to rocket motor components, they must be carefully characterized. This paper presents the results of basic tensile property tests on several neat LCP's. These LCP's are injection molded and are anisotropic with the injection flow. A significant "skin and core" effect can be noted, which limits the thickness of high performance parts. The macroscopic effects of unique Liquid Crystal Polymer microstructure are discussed.

Introduction:

The rocket propulsion community is facing some interesting challenges in the near future. With decreasing defence budgets and increasing costs of individual systems, the Air Force is striving to reduce the acquisition costs and total life cycle costs of its rocket systems, both while maintaining performance and improving system reliability. The drive toward lower cost and higher reliability has lead the propulsion community to search for new materials and manufacturing techniques for its components. Liquid Crystal Polymers show promise for future propulsion applications. The Advanced Polymer Components project at OLAC Phillips Laboratory (AFSC) (PL) is studying the application of Liquid Crystal Polymers (LCP's) to rocket motor and engine components. LCP's exhibit high specific strengths, good solvent resistance, and good thermal stability. Their relatively low coefficients of thermal expansion and good insulating characteristics have lead to applications in the electronics industry for computer circuit boards and components.

Auto manufacturers have been researching the use of LCP's for under-the-hood components because of their excellent solvent resistance and good thermal stability. These same characteristics make these materials attractive for rocket motor and engine components.

Materials:

The particular materials being researched at OLAC Phillips Laboratory are thermotropic liquid crystal polymers. Several manufacturers have injection moldable LCP's on the market. Some, not all, of the products are: Xydar (Amoco) , Vectra (Hoechst-Celanese), HX-4000 (DuPont), and Granlar (Montedison). Most of these polymers are marketed as filled injection molding compounds. Common fillers are chopped carbon fibers, chopped glass fibers, and talcs. Most LCP's are marketed as filled resins for two reasons: to reduce the inherent physical property anisotropy due to flow shear during molding, and to yield parts with acceptable surface finishes. OLAC Phillips Laboratory is researching both filled polymers and neat resins for their chemical and mechanical properties, and potential application to rocket components. Table 1 shows a comparison of some of the published physical properties of several advanced engineering polymers. (The Polyphenylene Sulfide (PPS) and Bismaleimide information is included only for comparison.) The properties shown were collected from the material suppliers and assume isotropic material behavior.

Table 1 Properties of Some Engineering Polymers¹

Name	Ultimate Tensile Strength (Kpsi)	Tensile Modulus (Mpsi)	Heat Deflection Temperature (°F)
Vectra B230	35.6	5.4	428
Vectra C130	23.5	2.2	464
HX4000	13.0	3.1	504
Xydar G-430	19.8	2.3	592
Granlar	20.0	1.85	609
PPS (Ryton)	12.0	0.63	N/A
BMI	7.7	0.52	N/A

Tensile property tests performed on neat resins at McClellan AFB show that these materials do exhibit anisotropy both in ultimate tensile strength and modulus. ASTM D638 tensile test data are presented in Table 2. The values shown are an average of five tests. The test specimen longitudinal axis is oriented parallel to the injection flow direction, while the transverse specimens are oriented across the flow plane. In all cases for which there is data, the longitudinal properties are higher than the transverse properties, some by as much as 300%. However, the strains to failure were comparable for each material. Neat LCP's exhibit ultimate strains between 0.5 and 2%. This data illustrates the dominant material anisotropy.

Table 2 Average Tensile Test Data

Material	Longitudinal		Transverse	
	Strength (ksi)	Modulus (Mpsi)	Strength (ksi)	Modulus (Mpsi)
Xydar 500	23.7	3.9	7.7	1.6
Xydar 300	14.9	2.9	6.1	0.92
HX-4000	12.5	1.9	4.9	0.56
Vectra	11.9	0.77	6.7	0.35
RC 210	12.1	2.5		

Early tensile tests were performed on filled LCP's by the Phillips Laboratory personnel. Test specimens displayed an approximate 30% difference in both tensile strength and modulus between the longitudinally oriented specimens and those oriented transverse to the injection flow direction. The differences measured are outside of the scatter in the data. This property difference implies that material anisotropy should be considered in designing highly loaded components.

Component peculiarities typical of the injection molding process must also be considered when designing highly loaded components of LCP's. The tensile property tests showed a strong tendency for specimens to break in the "cold shot" region near the end of the injection flow length at the mold boundary. Material weakness due to localized flow cooling or flow convergence lines must be very carefully considered when designing highly loaded parts. Rocket motor and engine components are both highly loaded and subjected to extreme environments.

Applications:

Liquid Crystal Polymers have been considered for application to several rocket motor and engine components. Their high strength, good thermal stability, coatability, and solvent resistance makes LCP's attractive for both solid and liquid system nozzles, or nozzle substructures, solid rocket cases and igniter cases, liquid propellant inducers, pump housings, and tankage. Several small demonstration articles have been molded and tested to determine the feasibility of using LCP's for rocket components. Two of the test article are: 2X4 solid motor cases, and hybrid demonstrator nozzle plugs.

2X4 Solid Motor Cases

2X4's are small, 2 inch diameter, 4 inch long solid rocket motors used to test propellant ballistic properties. The 2X4 motor cases used at PL are currently made of steel and are reusable. However, these cases provided an interesting, inexpensive, and relatively low risk vehicle for testing the application of LCP's to solid motor cases. Cases were injection molded of Vectra A625 (25% carbon flake filled), Vectra C130 (30% chopped glass fiber filled), and Ryton (30% glass filled PPS, not a liquid crystal polymer) with both 1/8 and 1/4 inch wall thicknesses. Of the 11 motors fired with 1/8 inch wall thickness, 4 failed due to over-pressurization. The maximum internal pressure achieved was approximately 1300 psi. The cases were designed to achieve approximately 2300 psi using the manufacturers' strength and modulus data. Using material properties generated from in-house testing, the cases should have been able to maintain pressures of 1100 to 1400 psi. This difference in design pressures illustrates an important point. As with many other composite materials, the translation of material properties from manufacturer's data to "as-produced" parts is not good. In this case, the as-molded part strength is only half of the manufacturer's quoted value.

Hybrid Demonstrator Nozzle Plugs²

The Hybrid Demonstrator is a simple hybrid engine with a polyurethane core and gaseous oxygen as the combusting agent. Small plugs were molded to fit the nozzle assembly of the demonstrator to provide long duration heat exposer and thermal shock information on the LCP's. All the materials tested were neat resins: Xydar SRT 300, and SRT 500, Vectra A950, and HX400. Tests ranged in duration from 1 up to 22 sec and from 50 to 90 psi internal

pressure. Significant charring and erosion was noted on all plugs, even after 1 sec of flame exposure. However, all the plugs survived the thermal shock of engine ignition. Loss of structural integrity occurred between 15 and 22 sec for all the materials tested.

Conclusions

Several "quick and dirty" tests have been conducted on Liquid Crystal Polymers to determine their suitability for use in rocket motor and engine components. Although not all of the tests have been completely successful, they have provided valuable insights into LCP processing, part design, and material performance. Many LCP's have very tight processing windows due to rapid melt transitions and high processing temperature requirements. Component weaknesses from flow cooling or flow convergence require careful mold design, mold temperature control, and careful part design. The translation of material properties from manufacturer's data to as molded part performance is not efficient. This poor translation requires that thorough screening and properties testing be conducted on candidate materials and processing techniques to determine suitable design parameters.

In spite of the difficulty of applying LCP's, these polymers present several interesting properties that require further research. A pronounced "skin and core" effect, where the material near a part surface is more molecularly oriented, and therefore stronger, than material closer to the centerline of the part, implies that the structural efficiency of LCP parts decreases with increasing part thickness. This effect may develop into strong, damage tolerant thin structures. Some LCP's may undergo a type of "physio-chemical annealing" that eliminates the melt temperature transition and increases the polymer degradation temperature. This "annealing" phenomenon, if properly developed, may lead to light weight polymer parts for high temperature applications.

Future research being conducted by OLAC Phillips Lab will include examination of the annealing behavior of Liquid Crystal Polymers, design property characterization of these materials, processing effects research, and further component development.

The author acknowledges the efforts of the following individuals who contributed to this paper: Chris Frank, McClellan AFB; Rich Griffen, Hill AFB; Hieu Nguyen, Andrew Kenny, Eric Schmidt, Tom Duffy, and John Rusek, OLAC Phillips Laboratory.

References

¹ Etheridge, L.J., "An Introduction to Liquid Crystal Polymers,"
breifing charts, OLAC Phillips Laboratory, Edwards AFB, CA, Feb
1990.

² Kenny, A and E. Schmidt, "Evaluation of LCP Hybrid Plug Nozzles,"
in-house document under review, OLAC Phillips Laboratory, Edwards
AFB, CA, 1991.

PROPERTY TRANSFORMATION OF THERMOTROPIC LIQUID CRYSTAL POLYMERS

J.J. Rusek, K.P. Chaffee, D.S. Silver
Phillips Laboratory, Edwards AFB CA

ABSTRACT

The advent of commercially available thermotropic liquid crystal polymers has led to novel uses of these plastics in the astronautics community. The Phillips Laboratory at Edwards Air Force Base has taken a strong interest in this area by constructing a large in-house initiative to explore these new materials for both liquid and solid propulsion applications. During the course of the program, a fundamental property, termed annealing, was empirically discovered whereby thermal and chemical resistance of certain thermotropes are increased dramatically by a defined heat cycle after molding.

A fundamental study of this annealing phenomena has shown it to be a function of both rigid rod location and intermolecular forces. X-ray diffraction and atomic force microscopy results will be shown to help understand the complex structure and surface morphology.

INTRODUCTION

Polymeric liquid crystal usage has been pervasive over the last two decades. Lyotropes are processed from an acidic solution. The first commercial lyotrope, KEVLAR, has been used for body armor, heat shields and structural components. The fundamental limitation of KEVLAR's use is in its processing; the most convenient form processed is a drawn fiber. While this geometry maximizes specific tensile strength, compressive properties of an ensemble of fibers are marginal. Macroscopic composites using lyotropic or graphite fibers dispersed in epoxy comprise the current state of the art.

Thermotropic liquid crystal polymers have been in existence for almost as long as the above lyotropes. These materials have not achieved the wide usage of the lyotropes because of high temperatures needed to process and the relatively high cost as compared to commodity resins. Conventional injection molding philosophy is to include fillers such as talc or chopped glass fibers to impart isotropic behavior to the finished part. The inclusion of these fillers also reduces final part mechanical strength by averaging the oriented portions of the part with the off-axis portions.

A proposed way to design and produce a finished part is to injection mold the piece at minimum thickness with no fillers. This assumes that only one preferred direction of strength is needed and that the high shear field of injection molding will create a thick enough boundary layer of highly oriented molecules. Since most real parts need strength in more than one direction at a time, this approach seems flawed.

The rational approach to component design is to focus on the system and see how to manufacture a complete component, not a part to fit an existing geometry. This involves the use of alternate processing techniques, such as blow molding, extrusion and compression molding in addition to injection molding.

Before any design or bulk fabrication can be attempted, the dynamics of the molecular processes of the new material must be studied. The Phillips Laboratory of the United States Air Force has been actively pursuing thermotropic liquid crystal polymers for the last two years by instituting an in-house research effort called Advanced Polymer Components. Many injection molded test articles have been produced with the full collaboration of researchers at Hill and McClellan AFBs. It soon became apparent that the molecular surface morphology and bonding played a key role in determining ultimate macroscopic physical properties. The program was restructured nine months ago to concentrate more on surface phenomena at the molecular level.

CHEMISTRY

Polymeric liquid crystals are generally synthesized by a condensation polymerization. A typical lyotrope, poly(p-phenylene terephthalamide), is conveniently prepared by reacting p-phenylene diamine with terephthaloyl chloride in N-methyl-2-pyrrolidone. The repeat unit structure is shown as Figure 1.

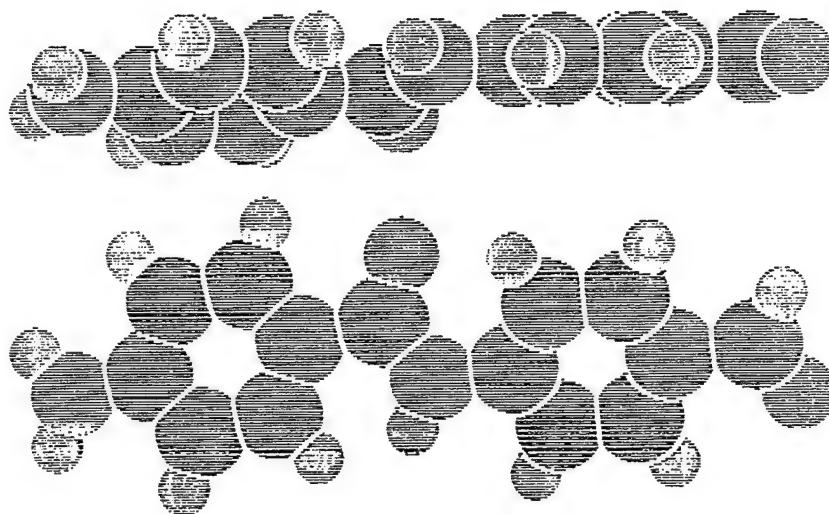


Figure 1
Repeat Unit of poly (p-phenylene terephthalamide)
Hydrogen connections added

An analogous thermotropic polymer, (1-phenylethyl-p-phenylene terephthalate), is produced by the reaction of 1-phenyl-ethyl hydroquinone with terephthaloyl chloride in methylene chloride using pyridine as an acid scavenger. The polymer repeat unit is shown as Figure 2.

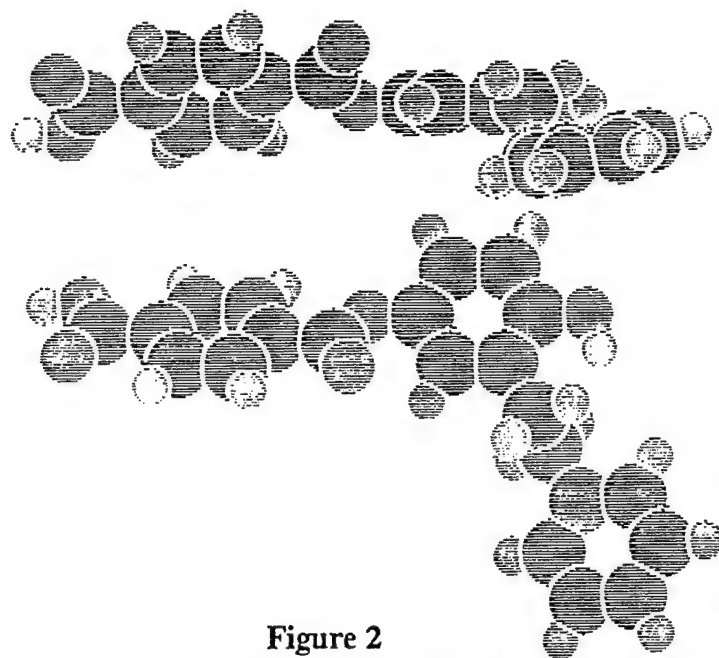
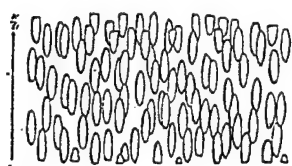


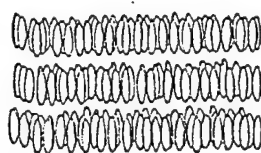
Figure 2
Repeat Unit of poly (1-phenylethyl-p-phenylene terephthalate)
Hydrogen connections added

A comparison of Figures 1 and 2 shows the lyotrope to be a more compact molecule, hence the need for a solvent to cause flow. The thermotrope, on the other hand, is bulkier lending itself to movement on the basis of thermal agitation alone. A side view of the molecules reveals a potential of the thermotrope to stack and lock via the pendant phenyl rings, causing a high degree of crystallinity. This molecular stacking manifests itself as a macroscopic annealing phenomena which has been noted in certain liquid crystalline polymers. True physico-chemical annealing obviates the melting point and improves solvent resistance by this molecular stacking/locking.

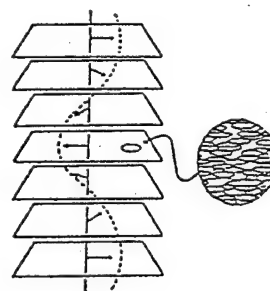
This effect can be made clearer by first understanding that the ensemble of polymer molecules is observed to exhibit only a nematic phase. Figure 3 depicts the three phases of liquid crystalline behavior: nematic, smectic and cholesteric.



NEMATIC



SMECTIC



CHOLESTERIC

Figure 3
Three phases of liquid crystalline behavior

The thermotropic species under investigation in our research are all nematic, having orientation only in the direction of a general geometric director. This can be considered fortuitous in that this should not create any apparent fracture surfaces as would be expected in the smectic case. Unlike an isotropic metal which contains small ($< 4\text{\AA}$) atoms in a defined lattice, the polymer lattice is enormous, containing large ($5 \times 90\text{\AA}$) elliptical molecules. The intermolecular forces determine the ultimate mechanical properties of the polymer article; rate of cooling then plays a profound part on this strength. Polymer annealing allows the molecules to have enough time to orient tightly with respect to each other.

Figure 4 shows the orientation of polymer fragments with respect to themselves.

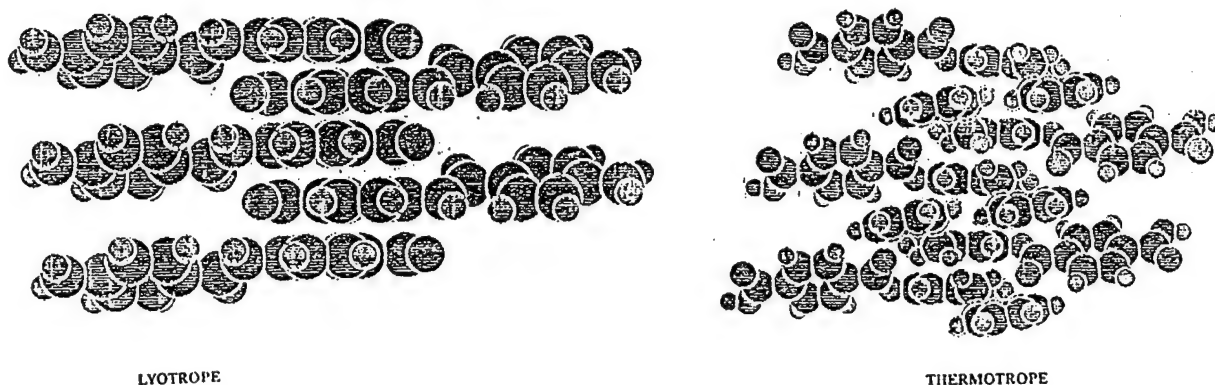


Figure 4
Two dimensional orientation of polymer fragments in model lyotropic
and thermotropic cases

The model lytrope shows a close packing, but it is quite evident that the model thermotrope forms a denser structure once locked. A polymer derived from this model has been synthesized and found to have no melt transition after procedural annealing.

The two largest practical problems to be overcome with the thermotropic species are determining heat transfer rates and delineating the geometric boundaries of the annealing phenomena. Heat transfer rates can be found by laser flash thermometry; this research is underway at the Phillips Laboratory. The definition of annealed regions is not as straightforward; intense x-ray and neutron sources are required to precisely define annealed regions. This is currently done by sectioning molded parts and analyzing end-capped group versus backbone atoms. The jump in this ratio defines an interfacial area where a high degree of orientation occurs. Again, this work is just starting with collaborators at the Deutsches Elektronen-Synchrotron and the Australian Nuclear Science and Technology Office.

X-RAY DIFFRACTION

X-ray diffraction (XRD) is a powerful tool for studying the arrangement of atoms and molecules. Electromagnetic radiation impinging on an atom will be scattered by that atom's electrons. If the target atoms are arranged in a periodic array such that the interatomic separation is approximately the same as the wavelength of the incident radiation, the scattered radiation can, under certain conditions, form interference patterns. The interference maxima are the diffracted beams. The intensity of the maxima depend on the identity of the scattering species. In general, the repetitive units in the array are not monatomic. The

mathematical relationship between the wavelength λ and characteristic length of the array D is given by the Bragg equation:

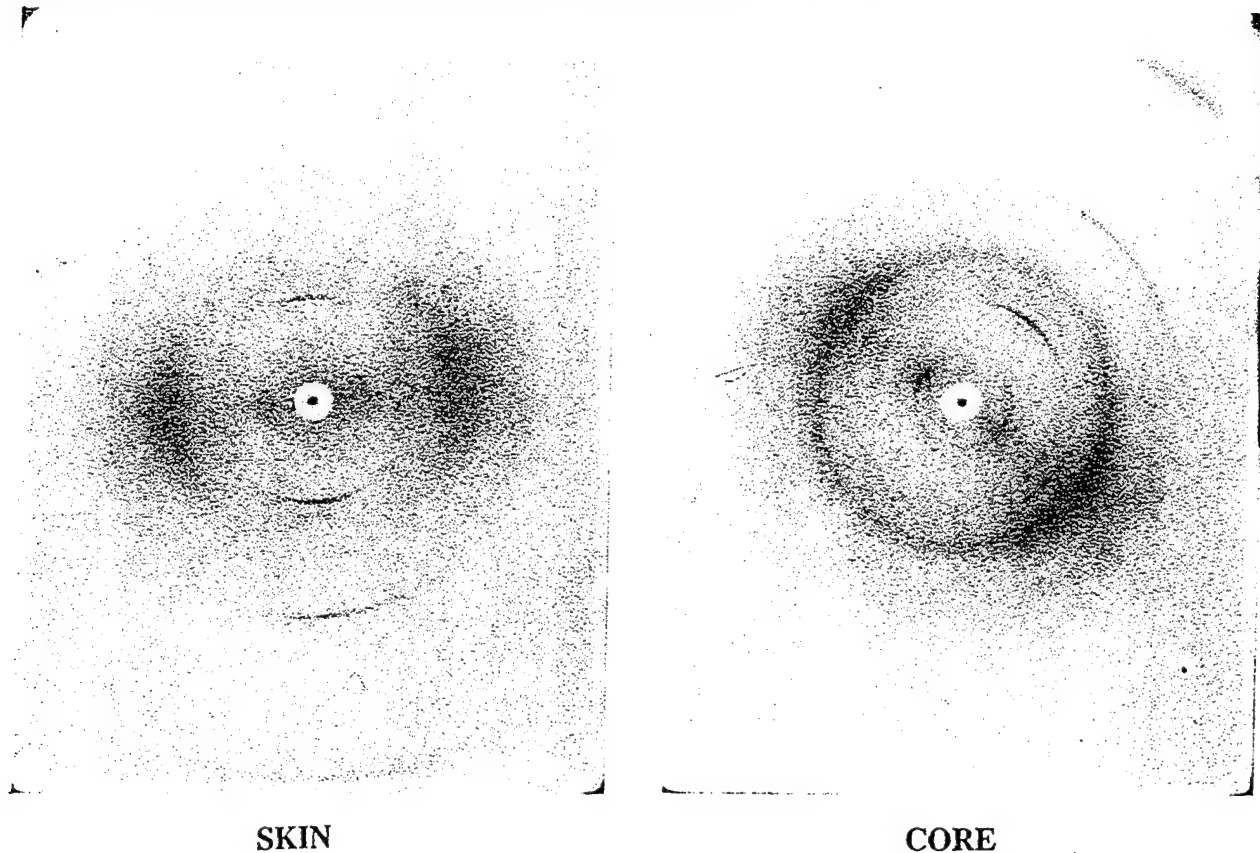
$$n\lambda = 2D\sin\Theta$$

where n is an integer and Θ is the half-angle between the incident radiation path and the diffracted beam. For a given wavelength and D , the angle θ satisfying the above equation is called the Bragg angle. The shapes of the diffracted x-ray beams are determined by instrumental effects and the crystallinity of the target.

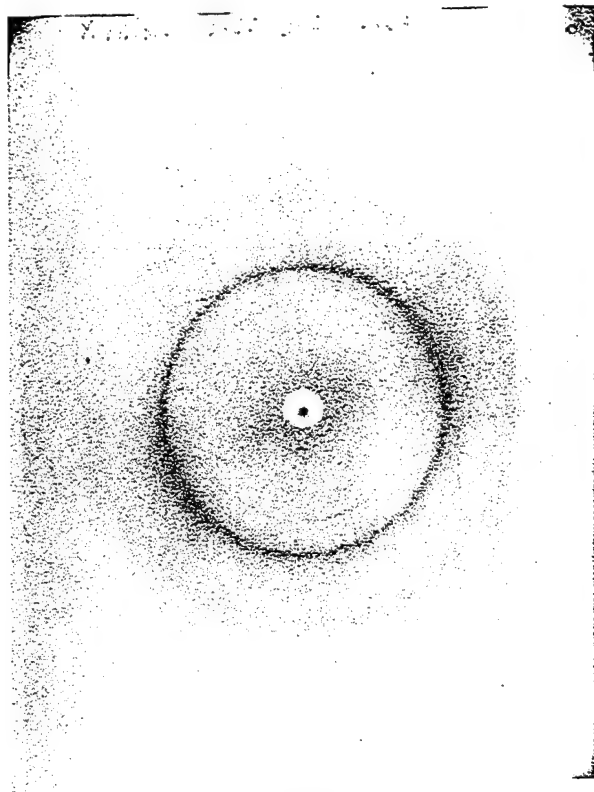
The XRD method applied in this study utilized x-rays produced by a Philips Electronics XRG3100 generator operated at 45 kV and 30 mA. The diffraction patterns were created with nickel filtered copper K_{α} radiation ($\lambda = 1.54$ Angstroms) and a flat plate camera with pin-hole collimation. Although accurate measurements of the diffracted x-ray location are easily obtained, the determination of quantitative intensity information from the photographic film is not possible.

The "skin" and "core" samples were prepared by milling 175–300 μm thick plates from the appropriate regions of injection molded thermotropic liquid crystalline polymer tensile specimens. The four commercially available polymers studied were XYDAR SRT-300 and SRT-500 (AMOCO), HX-4000 (DUPONT), and VECTRA A950 (CELANESE).

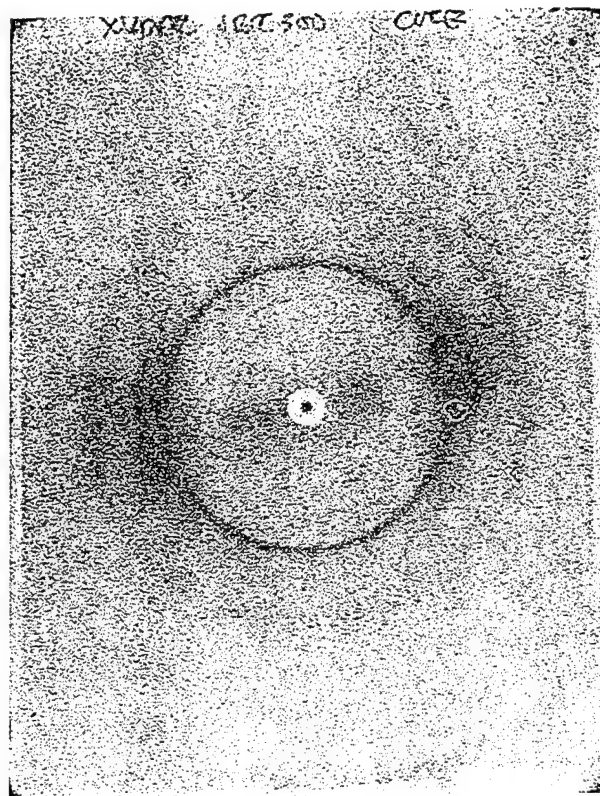
Figures 5,6,7 and 8 are the x-ray film exposures for HX-4000, SRT-300, SRT-500 and A950, respectively. The a. and b. portions denote skin and core regions, respectively.



Figures 5a and 5b
X-ray diffraction patterns of DUPONT HX-4000 polymer taken of skin and core regions

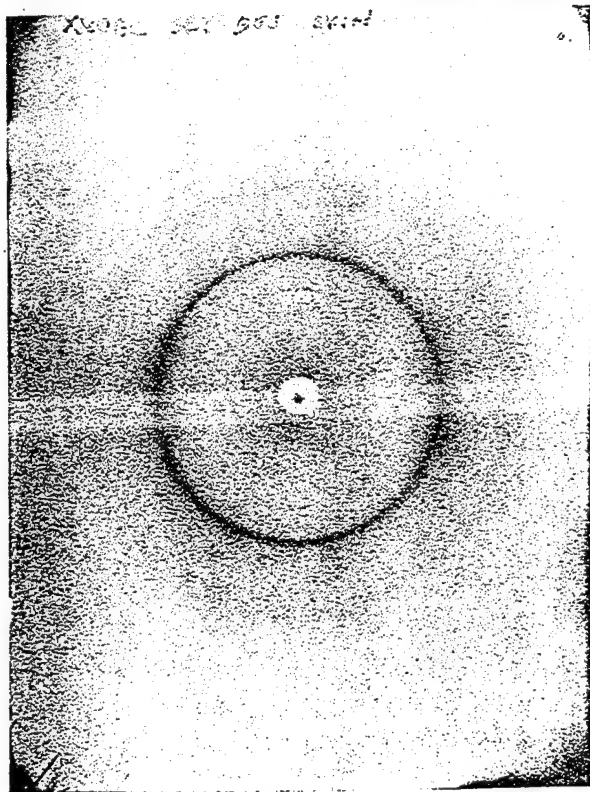


SKIN

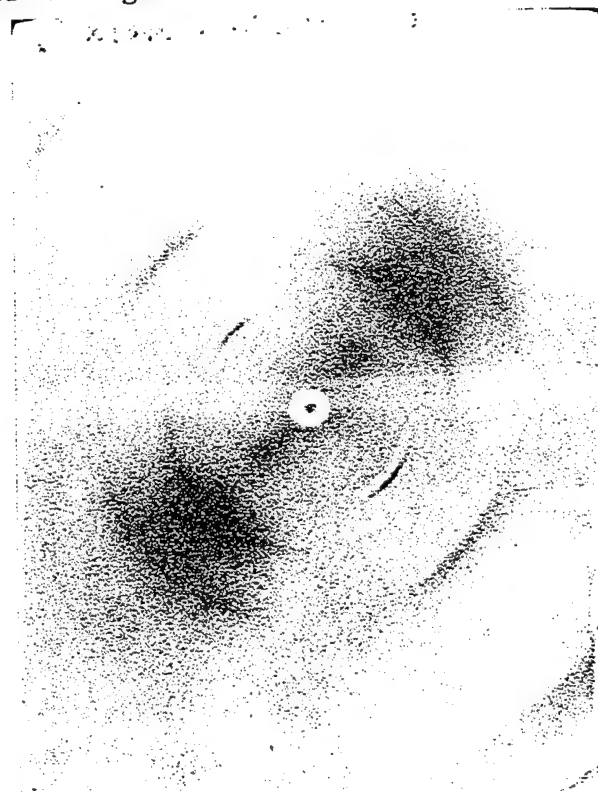


CORE

Figures 6a and 6b
X-ray diffraction patterns of AMOCO XYDAR SRT-300 polymer
taken of skin and core regions

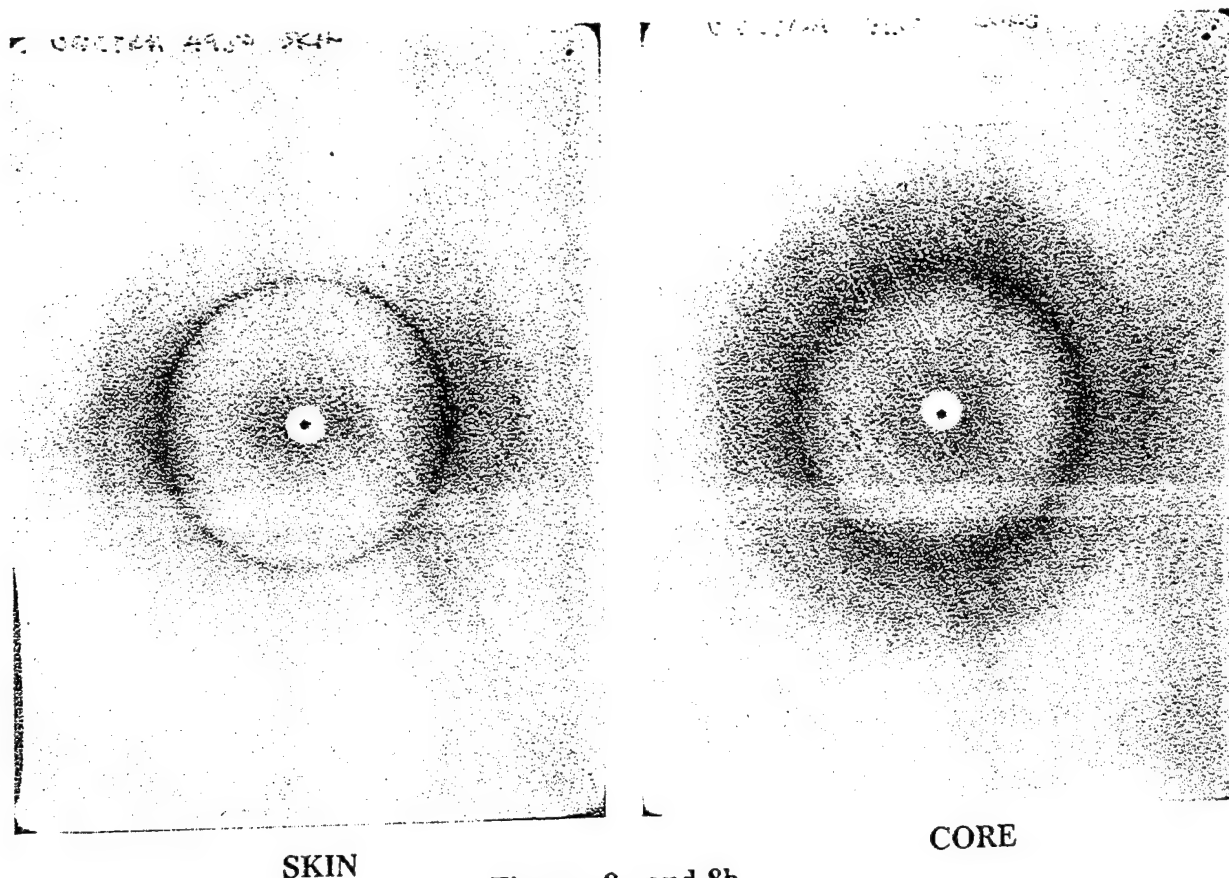


SKIN



CORE

Figures 7a and 7b
X-ray diffraction patterns of AMOCO XYDAR SRT-500 polymer
taken of skin and core regions



SKIN **CORE**

Figures 8a and 8b
X-ray diffraction patterns of CELANESE VECTRA A950 polymer
taken of skin and core regions

By measuring the ring radii and applying the above Bragg relation, interatomic and intermolecular distances were calculated. The most striking observation is that all of the polymers, both in skin and core, exhibit an interatomic spacing of 4.3 Å. A calculated absolute minimum spacing based on the common pendant carbonyl group yields a value of 3.94 Å, showing that the experimental value is in excellent agreement.

The patterns generated by both HX-4000 samples (Figure 5) show no difference between the skin and core along the length of the molecule, however a profound difference is noted between molecules. A common ring from 12.6 and 4.3 Å is noted in both, but a double ring at 6.1 and 6.4 Å is seen. These values do not fall in the range of harmonics and are indicative of a well-established crystalline domain in the core.

A comparison of Figures 6a. and 6b. with 7a. and 7b. shows the polymers to have identical habits. There is no discernable difference along the polymer major axis in both SRT-300 and 500, however, there is a profound difference between each skin and core between polymer molecules. The core regions contain a much richer crystal habit (more developed) than the skin. This is noted by the more defined diffraction rings.

The VECTRA A950 x-ray patterns, shown as Figures 8a. and 8b. show more striking differences. The parallel axis distances are obviated within the core, while the skin shows a strong ring at 6.5 Å. The intermolecular distances are the same for both skin and core. This is indicative of a total random mix of polymer rods in the core with locally established domains.

ATOMIC FORCE MICROSCOPY

The Atomic Force Microscope (AFM), introduced in 1986 by Gerd Binnig and Calvin F. Quate of Stanford University, is one of several scanning-probe microscopes that operates on similar principles as the

Scanning Tunnel Microscope (STM). The AFM allows three-dimensional imaging over a surface topography using a computer system that reproduces the images electronically on a color graphics monitor. The AFM consists of a shard of diamond fashioned into a sharp tip, which attaches to a metal cantilever about 100 to 200 microns in length. The tip and a specimen are brought together close enough such that the electron clouds between the two repel. The specimen is then scanned under the tip in an 'X' direction, while moving incrementally in the 'Y' direction with each successive 'X' scan. The STM senses surface morphology using a tunneling current rather than electrostatic repulsion and therefore is restricted to conductors and semi-conductors. Deflections of the cantilever vary along the 'Z' direction according to the surface relief. All three motions contribute to an image of the specimen's surface. Deflections of the cantilever result from electrostatic forces between the tip and the specimen, which can be an insulator, as well as a conductor. Deflections are detected by a laser beam from a laser diode focused upon a spot on the back of the cantilever foil which reflects it to a photodiode sensor. Movements in all three directions are made possible by a rigid piezoelectric tubing upon which the specimen rests. Piezoelectrics have the property of exhibiting mechanical strains, e.g. expansion and contraction, when placed under an electric field. A feedback loop uses the deflected beam as an input to control the 'Z' movement created by the forces between the tip and specimen by applying a voltage to the 'Z' portion of the piezoelectric tubing.

The data for the thermotropic liquid crystalline polymers (LCPs) presented here was acquired using a Digital Instruments NanoScope II. The images were obtained by the measurement of cantilever deflections as the polymers are scanned under the tip. The atomic forces involved are of the order of 10^{-9} Newtons.

Four LCPs were studied using the AFM, each having its surface characterized in two locations along the flow lines of the injection-molded material. One study was made immediately below the exterior portion of the skin, and the second study was within the interior or core region. Samples measuring 2mm^2 were dissected from each region and supported on a magnetic disk which rests on the AFM scanner. These samples were held in place by double-stick tape and were made flat so that the AFM tip could track over its surface with little resistance. The cantilever tip scans each section perpendicular to the flow lines. Figure 9 shows a schematic of the AFM.

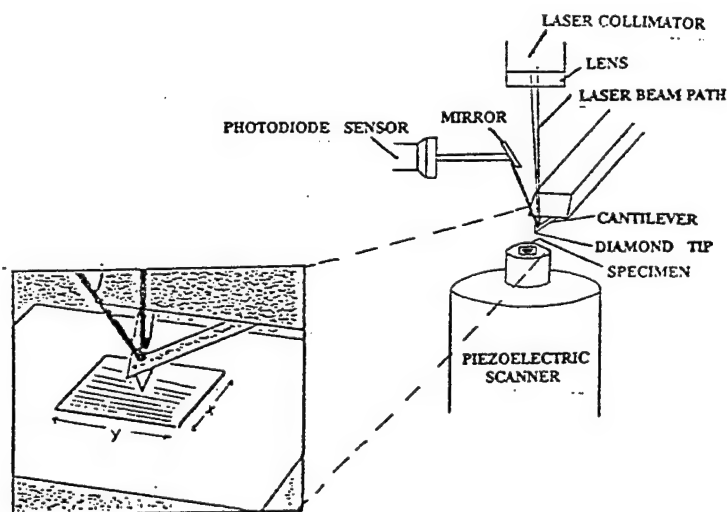
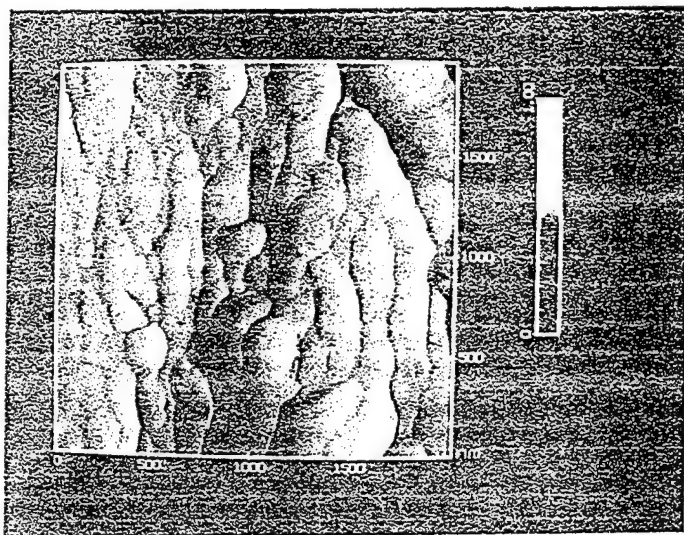


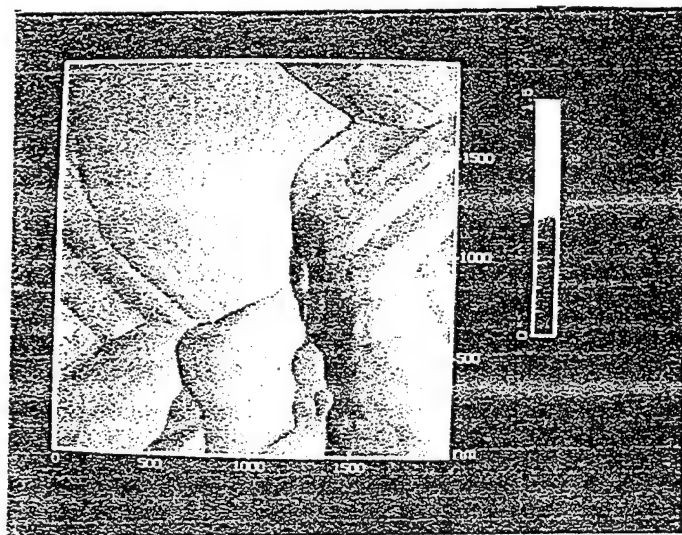
Figure 9
Schematic of Atomic Force Microscope

The AFM process under the best conditions proves to be time-consuming and labor intensive. The microscopic roughness, characteristic of these samples, made scanning particularly difficult since the surface roughness often inhibited or broke the tip and cantilever. Images that reproduce under many scans, at a scan rate of no more than 3.5Hz, are illustrated in this report.

Figures 10, 11, 12, and 13 depict AFM images of HX-4000, SRT-300, SRT-500 and A950. Both skin and core samples are shown as parts a. and b., respectively. Scan size is 2000 nm in all cases.

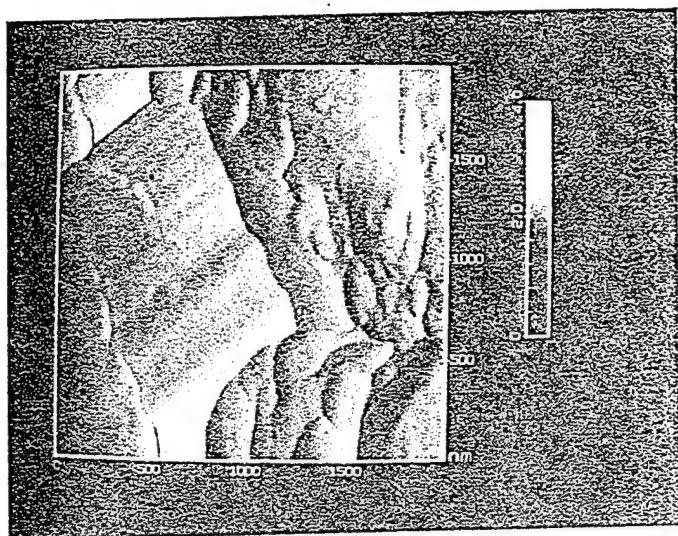


SKIN

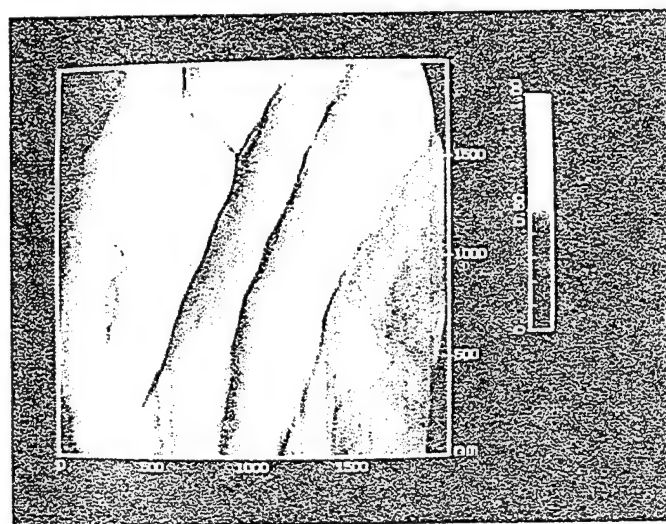


CORE

Figures 10a and 10b
AFM images of DUPONT HX-4000 polymer taken of skin and core regions

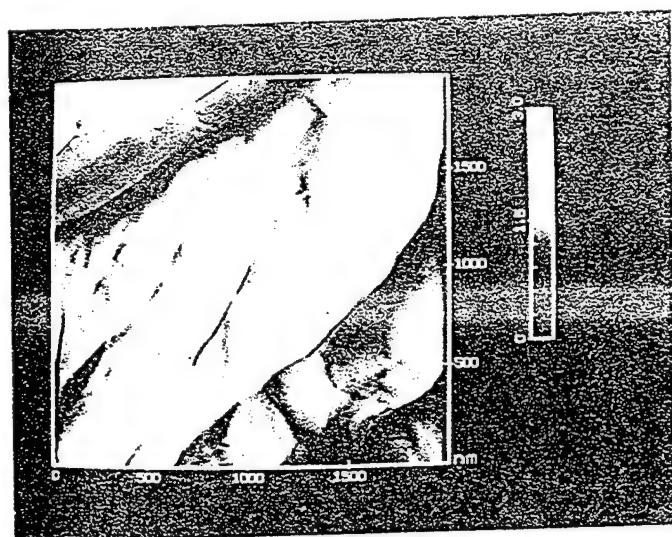


SKIN

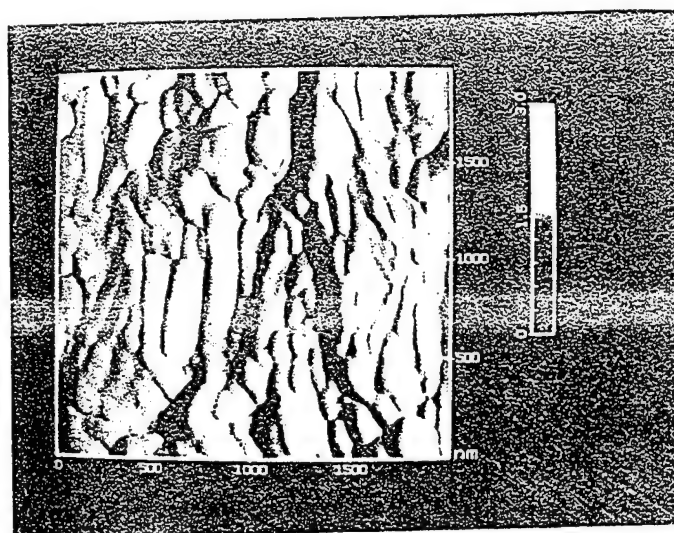


CORE

Figures 11a and 11b
AFM images of AMOCO XYDAR SRT-300 polymer taken of skin and core regions

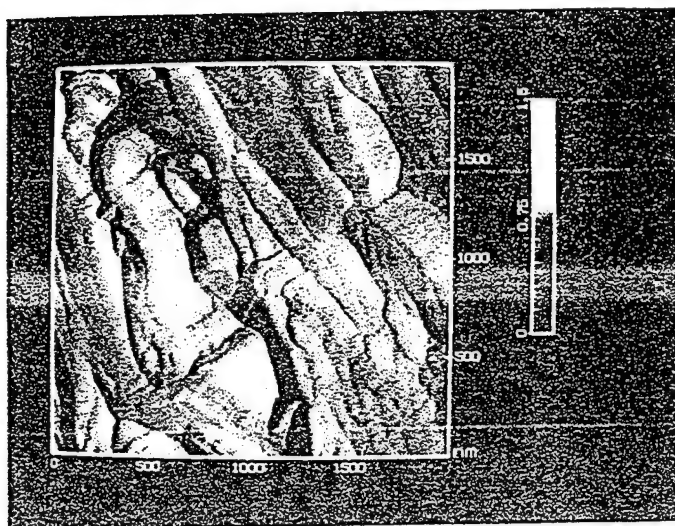


SKIN

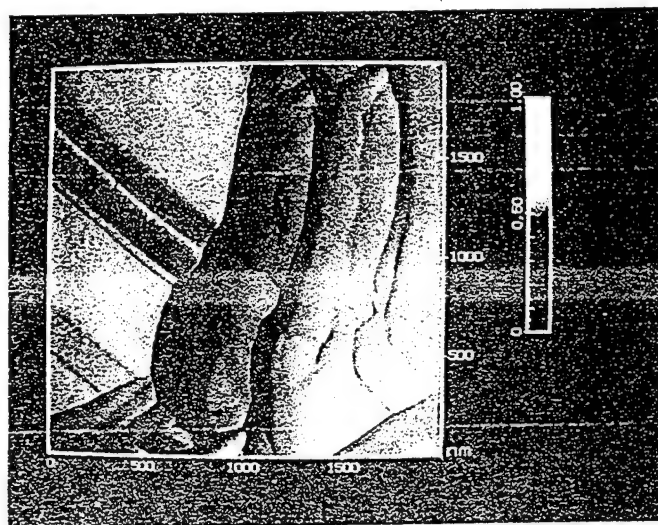


CORE

Figure 12a and 12b
AFM images of AMOCO XYDAR SRT-500 polymer taken of skin and core regions



SKIN



CORE

Figure 13a and 13b
AFM images of CELANESE VECTRA A950 polymer taken of skin and core regions

There is a pronounced difference between the skin and core sections; the skins show smaller crystallites while the core sections show larger, well defined crystalline regions. This observation is in agreement with the x-ray results discussed previously.

The AFM images of HX-4000, shown as Figures 10a. and 10b. both show the same orientation. The significant difference in skin and core is noted by the crystallite size. The skin shows average nodules that are 1X1 ellipses with widths of 300nm while the core shows 1X1 ellipses with average widths of 1000nm.

Figures 11a. and 11b. show AFM images of SRT-300 in skin and core regions. The skin region is highly oriented with small crystallites and the core shows large crystalline regions. Again, the skin crystallites are 1X1 ellipses with an average 300nm width. The significant difference is that the core contains 10X1 ellipses with 400nm average widths.

The companion polymer, SRT-500, is shown by AFM images as Figures 12a. and 12b. This polymer has the most pronounced orientation difference between skin and core. The small crystallites in the skin exist as 200nm 1X1 ellipses while the core shows average crystallites of 400nm width grown as 10X1 ellipses.

The final polymer, A950, is shown by its AFM images as Figures 13a. and 13b. The skin region is highly oriented along the flow axis while the core is essentially isotropic, having a multitude of large crystalline regions at random orientations. The skin shows crystallites of 200nm 1X1 ellipses and the core shows average crystals of a 10X1 geometry having a width of 1600nm.

SUMMARY AND CONCLUSIONS

It has been the intent of this paper to show the profound anisotropy that exists within injection molded specimens of liquid crystal polymers. From this it is clear that the morphology, hence the physical properties, change within molded articles as a function of depth. This should be regarded as a great strength of these materials since it is possible to produce rationally designed parts that behave as true molecular composites. The approach to arrive at this has been to use a diffraction technique and a morphological technique in concert to arrive at the following conclusions:

Anisotropy exists between the so-called skin and core regions in the tested commercial LCP resins.

All of the analyzed polymers exhibited an interchain spacing of 4.3 Å.

The most isotropic core was shown to be VECTRA A950.

All skins aligned with the formation of smaller nodules or crystallites.

All cores formed large crystals. This phenomena was most probably due to the slow (> 30 min.) cooling of the part core.

HX-4000 was shown to have the same general crystal shape within the skin and core.

SRT-300 and 500 exhibited similar physical behavior even though chemically different.

ACKNOWLEDGEMENTS

We would like to gratefully acknowledge the following: Joe Mallon and Pat Adams of Aerospace Corporation for taking the x-ray data and Chris Frank of McClellan AFB and Rich Griffin of Hill AFB who designed and manufactured the test specimen molds and dogbones.

POLYESTER SYNTHESIS
AND ANALYSIS

Brad M. Lormand
Student

Rosamond High School
2925 Rosamond Boulevard
Rosamond, CA 93560

Final Report for:
Summer Research Program
Phillips Laboratory

Sponsored by:
Air Force Office of Scientific Research
Bolling Air Force Base, Washington D.C.

August 1992

POLYESTER SYNTHESIS AND ANALYSIS

Brad M. Lormand
Student
Rosamond High School

Abstract

Polymers were created by an acid-base reaction of terephthaloyl chloride and three different hydroquinone monomers. The three used were hydroquinone, tertiary-butyl hydroquinone, and phenyl hydroquinone. Before synthesis, the three base monomers were purified by crystallization and the solvents used were distilled to insure a lack of contaminants. The polymers were formed by slowly adding the terephthaloyl chloride to a solution of one the hydroquinones in pyridine and methylene chloride or diethyl ether. When completed, the newly formed product was washed with distilled water followed by acetone. Then, Thermal Analysis and Fourier Transform Infrared (FTIR) spectroscopy were performed on the three different species.

POLYESTER SYNTHESIS AND ANALYSIS

Brad M. Lormand

INTRODUCTION

As the needs for space colonization and exploration increase, so does the need for lightweight materials that can be applied to rocket motor casings and other integral parts of the spacecraft and its propulsion system. Therefore, the need for new polymers is rising at a fever pitch. This summer's research dealt totally with the making of 3 hydroquinone polymers, the purification of the needed ingredients, and the analysis of the finished product by various means. These polymers had never before been made at Phillips Laboratory and success was questionable. However, the polymerization worked successfully and three species were created that proved to have the predicted thermal properties. The created substances were compressed into pellets and demonstrated high melting points or no melting points at all. Presumably, a practical use can be found for these polymers in some level of application.

PREPARATION

Before starting the actual synthesis, many preparatory steps were taken to insure the formation of the purest polymers possible. Unwanted impurities included non-reactive components that might inhibit proper polymerization. Each base monomer would need to be crystallized from a saturated

solution and the solvents used would have to be distilled to 99.9+% purity. To begin with, each hydroquinone monomer was tested for solubility in various solvents. Hydroquinone (HQ) was readily soluble in distilled water. Tertiary-butyl hydroquinone (TBHQ) and phenyl hydroquinone (PHQ) were both soluble in methylene chloride (MCL). Small samples of 5% solutions of each of these were made for analysis by the gas chromatograph/mass spectrometer. This gave an idea of impurities that were present in the products being used before crystallization. This piece of equipment was used again to analyze the purified products and to show whether or not the impurities were being removed.

The MCL and water needed for crystallization were distilled and collected in 5 liter glass flasks. For each crystallization, a small amount of solvent was poured into a flask and heated on a hot plate. One of the HQ monomers was added until no more could be dissolved. The solution was then gravity filtered into a sealable container and cooled. A seed crystal of the same monomer was added to start the formation of the crystals. When the process was complete, the mixture was then vacuum filtered and the purified monomer crystals were put in a dish and dried in a vacuum oven at 100 degrees Celsius to dry off all solvent used. These monomers would serve as the base half of the acid-base polymerization reaction.

The acid half of the reaction was created by adding a measured amount of terephthaloyl chloride (TCL) to MCL. This

can form terephthalic acid (TA), by reacting with water vapor in the air. Therefore, the chloride needed to be filtered by a syringe pump, thereby keeping it dry and chemically unchanged. The purified monomers and acid solution were then analyzed by the gas chromatograph and showed to be 99.5% pure or better (pgs. 17-13 to 17-20).

Another crucial part of preparation is the calculations concerning monomer/solvent concentration and polymer yield. Every monomer used an equal molar value, with the exception of pyridine, which was twice the molar amount of monomer. The theoretical yield of polymer was based on the equivalent amount of moles of reactants.

Also before the synthesis was performed, the predicted structures of the polymers were created using the computer program, Desktop Molecular Modeller by Crabbe and Appleyard, Oxford University Press. The program found the minimized energy state for each polymer and gave an accurate plot of each. The results of minimization (pg.17-10) showed that each polymer forms straight chains with each of its rings twisting in alternating directions.

POLYMERIZATION

The process by which all three polymers were synthesized used a 3-necked reaction flask, ice bath, hot plate, beakers, heating module, and vacuum filter. The reaction flask had a thermometer and stirrer. A neck held a container that was occupied by the measured amount of acid solution. This con-

tainer was equipped with a manipulatable regulator to control the addition of the acid inside into the reaction flask. The base solution was made with the proper amount of HQ, solvent and pyridine. MCL was used as the solvent for TBHQ and PHQ, but distilled diether was needed for HQ because of HQ's lack of solubility in MCL. The concocted base solution was then poured directly into the bottom of the reaction flask and brought down to zero degrees Celsius by placing an ice bath around the bottom of the flask. When the proper temperature was achieved, the addition of the acid solution began. This reaction proved to be highly exothermic, so the addition of the acid was kept very slow to avoid boiling away the solvent(s). When all the acid solution was finally added, the now milky mixture was cooled down to zero degrees. At this point, a white solid substance could be seen in the bottom of the flask. After a few minutes at zero degrees, the ice bath was replaced by the heating module. The acid container was then replaced by a condenser that led to another flask collecting vaporized solvent(s). During the heating of the mixture, an amount of water ten times the predicted polymer yield was added. This addition would aid in the removal of pyridinium hydrochloride, a by-product of the reaction. With almost all of the MCL having been removed, the reaction flask was removed and its contents poured through a vacuum filter. What remained appeared to be the desired polymer with a small amount of by-product contaminants. These unwanted substances were removed by multiple water and acetone washes, again each

being ten times the calculated theoretical yield by weight. Following each wash, the water or acetone and polymer mixture was again vacuum filtered. When all washes were done, the finished product was set in a vacuum oven to dry overnight.

Each of the three polymerizations performed with HQ, TBHQ, and PHQ were done in almost exactly the same way, with the exception of the making of the HQ polymer. The actual reaction seemed to be only slightly exothermic, so the ice bath was removed. All other steps described were applicable to all three polymerizations.

ANALYSIS

Following the making of the three polymers, some scientific analysis of the finished products was performed. Each polymer specimen was weighed and the actual yield was calculated. The making of the HQ/TA polymerization resulted in only a 59% yield. A substantial amount of low molecular weight polymer was lost in the vacuum filtering of the acetone wash. Some of the smaller particles fell through the filter paper into the collection of liquid impurities. The TBHQ/TA polymerization resulted in a 95% yield; PHQ/TA, a 78% yield.

Another of the analytical procedures performed on each polymer was FTIR spectroscopy. This equipment analyzed the frequency of the emitted radiation produced by molecular vibration. Careful analysis of the data produced gave an idea of the structure of each polymer. The data on page 17-11

shows the presence of the substituent tertiary-butyl and phenyl groups in their respective polymers.

Thermal analysis performed on compressed pellets of each polymer showed that all three exhibit high melting points or no melting points at all (pg 17-12). The TBHQ/TA polymer showed to have a melting point of about 392 degrees Celsius. The PHQ/TA polymer melted at about 320 degrees Celsius, but the HQ/TA polymer appeared to initially degrade at about 289 degrees Celsius without a melt.

CONCLUSION

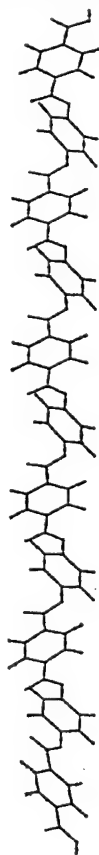
Over the course of eight weeks, much success was had in the synthesis of three relatively new polymers, the purification of the monomers and solvents needed for synthesis and the analysis of the finished products. The polymers made appeared to be suitable for many applications on Earth and in space, but only further testing and analysis can prove their usefulness. The research just done shows that each polymer can be made easily and with desirable efficiency.

ACKNOWLEDGEMENTS

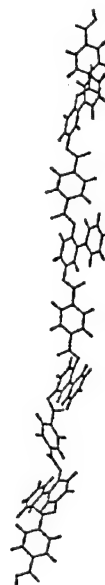
There are many people at Phillips Laboratory that deserve my gratitude for a successful summer of research. I would like to give a sincere thank you to my mentor, John J. Rusek, for guiding me through just about everything this summer. I would have been severely lost the whole time without him. Also, a great thank you to Dr. Kevin Chaffee, Dr. David Elliott of Arkansas Tech University, Steve

Osborn, Robert Behdadnia, Tracy Reed, Alex Kitty and Mindee Jeffery for various reasons including calculus and physics lectures, broadening of my computer literacy, reduction of data, and friendship. I also owe thanks to Mike Carr for all his patience in teaching me what GCMS and FTIR were actually doing and his assistance in collecting the necessary data. Finally, I give my love and thanks to my grandmother, Betty Willey who always gave me love and support and free rides to and from work.

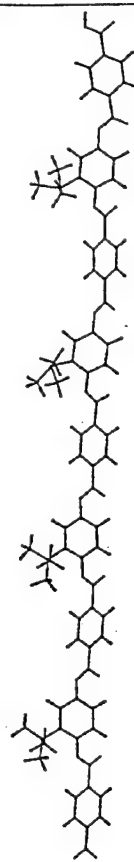
HQ/TA Polymer

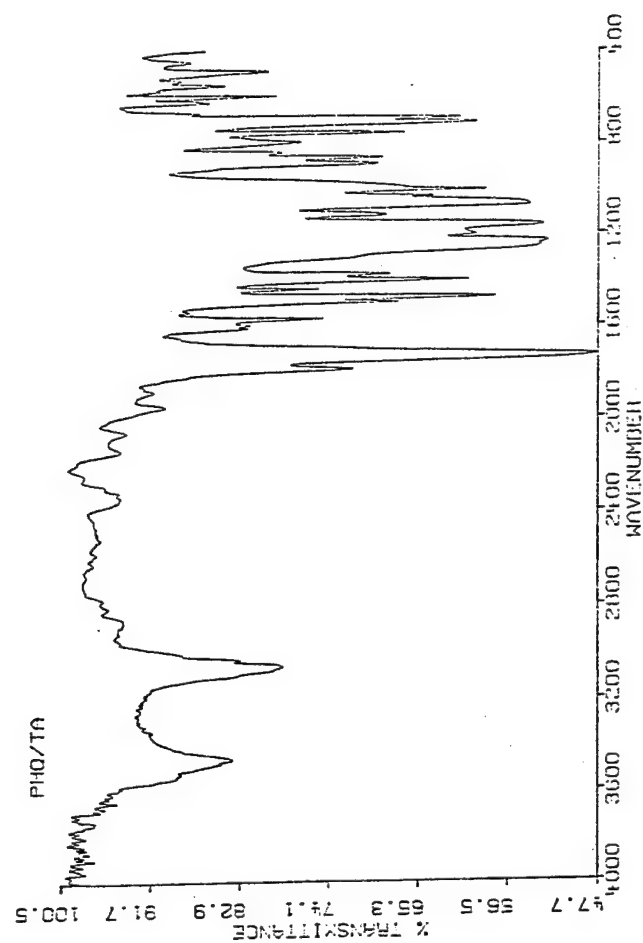
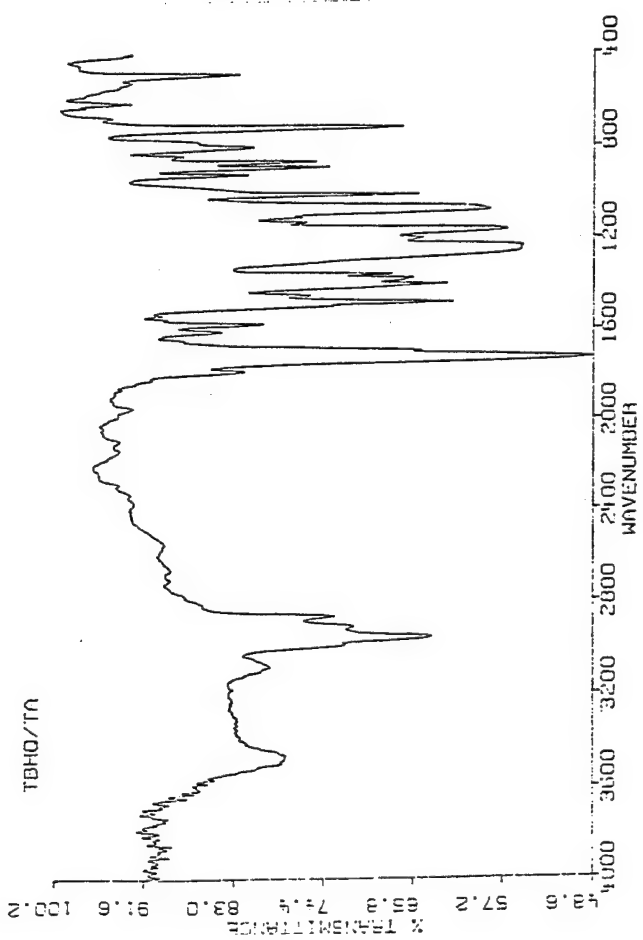
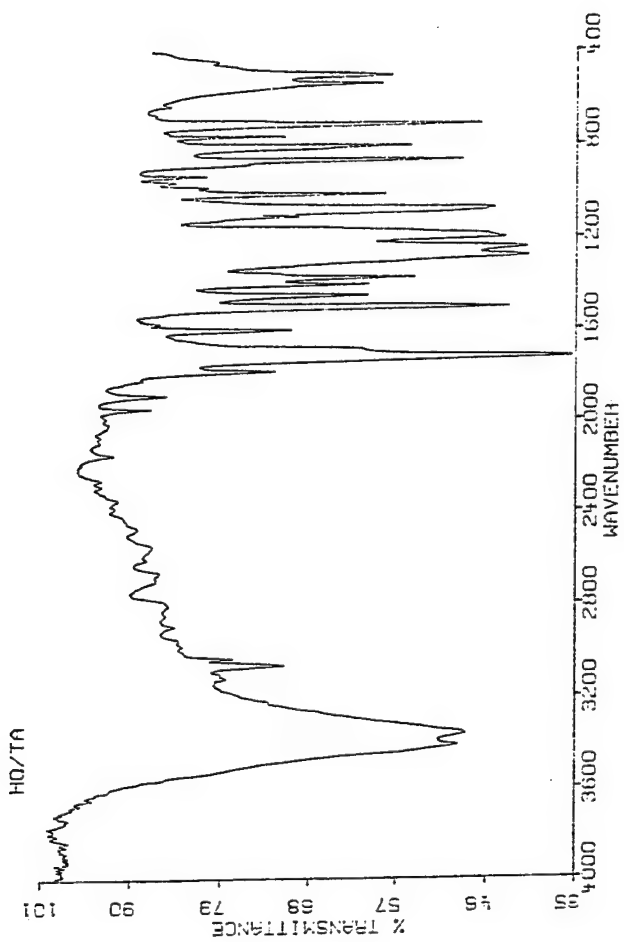


PHQ/TA Polymer



TBHQ/TA Polymer

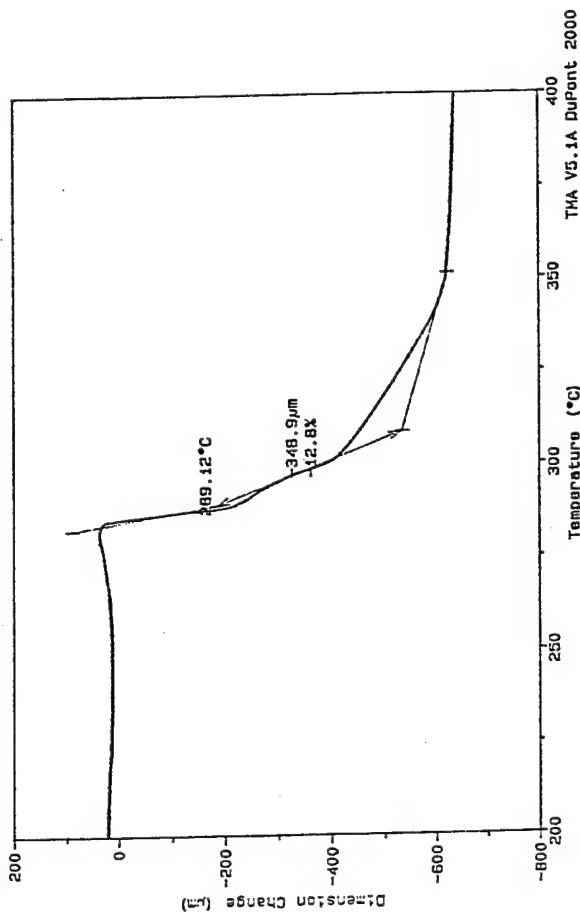




Sample: HQ/TA POLYMER
 Size: 2.7230 mm
 Method: TMA ON LCP
 Comment: RATE 3°C/MIN, NITROGEN ATMOSPHERE 50 ML/MIN, 10 GRAM HEIGHT

TMA

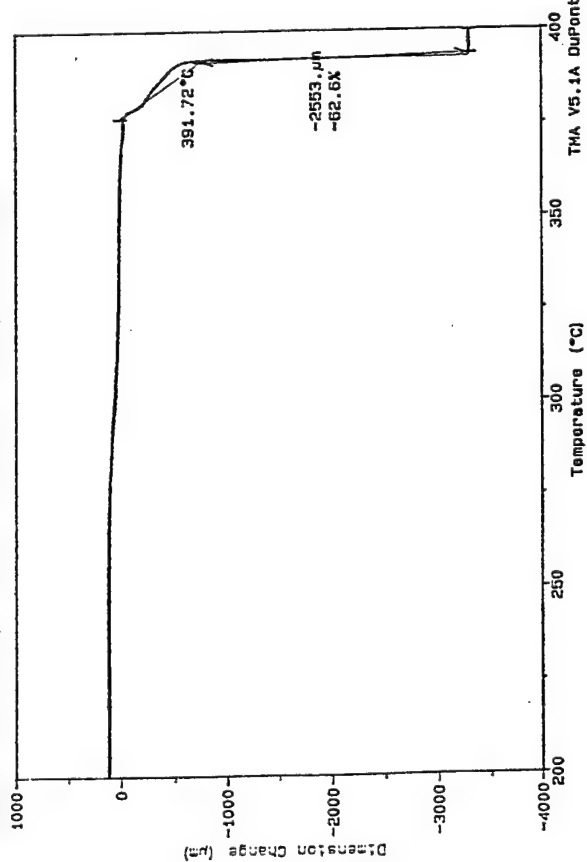
File: C:\TMAJOHN.30
 Operator: PAUL JONES
 Run Date: 6-Aug-92 12:15



Sample: TG/TA POLYMER
 Size: 4.0760 mm
 Method: TMA ON LCP
 Comment: RATE 3°C/MIN, NITROGEN ATMOSPHERE 50 ML/MIN, 10 GRAM HEIGHT

TMA

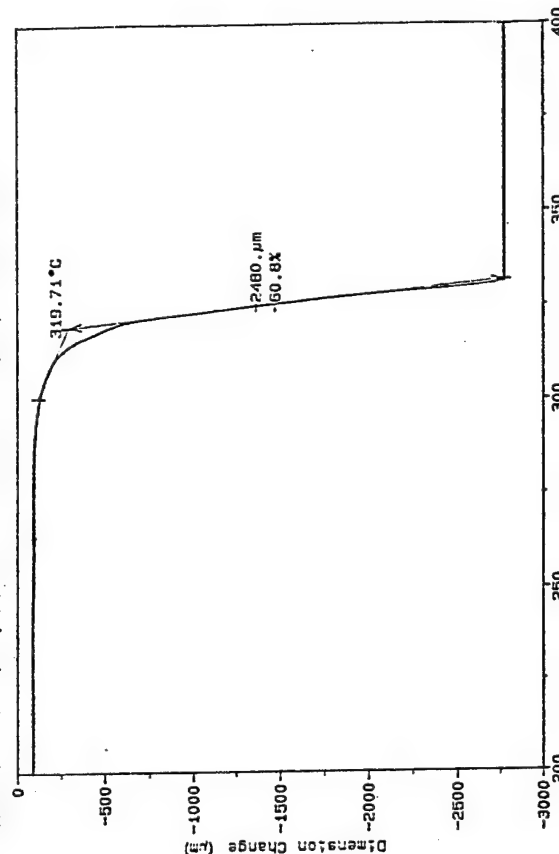
File: C:\TMAJOHN.31
 Operator: PAUL JONES
 Run Date: 6-Aug-92 15:42



Sample: PHQ/TA POLYMER
 Size: 4.0760 mm
 Method: TMA ON LCP
 Comment: RATE 3°C/MIN, NITROGEN ATMOSPHERE 50 ML/MIN, 10 GRAM HEIGHT

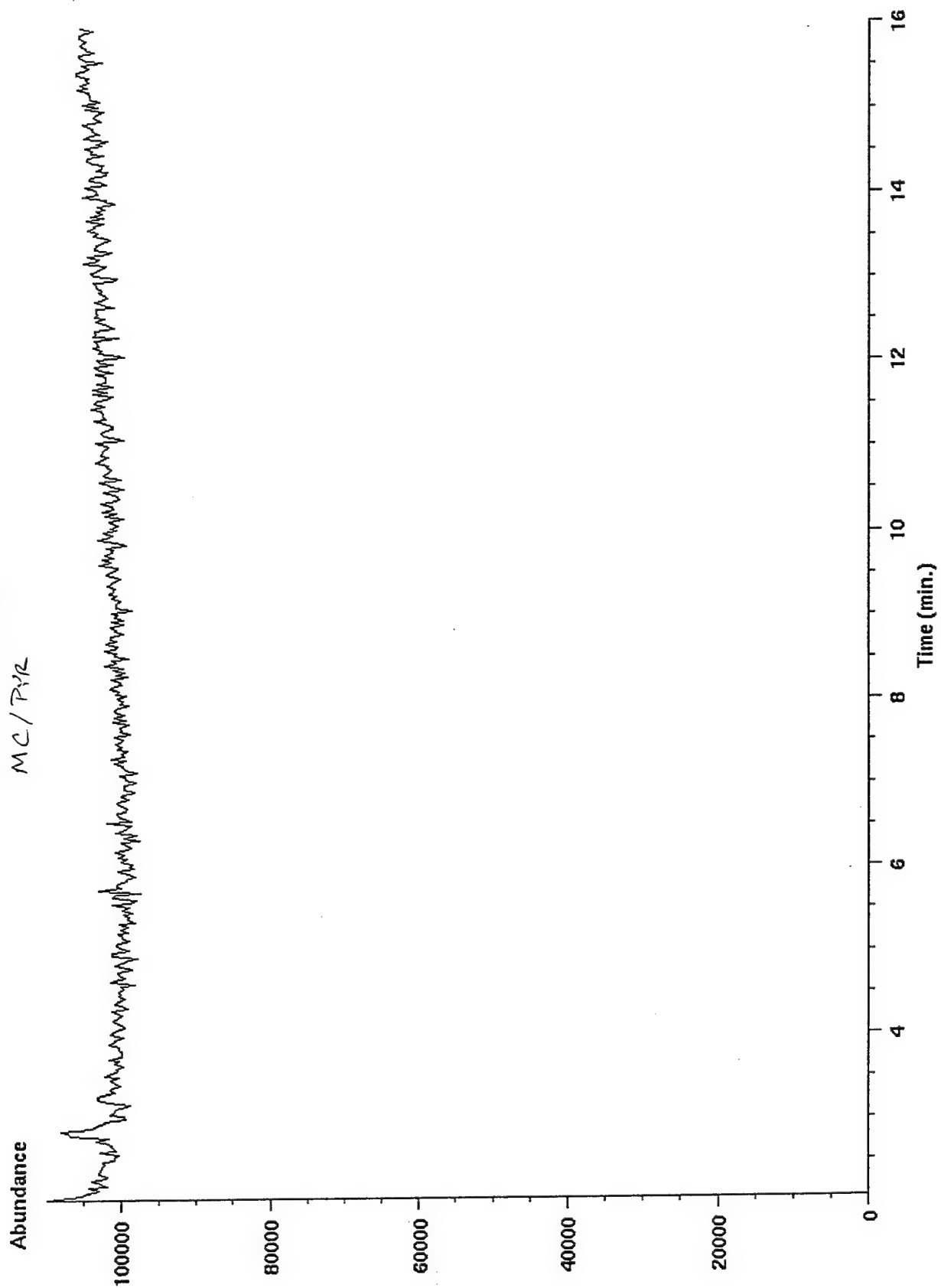
TMA

File: C:\TMAJOHN.33
 Operator: PAUL JONES
 Run Date: 7-Aug-92 07:30



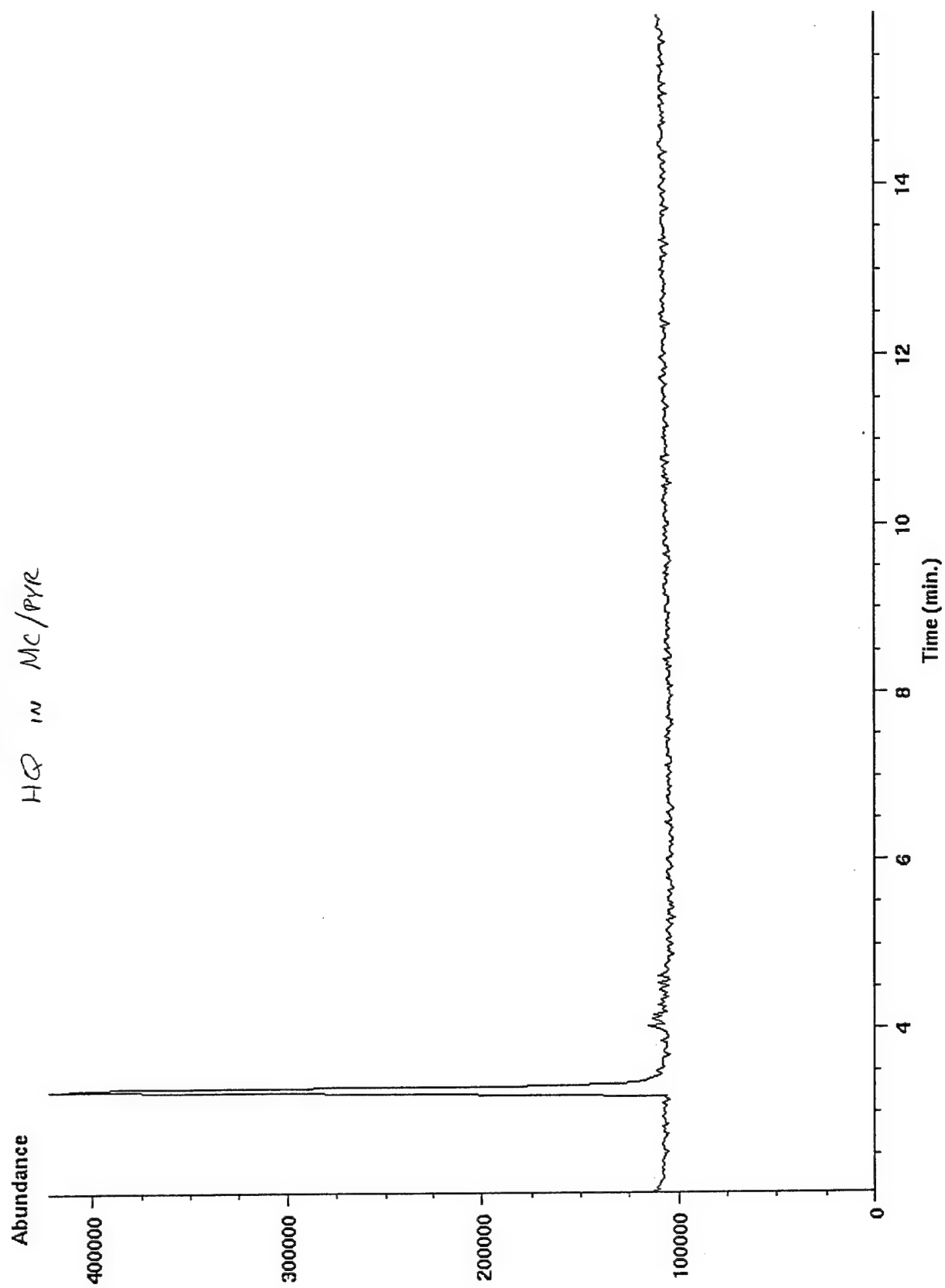
TIC of XHQ00401004.d

MC / PyR

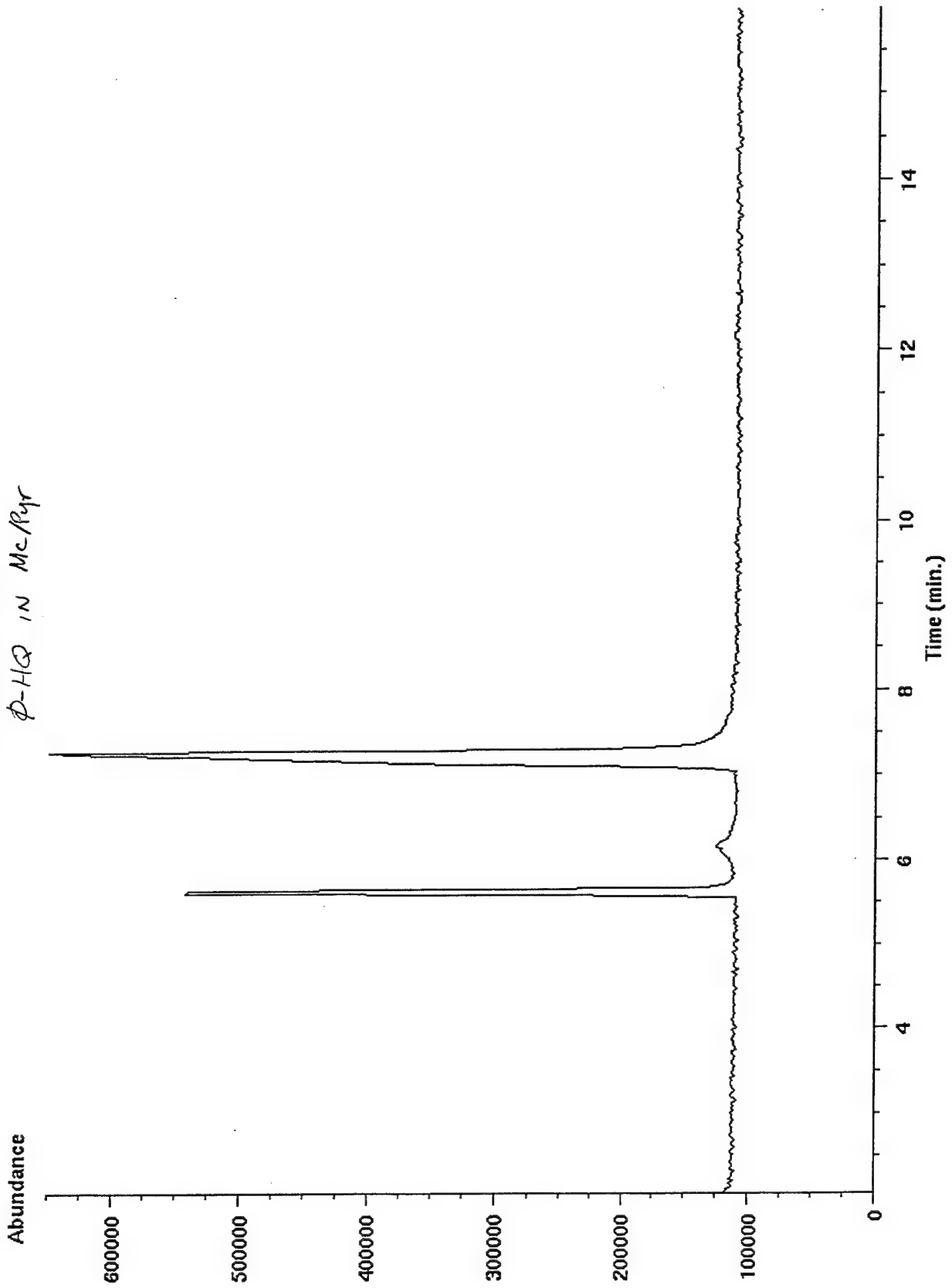


TIC of XHQ0501005.d

HQ in MC/PYE

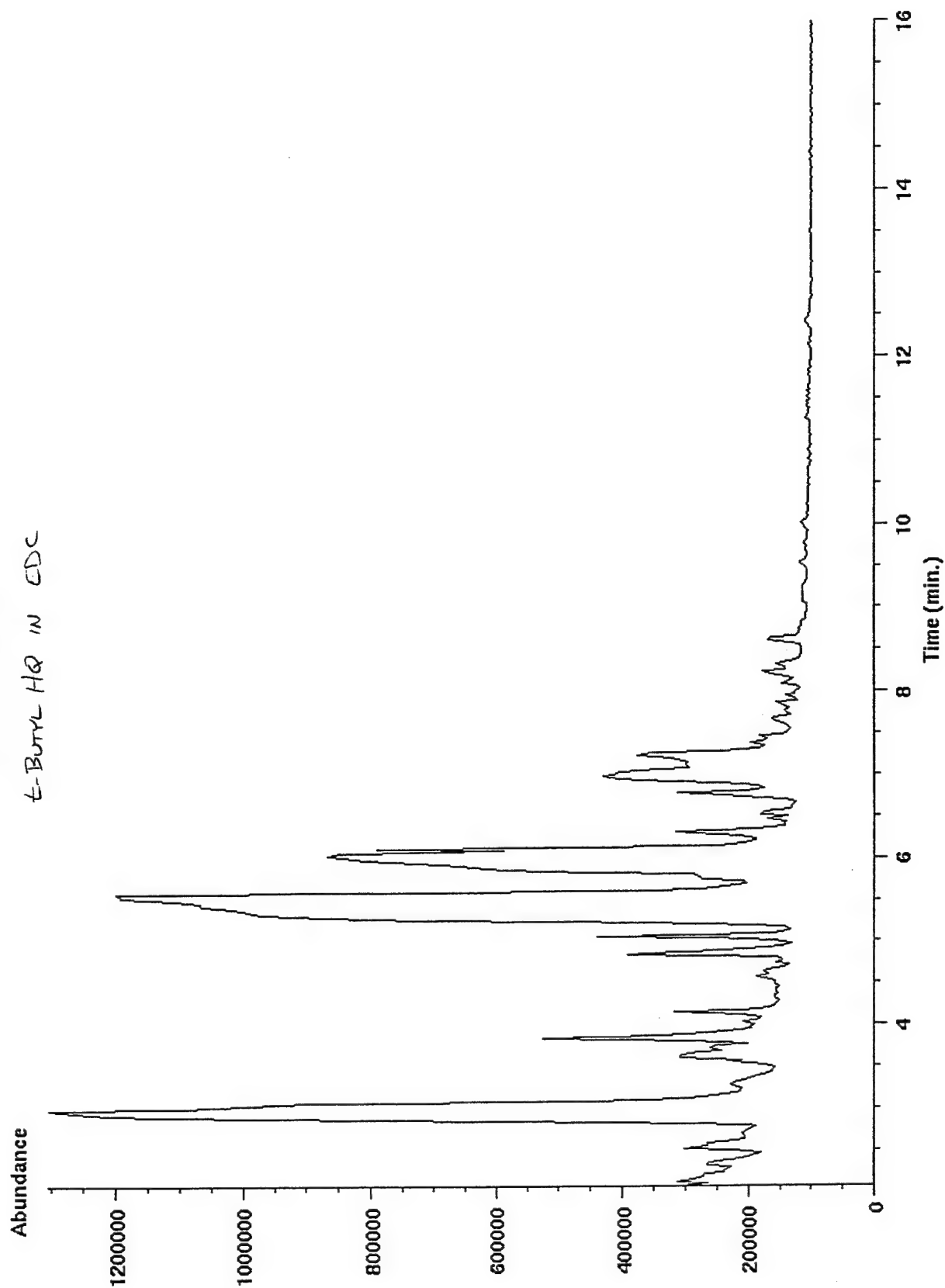


TIC of XHQ0601006.d
p-HQ IN McRyr



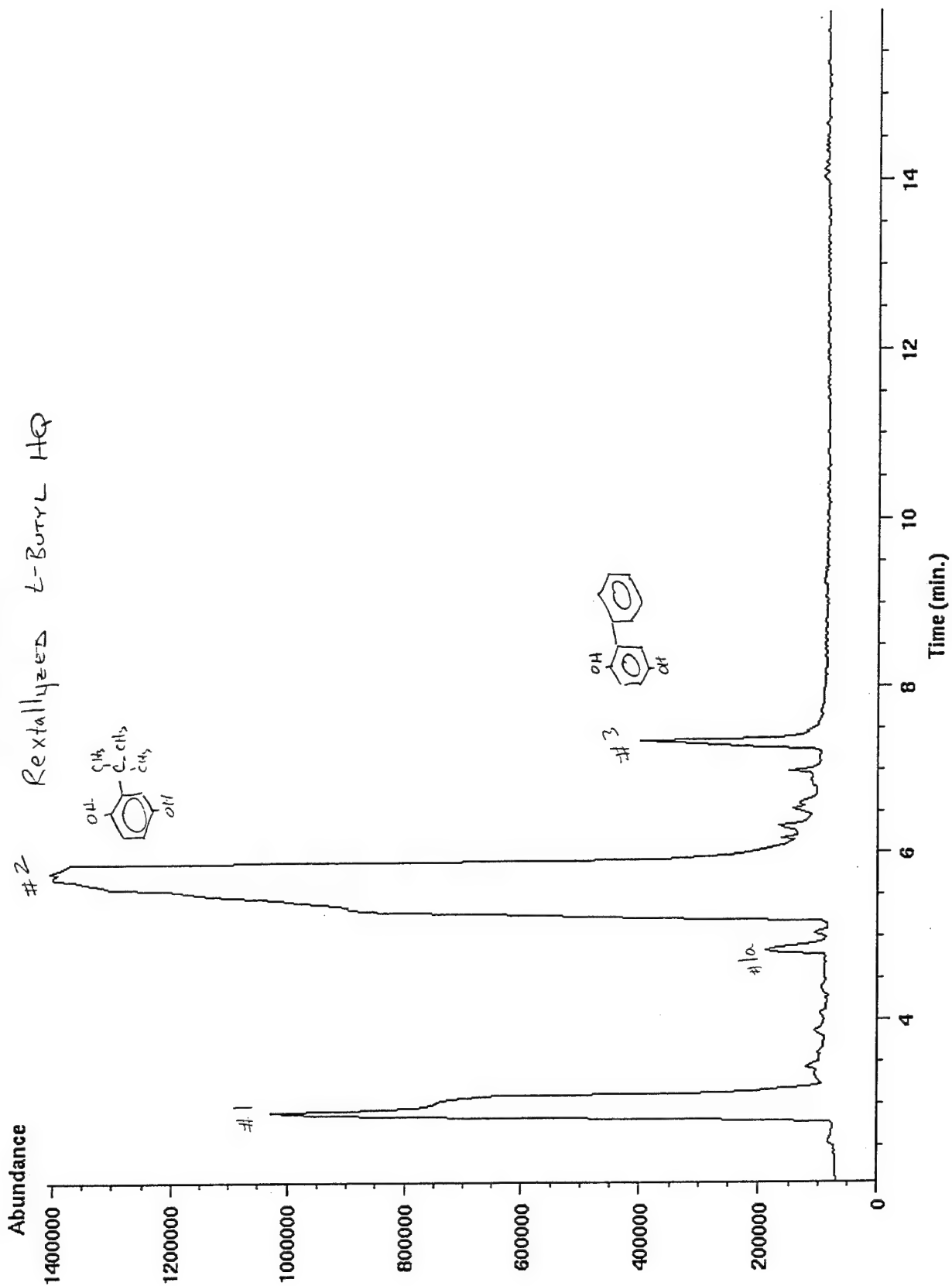
TIC of XHQ0301003.d

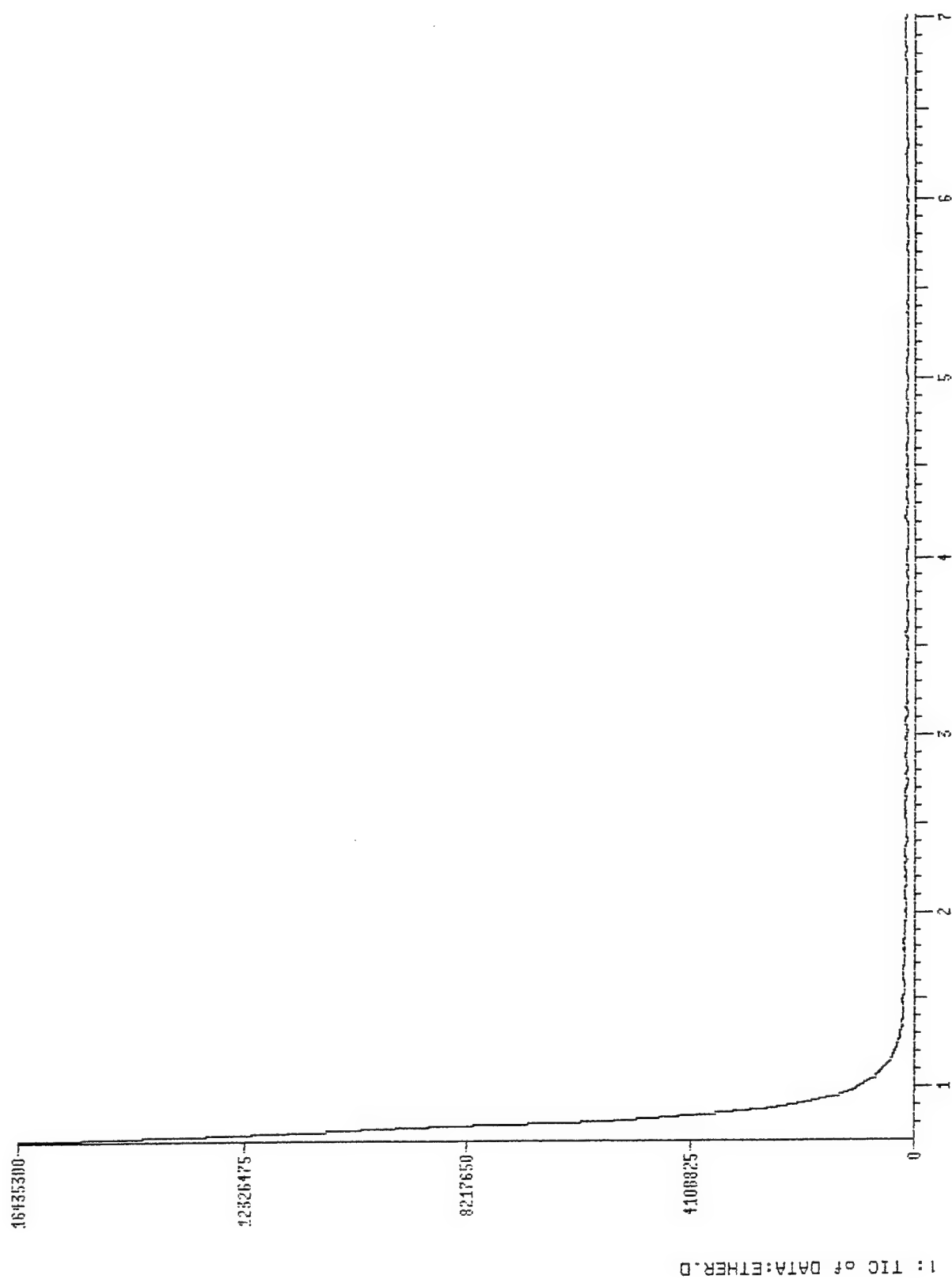
t-Butyl HQ in CDCl₃



TIC of XHQ0101001.d

Rectallized L-Butyl HQ





**1 Kilogram Synthesis of poly 2-[phenylethyl] para-phenylene
terephthalate/Post-synthesis Polymer Cleanup Procedures**

**Brad M. Lormand
Student**

**Antelope Valley College
Lancaster, CA**

**Final Report For:
WYLE Laboratories Summer Employment**

**Sponsored By:
Phillips Laboratory
Edwards Air Force Base, Lancaster, CA**

INTRODUCTION: Over a three month period, the synthesis of poly 2-[phenylethyl] para-phenylene terephthalate or phenylethyl hydroquinone/terephthalic acid (PEHQ/TA) polymer, was prepared in kilogram amounts with exciting success. All previous syntheses of this polymer at the Phillips Laboratory had resulted in smaller quantities by more laborious processes. The PEHQ/TA polymer is currently being studied as a possible material for rocket motor casings and many other unknown propulsion uses. The preparations and procedures involved with its synthesis will be outlined in the following report.

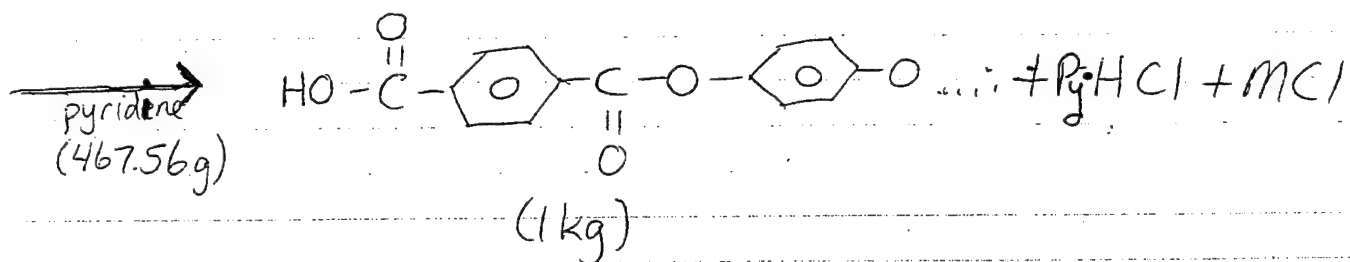
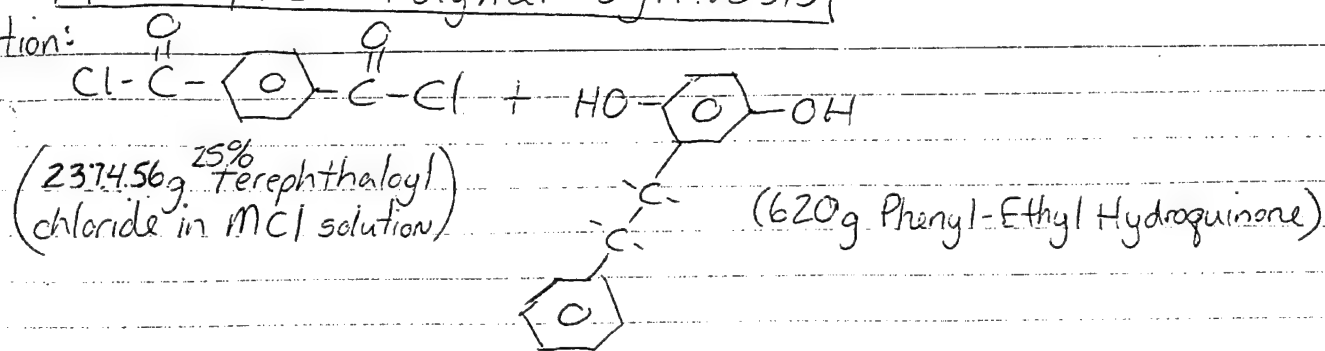
PREPARATION/PROCEDURES: The synthesis of PEHQ/TA was carried out by an acid-base reaction within solution. The stoichiometric calculations were performed for the initial acid and base solutions prior to the precise measuring and mixing together of their respective contents. The two monomers (PEHQ and TA) their quantities being in a one to one molar ratio, were dissolved in ample and separate amounts of methylene chloride.

The new 10 gallon reaction flask had been previously assembled and tested in all of its facets: heating and cooling mechanisms, stirring apparatus, computer controlled solution addition pump, and thermocouple. The setup of the glass reaction flask involved placing coiled plastic coated copper tubing attached to a water chiller/recirculator within the flask. The heating elements were affixed to the outside of the flask, and the computer driven pump empties into one of the 9 orifices on the lid of the flask. The thermocouple was placed within a long glass tube which reached far down inside, the end of the tube being immersed in liquid during the reaction. A cold condition (about 5 degrees C) must be maintained within the flask during the reaction of the acid and base solutions, and the heating elements helped to drive off the unwanted methylene chloride after the polymer had been made.

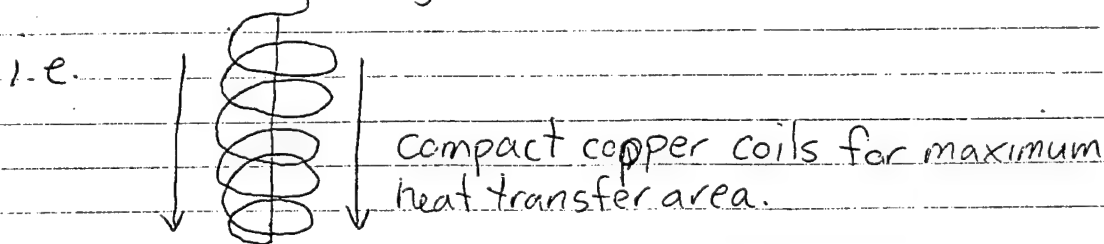
CONCLUSIONS: The upscaling of the synthesis gave promise to the production of larger, testable quantities of a perhaps useful and cost effective polymer. It netted about .95 kg, after numerous washings and filterings. The flask setup allowed for more control over the reaction temperature, and the computer driven pump made the rate of solution addition controllable, no longer guesswork. This synthesis showed that this polymers production is feasible and produced a workable amount on which future research may be performed.

PEHQ/TCI Polymer Synthesis

reaction:



- Reaction temperature = 0-10°C
- Acid Addition Rate = ~ 50 mL/min
- With Inefficient cooling system: Total acid addition time = 225 mins (3hrs 45mins)
- Suggestion: increased cooling surface area



- Post-synthesis washings done within reactor very efficiently

Post-synthesis polymer wash procedure

1. Wash in 5x volume of chloroform(CHCl_3) at 50-55°C for 20 minutes. Pour through vacuum filter for removal of pyridinium hydrochloride.
2. Repeat step 1.
3. Repeat step 1 if deemed necessary by analysis of waste chloroform.
4. Dry in vacuum oven at 70°C for 1 hour.
5. Wash in 3x volume of dimethyl sulfoxide (a.k.a. methyl sulfoxide) at 110-120°C for 1 hour. Vacuum filter hot to remove terephthalic acid.
6. Wash gelatinous slurry in 5x volume of boiling water for 45 minutes. Vacuum filter hot to remove excess dimethyl sulfoxide.
7. Wash in 5x volume of acetone at 50-55°C for 30 minutes. Filter.
8. Dry in vacuum oven overnight at 70°C.
9. Repeat 6 and/or 7 if less than favorable smell is detected in polymer.

**ON THE ANNEALING QUESTION IN LIQUID CRYSTAL POLYMER SYSTEMS:
SURFACE AND NEAR SURFACE EFFECTS**

**J. Adin Mann, Jr.
Case Western Reserve University**

**John J. Rusek
United States Air Force**

**On the Annealing Question in Liquid Crystal Polymer Systems:
Surface and Near Surface Effects**

J. Adin Mann, Jr.
Department of Chemical Engineering
Case Western Reserve University
Cleveland, OH 44106

John J. Rusek
Phillips Laboratory
Edwards AFB, CA 93523-5000

ABSTRACT

The class of liquid crystal polymers represented by co-polymers of p-hydroxybenzoic acid, 6-hydroxy-2-naphthoic acid, and 2-substituted poly paraphenylene terephthalates are the focus of this report. Certain questions of alignment and structure require the use of various model compounds that differ in their chemical structure but provide physical insight into alignment processes that obtain by annealing especially in the surface and near surface. Various tools from surface science were used and evaluated during this study. In particular Raman spectroscopy, ellipsometric spectroscopy, ellipsometric microscopy, x-ray reflectivity, atomic force microscopy and a new surface force imaging technology were utilized. Theoretical work reported herein emphasizes the application of force imaging in the study of surface properties of liquid crystal polymers.

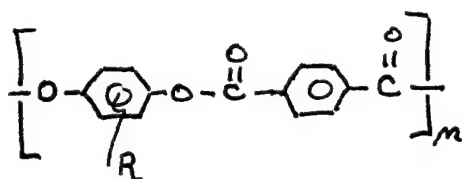
INTRODUCTION

Since the first commercialized liquid crystal polymer was developed in the 1960's at DuPont (Kevlar), the interest and applications in these systems has grown exponentially. The reason for this is that the physical properties of these materials can include high moduli and they can form structures that can be used in diverse applications ranging from rocket motors to protective vests to high-definition displays. These polymers include the strongest thermoplastic materials available and their alignment

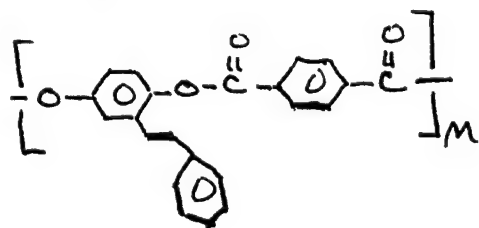
properties provide unique surface properties which in addition can control alignment of low molecular weight liquid crystal systems that can be used for displays.

The Phillips Laboratory has taken the lead in using these materials in propulsion applications. Initial studies utilized commercial resins and mixtures to assess the usefulness of thermotropic liquid crystal polymers in solid rocket motor cases, nozzle substructures, liquid and nuclear propulsion tanks and exterior ablative surface components. During this initial development, a phenomena called polymer physico-chemical annealing was noted: there was increased resistance to chemical attack and a dramatic increase of the polymer melt temperature. Past work suggests that this annealing phenomena does not involve cross-linking (to any great extent) or large chain-extension as observed in other polymeric systems (1).

A focus of this paper is to describe a set of surface science tools that can be applied to dissect the annealing phenomena at the surface and near surface of LCP (liquid crystal polymer) materials. Of particular interest is the class of polymers that have the form

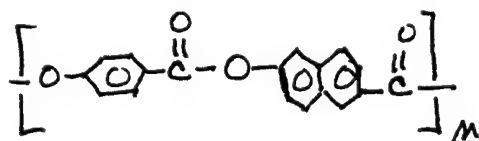


I. poly 2-p-phenylene terephthalates



Ia. SYN 10

called the SYN systems. As well as the VECTRA™ class



II. HBA/HNA

which is a co-polymer of p-hydroxybenzoic acid (HBA) and 6-hydroxy-2-naphthoic acid (HNA). The liquid crystal properties of these systems can be adjusted by, for example, adjusting the mole ratio of HBA and HNA or adding substituents of various sorts. The vectra structure can be regarded as “smooth, semi-rigid rods” which we denote as SSRR and the SYN structure which might be thought of as hairy rods, denoted as HSRR.

We remind the reader that small-molecule liquid crystal systems such as the nCB series.



can organize in three different ways (2):

1. Nematic liquid crystals are isotropic in their center of mass distribution but the molecular “rods” are oriented in space along a direction characterized by a director, \hat{n} .
2. Cholesteric liquid crystals that are oriented in the sense of a helix of directions organized on a macroscopic length scale along a particular direction but isotropic in the center of mass positions.
3. Smectic liquid crystals have ordering of the molecular centers of mass in planes perpendicular to a particular direction and these in-plane molecular rods are also oriented along a specific direction, which may vary from plane to plane. Complex, organized structures can be formed.

The major difference between LCP and the nCB class of liquid crystals is the extended structure of this polymer compared to the relatively compact structure of, say, 5CB. The semi-rigid LCP systems are of substantial chain length but, because of fewer degrees of freedom, cannot form tight, coil-like structures. Therefore, the nematic phase

implies orientation of large segments of these chains but not the entire chain. In contrast, flexible, block co-polymers may have sufficient bend such that "rigid" segments can orient providing LCP behavior such as optical anisotropy. We suggest that small chain length LC can give insight into the physical behavior of semi-rigid LCP. This assumption is exploited in this paper.

In this paper we report work using LCP materials provided by the AF Phillips Laboratories. The following surface science techniques were used: Raman spectroscopy, ellipsometric spectroscopy, ellipsometric microscopy, x-ray reflectivity, and atomic force microscopy as well as theory. We studied the application of a new tool call surface force imaging, SFI, to the problem of surface structure of LCP and annealing in the microlayer.

MATERIALS AND METHODS

Thin Films of SYN

Co-polymers of the SYN series were synthesized by one the Phillips Laboratory which have the basic structure I. In particular, we focused on the SYN 10 (structure Ia) system as representative for Raman studies. We used the following recipe (JJR) to prepare samples.

On a microscope hot stage, pre-heat a standard glass microscope slide to 20°C melting point. Deposit ca. 1gm. of powdered LCP on the slide. Quickly cover this with a second pre-heated slide and compress manually until the entire surface wets out. Remove from the hot stage and allow to cool slowly to ambient temperature. Cleave with a single edge razor blade in one quick motion. This procedure produced two thin films on silica, each about 10 μm in thickness.

These films were sufficiently rough that certain of our surface science experiments were difficult. In particular atomic force microscopy (AFM) did not work at molecular resolution on these samples. The effect of roughness was evident in the Raman work as well. However, the questions being investigated dealing with the annealing process in the surface is open to modeling with molecules that while not closely related chemically to SYN still provide analogs for the physical interactions.

Langmuir Blodgett Films

For a part of this work we employed a Brewster angle microscope built in our laboratory from inexpensive standard components and analog LCP shown in Figs. 10 and 11. We used an arrangement with one to two lenses, similar to the Mobius setup (3), which allows image acquisition in real time. The light source was a 10-mW HeNe laser (Melles-Griot) which emits a polarized beam with a wavelength of 632.8 nm. The image was registered by a Pulnix TM-7Cn CCD camera and captured by a Perceptics Pixelbuffer frame grabbing card, interfaced to an Apple Macintosh computer. Captured images were processed with NIH Image and HIPG DIP Station image processing software. The image processing procedure included an expansion of the image to correct for the incident angle and a filtering operation to reduce interference fringes and noise. Furthermore, the brightness of each image was scaled to improve contrast.

Contrast in the images is provided by gradients of the thickness, density, and optical dispersion properties of the film. Moreover, the polarization state of the reflected light, and therefore the optical anisotropy of the film, may be determined by adding an analyzer. All images reported here were recorded without using an analyzer in the path of the reflected beam. However, separate experiments were done to analyze the optical anisotropy in the films and hence the molecular tilt variations, in which case an analyzer was used.

The microscope was mounted over a commercial film balance (Lauda) equipped with a floating barrier for surface pressure measurement with a precision of ± 0.1 mN/m. A second moving barrier was operated by an IBM PC computer, so that isotherms could be recorded automatically. The temperature of the trough could be controlled with a precision of ± 0.5 K by circulating water from a water bath. However, the experiments reported here were recorded at room temperature to avoid thermal circulation in the subphase which disrupts the monolayer domains, an effect that occurs even at trough temperatures a few degrees higher or lower than ambient. Note also that keeping a specific section of the film under the laser footprint to observe its evolution in time was not possible in our setup, since the domains drift with a velocity of up to 1 mm/s, partially depending on the speed of the moving barrier. The microscope, film balance,

and computers were located in the Polymer Microdevice Laboratory, a large class 100 clean room at Case Western Reserve University.

Langmuir Blodgett deposition was done on the Lauda trough using the classical dipping technique with the monolayers compressed to the solid state (4,18,22). Then Ellipsometric microscopy can be used to image optical anisotropy in the surface and near surface. However, surface roughness can produce image artifacts. This is not a problem with LB films but is a difficulty using the splitting technique described above and applied to the SYN 10 systems.

Spectra Acquisition

A Dilor XY modular multichannel Raman spectrometer, equipped with a charge-couple-device (CCD) detector and a krypton laser, was used to acquire the Raman spectra. The spectrometer had a built-in Olympus microscope with a computer controlled x-y stage.

The Raman measurements were carried out with both 568.19 nm (green) and 647.10 nm (red) excitation lines. Slit widths of 150-200-150 μm and smaller and a resolution of 1.5 cm^{-1} and better, and integration times of 200, 300 and 1500 seconds were used. The Raman signals were collected in back scattering geometry through the microscope. The spectra were collected in the region from about 400 cm^{-1} to 1800 cm^{-1} . The baselines of the spectra as obtained were not flat but could be fitted with quadratic functions; the spectra were corrected for the systematic variation of the baseline, e.g. fig. 1.

Computer control allowed the recording of spectra at various locations on the clear SYN 10 surfaces at various resolutions ranging from 50 μm and better from spot to spot.

Samples of SYN 10 prepared as described above were mounted on the stage with the laser beam coming from above. The Laser beam was focused with an optical microscope using a 1000x magnification lens. After focusing, the laser beam was admitted to the microscope with power generally between 0.5-0.8 watt. An IBM 286

personal computer was used to record the signal. A wave length range of 400-4000 nm was scanned for Raman bands.

To detect the possible variation of the Raman signal over the surface, a surface scan was performed for the samples that gave a good Raman signal. An area (800 μ m x 800 μ m) of the film was scanned using the movable stage under computer control. The area was divided into grids of size (50 μ m x 50 μ m) and data was taken at each grid point. These data were scanned for the major Raman band; the same band at each set point on the surface was recorded. The data tables of Raman peak frequency and FWHH were recorded and plotted as surfaces, figures 2, 3.

AFM

Atomic Force Microscopy (AFM) was done with a Nanoscope III sold by Digital Instruments, Inc. The images shown herein (structure is shown in Fig. 10, poly-diacetylenes) were done using contact mode and care was taken to prevent artifacts associated with the "plowing" motion of the tip.

Ellipsometric Spectroscopy

Ellipsometric spectroscopy was done in the visible to near infrared wave lengths using several instruments manufactured by Woolam, Inc. e.g., their Model Type III, the substrates were silicon wafers which were carefully cleared before deposition of the multi layers of the various co-polymers used in this study. An attempt was made to use infrared ellipsometric spectroscopy. SYN 10 samples were not sufficiently smooth for this technique. A co-polymer analogue to I gave very interesting spectra but LB films of 8,12-diacetylene were better characterized by Raman and other methods discussed herein.

X-ray Reflectivity

X-ray reflectivity (5) was determined using the surface diffractometer of beam line x23B at the Brookhaven National Laboratories light source. To examine the layer structure synchrotron x-ray reflectivity is used. X-ray reflectivity measures the intensity, $R(\vec{q})$, of the reflected x-ray as a function of the angle of incidence from which the

momentum transfer vector \bar{q} is computed. The geometry of the experimental set-up is such that the scattering wave vector is parallel to the normal to the films. Thus, the experiment provides an average variation of the electron density normal to the sample surface. Equation 1 implies that the major contribution to the reflectivity occurs where the gradient of the electron density is large. In multilayers on a substrate the gradients come from the periodic modulation of electron density in the film and the abrupt change of electron density at the interfaces. Experimentally the reflectivity profile shows Bragg peaks and Kiessig fringes. The analysis of the profile give information regarding film thickness, electron density and surface roughness. Kiessig fringes provide a way of estimating accurately the total film thickness. When the surface roughness increases due to pinholes or stress relaxation, the amplitude of the Kiessig fringes is damped. However, the Bragg peaks are not affected when the roughness is in a micron size or larger than the crystallite size. The reflectivity is

$$R(q_z) = R_F \left| \rho_\infty^{-1} \int_{-\infty}^{+\infty} \langle d\rho_{el} / dz \rangle \exp(iq_z z) dz \right|^2 \quad (1)$$

where $q_z = 4\pi\lambda^{-1} \sin(\theta)$. R_F is the Fresnel reflectivity and ρ_∞ is the electron density of the substrate. Figure 4 presents the x-ray reflectivity data for the 1, 2 and 3-layer samples. The primary minimum shifted to lower 2θ for a thicker film. For a given 2θ (i.e. 1° to 2.5°) the number of maxima corresponds to the number of layers. Figure 5 shows the x-ray reflectivity profile for the 10-layer LCP Cop11 sample with the Kiessig fringes. The average monolayer thickness is larger than the x-ray diffraction value of 35.0 Å. In addition, the 10-layer sample shows a Bragg peak suggesting an ordered film formation. Application of this technique to the problem of annealing will be discussed in the last section of this paper.

Houston Interfacial Force Microscope

It is our view that since the desirable properties imparted by annealing are in part mechanical, it follows that detecting surface visco-elastic effects quantitatively is important for practical reasons and useful in coming to some understanding of the

changes in molecular structure that provide good mechanical properties. A new imaging technique developed by Houston, *et. al.* (8), IFM, provides the possibility of determining surface mechanical properties at locations determined by scanning. The design immediately opens up a new world of IFM/AFM wherein artifacts produced by contact mode AFM are eliminated or minimized. Resolution is in the nanometer range but not yet of molecular lengths.

What is so important about this surface science instrument is the possibility of obtaining the entire force spectrum including indentation at places chosen during the scan mode of operation. Moreover, reactive group can be sensed although this has not been exploited for LCP.

Briefly (see Joyce *et. al.* (8) for details), the sensor for determining forces is a feedback controlled system based on capacitors. See fig. 6. An rf bridge arrangement is used to sense the displacement that obtains resulting from the forces acting between the probe and the surface. The balance of the torsion arms can be re-established by applying a potential drop (i.e. a force) across one of the plates. The result is a system that allows great sensitivity in the measurement of force without the mechanical instability of the lever arm arrangement of the common AFM design (7).

The probes can be made of a wide variety of materials and shapes. Electrochemically etched tungsten tips work well, gold tips on which tiny gold balls are produced by heat can be made, etc. Of special interest is the fact that molecules of a variety of structure can be self-assembled on tips of small radius so that interactions between surface groups and adsorbed molecules can be probed. In particular it is possible to sense the structure organization of surface regions with both AFM and IFM. However, it is possible to go further and probe the visco-elastic response of the surface and microlayer of LCP such as the SYN series.

Theory of Surface Force Microscopy

There are two domains in determining the variation with separation of force between a small probe and the surface of a LCP. The first domain is that up to contact, the second is that after contact which includes indentation.

There has been a considerable discussion in the literature about how to model the first domain which should be recognized as the problem of describing the adhesion of two condensed bodies (9). The second domain has been studied as a problem in the mechanics of materials and is the basis of indentation techniques for determining the hardness of materials. The IFM technique is a local probe in the nanometer range, with which carefully controlled indentation experiments can be done to sense local viscoelastic effects.

Consider the force before contact. The modern theory of van der Waals forces (9) was used to simulate the forces observed by an AFM or IFM tip. The basic idea is that of summing the fluctuations of electro magnetic fields that always exist between the tip and the substrate. All tips we have used can be represented by a sphere of small radius attached to a shank of comparable radius. The force of interaction as a function of separation, h , is then of the form

$$F(h) = 2\pi RW(h)$$

where R is the radius of the tip and $W(h)$ is the free energy per unit area (referenced to $W(+\infty) = 0$) of two flat plates. $W(h)$ turns out to be easier to calculate than a direct calculation of $F(h)$. The formula is satisfactory where $h \ll R$ and this will usually be the case; even when R is 10 nm h will be 1 nm or smaller. For the purpose of this article, corrections for $R \sim 1$ nm will not be needed. Therefore, it will be sufficient to compute the free energy between two parallel plates of the same material as the LCP surface and the tip which may have a self-assembled, molecular film chemisorbed to its surface. The general situation is shown in figures 7 and 8. It is useful to first do an extension of the calculation first done by Hamaker (9) to show the role of LCP surface structure in AFM. We follow the formalism developed by Girard and Maghezzi (10).

Consider two arbitrary condensed matter blobs interacting, several realizations of which are shown in fig. 8. The free energy is then

$$W = -\frac{h}{2\pi} \int_0^\infty d\xi \int_{V_1} \int_{V_2} d\vec{r}_1 d\vec{r}_2 \chi_1(\vec{r}_1, \vec{r}_2, i\xi) K_2(\vec{r}_1, \vec{r}_2, i\xi) \quad (4)$$

where K_2 characterizes the susceptibility of the electric potential (fluctuations in electron density) generated by system two and χ_1 represents the linear susceptibility of system 1, the LCP in this case. This formula is accurate with the appropriate definitions of χ_1 and K_2 .

Let the LCP occupy the lower half space, $Z < 0$, and may be ordered to some degree or may be crystalline. Neglect the many-body contributions within the LCP so that χ_1 is a sum of individual susceptibilities associated with LCP molecules. Next, certain assumptions of additivity are used that are less accurate than the theory leading to equation 4.

The location of the center of mass of each LCP chain with respect to the center of the spherical tip is

$$R_{n_1, n_2, p} = n_1 \bar{a}_1 + n_2 \bar{a}_2 - (h + pb) \hat{e}_z - \bar{\ell}$$

where \bar{a}_1 and \bar{a}_2 are surface net vectors, $\bar{\ell} + h\hat{e}_z$ locates the tip with respect to the mathematical surface $z = 0$, $-pb\hat{e}_z$ locates the pb plane below the surface. In addition, the tilt of the molecule must be included and this can be done by defining three Euler angles for each molecule. This assumes that the LCP molecules are rigid (rather than semi-rigid). The numbers n_1, n_2, p will be integer if the system crystallize into a lattice where $b\hat{e}_z$ would be the lattice vector parallel to the surface normal. Then within the dipolar approximation write

$$\chi^{(1)}(\vec{r}_1, \vec{r}_2, \omega) = \sum_{n_1, n_2} \sum_p \chi^{(1)}_{n_1, n_2, p}(\vec{r}_1, \vec{r}_2, \omega; \theta_1, \theta_2, \theta_3) \quad (5)$$

where here \vec{r}_1 and \vec{r}_2 are positions in the two media and ω is the frequency of the electromagnetic fields that each body produces by fluctuations. The triple of numbers n_1, n_2, p locates the center of mass for each molecule and $\theta_1, \theta_2, \theta_3$ specify the orientation. Since we are interested in nematic structures, assume that a single angle, θ , computed with respect to the surface normal \hat{e}_z and in the $x - z$ plane is sufficient; $\hat{n} = (\cos \theta, 0, \sin \theta)$.

It is possible to write the free energy as

$$W(h, \theta) = - \frac{h}{2\pi} \int_0^\infty d\xi \sum_{n_1, n_2} \sum_p \underline{\alpha}_l : \underline{S}_2 (\bar{R}_{n_1, n_2, p} (i\xi)) \quad (6)$$

Here $\underline{\alpha}(\theta, \omega)$ is the polarizability of the LCP chain and in this case will depend on the director angle θ as well as the frequency ω . After several approximations the result is that

$$W = - C \sum_{n_1, n_2} \sum_p \frac{1}{(R_{n_1, n_2, p}^2 - a^2)^3} \int_0^\infty \alpha_l(\theta, i\xi) \frac{(\varepsilon_2(i\xi) - 1)}{(\varepsilon_2(i\xi) + 2)} \quad (7)$$

where ε_2 is the dielectric function for the spherical tip and a is the radius. Recall that the tip surface separation, h , is in $R_{n_1, n_2, p}$. Indeed, it is clear from this development that even if the tip is spherical with radius $a > 1nm$, the properties of the LCP will be observable through α_l and $R_{n_1, n_2, p}$ if the gap, h is sufficiently small. Use will be made of formula (7) in the discussion.

The numerical analysis was done using a somewhat different model for practical reasons. A program using the Lifshitz and Dyzaloshinski (9) formulation of the problem for parallel plates was available (11). While necessarily the direct dependence on the director and the details of the LCP structure are lost, it was possible to include the effect of the organic monolayer adsorbed to the tip. The results of these calculations are shown in fig. 9 and will be discussed later. Recent work in our laboratory to make quantitative the ellipsometric microscopy of nCB monolayers in their ordered phases shows that it is possible to estimate the dielectric anisotropy of these thin films. This result suggest that it may be possible to extend the force calculation to take liquid ordering into account in the lifshitz calculation.

The second domain, the indentation produces a distortion in the structure of the surface necessarily. In essence, even though the force that the IFM can apply is relatively small, the radius of curvature is also small so that an indentation spectrum can be recorded (depth of penetration as a function of force). The traditional literature of surface science (9) distinguishes between several cases. Firstly, assume that the spherical tip and LCP are rigid. This case, while unrealistic, can be treated simply: the force, F is

$$F = 4\pi R\gamma_{12}$$

where γ_{12} is the interfacial tension between the two solids in the presence of air. If this were truly the case, a very powerful technique would be available for uniquely determining the specific surface free energy which would be sensitive to structure and structure changes in the LCP. However, this behavior is not observed since neither the LCP or the tip are rigid.

For our situation, still roughly but reasonably, the contact area will have a radius, a , given by

$$a^3 = \frac{R}{K} \left(F + 3\pi R\gamma_{12} + \sqrt{6\pi R\gamma_{12}F + (3\pi R\gamma_{12})^2} \right) \quad (8)$$

where R is the radius of the tip, F is the load force, γ_{12} is the interfacial specific free energy, and K is an elastic modulus. If adhesion forces are small, γ_{12} are small, and deformation is small, a limit is observed with a rather different pull-off force. Formula 8 is an approximation. Further, even if the material is isotropic, a second elastic modulus, a poisson ratio should appear. In fact, this extension can be made to include the anisotropic case of locally organized LCP but this additional complexity will not be discussed herein. See reference 12 for one approach.

Dynamics of LCP Motion

The last topic that is important to a discussion of the annealing process is that of polymer dynamics for LCP systems. Here we provide some remarks to be used in the discussion section of this paper. Clearly atoms and group of atoms move, however, these remarks focus on rigid rods as segments of the LCP and their Brownian motion. See Bird *et. al.* (13) for a detailed discussion of the formulas quoted next.

Sphere as a degenerate rod. For spherical particles the rms displacement is

$$\sqrt{\frac{l}{2} \langle (x - x_o)^2 \rangle} = \sqrt{Dt}$$

and a characteristic time τ can be defined, say, in terms of the time to move a distance of the size of the segment, a . If the solution is dilute the diffusion coefficient is

$$D = \frac{kT}{6\pi\mu a}$$

where T is temperature, η the viscosity of the solvent and a the radius of the particle. At modest concentrations

$$D = \frac{kT}{6\pi\mu a} (1 - 1.83\phi)$$

where ϕ is the volume fraction. It is clear that $\frac{1}{2} \frac{a^2}{D}$ is a characteristic time for motion of the particle over the length a (the radius of the particle) and can be estimated from well known numbers.

Prolate Spheroids. The translational diffusion problem for these particles depends on the ratio of the lengths of the minor axis to major axis, $q = b/a$. Our interest is for the case for $q \rightarrow 0$. Suppose the suspension is of a sharp orientation distribution along the director, then

$$D = \frac{kT}{\zeta_{\parallel}} + \frac{kT}{\zeta_{\perp}}$$

where the friction coefficients ζ_{\parallel} and ζ_{\perp} obtain for motion parallel to the director and perpendicular to the director. Approximately, these functions are

$$\zeta_{\parallel} = \eta 1.2\pi a (4 + \frac{1}{q})$$

$$\zeta_{\perp} = \eta 1.2\pi a (3 + 2 \frac{1}{q})$$

Clearly, when $q \rightarrow 0$, $D_{\parallel} > D_{\perp}$ and in fact in the limit of small q , $2D_{\perp} = D_{\parallel}$. It is also clear that for long rods both D_{\perp} and D_{\parallel} become small as the LCP length, a , grows.

When the ratio of the minor to major axis (b/a) is small the formula for the rotational diffusion coefficient simplifies to

$$D_{rot} = \frac{3kT}{32\pi\eta a^3} \left\{ 2 \log \left(\frac{2a}{b} \right) - 1 \right\}$$

From these formulas approximate relaxation times can be estimated for reorganization of LCP systems. Again as the LCP grow in length, the rotational diffusion coefficient becomes small and the time scale for rotation is long. A different way of thinking about the diffusion is based on early work by deGennes (14) and will be discussed next.

Reptation Approximation. This model suggests that polymer molecules move with a snake-like motion “on the average” in the direction of the chain along a kind of “tube” that exists for a short period of time. This motion is relative to whatever macroscopic velocity field might be imposed on the system. Consider four segments μ , $\mu-1$, ν , and $\nu-1$ with directions \hat{e}_ν and \hat{e}_μ in the laboratory frame. Then in a momentum average, $\langle \bullet \rangle_p$,

$$\left\langle (\dot{\vec{r}}_\nu - \vec{v})(\dot{\vec{r}}_\mu - \vec{v}) \right\rangle_p = \alpha (\hat{e}_{\nu-1} + \hat{e}_\nu) (\hat{e}_{\mu-1} + \hat{e}_\mu)$$

where α is a scalar coefficient. This formula can be taken as the definition of α . An estimate can be written down (13) which amounts to

$$\alpha = \frac{4(N-1) \frac{kT}{m}}{N + \sum_\nu \hat{e}_{\nu-1} \cdot \hat{e}_\nu} \approx \frac{2kT}{m}$$

where m is the mass of each segment and N is the number of segments. The approximation obtains when N is large. We remark that $|\hat{e}_{\nu-1} + \hat{e}_\nu| \leq 2$ and the vector $\hat{e}_{\nu-1} + \hat{e}_\nu$ represents the direction and relative magnitude of reptation “hump” of that segment.

Another useful formula is that for the diffusion coefficient of the reptating LCP, D_{rept} :

$$D_{rept} = \frac{kT}{N \zeta_{rept}}$$

where again, N is the number of segments in the chain and ζ_{rept} will be an average of ζ_{\parallel} and ζ_{\perp} .

Finally a characteristic time can be defined in terms of the time necessary for a molecule to move its length by reptation:

$$\tau_{char} = \frac{N^3 \zeta_{rept} a^2}{2kT}$$

where N is the number of segments of length a making up the molecule and ζ_{rept} is the friction coefficient of a segment.

These diverse materials and methods leads to results which can be used to develop a model for the annealing process that is the focus of this study. We develop these notions in the next and final section of this paper.

RESULTS AND DISCUSSION

The annealing problem for LCP systems should be considered in terms of structure, dynamics which then lead to function. In this case the function to obtain is that of resistance to chemical degradation under extreme conditions of temperature and resistance to stress. This is a challenge that a few years ago could not be handled by polymer technology. The fact that Kevlar has been used in function beyond what is expected for normal polymers suggests that the synthesis, structure and properties of LCP should be studied intensively.

At this time, there is not enough information available to provide design methodology for optimizing the function desired for LCP systems. Nevertheless, we focus the discussion by setting out some design principles developed as a result of studies of the surface properties of a range of LCP. From this work follows that the processes starting from synthesis to manufacturing of parts must take into account the details of molecular structure and its dynamics so as to obtain materials that reach design objectives of function.

It is clear that LCP derive their essence from the state of partial order that characterizes liquid crystals. Indeed, specimens of LCP systems that have been formed into parts by injection molding usually show a skin which is, under certain conditions (surfaces of the mold are cold), an amorphous, glassy structure showing little ordering. Under this skin is structure that does show order. The core may or may not be ordered. Immediately one knows that this part will not have the properties of a LCP fully developed. How can processing be designed to optimize the order?

When the surfaces of the mold in contact with LCP are at a temperature in which the nematic phase obtains, the skin is well ordered (15). However, the core may have a defect density greater by six orders of magnitude and may be amorphous (1,15). Again the question is how can processing be designed to optimize order?

It is well known (15) that the tensile modulus of poly HBA/HNA drawn fibers is ~ 65 GPa while the shear modulus is ~ 1 GPa. This can be understood in terms of well ordered, 200nm long poly HBA/HNA molecules oriented along the fiber axis. A quick assessment of the intermolecular forces involved suggests the reason for this anisotropy.

While somewhat conjectural, this and other data on the mechanical response of LCP systems suggest that a purely crystalline phase will not have appropriate function because of easy fracture planes. Suppose a part designed for high-stress and high-temperature operation was processed to be a simple crystal LCP phase. Then the same reasoning used for the well oriented fiber obtains (15), there will be easy fracture planes. However, amorphous polymers are known to fail in situation where LCP work well. Therefore, the optimum organization for a given molecular architecture is a nematic liquid crystal.

Similar reasoning suggests that smectic phase LCP will fail along fracture planes corresponding to the smectic planes. However, the in-plane organization may provide large moduli when stressed parallel to the smectic planes.

These arguments suggest that the optimum function will be obtained with nematic LCP systems. The remainder of this discussion will focus on this hypothesis. The questions will then involve control of the director fields and the defects in the director field that must be accommodated in part shapes that are anything other than of simple cylinder geometry.

There are several methods by which director fields can be controlled once the LCP is in the proper state above the glass transition temperature where large scale molecular motion is allowed.

- Fluid flow fields
- Electric fields
- Surface force fields

Since the LCP systems we are discussing are either smooth, semi-rigid rods (SSRR) or hairy, semi-rigid rods (HSRR) of large aspect ratio, these molecules will orient in a smooth flow field with the molecular director aligning along the direction of the velocity field, $\frac{\vec{v}}{|\vec{v}|} = \vec{e}_v$. The time scale for alignment of \hat{n} along \vec{e}_v is many orders of

magnitude shorter than pure diffusion would allow. It is essential that such fields be used to obtain ordering in forming a part. But for parts of complicated geometry, the flow fields will not be everywhere smooth so that director gradients will obtain and lead to structure defects that cannot be easily controlled.

In fact even simple parts show structure variations after the injection molding process is complete (1). As mentioned, if the mold is cold, the skin may be amorphous. Indeed, conditions can be found such that the skin is ordered as well as the under layer. However, often the core of the mold is amorphous. These observations (1) suggest that hydrodynamic ordering was not effective for the core or that diffusion processes in the core worked to disorganize the LCP.

It is well known that strong electric fields can orient molecules with dipolar groups. The effect of electric field poling is to provide highly oriented thin films at $T > T_g$ which stay organized if the temperature is lowered below T_g with the field on. This effect should be kept in mind but will not be discussed in this paper.

The remainder of this section will focus on surface effects in inducing orientation. This is a topic of intense investigation for applications in liquid crystal display technology where the director fields of the display must follow a designed pattern accurately. The main concept is that of anchoring of LCP at solid surfaces (2). The surface structure is manipulated so that liquid crystal molecules will adsorb and strongly anchor at a particular (by design) tilt angle. The tilt at the surface is propagated through the entire LCP phase. Figures 10 and 11 show how the surface can be modified to provide anchoring to the LCP phase.

It is fairly straight forward to modify surfaces of a wide range of materials using the chemistry suggested in figures 10 and 11 to obtain either alignment along the normal to the surface or parallel to the surface. It is more delicate to obtain intermediate angles but that may not be an issue for the fabrication techniques we are modeling.

The design feature we are adding is based on this principle: Adjustment of LCP alignment can propagate from the surface through a persistence length that can range from the near surface (μm) and beyond. Annealing will be the process by which the persistence length can be optimized.

The work of Shih (16) and Albarici (19) as well as unpublished work from the Polymer Micro Devices Laboratory (20) have shown how any surface can be modified so as to obtain strong anchoring with LCP molecules oriented in a designed direction. It is easy to provide a surface, the alignment layer, on which the LCP will orient parallel to the surface. We remark that surface roughness with elevation correlation functions showing maxima in the direction of ordering will aid the process.

The mold surface should be designed so that the surface x-ray reflectivity spectra of adsorbed layers should show ordering as indicated by figures 4, and 5.. Also see the AFM scans of figure 14. The formation of such structures ensure a well organized LCP. This perfection is further indicated by ellipsometric spectroscopy which allowed measurement of film thickness which was consistent with x-ray data and the complex refractive index of the film, figure 12. Note that the refractive index is high and varies smoothly and that the extension coefficient is small until about 400nm where co-absorption occurs.

Another measurement that can be used to characterize the alignment layer uses the Houston IFM technology. Ross reported (21) the interaction between a self assembled film on the problem presenting amine groups to the surface covered by another self assembled film presenting carboxyl groups to the gas phase. The data is shown in figure 13. Note the remarkable attractive force that shows a minimum at $h \sim 1.5\text{nm}$ and a force of -4500 mN/m in contract, the surface specific force energy of organic surfaces is generally less than 50mN/m on a comparable scale. The range of the interaction is *ca* 5nm which is very long.

There are two conclusion that can be drawn from this data. Firstly, forces of this magnitude will orient LCP systems in contact with such a substrate and the persistence length will be long. It remains to determine the persistence length experimentally.

Secondly, IFM scans will show the orientation of surface groups that will anchor LCP over an arbitrary area of interest. The anchoring layer can be design on flat plates and the process used to form alignment layers on parts of nearly arbitrary shape through the self assembly process. See Ulman (22) for details about the technology.

Interfacial Raman spectroscopy was used to establish the structure of SYN 10 films, figures 2 and 3. These results show a tendency to patch by patch organization and that the majority of $C = O$ groups are not oriented to give a strong Raman signal. This technique samples the entire film but the majority of the signal comes from the top one micron (microlayer) of the film. It may turn out that this is a sensitive test for resistance to surface reaction under the conditions of high temperature and pressure.

The two techniques of IFM and scanning Raman are complimentary although IFM is surface sensitive. Other insights into the structure of the alignment layer can be obtained by monolayer studies (3, 19). Of special interest is the defect structure discussed in reference 3 using the Brewster Angle Microscopy (BAM) technique we have discussed in a previous section. We found conditions under which various defects were observed. In general, the director fields of the alignment layer would form point defects around which the director field would bend and splay. Moreover, recent work by deMul has shown how to compute the anisotropic dielectric tensor for these films. This opens new possibilities for computing surface to surface forces for liquid crystal media.

It occurs to us that this control of the alignment layer on the surface of a mold for forming LCP parts can provide a way to induce alignment for strength around corners in the mold. Again, the science and engineering details can be determined on single geometries that allow the use of measurement technique we have described.

It is clear that IFM will play a crucial role in two ways. As equation 7 shows, the problem will be able to pick up the local effects of structure. This can be done on the alignment layer as well as on the surface of LCP in contact with the alignment layer. We calculate that, the effect shown by Ross (21), will provide rich information about structure through acid-base interactions.

Moreover, the IFM provides for observing indentation spectra. Equation 8, which is approximate, shows that a set of local elastic moduli. While equation 8 includes only one modulus, the theory can be extended with some difficulty to include the moduli required for the symmetry. At this time we are investigating the use of AFM tapping mode both for superior imaging (fewer artifacts) and to us the frequency shift and quality factor, Q , as to measure the visco-elastic response of "soft" surfaces.

These techniques will be able to show patterns in the variation of elastic moduli with structure over the surface of prototype LCP that have been optimized by alignment layers.

It is clear from reference (1) and our work that we will not be able to attain optimum alignment of the LCP by flow alone. Annealing will be a part of the protocol in making parts through the molding. We maintain though that control of the alignment layer and the flow fields during the initial processing of the part sets the system for the reorganization that will go on during annealing.

The formulas for several relevant time constants for the annealing process were developed in the last section which should be kept in mind; τ_{\parallel} , τ_{\perp} , τ_{rot} , and τ_c . τ_{\parallel} and τ_{\perp} are the characteristic times for displacement parallel and perpendicular to the symmetry axis by a segment length of about 1nm. τ_{rot} was estimated for a rotation of 180°. τ_c is that for reptation of N segments a distance $N \times 1\text{nm}$. For the purpose of discussion, we assumed an annealing temperature of 475°K, a molecular weight of 30,000 Daltons and a segment molecular weight of 300 Daltons. The segment size was assumed to be 1nm x 0.5nm with $b/a = .5$. The relevant time constants are: $\tau_{\parallel} = 34\text{nsec}$, $\tau_{\perp} = 40\text{nsec}$, $\tau_{\text{rot}} = 285\text{nsec}$ and $\tau_c = 18.7$ milliseconds.

Suppose that the alignment layer is effective so that with the flow field the nematic order has a persistence length of a few micrometers from the surface. Even beyond that length scale, there will be some orientation order; only small displacement molecular realignment and reptation need take place to obtain nematic order throughout the entire wall of the part, say a few millimeters in thickness or more.

If the alignment layer and flow field are coherent, then the LCP will have a template for annealing. Note that local alignment can be obtained in time scales of a few hundred times τ_{\parallel} perhaps in the order of a fraction of a millisecond. While reptation is a slower process, most molecules will not need to move far to find a minimum energy configuration *dictated* by the boundary conditions of the alignment layer.

Annealing to a uniform nematic will take more time than τ_{\parallel} simply because there must be a global optimization of structure. For this molecular dynamics can give insight for molecules somewhat shorter than 1nm, roughly 10^6 time steps of 1p sec are required to go from a poorly ordered system to the final structure. Translating that to the present model by scaling, reasonable nematic order can happen with annealing times of a few minutes. Clearly, annealing will be a much slower process as $T \rightarrow T_g$ since the viscosity increases very rapidly in this limit. Processing will need to be designed to allow annealing at temperatures where mobility is sufficient to allow reorganization in a reasonable time. That time scales directly with the viscosity of the state; below T_g this process will be very slow. However, in this case some reorganization is possible by local molecular motion.

The work of McCullagh (15) shows that in copoly esters transesterification must be considered. This is a process that does not involve cross-linking but rather a reorganization of the chains by bond breaking and reforming. This can happen only when the ester groups are close enough (a fraction of a nanometer) to allow the chemical reaction to occur. This process could be controlled to produce better function.

Summary: The annealing process can be exploited to obtain better function if:

- The alignment layer is effective
- Transesterification is controlled.
- Velocity fields are controlled in the production phase
- The effects of molecular structure are taken into account in detail.

Moreover, the key to the entire process is the surface science of the alignment layer at the surface of the part. Indeed this paper provides the description of a set of tools for understanding the annealing process at the molecular level.

Acknowledgment

The work reported herein was supported by a grant from the Phillips Laboratory, EAFB. Contract number: FO 4611-92-c-0024. JAM thanks Dr. Grabbe for copies of his software for computing forces between multilayers and Dr. Houston for discussions of AFM and Dr. Ross for sharing his thesis work.

REFERENCES

1. Rusek, J.J. "*Proceedings of the Second Annual Advanced Polymer Components Symposium*," Vol. 1, 2, 3, Phillips Laboratory, EAFB, 1992.
2. deGennes, P.G. and Prost, J., "*The Physics of Liquid Crystals*," Second Edition, Oxford Science Publications, 1993.
3. deMul, M.N.G., and Mann, Jr. J.A., "*Multilayer Formation in Thin Films of Thermotropic Liquid Crystals at the Air-Water Interface*," *Langmuir* **10**, 2311 (1994). Also see Hönig, D. and Möbius, D., *J. Phys. Chem* **95**, 4590 (1991).
4. Adamson, A.W., "*Physical Chemistry of Surfaces*," 5th ed., John Wiley & Sons, Inc., New York, 1990.
5. Rieutord, F., Benattar, J.J., Rivoira, R. Lepetre, Y., Blot, C., Luzel, D. *Acta. Cryst.* **A45**, 445 (1989). Meusinger, H., Stamm, M. Boeffel, C., *J. Chem. Phys.* **96**, 3183 (1992).
6. Wasserman, S.R., Whiteside, G.M., Tidwell, I.M., Ocko, B.M., Pershan, P.S., Axe, J.D., *J. Amer. Chem. Soc.*, **111**, 5852 (1989).
7. Nguyen, D.Y.M., "*Microprocessing: The Preparation and the Characterization of Polar Ultra-Thin Films for Optical Applications*," M.S. Thesis, Case Western Reserve University, 1995; Nguyen, D.Y.M., Mayer, T., Hubbard, K., Singer, D., Mann, J.A., Lando, J.B., *Langmuir*, submitted 1995.
8. Joyce, S.A., Houston, J.E. *Rev. Sci. Instrum.* **62**, 710 (1991).
9. Israelachvili, J., "*Intermolecular and Surface Forces*," 2nd ed., Academic Press Inc., San Diego, CA, 1995.
10. Girard, C., Maghezzi, S., "*Dispersion Forces Between a Spherical Tip and a Periodic Crystal: Study of Different Asymptotic Cases*," *Surface Science Letters*, **255**, L571 (1991).
11. Grabbe, Alexis, Personal Communication and Software for the Lifshitz Calculations. See reference 9 for an introduction to the basic theory.
12. Ling, F.F., "*Surface Mechanics*," John Wiley & Sons, New York (1973).
13. Bird, R.B., Curtiss, C.F., Armstrong, R.C., Hassager, O. *Dynamics of Polymer Liquids*, " 2nd ed., Vol. 2, Kinetic Theory, John Wiley & Sons, New York, 1987.

14. deGennes, P.G., J. Chem Phys., **55**, 572 (1971) also Phys. Today, **36**, 33 (1983).
15. McCullagh, C.M., "*Transesterification in Blends of Liquid Crystalline Copolyesters*," Ph.D. Thesis, Case Western Reserve University, May, 1995. Available through Michigan Microfilm Service.
16. Shih, R.C-C., "*The Characterization of Diacetylene Acid Langmuir and Langmuir-Blodgett Films*," Ph.D. Thesis, Case Western Reserve University, 1994. Available through the Michigan Microfilm Service.
17. Yu, L., "*Vibrational Spectroscopy of Diamond Films, Longmuir-Blodgett Films and Aromatic Polyethers*," Ph.D. Thesis, 1992. Available through the Michigan Microfilm Service.
18. Mann, J.A., "*Dynamics, Structure and Function of Interfacial Regions*," Langmuir, **1**, 10 (1985).
19. Albarici, Aparecido, "*Langmuir-Blodgett Films as Alignment Layers for Nematic Liquid Crystal Displays*," MS thesis Case Western Reserve University, Cleveland, OH, 1994.
20. Lando, J. and Mann, J.A., Directors. The Polymer Microdevices Laboratory supports a number of projects involving the anchoring effect in LCP for display and sensor applications.
21. Ross, C. Thomas, "*Chemical Reactivity and Mechanical Properties of Well-ordered Organic Films Confined to Conducting Substrates*," Ph.D thesis, University of New Mexico, Albuquerque, NM, 1994.
22. Ulman, A., "*An Introduction to Ultrathin Organic Films: From Langmuir-Blodgett to Self-Assembly*," First ed. Academic Press Inc., Boston, MA, 1991.

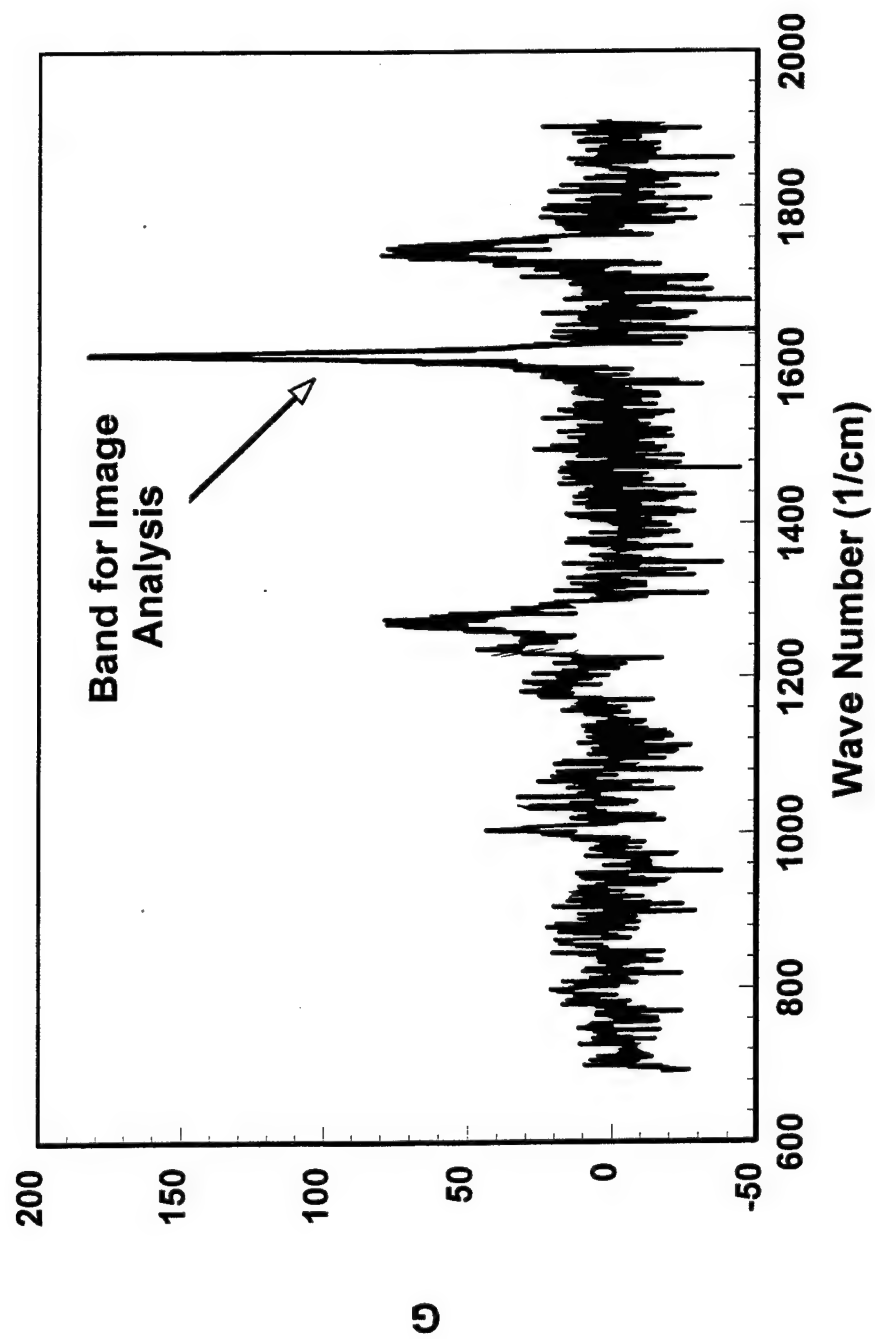


Figure 1: Representative Raman Spectrum of the Surface of SYN 10 thin film. The band used in the surface scan is marked.

Signal vs Position on SN10

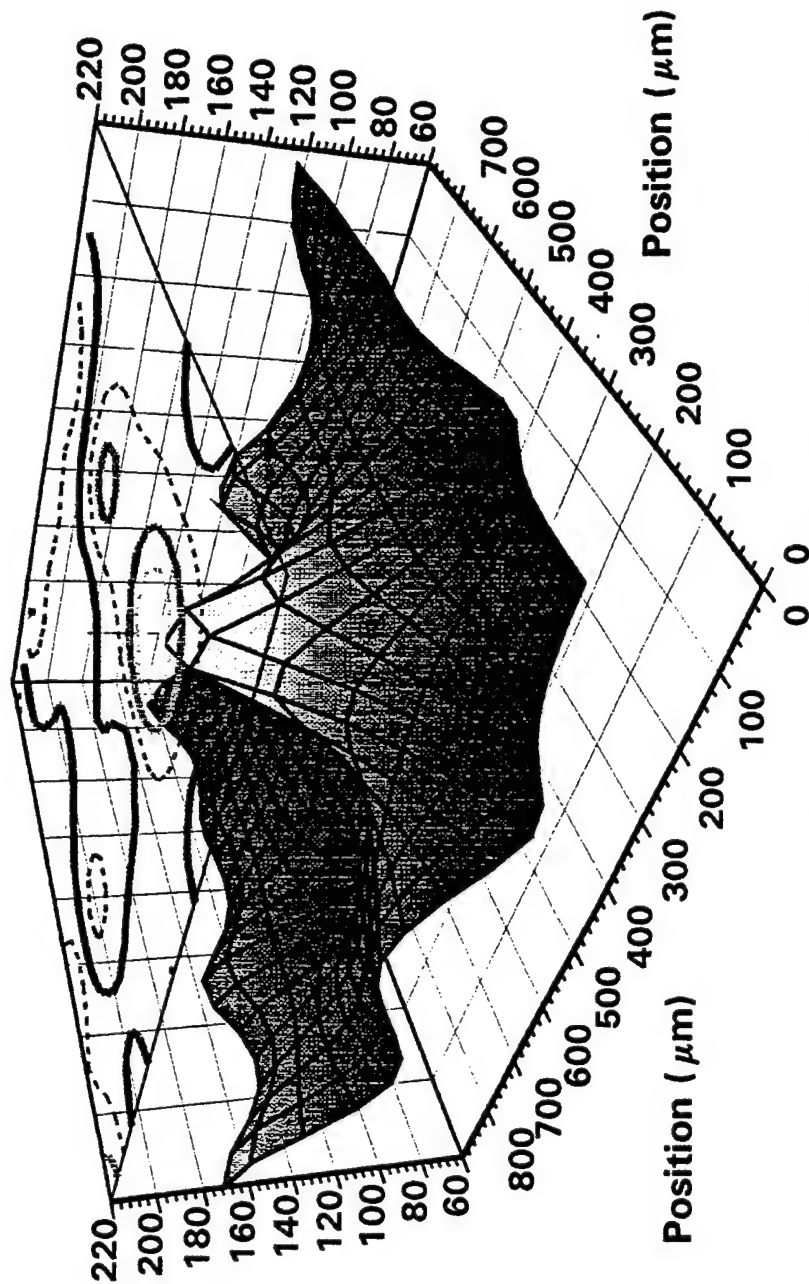


Figure 2a: The signal strength of the CO mode of SYN 10 as a function of location on a 800 x 800 μm patch of a thin film some 20 μm thick.

Signal vs Position on SN10

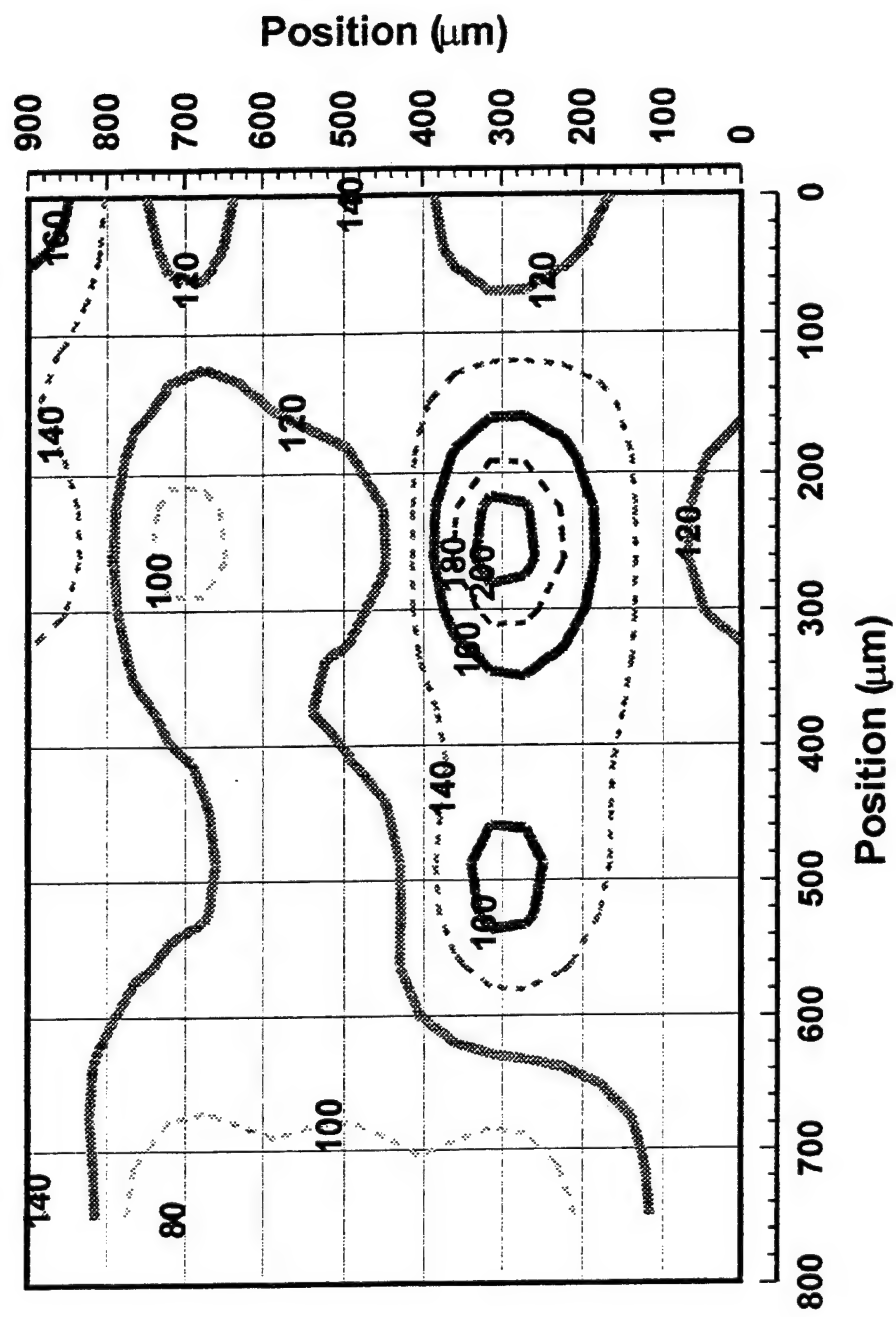


Figure 2b: The equi-intensity curves for the data shown in a. Notice that there are intensity gradients on the surface.

Band Width vs Position on SN10

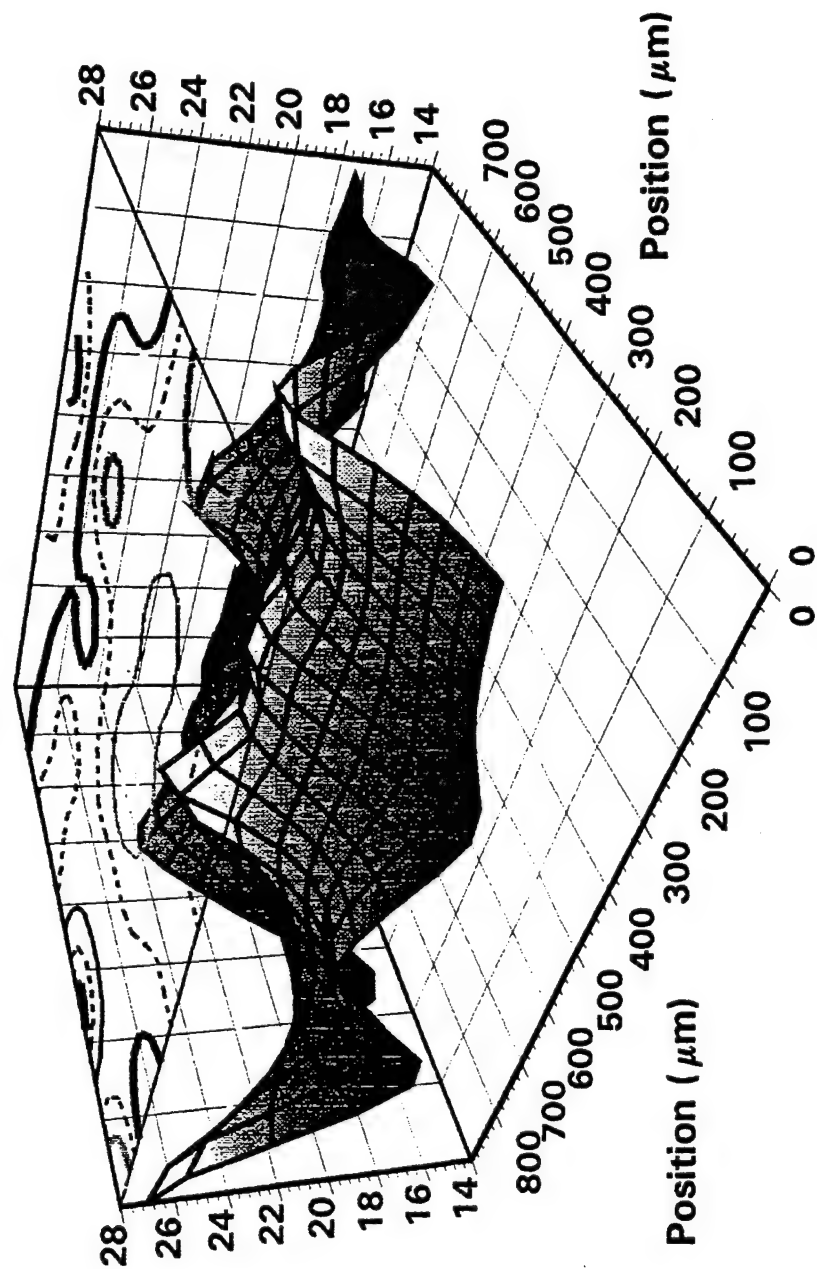


Figure 3a: The Raman CO band width as a function of position on a 800 x 800 μm patch of a SYN 10 thin film some 20 μm thick.

Band Width Vs Position SN10

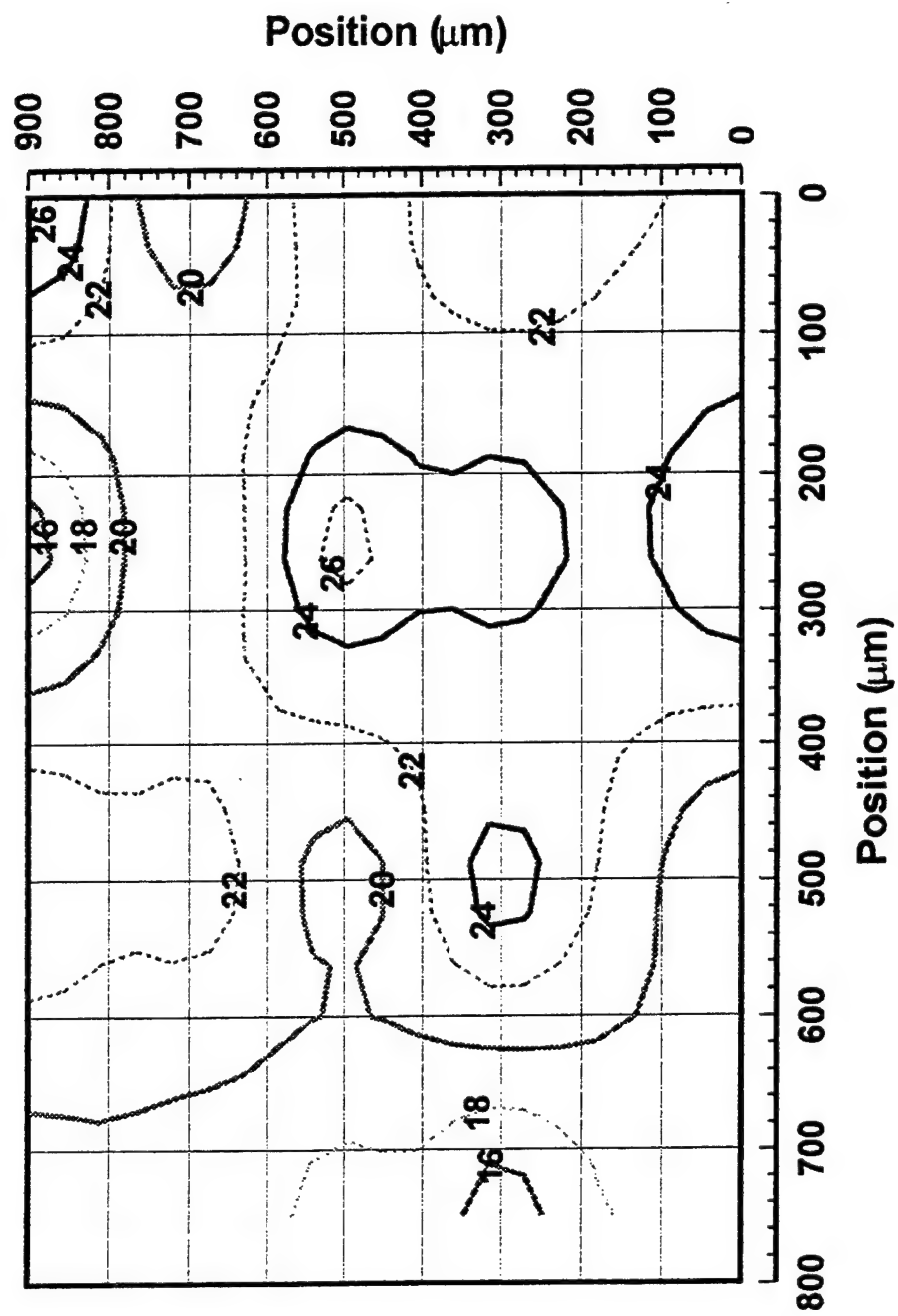
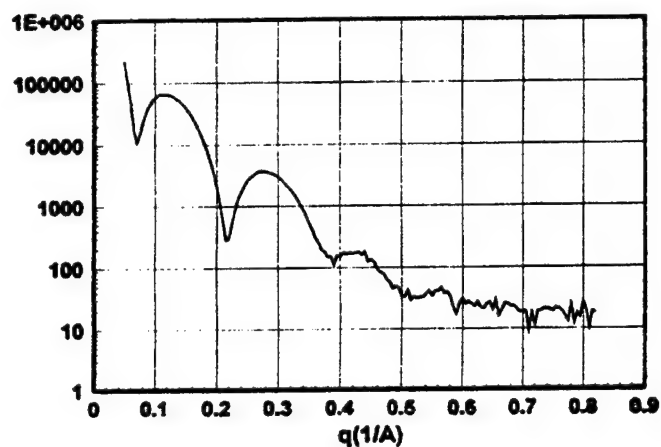
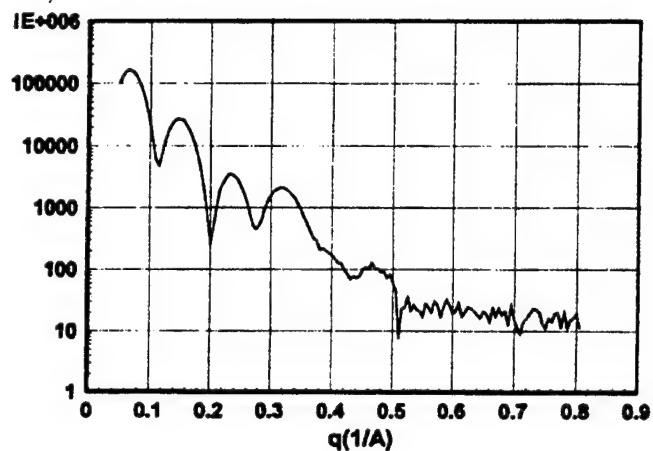


Figure 3b: The equi-intensity curves for the data shown in a. Notice that there are shift gradients that don't always correspond to intensity gradients. Compare figures 2 and 3.

One Layer Copolymer LB



Two Layer Copolymer LB



Three Layer Copolymer LB

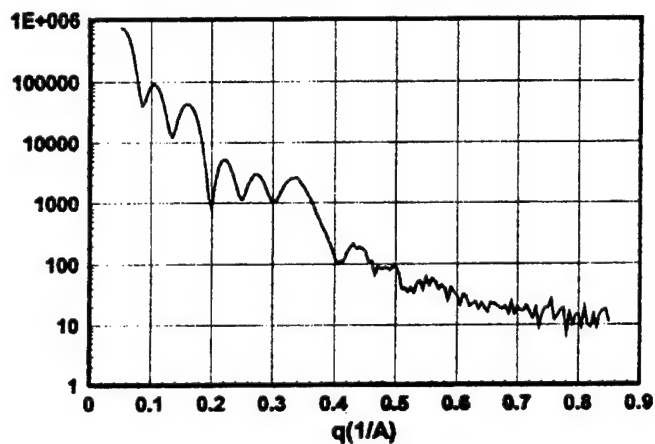


Figure 4: A, B, C represent one, two and three layer LB films of a co-polymer LCP serving as a model material. Note the change in sharpness of the fringes as the outer layers build up on the alignment layer.

Ten Layer Copolymer LB

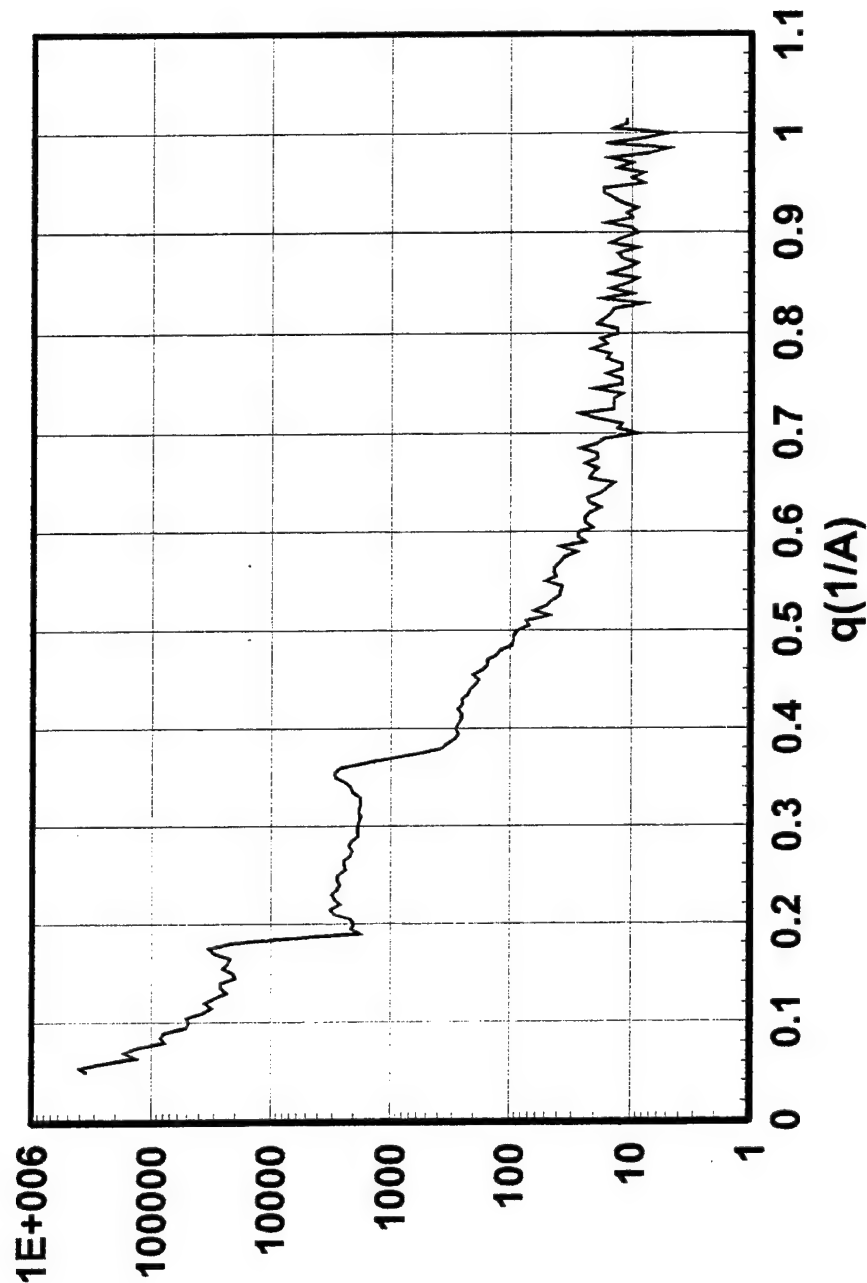
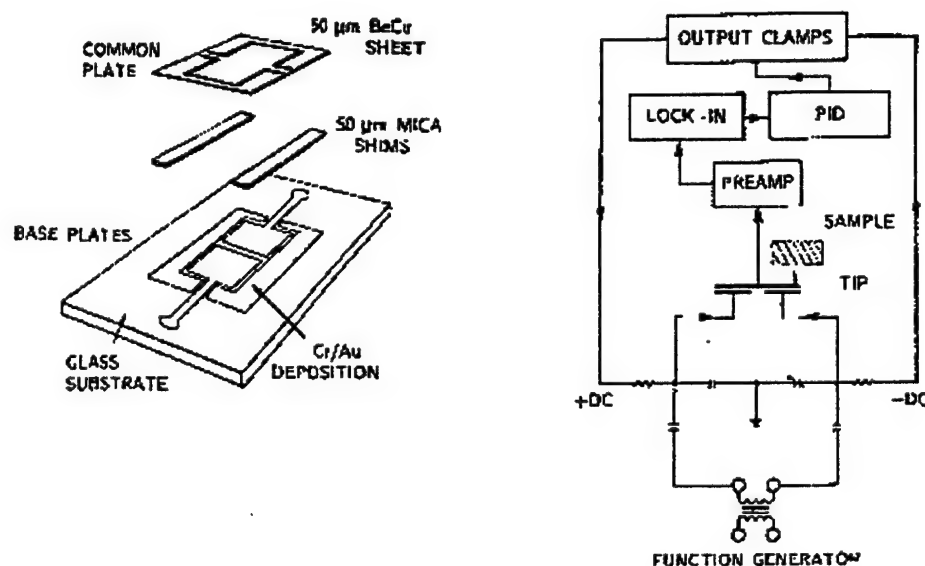


Figure 5: The x-ray reflectivity of a ten-layer LB film of the co-polymer model. Notice the sharp fringes implying well ordering of the layers that were deposited on top of the alignment layer. Full order was obtained in 10 layers and was maintained beyond that to as many layers as was deposited.

Houston's AFM



Rev Sci Inst. 62(3), 710(1991)

Figure 6a: Schematic of the Houston form of the AFM.

Houston System

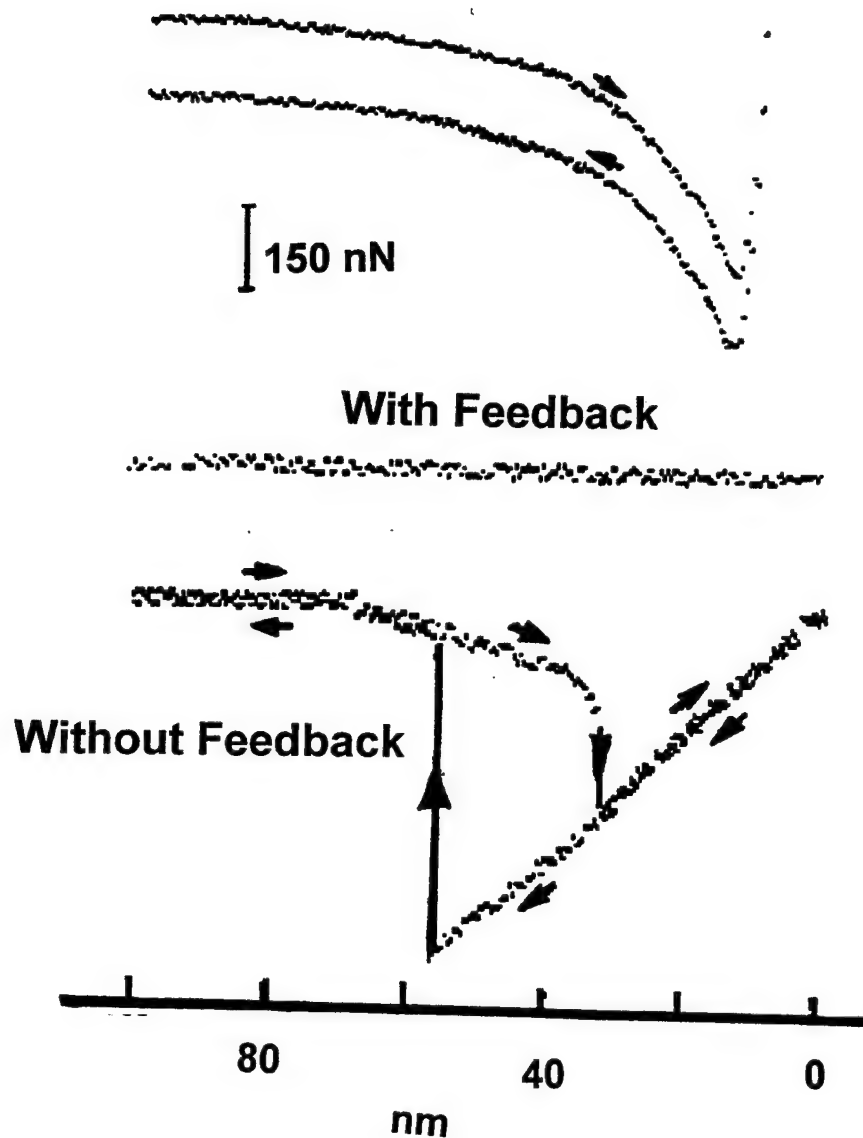


Figure 6b. Data from Houston et al. (8) showing the effect of the feedback stabilized design. Note that the tip does not snap to the surface when sufficiently close.

Atomic Force Microscope

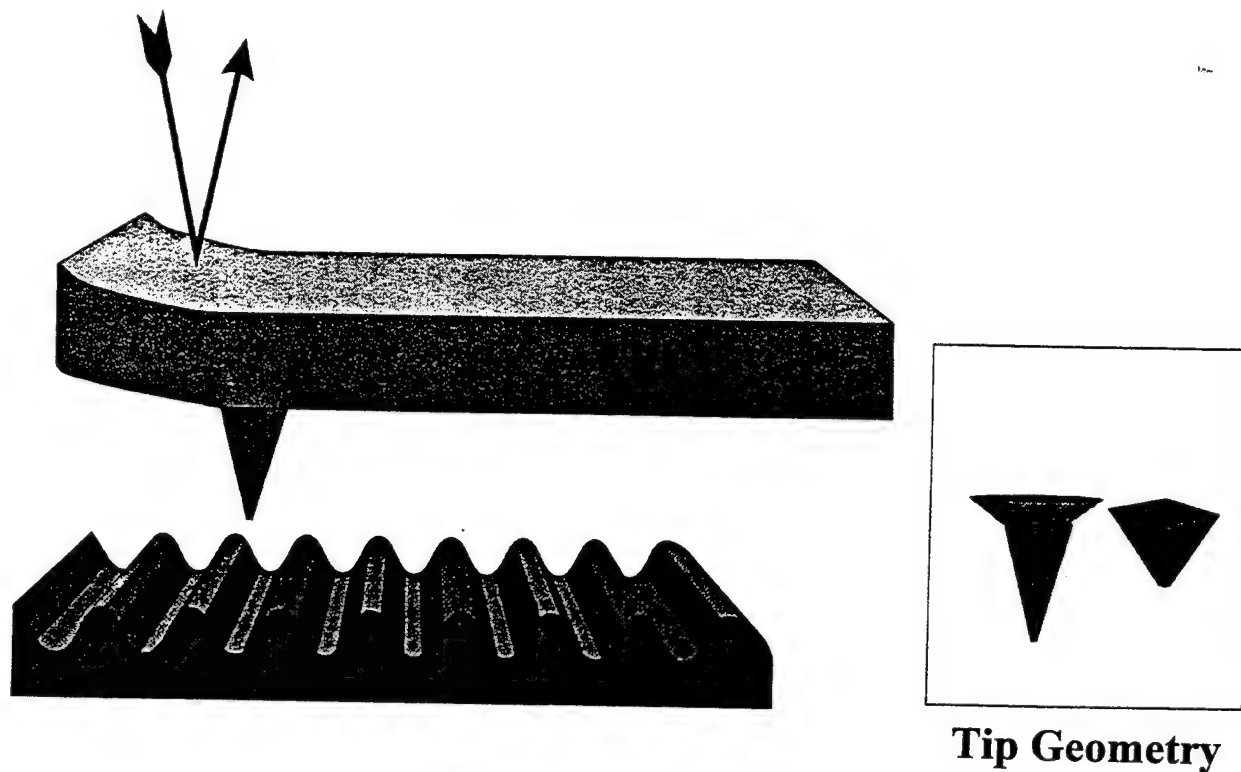


Figure 7: The conventional AFM tip-surface configuration. Note that films can be self-assembled on any tip that can be used with either the Houston system or the conventional system.

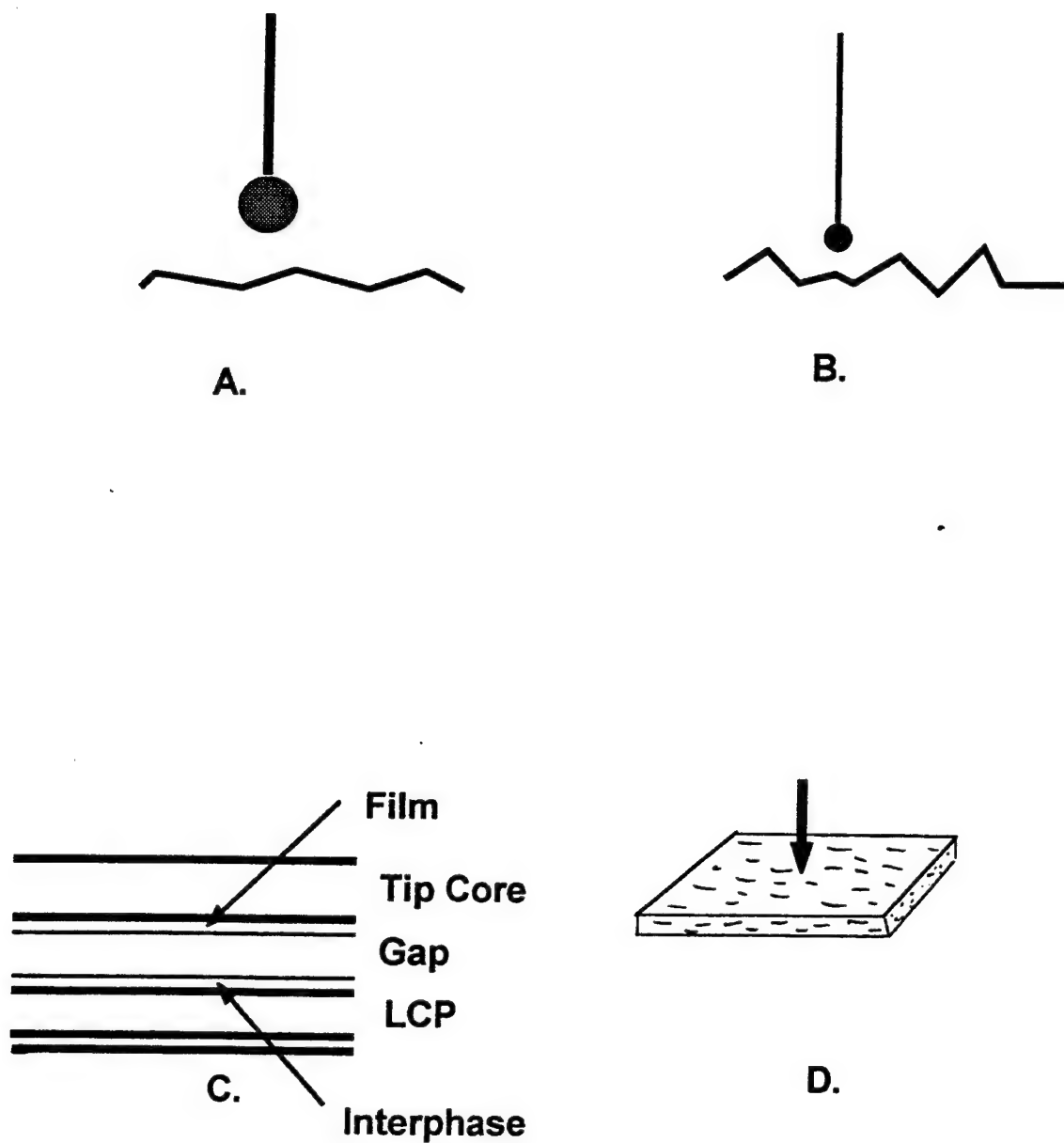


Figure 8: A. and B. suggest the effect of the probe diameter in the resolution of nanometer scales. C. shows the parallel plate calculation for the force of interaction. D. suggests that sufficiently sharp probes will be able to resolve the surface structure when made basic by self-assembly of amine surfactants.

Force Spectrum for PROBE/SAF/AIR/POLYMER Liquid Crystal Film

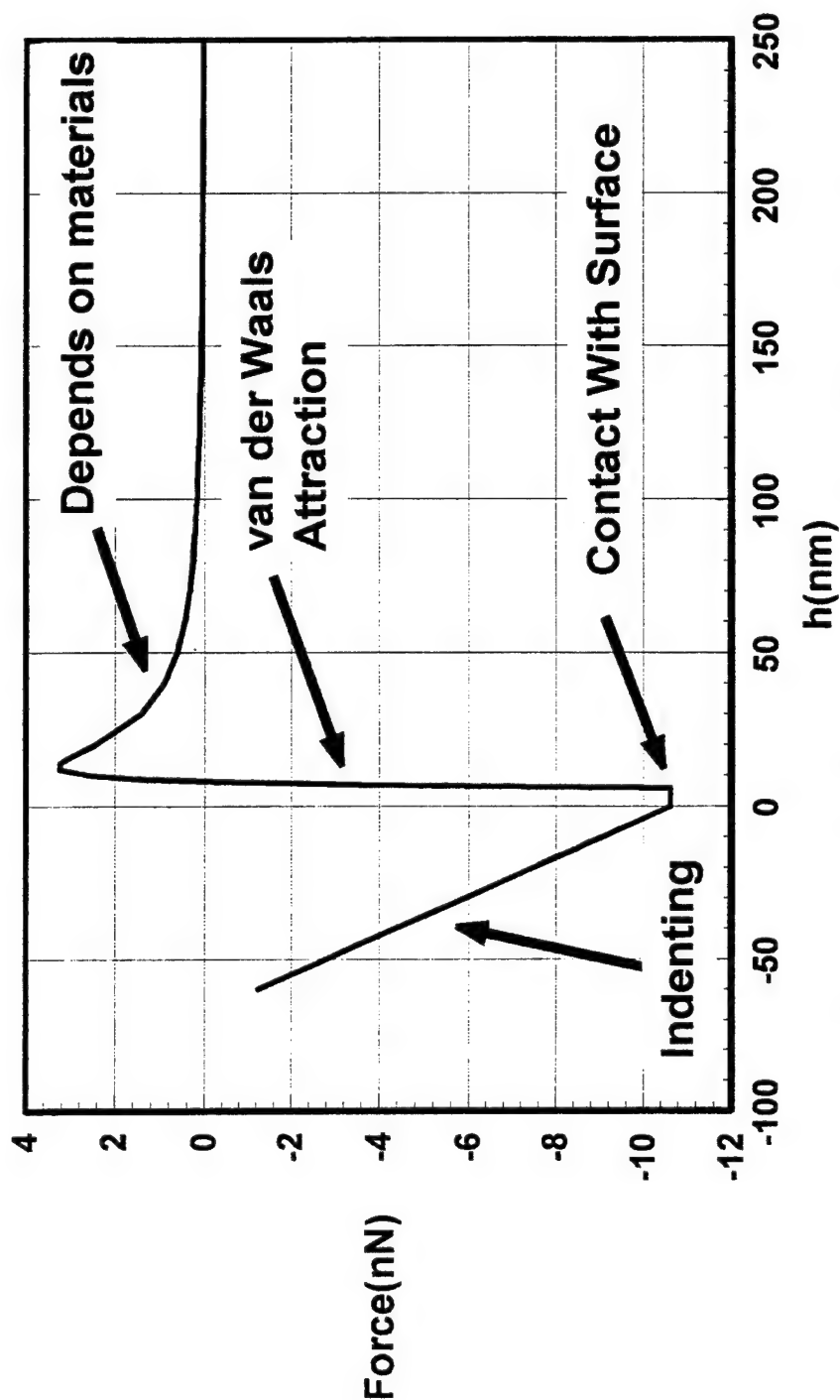


Figure 9: Calculation of a force spectrum using the full Lifshitz theory including a self-assembled monolayer on the probe and a model LCP as the substrate. Note that only one elastic modulus was used for the indentation curve but the model can be generalized.

The Chemistry of LB and SAF Alignment Layers

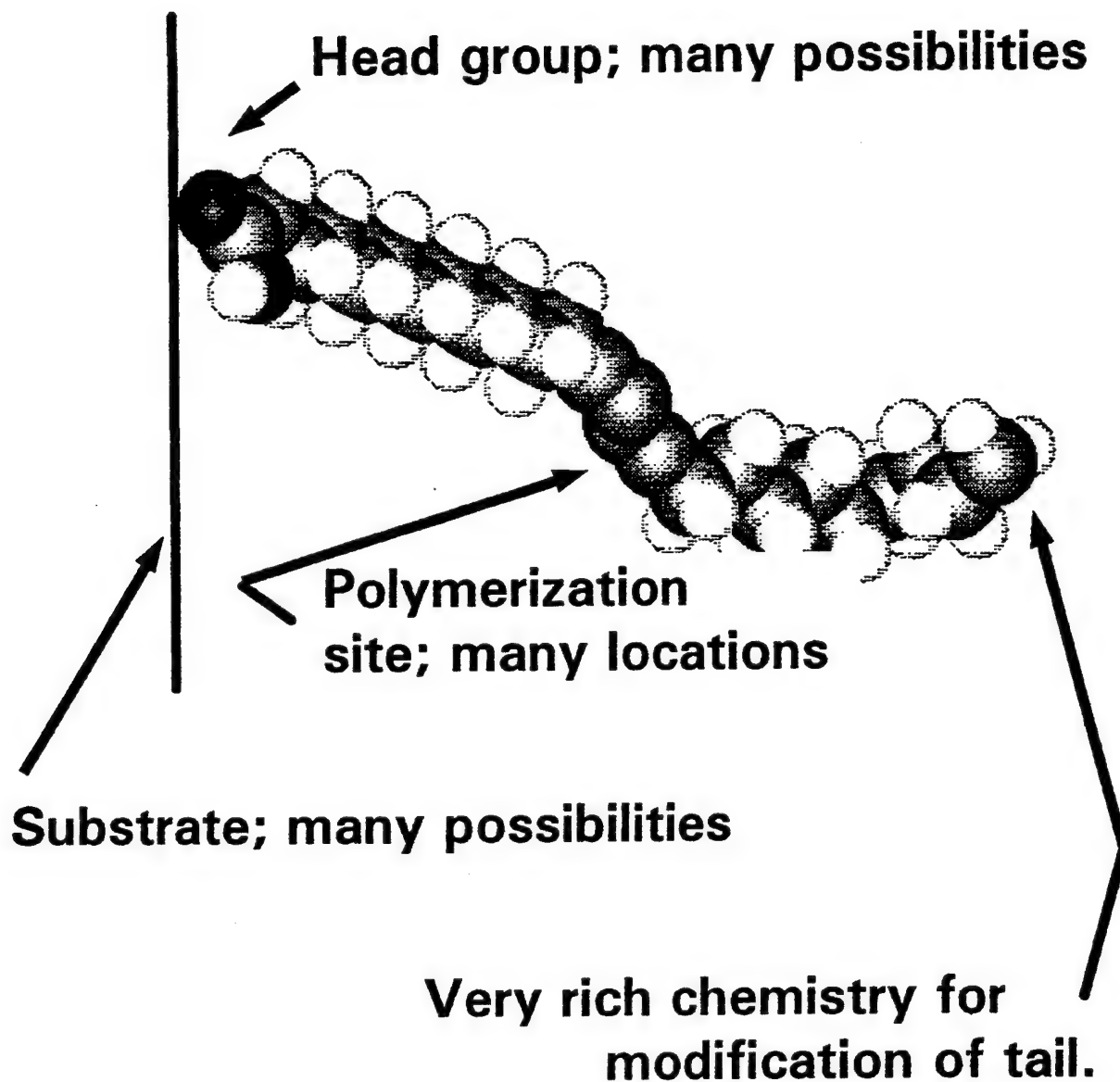


Figure 10: The chemistry of the alignment layer. Note that the diacetylene system suggested here are stable to high temperature when cross-linked by UV radiation.

Symmetry Considerations And Surface Chemistry

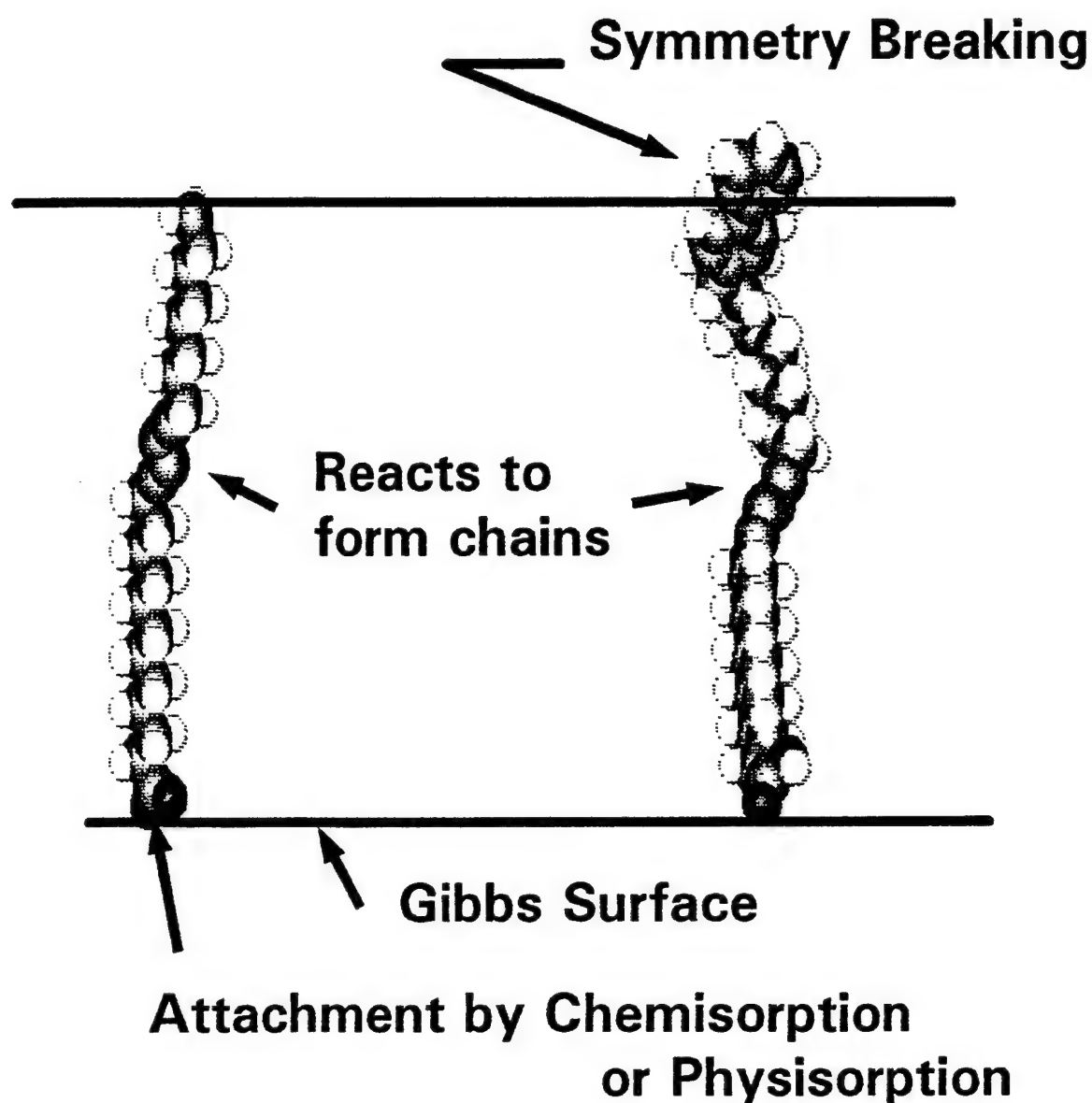


Figure 11: Symmetry conditions of the alignment layer. Note that attachment to the substrate can be done by a chemical band.

n and k for the cop10 a Liquid Crystal Copolymer

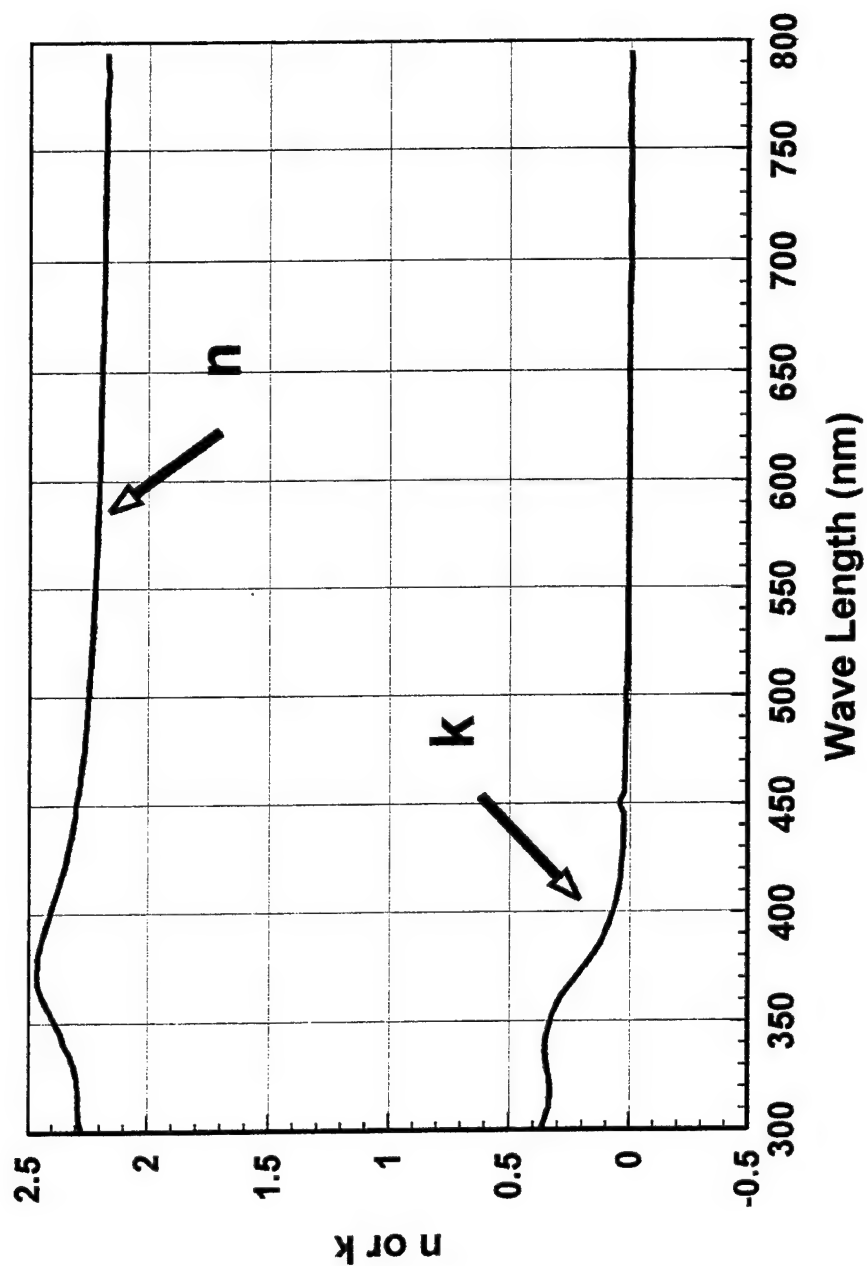


Figure 12: The ellipsometric spectroscopy for LB films of the model co-polymer used as an alignment layer. The spectrum of n and k implies strong ordering.

Car SAF - Am SAF

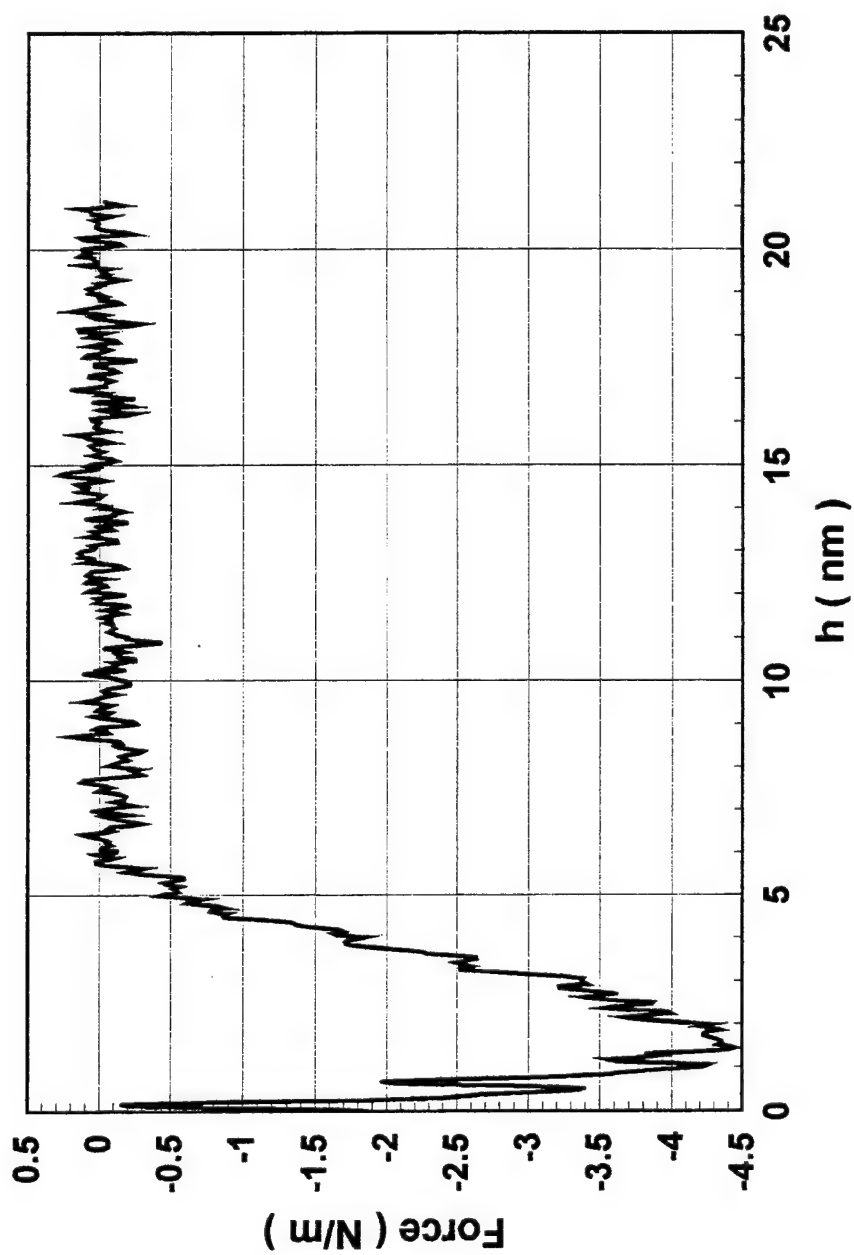


Figure 13: Force vs. h data from the thesis of Ross (21) showing strong acid-base interactions. This suggests that amine self assembled films be used on the tip.

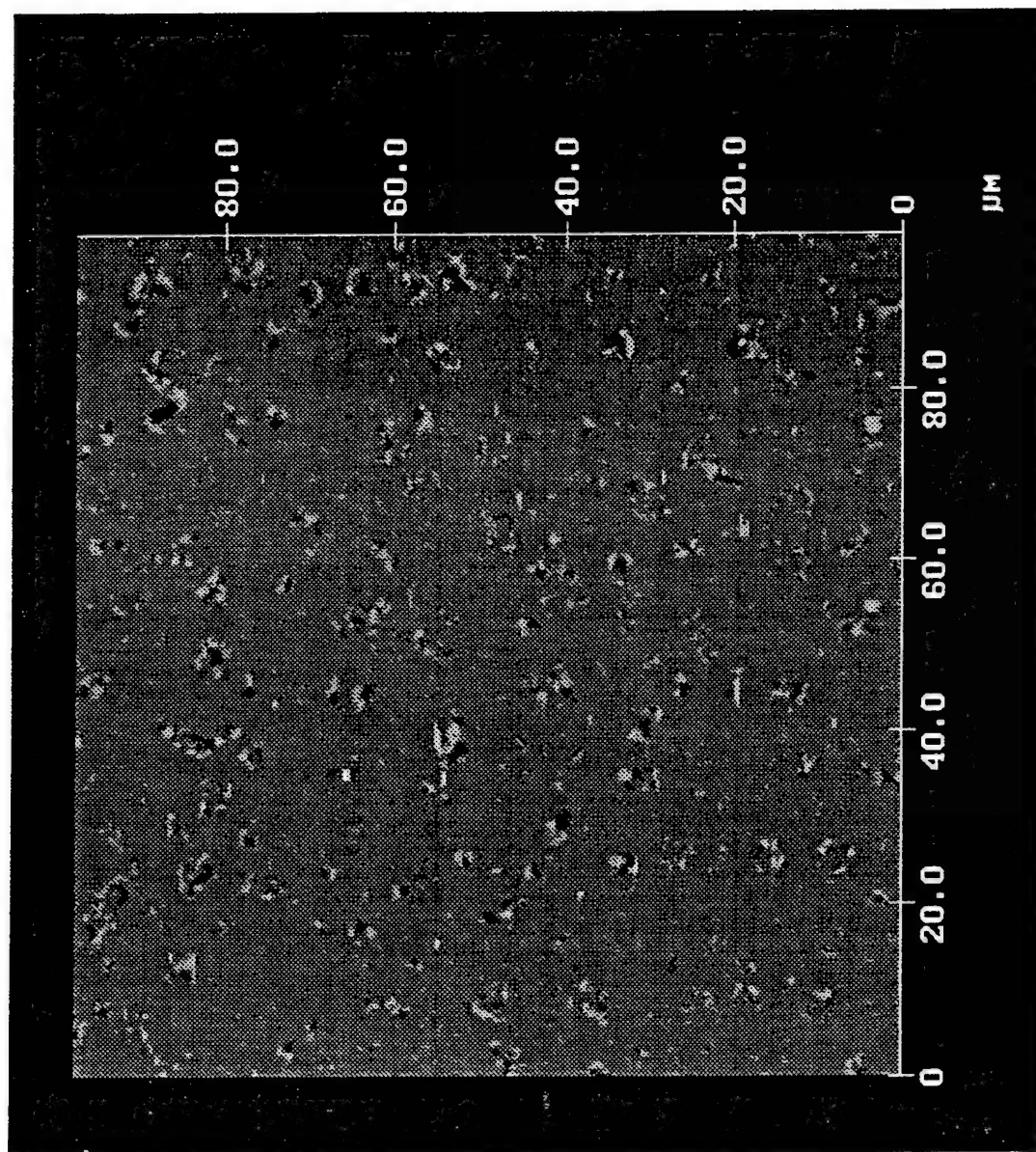
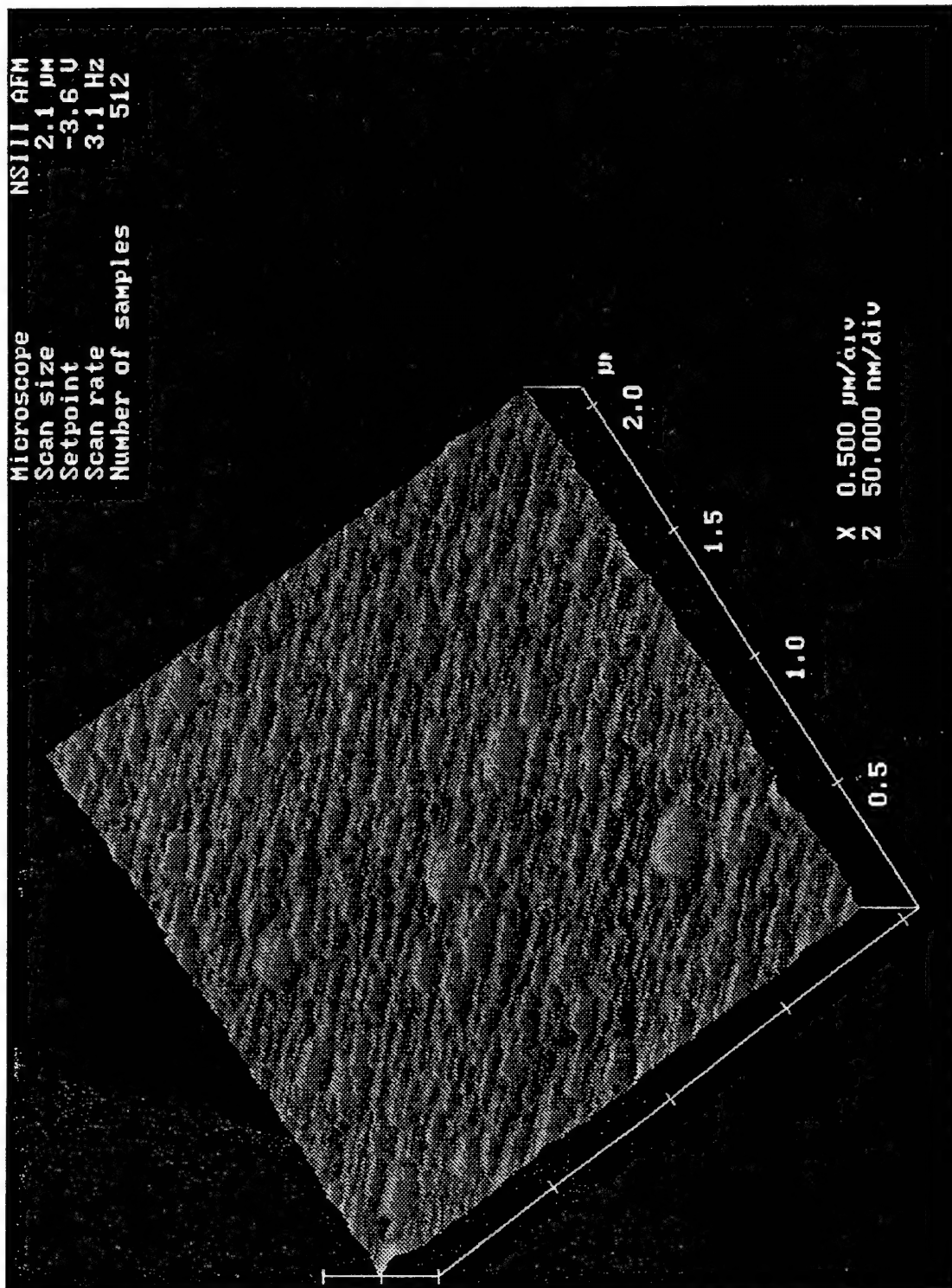
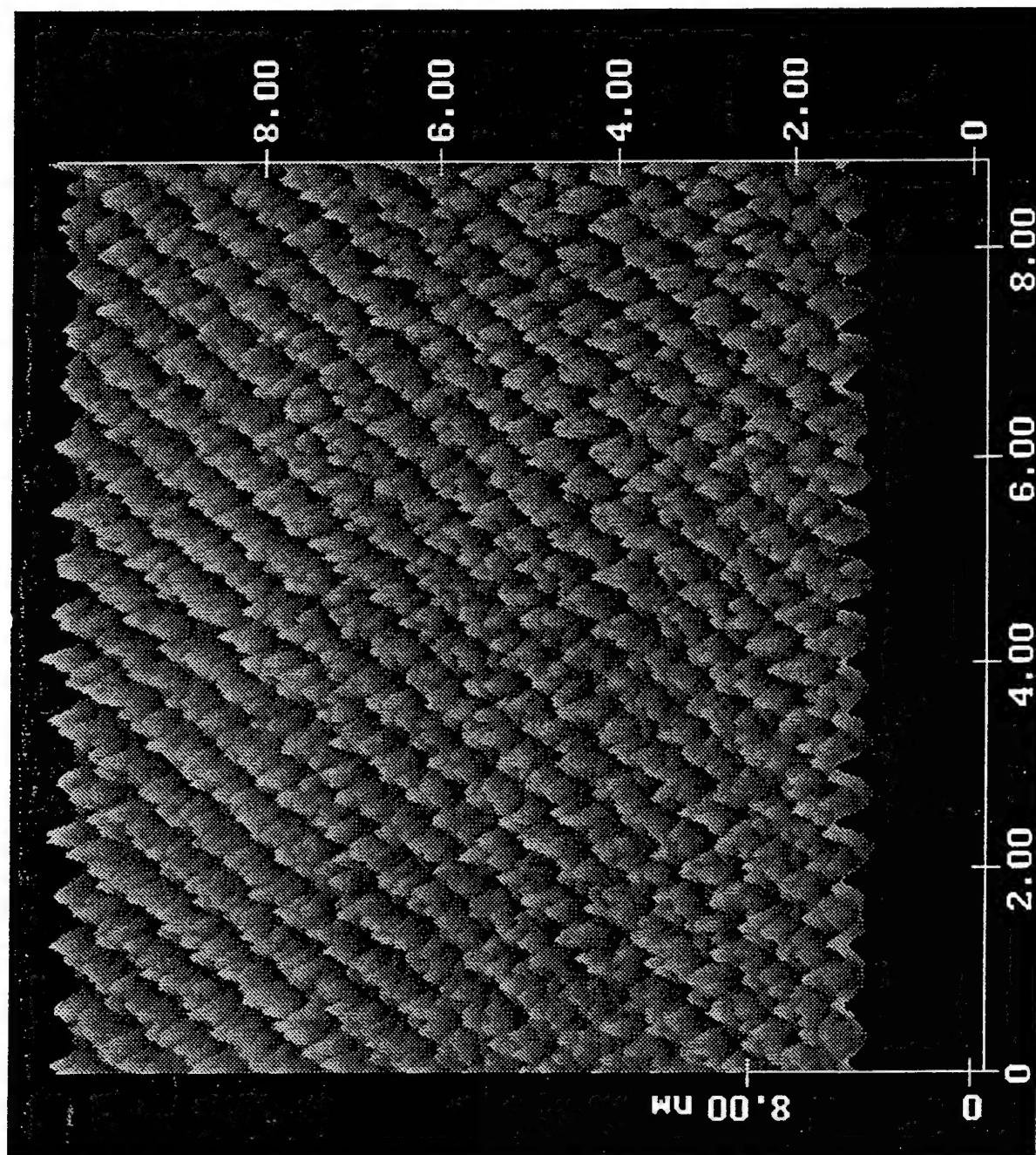


Figure 14: AFM images of a model alignment layer shown in figures 10 and 11, but specifically the 12-8 diacetylene system. Different magnifications are shown from the 40 μm length scales. Notice how molecular scale roughness develops and the probable effect of the LCP discussed in the text. From Shih (16).





RDL AFOSR Final Report

SYNCHROTRON RADIATION STUDIES OF LIQUID CRYSTAL POLYMERS

R. W. Hoffman

Phillips Laboratory
Edwards AFB CA

22 August, 1991

ABSTRACT

XAFS of AP and AP/Binder Systems

Techniques of Lytle detection in x-ray fluorescence were applied to 26 distinct chemical samples at the Cl edge, 1 at the K edge, and 7 at the Ti edge. The specimens commonly were pressed from powders, 2.5 μm particle size in the case of AP to thicknesses of about 1/32 in., thus obtaining samples for further experiments of adding binders or remaining uncoated. A special sample holder was designed and constructed to aid in the specimen transfer. The sample thickness necessitated fluorescent detection with an estimated probing depth of 25 μm . The experiments were carried out on beam line X-19A at Brookhaven National Laboratory and are in the process of being quantitatively evaluated. Differences in the XANES spectra between binders are noted, and tentatively related to the steric chemistry and to the local structure and valence of the Cl containing samples. Several new polymeric materials were also examined.

Introduction

The prime commitment to the RDL/AFOSR Summer Research Program was to make XAFS techniques available to the Phillips Laboratory, Edwards AFB and especially to certain persons who would be trained or updated in many phases of Synchrotron Radiation (SR) research involving absorption fine structure spectroscopy. The persons participating directly in this activity were Dr. John Rusek and Dr. Kevin Chaffee, Phillips Laboratory, and Professor Richard Hoffman and Mr. Guy DeRose, participants in the Summer Research Participation Program. A secondary goal was to explore the conductivity limits for the samples used in Scanning Tunneling Microscopy using the STM existing in the Phillips Laboratory, and will not be discussed in this paper.

The preliminary steps necessary to be able to carry out an XAFS actual sample data acquisition at a synchrotron include

- Synchrotron Selection
- Beam Line selection
- User proposal and approval
- Safety approval
- User financing
- Experimental design, including sample preparation and selection of spectroscopy and apparatus availability.
- Scheduling of experimental time with beam line personnel, including beam line training in safety and operation

For orientation, background information taken from the NSLS literature and relabeled as Figure 1 is reproduced on the following page.

The steps above must be completed prior to actually obtaining data and will not be discussed in detail in this report. In our case 5 days were scheduled from 7-12 August, 1991. AP, various standards, and other runs were completed at Brookhaven National Laboratory at the National Synchrotron Light Source (NSLS), Upton NY during that time. The items to be discussed in this report are concerned with the equipment alignment, data acquisition, and some of the problems arising during the actual run period. Additional details as to the data reduction will be found in the report by Guy A. DeRose to RDL.

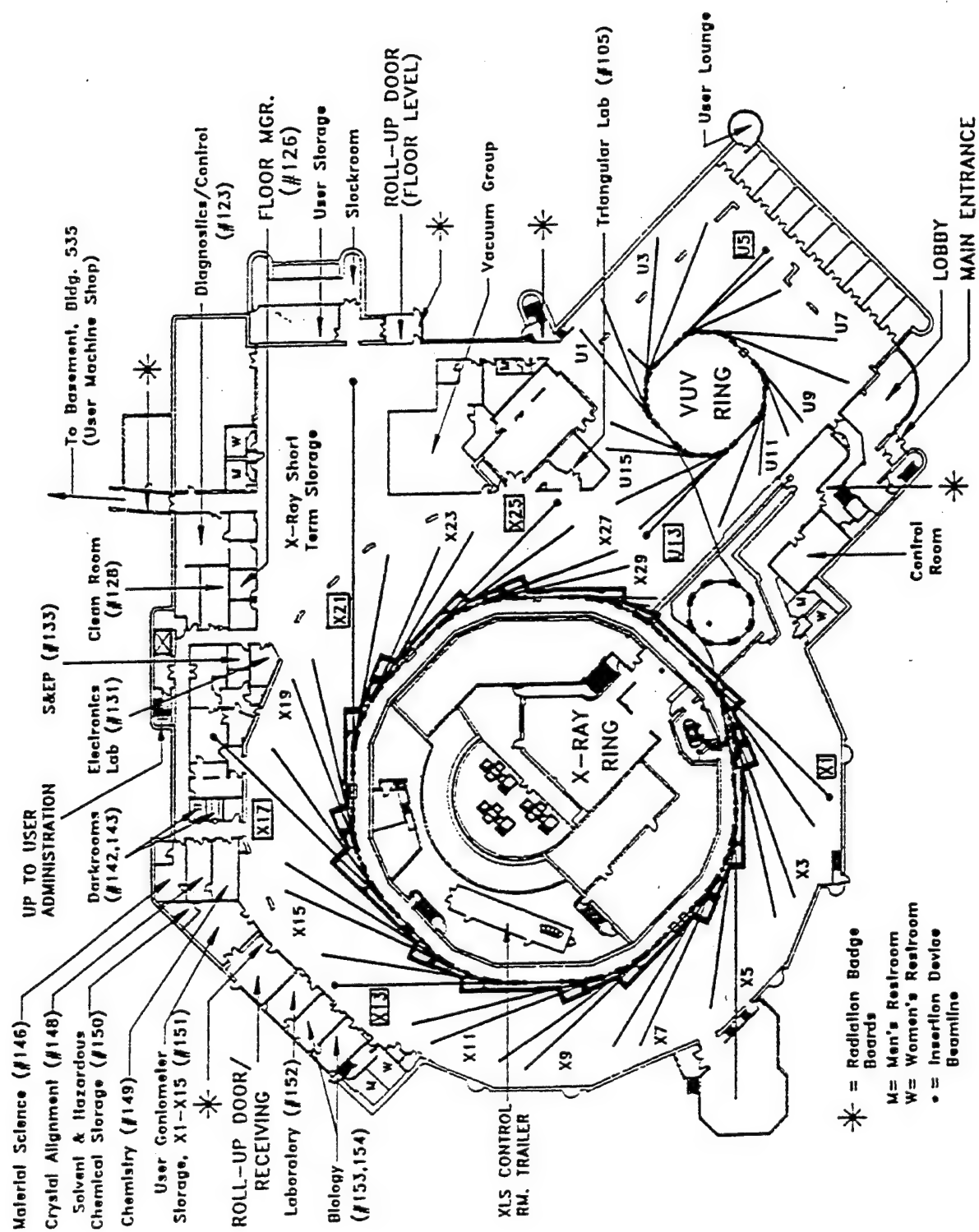


Figure 1. Floor plan of the National Synchrotron Light Source experimental area.

X-ray Absorption Fine Structure

XAFS is the short hand algorithm for both Extended X-ray Adsorption Fine Structure (EXAFS) and X-ray Absorption Near Edge Structure (XANES) or as is it sometimes called Near Edge X-ray Absorption Fine Structure (NEXAFS). EXAFS as practiced for surfaces is called SEXAFS and uses Auger electron detection. EXAFS, the earlier technique is the generation of outgoing spherical photoelectron waves of varying wavelengths following photoemission and the subsequent backscattering from nearby atoms in coordination shells and the analysis of the resulting raw data to provide elemental coordination distances and numbers in crystalline and modestly disordered samples. All XAFS techniques are commonly practiced using the high intensity SR sources (typically 10 billion photons per second). The Bremstrahlung radiation arising from bending magnets forms the white radiation of the beam line used (X-19A) for these experiments. The beam line has Si (111) oriented single crystals used as a monochromator to be wavelength tuneable to scan the absorption as a function of energy through and between various edges and is a polarized x-ray source, not used in these first experiments since the samples were powders of all orientations. This beam line was selected for its specialization to low energies and its availability with known personnel. It was well suited to our needs since a feedback system made vertical translation of the sample unnecessary as the energy was scanned. It suffered from having very limited on-line data analysis. Figure 2 on the following page give X-19A beam characteristics and other data.

XAFS Techniques

The XAFS information may be obtained in transmission, fluorescence emission, photoelectron emission, with X-ray, electron or ion detection using ion chambers or other detectors. One of the most common and versatile is the Lytle detector, a combination of transmission and fluorescence geometries, commonly using ion chambers and optimized for the 3d transition series and using Soller slits and x-ray K beta filtering techniques. For our experiments the Soller slits serve no useful purpose and no simple filters exist and were not used in either the CWRU or UK (X-19A) detectors. In the design of the experiment, proper consideration of the sample and detection geometry must be taken into account to optimize the data for easier analysis. While certain corrections may be made during

the data analysis, it is better to have good data in the beginning. In addition to the noise questions, one important parameter is the depth in the sample to be probed. For the Cl edge in most of the materials studied here, the absorption length is about 17 μm at energies above the Cl edge energy. Since we found in preliminary experiments in preparing samples it was not possible to press sample powders to make proper specimens with thicknesses less than 35 μm for transmission due to the soft radiation (2.623 KeV) used. As the samples were not electrically conducting, and we wished to probe a distance greater than 100 \AA in order to study buried interfaces, the fluorescent technique was selected and will be emphasized in this report. As stated earlier, we did not take advantage of the polarization of the X-ray beam in this run, but hope to examine oriented samples in the future.

SR Experience during August, 1991

Dr. John Rusek, Dr. Kevin Chaffee, Prof. Hoffman, and Mr. Guy DeRose went to the NSLS at BNL to make the measurements. We traveled from EAFB to BNL as a group. Since we had 5 days of beam time and we needed to operate 24 hours per day, we operated in two 12 hr shifts. Except for a major unscheduled beam dump (no X-rays) for a construction mishap and another for natural lightning strikes causing power failures for a total of some 36 hours, we were able to make full use of the NSLS facility and finished most of the samples that were available. Some beam time loss due to beam decay is expected. Taken from our log and end of run report, some statistics follow; more are available upon request.

Table I Beam Statistics 7-12 Aug., 1991

Possible time available (8 hr shifts)	15
No beam for many reasons (8 hr shifts)	6
Beam available (shifts)	9
Initial set up time (shifts)	1.5

Sample Preparation

Consistent with the necessity of using fluorescent radiation and a Lytle detector we investigated the pressing of AP and other materials into pellets in a die similar to a KBr press. Mr. David Cooke fabricated a very useful die that made samples nominally 3/8 in. in diameter. The samples were made 1/32 in. thick by filling the die with some 100 mg of AP. These samples were pressed to an oil pressure of about 1000 psig in a Carver press in Cell No 6 at the Chemistry Lab at Phillips Laboratory. We produced about 150 samples which were strong enough to withstand handling and shipment and thus serve as reproducible samples. Mr. Tracy Reed assisted with the final pressing.

This die was successful in making samples not only of AP but other standards, perchlorates and polymer samples for XAFS studies. Earlier studies to optimize pressing conditions showed a rather wide range of conditions possible, but a particle size of 2.5 μm was selected for AP. The pellet samples were removed from the die by light pressing. For AP the final pellet density increased slightly with particle size decrease and increased with increasing pressure of pressing. The final density was about 1.7 gm/cm³ or about 90% of the bulk crystalline density with a volume contraction of about 3 times. Upon extrusion from the die, the first exposed (Upper or Top surface) had a few fine cracks and some surface debris and was noted in the earlier studies. Only TiO₂, a standard (calibration) sample was not able to be pressed and required the addition of a binder. It and a CuClO₄ sample were vice pressed at BNL. The pelletizing technique provided samples of low mass that were easily transported and handled, and is recommended for future use. An appropriate sample holder was designed and fabricated to facilitate the sample insertion into the Lytle detector at the beam line. The geometry is shown in Figure 3 which follows. Reference 1 may be consulted for more details about XAFS experimental design.

Apparatus and Procedures used at BNL

Most of the operating hardware for the XAFS data acquisition and a Lytle detector was available as part of the X-19A apparatus. We provided the CWRU Lytle detector, samples, and operating experience. Some beam line specifications were reproduced in Fig 2. It is important to contact beam line personnel until the user is familiar with the beam line operation. In our case, Dr. Kumi Panigrahi, a former student,

Beamline:	X19A
Ring:	X-Ray
Operational Status:	Operational

Participating Institutions: NSLS, U. of Kentucky, U. of Michigan, BNL - Department of Applied Science (members of the X19A Stewardship Group)

Local Contact: Fu-Long Lu (516)282-5619, 2338 @ BNL

Spokesperson: Stephen Cramer (BITNET address: CRAMER@BNLCL1)

Research Program: X-ray absorption spectroscopy, EXAFS

Energy Range (keV)	Crystal Type	Resolution ΔE (eV) @8 keV, Si(111) @12 keV, Si(220)	Flux (photons/sec.)	Spot Size (mm)	Total Horizontal Angular Acceptance (mradians)
2.1 - 7.9	Si(111)	8.1 - 0.7*	$\sim 10^{11}$	40H x 5V unfocused	2.4(unfoc.)
3.4 - 12.9	Si(220)	12 - 0.8	@ 5 keV (100 mA, 2.5 GeV)	-1 mm diam focused	1.3(foc.)
7.6 - 13.4	Si(111)	8.1 - 0.7	$\sim 5 \times 10^{11}$	40H x 5V unfocused	2.4(unfoc.)
12.5 - 23.0	Si(220)	12 - 0.8	@ 11 keV (100 mA, 2.5 GeV)	-1 mm diam focused	1.3(foc.)

*Largest value corresponds to 2 mm slit. Small value is for 0.1 mm slit.

Optical Configuration

- Monochromator**
NSLS boomerang-type double flat crystal monochromator; fixed exit geometry; first crystal is water-cooled; operates at UHV; two presettable Bragg angle ranges of 14.5° - 70° and 8.5° - 15°; located 9.3 meters from the source. Operates primarily in low energy, Si(111), unfocused configuration.
- Mirror**
Cylindrical aluminum focusing mirror, electroless nickel plated and overcoated with rhodium, for focusing beam onto sample at 18.5 meters from the source; 3 mradian incidence angle; 23 keV high energy cutoff; mirror may be dropped out of beam path for unfocused mode; located 10.5 meters from the source.
- Windows**
Beamline is UHV up to window located inside radiation hatch; a 6 μ m graphite filter is in the beam at all times; the exit window for non-vacuum operation is 10 mil Be.

Experimental Apparatus

Positioning table using stepper motor controls, two perpendicular translations and effectively three mutually perpendicular rotations. Germanium array detector available by special arrangement with S.P. Cramer.

Computer System Hardware and Software

MicroVAXII computer with CAMAC interface running Micro-VMS operating system; Ethernet link to AMD cluster and major networks.

December 5, 1990

Figure 2 X-19A Beam Line Data

—X19A—

and other beam line people were very helpful. Although many beam lines are similar in their operation, differences exist between PRT groups resulting in differences in data collection and beam line operation. Most beam lines provide documentation and help to new users in order to obtain useful data from the beginning. In our case the CWRU Lytle detector failed near the beginning of our time necessitating the use of the University of Kentucky X-19A ion chamber and electronics being wedged mechanically to the sample chamber of the CWRU instrument. This was successfully accomplished at NSLS. To minimize the absorption of the X-rays of low energy in the air path, we selected a uhv beam line and filled the Lytle detector with helium in the sample region. Helium was also sent to the Io (first) ion chamber after it was repaired. The second (If) ion chamber was filled with nitrogen gas to absorb most of the K beta radiation and maximize the signal. The analog signals from the ion chambers are amplified and sent to a voltage to frequency converted before the signals were recorded by the beam line computers. Background (offset) readings are taken after any X-ray changes. The tuning of the Bremstrahlung is accomplished by computer control of the monochromator and proper alignment of the X-ray beam. This alignment must be carried out at the beginning and minor realignment done each time a new electron fill is made to the storage ring, approximately once each shift. Part of the alignment procedure is to adjust, by calibration with a known standard sample, the position of the monochromating crystals to the calculated edge energy by following a predetermined (computer) procedure.

The computer for the X-19A operation was able to preload scans for various energies and predetermined integration times to reduce the total time at the expense of a given scan time. This procedure also set the energy resolution of the monochromator. As the data evolved, it was obvious that the XANES region would be more important in showing differences than the EXAFS region so the scans were adjusted to optimize to provide better energy resolution near the edge of interest.

Realignment to find the position of the beam so that the sample may be placed in the proper position, calibration of the energy, and using standard known samples for phase and amplitude information necessary for the data reduction usually takes about half of the total available beam time; thus making use of the 24 hour a day 7 days a week schedule is required. Fortunately, the persons going to NSLS for this run all had prior SR experience.

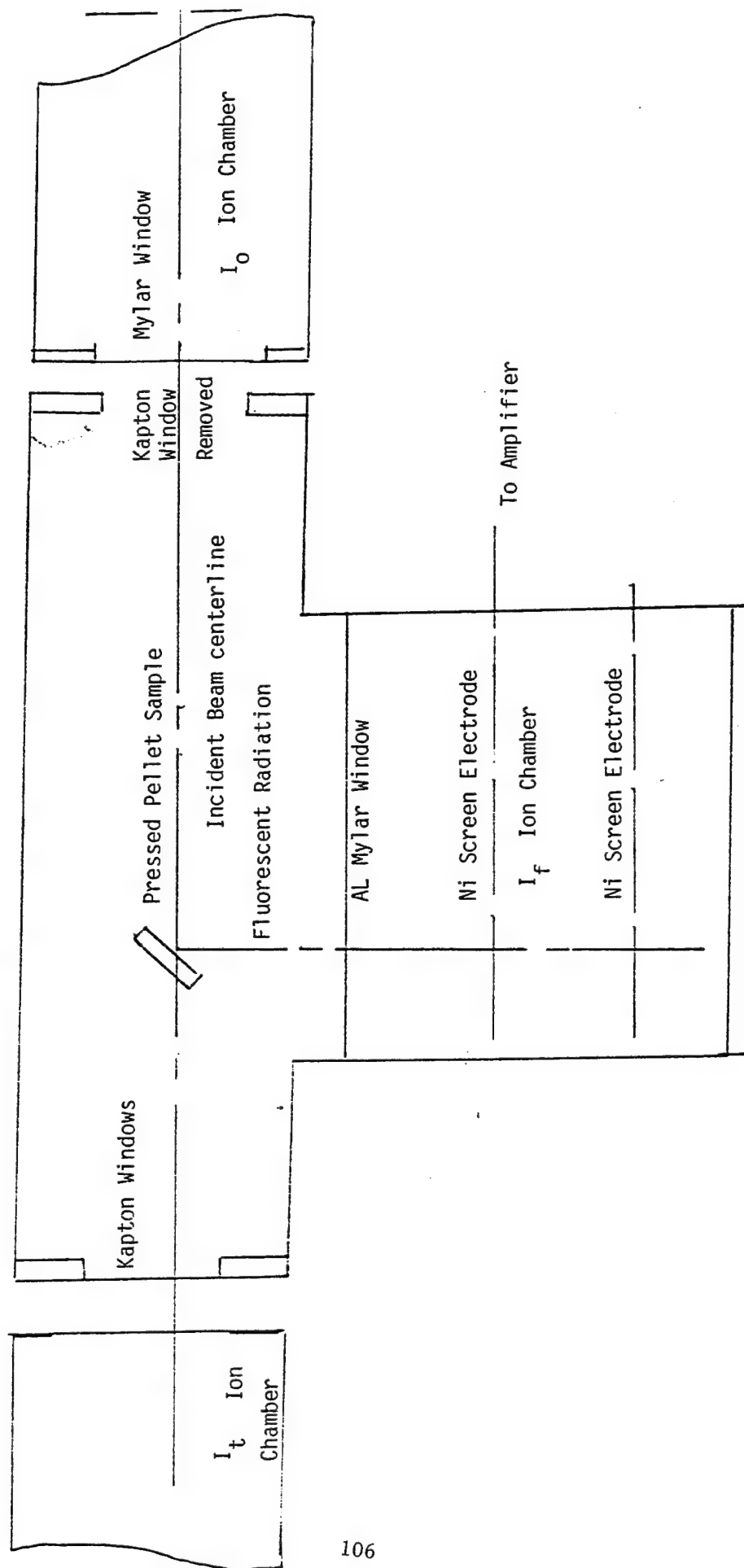


Figure 3 (CWRU) Lytle Detector for Fluorescence Detection of XANES and EXAFS

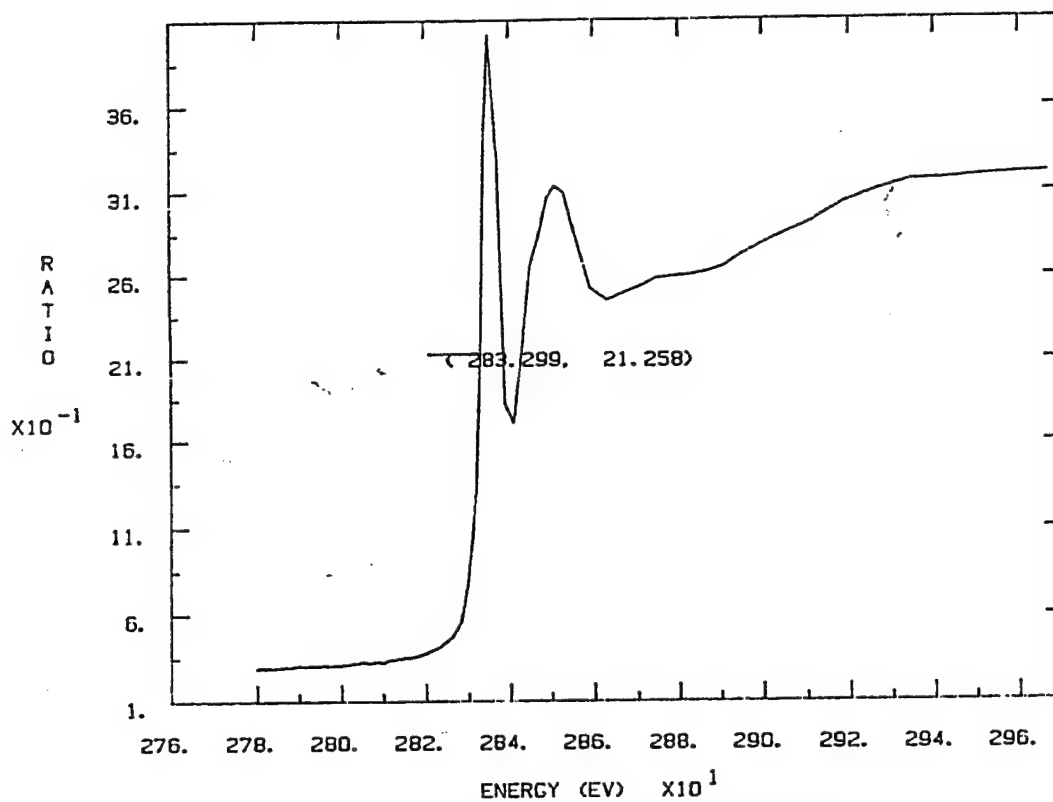
Analog Results

As stated earlier, no on-line data reduction exists on X-19A so that only data in the form of analog plots were available to bring back. These have been examined with the results reported below. All together some 143 separate scans were carried out. Many of these were for beam alignment purposes and covered only the Cl edge region. Later edge scans were set up to include both the Cl and Ar edges for a reference energy built in to each scan. Finally some full data scans from below the Cl edge to above the K edge were set up to minimize the statistical errors while maximizing the number of specimens that could be examined in a given time. These later scan parameters were used when time was limited during the last two days. In all, the following samples were examined as shown in Table II below:

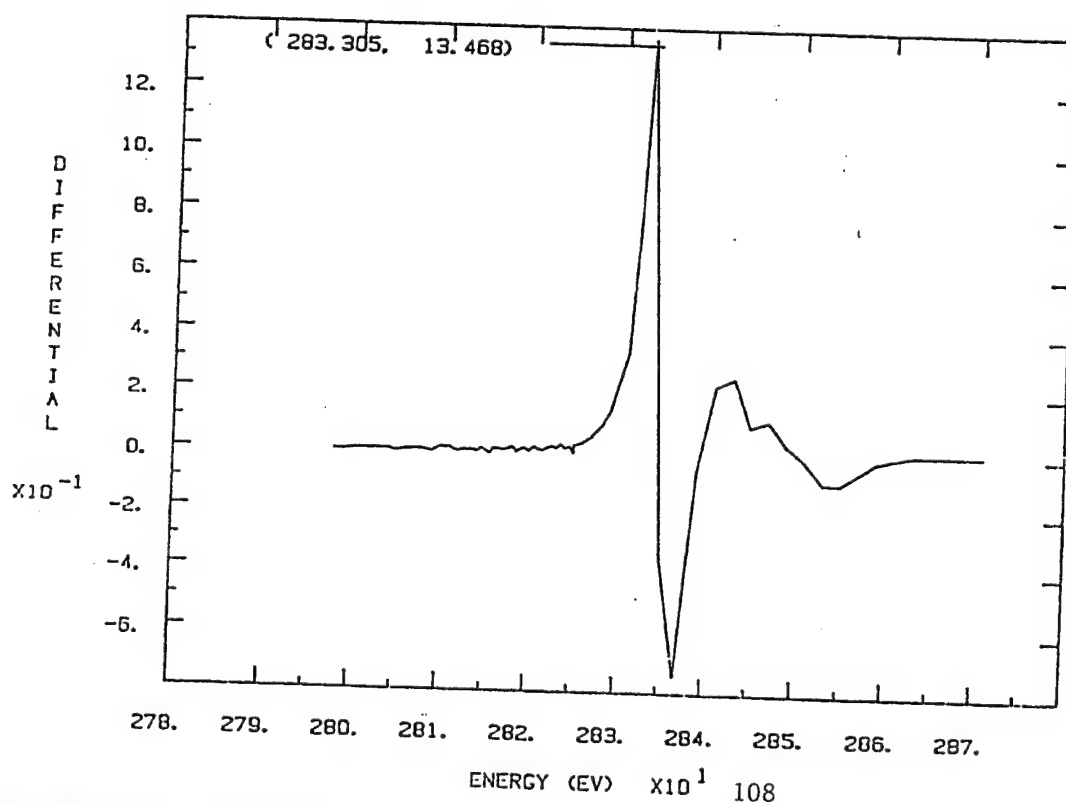
Table II Sample Summary Scan Data

Sample File	No. of Samples	No. of Scans
AP CLO4NH4	1	30
CLNH4	1	10
CLEDGE	2	22
STD Various		
KCl KCL & CLK	1	8
AP/binders Various	17	37
New Polymers SYN Var.	4	12
TI CVD Various	2	5
TI STD Various	5	12
Various polymer window films	3	3
Totals	36	109

Representative data are shown in Figures 4-8 for both energy calibration, XANES (Multiple scattering), and EXAFS (Single scattering) regions. Details are not given here, but file numbers are on the figures and some details are given in the Figure Caption list.



CLO4NH4. 301V/ 3/1 8-AUG-91 Figure 4a Cledge scan for energy calibration



CLO4NH4. 301D 3/1 8-AUG-91

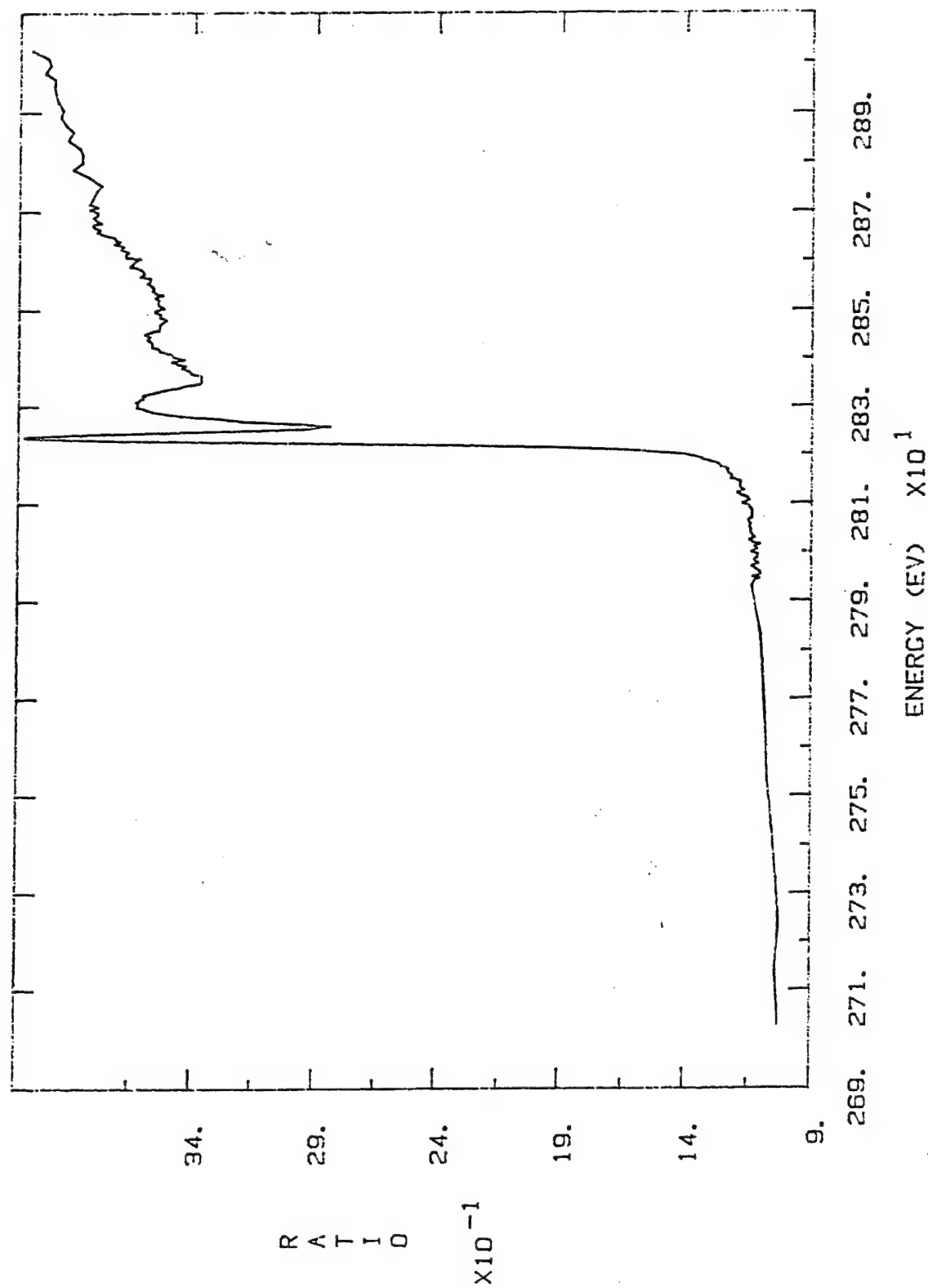


Figure 5 C1 XANES Scan of Chlorohydroquinone

CLCLHQ.002 ✓ 3/1 11-AUG-91

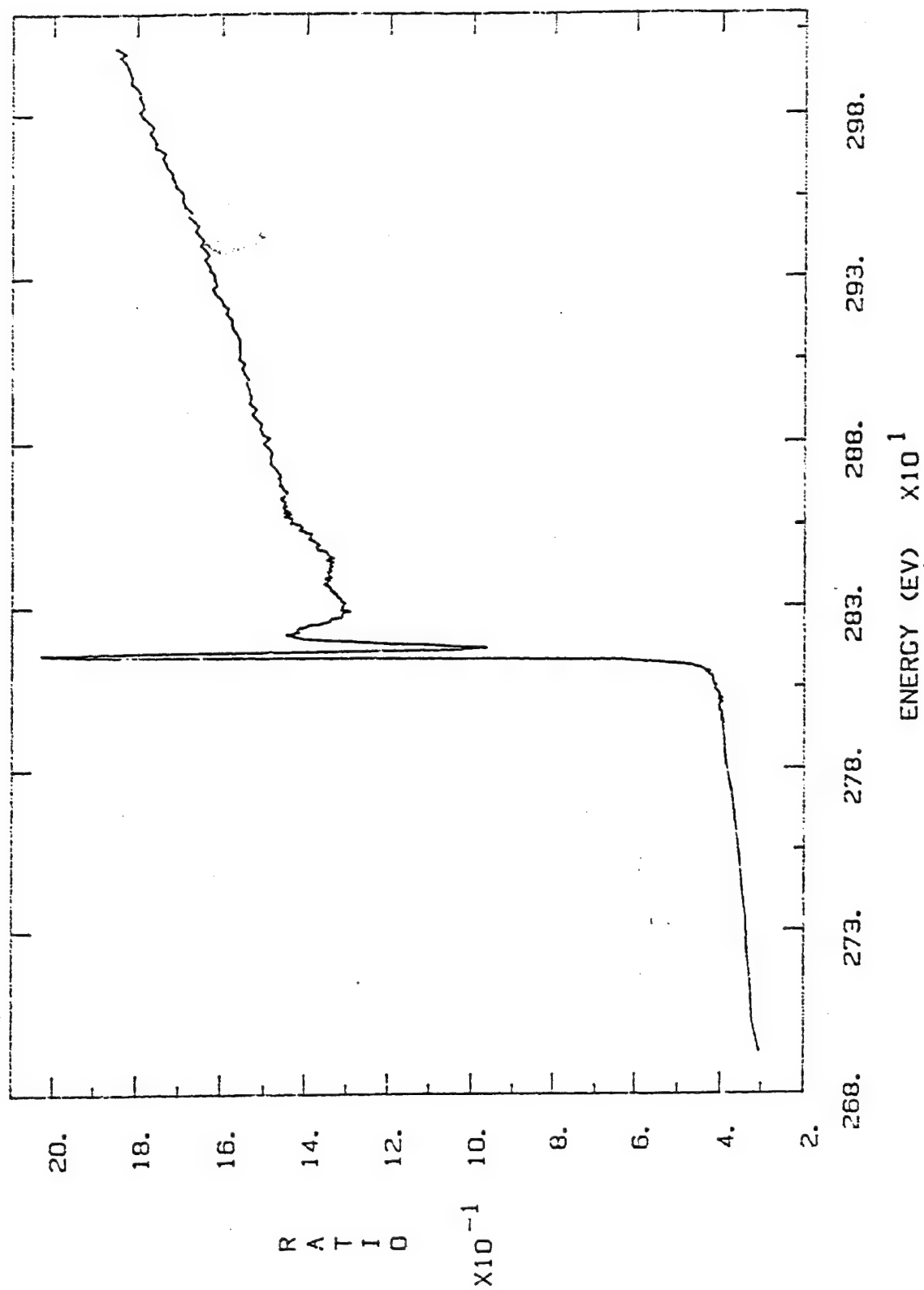
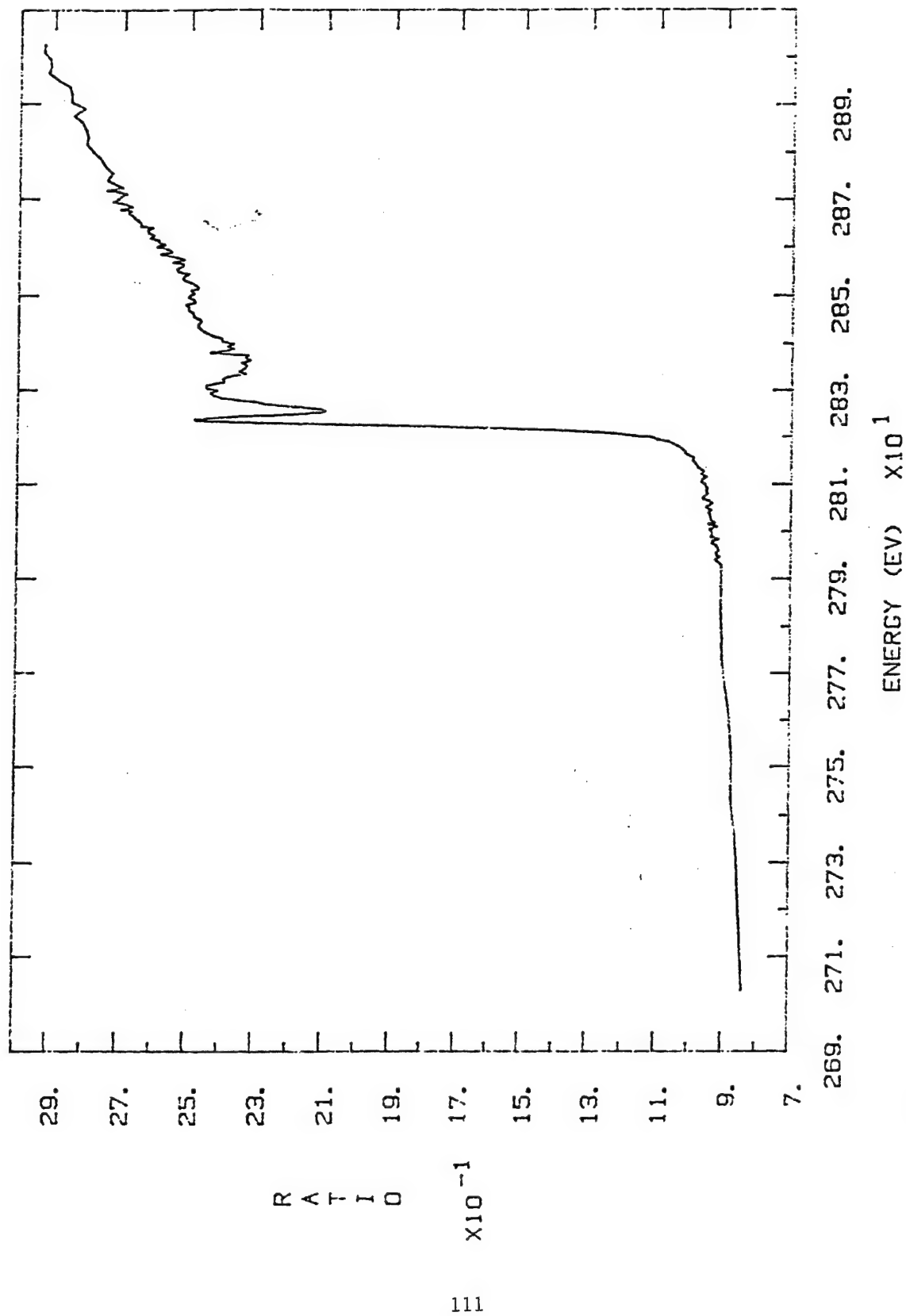
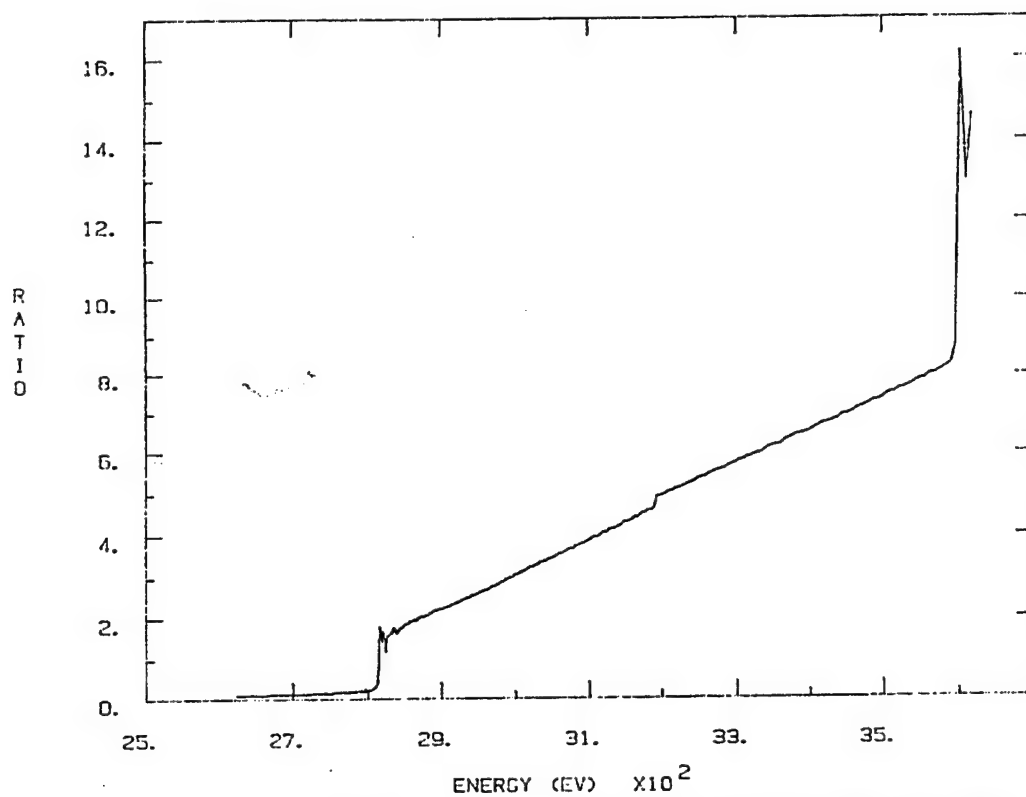


Figure 6 C1 XANES Scan of Newly Synthesized Polymer

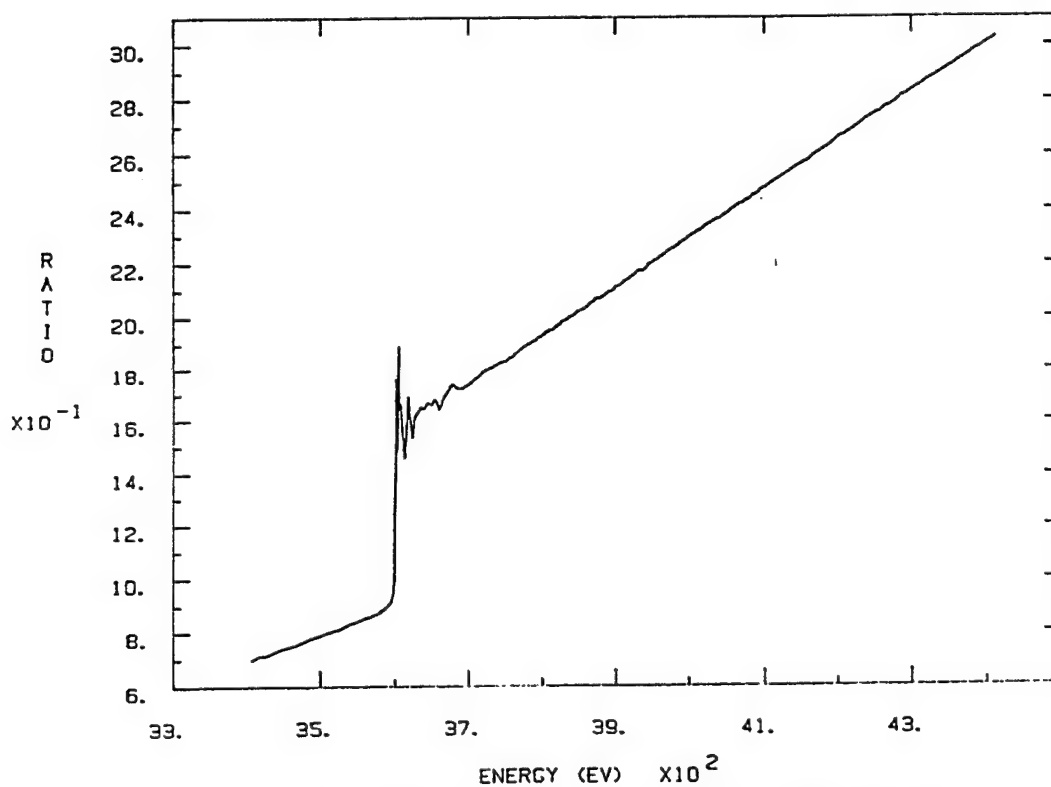
CLSYN14.002 3/1 10-AUG-91



CLPACP.001W/3/1 11-AUG-91 Figure 7 C1 XANES Scan Of AP/Binder



CLK.001 3/1 9-AUG-91 Figure 8a KCl Cl edge full scan showing A and K edges and Cl EXAFS.



KCL.002 3/1 11-AUG-91 112 Figure 8b KCl K edge full scan showing K XANES and EXAFS

From the analog data, certain qualitative information may be obtained. For EXAFS, quantitative information may be deduced by carefully fitting the file data by averaging scans to reduce noise, performing background subtraction and energy calibration to obtain the inner potential, then transforming from energy to k space followed by a Fourier transform to obtain the (uncorrected) Radial Structure Function which is similar to a Radial Distribution Function and allows one to select the coordination spheres for proper fitting. This is a long process of interactive data processing involving both standard data from known compounds with a similar coordination and varying degrees of sophistication depending on the program used. It is our purpose to make these programs available to the personnel at Phillips Laboratory as needed for their future work.

It follows for this report that only analog examination is possible at this time. Nevertheless, we have formed the following conclusions based on our first Cl edge experience.

1. It is possible to work at the Cl K-edge with a Lytle detector minus Soller slits and filter. This poses no additional difficulty providing the small adsorption length for the soft radiation is taken into account. Beam line X-19A is an appropriate line for the Cl and Ti edge. The beam must be detuned drastically (70%) to reduce the third harmonic in the incident beam to less than 1/1000 and the contribution from all K emission lines is observed and may need to be corrected in the data analysis.

2. After changing samples, a decreasing intensity Ar edge is found which arises from the impurities in the air that can enter the Lytle detector sample chamber. This edge provides an automatic energy calibration for the Ar edge and, hence, an energy reference for the Cl edge, assuming linearity in the monochromator. We will test this approach since the reference energy for each scan eliminates one additional beam line vagary.

3. The Cl EXAFS region shows rapid damping and will be difficult to quantitatively treat. Good quality data was obtained for the samples. The minimum sample thickness was not determined, but most of our data was obtained from the first adsorption length in the sample. (from a surface layer about 25 um deep; we estimate a sensitivity limit of about 100 A for this technique at the Cl edge.)

4. The XANES region was extremely rich and worthy of detailed study. It is unfortunate that this energy region is the poorest understood from an analysis point of view, but theoretical progress in curved wave and multiple scattering formulations is being made rapidly. This region shows major differences in structure from one sample to another, especially in the white line region which reflects the multiple scattering in the low energy (above the edge) region. For additional recent

information, see references 1, pg. 573;ref. 2 and 3.

Figure Captions

Fig. No.	Caption
1.	NSLS Site plan.
2.	X-19A Beam line data.
3.	Lytle detector geometry, (CWRU).
4a.	Cl edge determination by on line computer windowing.
4b.	Cl edge determination by differentiation. (preferred)
5.	Chlorohydroquinone Cl XANES.
6.	Polymer Cl XANES.
7.	AP/binder Cl XANES.
8a.	KCl Cl full scan showing Ar and K edges and Cl EXAFS.
8b.	KCl K full scan showing K edge XANES and EXAFS.

References

1. X-Ray Absorption, Principles, Applications, Techniques of EXAFS, SEXAFS and XANES, Edited by D. C. Koningsberger and R. Prins, Eindhoven University, John Wiley and Sons, 1988, ISBN 0-471-87547-3 (hardcover).
2. X-Ray Absorption Fine Structure, Proceedings of the sixth International Conference on X-ray Absorption Fine Structures (EXAFS and XANES), York, UK 1991, (Organized by Daresbury Laboratory), Edited by S. Samar Hasnain, Daresbury Laboratory, Ellis Horwood Limited, 1991, ISBN 0-13-973199-7 (hardcover).
3. EXAFS and XANES studies of lead oxides and solutions of Pb(II) and Pb(IV) ions, James McBreen Department of Applied Science Brookhaven National Laboratory Upton, NY 11973 (private communication, submitted for publication 1991).

Future Work

Little quantitative data reduction has been carried out to date owing to the recent (13 August, 1991) acquisition of the first data. It is also clear that the Xanes data is the most instructive and needs quantitative effort. It is also true that the next scheduled time is 4 days at X-19A during early October, 1991. It is suggested that those runs repeat any required data and concentrate on the determination of buried interfacial differences by fluorescence detection and electron detection or grazing incidence fluorescence be attempted in order to gain sensitivity. Use of the polarized X-ray beam is also recommended for oriented specimens.

REDUCTION AND ANALYSIS OF SYNCHROTRON SPECTROSCOPIC DATA

**Tracy R. Reed
Student
Tehachapi High School**

**Final Report for:
Summer Research Program
Phillips Laboratory**

**Sponsored by:
Air Force Office of Scientific Research
Bolling Air Force Base, Washington, D.C.**

July 1992

REDUCTION AND ANALYSIS OF SYNCHROTRON SPECTROSCOPIC DATA

Tracy R. Reed

Abstract

During Aug. 1991 and Oct. 1991, Air Force scientists used the National Synchrotron Light Source at Brookhaven National Laboratory to collect EXAFS spectra of various Liquid Crystal Polymers (LCP's) which had been synthesized at Phillips Laboratory, as well as spectra of Ammonium Perchlorate pellets treated with bonding agents. The goal of this experiment was to determine local chlorine chemical coordination by viewing the radial structure function derived from the EXAFS data after computer processing.

REDUCTION AND ANALYSIS OF SYNCHROTRON SPECTROSCOPIC DATA

Introduction

In order to truly understand the nature of a material and how it interfaces with itself and others on an atomic level, it is necessary that one know the positions of atoms in the molecule and their distances. This information can be obtained by using Extended X-Ray Absorption Fine Structure Spectroscopy (EXAFS). Liquid crystal polymers (LCP's) and ammonium perchlorate (AP) treated with binders are perfect candidates for EXAFS study. By using this method, a greater understanding of how the polymer chains are positioned and how they might be annealed as well as how bonding agents actually bond the AP in a solid rocket motor can be obtained. This experiment was performed at Brookhaven National Laboratory using the National Synchrotron Light Source (NSLS). Once the data was obtained, it had to be converted into usable form and analyzed using a computer. The computer used was a VAX computer located at Phillips Lab. The program used to analyze the data is called EXAFS. EXAFS was written by Dick Koningsberger and obtained from Case Western Reserve University.

Synchrotron radiation is the electromagnetic radiation emitted from electrons at near light velocities when they are diverted from moving in a straight line(1). This change in velocity causes the electrons to give up some of their energy in the form of synchrotron radiation. Electrons are first accelerated to velocities near that of light by a linear accelerator. They are then injected into a relatively small booster ring where they are accelerated further and collected into bunches. The electrons are then injected into a storage ring where their path is curved periodic points by the dipole bending magnets that hold them in the center of the ring, thereby emitting the synchrotron radiation. As the electrons lose energy, the energy must be replaced. This is

accomplished by placing an RF cavity after each curved section. There are also various focusing devices to keep the beam centered and collimated in the pipe. The NSLS is a high energy synchrotron ring. It has an electron kinetic energy of 2.5 GeV.

The synchrotron radiation is allowed to proceed down an evacuated beam transport tube towards the experiment contained within a small hutch. The experimental hutch protects the operators from accidental exposure to the synchrotron radiation. A two crystal monochromator of the boomerang design was used to step through the energy range. The crystals are large pieces of high purity, defect free silicon. As their angle is changed by a stepper motor with respect to the incident radiation, the energy of the radiation being reflected by the crystals changes. The monochromatic radiation then passes through the I_0 chamber. This chamber basically gives a current proportional to the number of photons in beam. After it leaves the I_0 chamber, the radiation goes into the sample chamber and hits the sample pellet. A fraction of the incident X-rays will be absorbed by the electrons of the atoms in the sample. As these atoms de-excite, they emit fluorescent X-rays. This fluorescence is measured in the I_f chamber, which is placed on the side of the sample chamber at a right angle to the beamline. I_f is divided by I_0 and plotted over the energy range to get a visual representation of the energies at which the sample was emitting radiation. Each element has specific energies at which it will absorb synchrotron radiation in the X-ray region. This will produce what is called an edge in the spectrum. These experiments were done in the energy range of approximately 2600-3600 eV. The K edge is located at 2823 eV. Shortly after the edge is what is known as the EXAFS region. This is where the most informative data is located.

Procedure

There are five main steps that one must go through in order to get meaningful information from the EXAFS data. The first step is initialization. In this step, the program is told what kind of EXAFS data it is. In this case, it was fluorescence. The

program then reads the file and converts it into an unformatted FORTRAN file for its own use. This file ends in an .INI extension. It is in this file that the program makes any changes to the data. The original data file is never changed. The program then makes another file, ending in an .JOU extension. This is where a record of all changes to the data is kept.

The second step in the data reduction is the pre-edge subtraction. In this step, the data before the edge is removed so that it doesn't show up when the chi of k is graphed after the subtraction of a cubic spline from the rest of the data.

The next step in the data reduction is inner potential determination. In this step, the location of the edge is determined. The program automatically finds the location of the edge, but it is not always to the users liking. It is customary to set the location of the edge as the middle of the edge, or on a feature that might appear near the middle of the edge. The number that describes the location of the edge is called E_0 . This E_0 tells the program where to start subtracting background from. The middle of the edge is marked with a small triangle. See figure 1.

The fourth step is the dejumping and deglitching. Occasionally, one gets data with a spike, or glitch, in it. This can be caused by several things. One of which is a jolt to the monochromator during the experiment. This is removed by simply moving the offending point down in line with the other data. Another type of fault in the data is called a jump. A jump is a large apparent increase or decrease in the florescence of the sample. It looks like a small edge. The jump can be a jump up or down, depending on what is causing it. If there is a leak in the I_0 chamber, the jump will go down. If it is a leak in the I_f chamber, it will go up. The jump will be located at whatever the electron binding energy for the impurity is. When this experiment was conducted, it was found that there had been a leak in the I_0 chamber for most of the time the experiment was taking place. Consequently, nearly all of the data files had jumps in them. See figure 2. In this case it was argon that caused the jump. The electron binding

energy of argon is 3205 eV. This jump had to be removed before the data could be processed any further, adding significantly to the time it took to process the file. The procedure for removing a jump is to give the program the number of the data point immediately proceeding the jump. It will then take the difference between that point and the next and move all data points thereafter by that amount. Figure 3 illustrates the data after dejumping.

The last step in the data reduction is the background subtraction. It is unclear how the program subtracts the background, but it is suspected that a cubic spline is taken. The data is then Fast Fourier Transformed and plotted. This is known as the radial structure function. See figure 4. If the data is normalized, the radial structure function contains one peak for each of the groups of nearest neighbors. Its height tells how many nearest neighbors there are, and its position shows the distance. This will be done sometime in the near future using another program on the VAX.

Results

It was found that the EXAFS spectra for the AP and polymer pellets were very different. There were even significant differences between one AP spectra and another due to the bonding agent that was applied. A total of 118 files of EXAFS spectroscopic data were reduced. A much better understanding of the software being used was also gained. Before, it was unclear as to how certain operations, such as the corrections of error in the data were to be done. But now, these kind of problems can be taken care of quite easily. Several bugs in the program were also found. When an unexpected input was given to the program, the program would often crash. The interatomic distances and structure of the specimen can now be determined, leading to a much better understanding of the specimens.

References

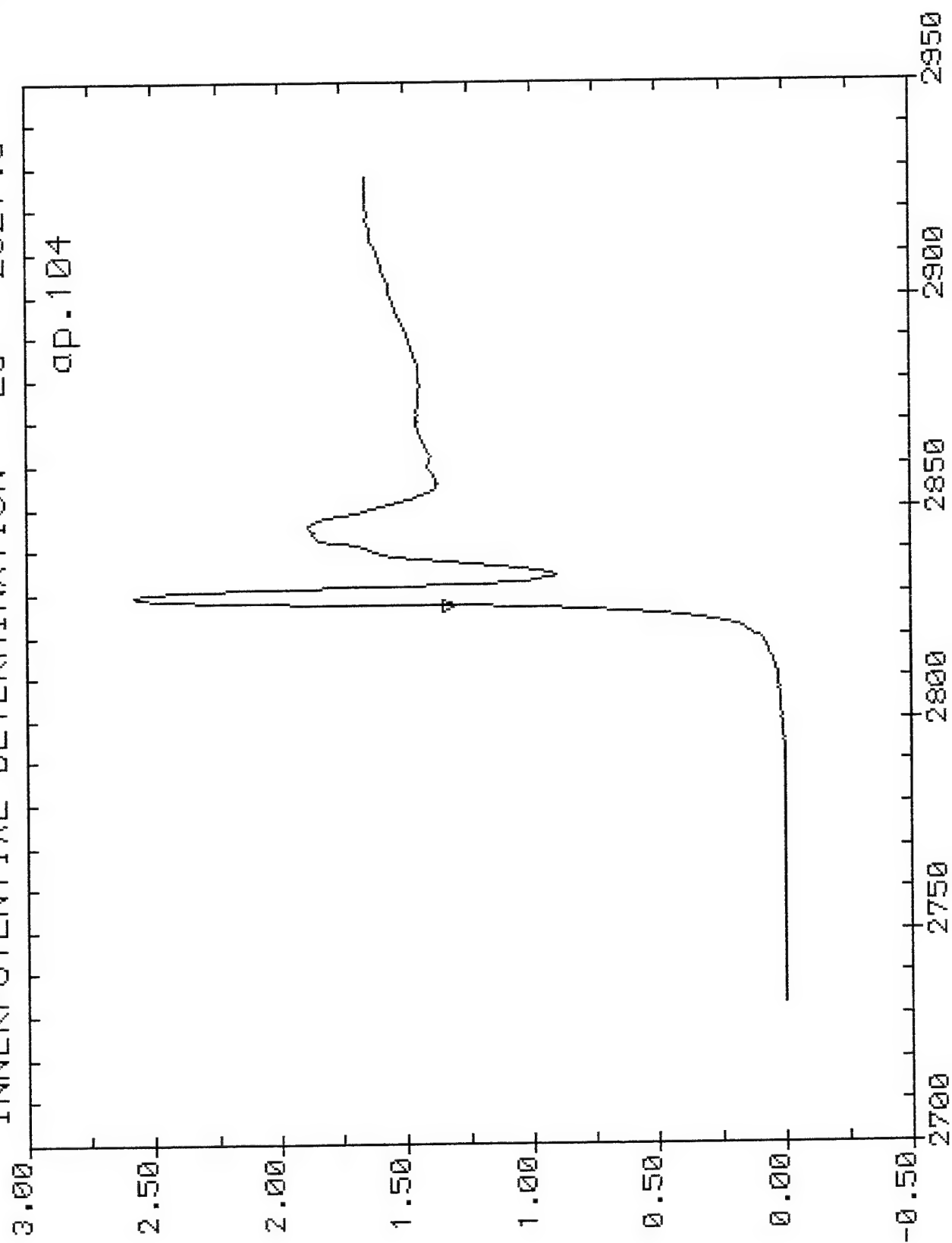
- (1) C. Kunz, "Synchrotron Radiation: Techniques And Applications", Springer-Verlag, New York, 1979
- (2) Guy Arthur Derosé, "X-Ray Absorption Fine Structure Strain Determination In Thin Films", Case Western Reserve University, Cleveland, 1992

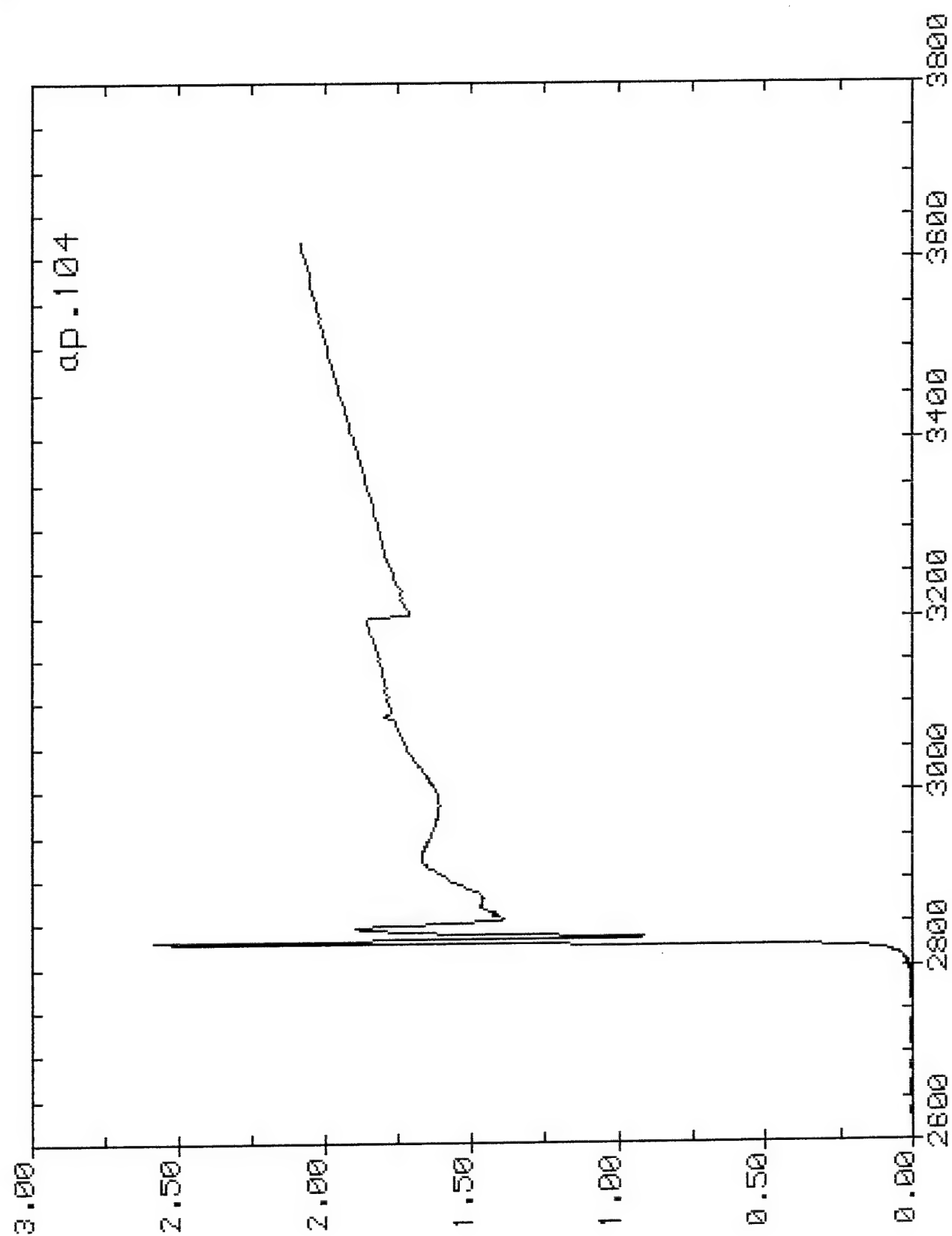
Acknowledgments

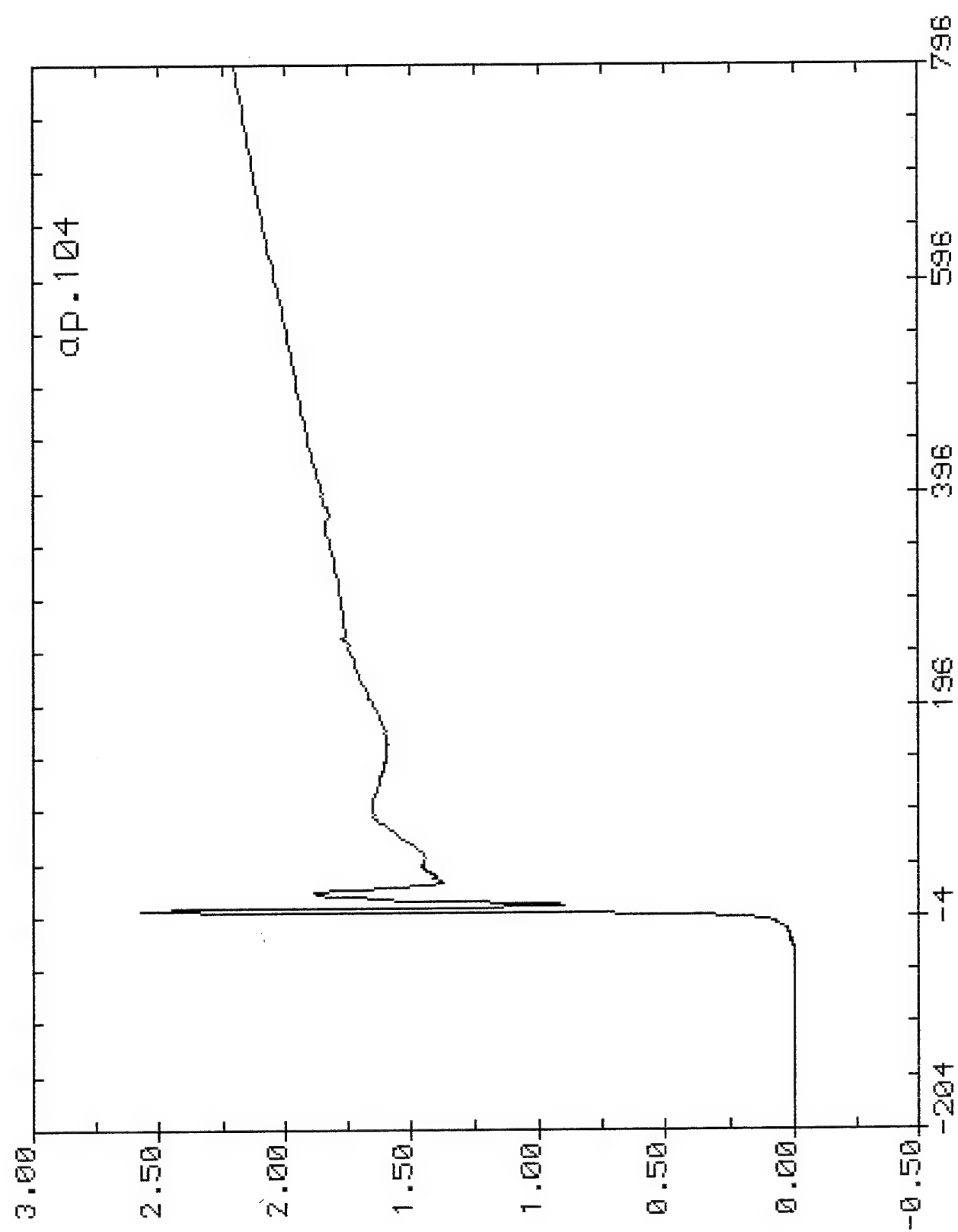
I wish to thank Dr. Kevin Chaffee for all he has taught me and all of the questions he has answered for me. I also wish to thank Dr. John Rusek and Mr. Steven Osborn for all of their help and support throughout the summer.

INNERPOTENTIAL DETERMINATION E0= 2827.0

ap.104

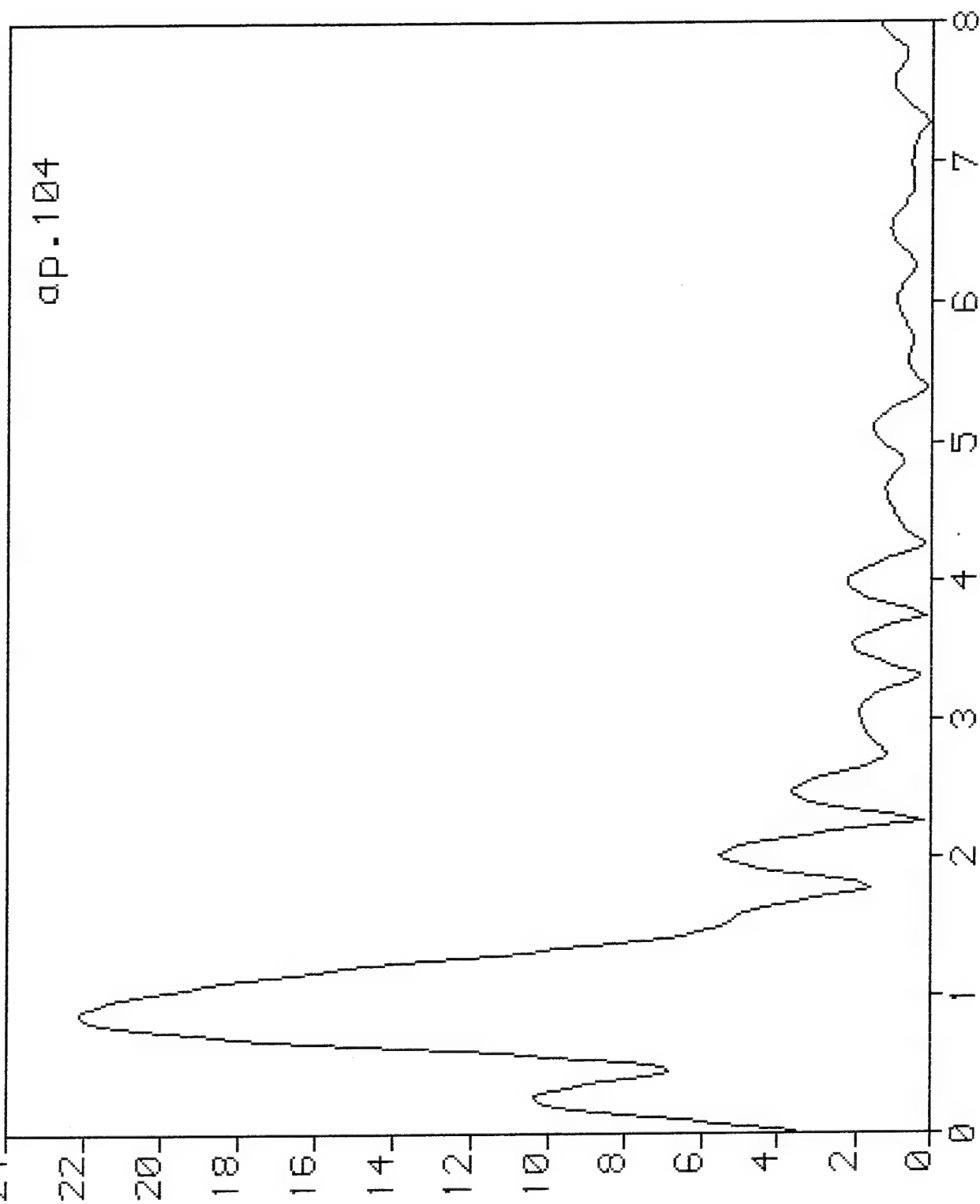






$\times 10^{-2}$ KMIN= 3.00 KMAX=12.00 KWT= 1 SM1=0.0400 WE=0.075

ap.104



PREPARATIONS FOR NEUTRON SCATTERING INVESTIGATIONS
OF LIQUID-CRYSTAL POLYMERS

David M. Elliott, Ph.D.
Associate Professor
Department of Engineering

Arkansas Tech University
Russellville, AR 72801

Final Report for:
Summer Research Program
Phillips Laboratory
Edwards Air Force Base

Sponsored by:
Air Force Office of Scientific Research
Bolling Air Force Base, Washington, D.C.

September, 1992

PREPARATIONS FOR NEUTRON SCATTERING INVESTIGATIONS
OF LIQUID-CRYSTAL POLYMERS

David M. Elliott, Ph.D.
Associate Professor
Department of Engineering
Arkansas Tech University

Acknowledgement

The author would like to specifically acknowledge the efforts of Dr. Kevin Chaffee and Dr. John Rusek for their constant help and encouragement during this Summer Research Project. The technical competence of these Phillips Laboratory researchers is truly world class. It was a distinct pleasure to work with both of them on this extremely interesting and challenging research project.

PREPARATIONS FOR NEUTRON SCATTERING INVESTIGATIONS
OF LIQUID-CRYSTAL POLYMERS

David M. Elliott, Ph.D.
Associate Professor
Department of Engineering
Arkansas Tech University

Abstract

Researchers at the Phillips Laboratory at Edwards Air Force Base have been instrumental in the development and characterization of thermotropic liquid crystal polymers (LCPs). One of the most interesting and potentially valuable areas of research on these materials is the question of physico-chemical annealing. The mechanical and chemical properties of some of these materials are known to dramatically improved upon annealing. In order to realize the full potential of annealed LCPs, a firm understanding of the molecular structure, morphology, texture, and the dynamics and mechanism of formation of the annealed state must be obtained. Neutron scattering techniques are thought to be capable of providing much of the basic structural information necessary to develop that understanding.

During the summer of 1992, the author was privileged to have participated in the Phillips Laboratory LCP Research Program at Edwards Air Force Base. His work was primarily involved with preparations for a series of planned neutron scattering experiments. A preliminary search of the literature available about neutron scattering in general and small angle neutron scattering in particular was completed. The information obtained from the literature search was used to investigate some preliminary experiment design considerations for a small angle neutron scattering experiment on LCPs. In addition, a survey of world wide neutron scattering facilities was made. Both their physical capabilities and their user requirements were determined. The results of the survey and the preliminary experiment design considerations were used to recommend a primary and a first alternate neutron scattering facility at which to perform the planned experiments.

PREPARATIONS FOR NEUTRON SCATTERING INVESTIGATIONS OF LIQUID-CRYSTAL POLYMERS

David M. Elliott

INTRODUCTION

The development of advanced new materials possessing very high specific strength and specific modulus is critically important to the Air Force mission in both the exploration of interplanetary space and the development of higher performance and lower cost missile systems. Composite materials with superior mechanical properties have been made from high-strength fibers and graphite. Parts and structures made from these composite materials are, however, relatively costly because of the complexity of the manufacturing process. The high-strength fibers used in these composite materials are prepared from stiff-chain aromatic polymers. These polymers are called stiff-chain polymers because the molecules tend to be quite elongated in solution or in the melt. These elongated molecules have a propensity to form a definite crystalline organization in the liquid state (either solution or melt) and consequently they are referred to as liquid-crystal polymers (LCPs). In addition to high-strength fibers, LCPs can be injection or blow molded inexpensively into complex shapes. The liquid crystalline order persists and is often enhanced as LCPs are carried into the solid state. Solid materials made from LCPs are, however, inhomogeneous and highly anisotropic. They can be thought of as molecular composites.

The mechanical properties of solid LCPs depend importantly on the processing as well as on the material itself. Flow, either in the spinning of fibers or in the molding of parts, can result in an increase in the crystalline order and this in turn can result in significant enhancements of both strength and modulus. Temperature is also an important processing variable. Some LCPs are known to undergo very significant and favorable changes in both mechanical and chemical properties after thermal annealing. The relationships between molecular conformation and crystalline order and mechanical and chemical properties are not well known yet understanding these relationships is vital to developing these molecular composites to their full potential. Recognizing this, researchers at the Phillips Laboratory are pursuing a

program of both theoretical and experimental studies to characterize the molecular structure, dynamics, and mechanism of formation of the annealed state in selected linear LCPs. The experimental part of the program necessarily involves a number of different techniques including thermal and mechanical as well as atomic (X-ray) and nuclear (neutron scattering).

The nuclear techniques will include as a minimum small angle neutron scattering and neutron diffraction and may include neutron reflectometry as well. The neutron scattering and diffraction experiments being considered for this program will require very high integrated neutron fluxes and complex experimental facilities which are available only at large centrally located facilities. There are very few facilities in the world where these experiments can be carried out, probably less than twenty five in total. The neutrons are produced either by high-energy positive ion accelerators or by nuclear research reactors. The accelerator sources produce higher instantaneous neutron fluxes (and higher neutron energies) but their beams are pulsed resulting in somewhat lower integrated fluxes. The facilities based on accelerator sources have historically concentrated on pulsed source instrumentation and techniques. The development of equipment and techniques for the exploration of basic issues in condensed-matter science has taken place largely at research reactor based facilities. For these reasons, only research reactor based neutron scattering facilities are being considered for the Phillips Laboratory LCP experimental research.

The objectives of the present work are all related to preparations for the neutron scattering investigations to be carried out in the immediate future. In close cooperation with other researchers at the Phillips Laboratory, the following principal tasks were initiated:

1. Preliminary search of the literature for information about SANS and liquid crystal polymers.
2. Preliminary design of SANS experiments.
3. Survey of world-wide neutron scattering facilities appropriate for the Phillips Laboratory LCP experimental work and selection of a primary and first alternate facility.

NEUTRON SCATTERING AND APPLICATIONS TO LCPs

Neutrons are electrically neutral sub-atomic particles with a mass of $1.675 \times 10^{-27} \text{ kg}$, spin $1/2$, and a magnetic moment of 1.913 nuclear magnetrons. The de Broglie relation, $p = h\lambda/2\pi$, is the basis for conversions among neutron properties expressed in terms of momentum (p), velocity ($V_n = p/m_n$), wave vector (k), wavelength (λ), and kinetic energy (E). Table 1. (Reference 1) gives some useful conversion relations.

Energy E (meV)		1	10	50
corresponds to	defined by			
Angular frequency ω (rad/sec)	$\omega = E/h$	1.52×10^{12}	1.52×10^{13}	7.6×10^{14}
Frequency ν (Hz)	$\nu = E/h$	2.42×10^{11}	2.42×10^{12}	1.21×10^{13}
Optical wave number $\tilde{\nu}$ (cm^{-1})	$\tilde{\nu} = \nu/c$	8.065	80.65	403.3
Temperature (T , K)	$T = E/k_B$	11.605	116	580
Neutron velocity v_n (m/sec)	$v_n = (2E/m_n)^{1/2}$	437	1383	3093
Neutron wavelength λ (Å)	$\lambda = h/(2m_n E)^{1/2}$	9.04	2.86	1.28
Neutron wave number k (Å $^{-1}$)	$k = (2m_n E)^{1/2}/h$	0.695	2.2	4.91

Table 1. Neutron Conversion Data

Neutrons in thermal equilibrium with their surroundings (called "thermal neutrons") turn out to be an extremely useful probe of the structure of condensed matter. This fact was recognized by physicists soon after the discovery of the neutron in 1932. Table 2. (Reference 2) shows some characteristics of neutrons at selected energies.

Quantity	Unit	Definition	Ultracold	Cold	Thermal	Epithermal
Energy E	meV ^a		0.00025	1	25	1000
Temperature T	K	E/k_B	0.0029	12	290	12,000
Wavelength λ^b	Å	$h/(2mE)^{1/2}$	570	9.0	1.8	0.29
Wave vector k^c	Å $^{-1}$	$(2mE)^{1/2}/h$	0.011	0.7	3.5	22
Velocity v^d	m/s	$(2E/m)^{1/2}$	6.9	440	2200	14,000

Table 2. Characteristics of Neutrons at Selected Energies

Some of the reasons why neutrons are such useful probes of condensed matter listed below. (Reference 1)

1. The interaction of thermal neutrons with matter is weak.
2. The absorption of thermal neutrons by matter is often very small.
3. The wavelength of thermal neutrons is comparable to atomic and molecular spacing.
4. The nonmagnetic scattering amplitude of neutrons does not depend on the electronic structure, rather it depends on the nuclear structure. It is often very different for different isotopes of the same element.

The weak interaction and small absorption of neutrons allows them to be used to probe at much greater depths into a material than electromagnetic radiation (X-rays or light). The ability to probe at depth is critical to the current LCP research because the molecular orientation and perhaps the conformation as well are strong functions of position within the material and particularly near the surface.

Neutron scattering is a relatively new technique of material science, having been extensively utilized only over the last fifteen years or so. A considerable amount of fundamental research using neutron scattering techniques has been done on polymers and the experimental techniques are relatively well developed. The picture is, however, not as bright for LCPs. Very little neutron scattering work has been done with LCPs. The majority of the work that has been done in this area is very recent and was done in Europe. (References 7-10)

Neutron scattering can, in general, be reduced to the simple form: (Reference 15)

$$\frac{d^2\sigma}{d\Omega dE} = AS_{\alpha\beta}(Q, \omega)$$

Where: The measured intensity is proportional to
(perhaps integrated over E)

$$\frac{d^2\sigma}{d\Omega dE}$$

A is a (known) constant which contains all of the neutron properties

$S_{\alpha\beta}(Q, \omega)$ is determined solely by the sample.

$$Q = k_1 - k_2$$

$$E = \hbar \omega = (\hbar/2m) * (k_1^2 - k_2^2)$$

and α, β label the spin state of the neutron before and after the scattering event.

$k = 2\pi/\lambda = mv/\hbar$ and k_1 and k_2 are the neutron wave vectors before and after the scattering event respectively.

Thus a neutron scattering experiment reduces to a determination of the magnitude and direction k both before and after the scattering event.

In the experiments of interest for the current program, the scattering is elastic. The magnitude of the neutron wave vector is thus unchanged during the scattering event. For these experiments, one needs only to measure the magnitude of the wave vector (or the energy) once, usually before the scattering event. One then measures the direction of the emergent neutrons after the scattering event. These experiments are simple in theory. The difficulties, as usual, lie in the details. It is the details that must be determined in the design of specific experiments.

RESULTS

Preliminary Literature Search

The experimental phase of the Phillips Laboratory LCP Research Program contemplates using a number of different neutron scattering techniques. As mentioned previously, these techniques include neutron diffraction (ND), neutron reflectometry (NR), and small angle neutron scattering (SANS). The SANS technique produces a wider variety of useful information than do the others. Not surprisingly, SANS is the most demanding of these techniques. SANS requires a much greater integrated neutron flux, better collimation and wavelength selectivity, a more massive, complicated, and higher precision spectrometer, and a position sensitive detector. Perhaps because they are so complicated and expensive, there is more variability in the capabilities of

the SANS instruments at different scattering research facilities than in the instruments used for the other techniques. For these reasons and because the principal objective of the author's summer work was to recommend a primary and a first alternate reactor based neutron scattering facility, the literature search began with and still concentrates on small angle neutron scattering.

The essential objective of the SANS literature search is to locate and obtain copies of references that will provide or support the development of:

1. A thorough understanding of the theory of the various possible scattering interactions, particularly SANS.
2. The ability to model the contemplated SANS experiments and predict specific results based on knowledge of the experimental conditions and of the scattering medium.
3. A knowledge of the techniques used and the specific results obtained for polymer systems in general and LCPs in particular.

During the summer, copies of a number of good references were obtained. Three chapters in two books and one journal article were obtained which provide an excellent introduction to the theory of neutron scattering. (References 1-4) Five references dealing with the application of SANS to polymer systems (References 5-9) and five dealing with specific applications to liquid crystal polymers (References 10-13, 15) were obtained. These references have already proven their worth in providing information useful in the preliminary design of SANS experiments.

Preliminary SANS Experiment Design Considerations

One important purpose of the initial preliminary SANS experiment design was to secure sufficient information to assess the suitability of a number of candidate neutron scattering facilities for performing the planned LCP experiments. The SANS experiment design was used for this purpose because it is more demanding than ND and because virtually every neutron scattering facility has adequate ND capabilities. The SANS technique is extremely versatile and a number of different parameters of interest can be measured.

Two Q regions of interest to the polymer scientist are often identified within the small angle range. (Reference 8) The first and lowest region is known as the Guinier region and is defined by $1/Q > R_g$ where R_g is the radius

of gyration or the second moment of the distribution of the scattering centers. In this region, the scattering is sensitive to the dimensions of the chains and not their detailed shape. The second region is defined by $1/R_g < Q < 1$ where l is the length of a characteristic segment of the chain, usually a few monomer units. In the second region, the scattering becomes very sensitive to correlations between segments and thus to the shape of the molecule. In this region, $S(Q)$ varies as $1/Q$ for a rod like structure and as $1/Q^4$ for a sphere.

The first experiment considered was solid state molecular weight determination for amorphous LCPs. This experiment utilizes a variation of the Zimm plot technique. (Reference 7) Here Q is approximately in the Guinier region and the desired information is obtained from a plot of the inverse of the scattered intensity as a function of the square of Q . Since the Guinier region is defined as $1/Q > R_g$, the high end of the Q range is roughly $1/R_g$ and the low end is as low as the instrument will allow. In the literature, these Q ranges usually extend over a factor of from four to ten. (References 10,11,12) The materials of interest for the current LCP research are rod like molecules with a length on the order of 90 Å. This would suggest a radius of gyration of about 26 Å. The corresponding Guinier range (in Q) for these molecules would be about 0.005 to 0.04 Å⁻¹. This then was taken to be the Q range that had to be available. The low end of this range is at about the limit of some SANS machines. Most machines will cover up to at least 0.4 and some will go up as high as 1.0.

Given that the Q range is acceptable, probably the next most important factor is the neutron flux available on the sample at the required wavelengths. A number of things affect the available flux. The most obvious of these are the peak thermal flux available in the reactor and whether or not a cold moderator (cold source) is present. The peak thermal flux available in the high power reactors (60 - 100 MW) is about 10¹⁵ n/cm²/sec. The medium power reactors (10 - 20 MW) have peak thermal fluxes on the order of 10¹⁴. The addition of a cold moderator will increase the flux of neutrons of interest in SANS experiments by about a factor of 5. The flux available at the sample is a very important factor in determining the time required to perform a given experiment (counting time for adequate statistics). For the best combination of a high power reactor with a cold moderator, counting times for typical SANS experiments with polymers vary from about 5 to about 60 minutes for isotropic scattering and from about 25 to about 300 minutes for anisotropic scattering (as in ordered polymer systems). (Reference 7) Without using any tricks to optimize the experimental setup, these times would increase by about a factor of 50 for a medium power reactor without a cold

moderator. Fortunately, there are a number of tricks that can be used to increase the total number of neutrons being scattered from the sample as well as those impinging upon it.

The large difference in scattering length between deuterium and hydrogen provides excellent contrast between molecules labeled with deuterium and those that are not. Increasing the concentration of deuterated chains up to a maximum of 50 percent or so increases the signal to background ratio. On the other hand, deuteration is not without its potential drawbacks. One major drawback is the relatively high cost. Another is the possibility that deuteration may affect the results of the experiment in subtle and unpredictable ways. "One of the basic assumptions of SANS is that deuterium labeling does not affect the properties of the chains. In the case of PE, deuterium labeling causes a 6° difference in the melting temperature, and thus during slow-melt crystallization a nonrandom distribution of deuterated chains occurs. (Reference 7) "The SANS method is extremely sensitive to small deviations from a statistical distribution. (Reference 5)

The size of the sample, of course, impacts the number of neutrons reaching the detector. In general, the sample diameter should be as large as possible within the confines of the beam geometry at the sample. The sample thickness will be governed by the specific material under investigation and the concentration of deuterated chains. The literature provides some useful guidance here. "Small angle scattering is usually carried out with samples that have 50% transmission. A mainly hydrogenous sample will be about 1 mm thick, whereas a sample that contains a high proportion of deuterium can be 5-10 mm thick." (Reference 7)

Neutron Scattering Facility Survey

One important question that needed to be answered early in the program was: Which neutron scattering facilities would be likely to have both the required physical resources and a user policy that would allow the planned experiments to be carried out in a timely and cost effective manner. The Phillips Laboratory program plan calls for the neutron scattering experiments to be done over a relatively narrow time frame beginning in the very near future. To complicate matters even further, the program must operate under very tight budgetary constraints. To begin the process of answering this question, a list of all of the major reactor based neutron scattering facilities in the world was made. Entries on this list were obtained from the literature and a from a series of personal contacts and telephone calls.

Table 3. lists all of the major facilities currently known to the author.

All of the facilities listed in Table 3. have a number of different neutron scattering instruments and all have at least one SANS spectrometer. If any facility could not meet the physical requirements of the proposed experiments, it would most likely be because of limitations of the SANS instrument. Preliminary experiment design considerations suggest that the most probable limiting factors are the Q range and the neutron flux available on the sample. It turns out that any of the facilities listed in Table 3. would be physically capable of performing all of the planned experiments. The main physical difference among these facilities would be the time it takes to perform each individual experiment. The high power reactors with a cold moderator can do the experiments in much less time.

Having developed rapidly over the past fifteen years or so, neutron scattering is now seen as a core competency in materials science and engineering. From Table 3. one can see that the total number of neutron scattering facilities in the world is very small. The result is that most of the world's neutron scattering facilities are over subscribed, some by as much as a factor of three. There are simply more good experiments to be run than there are facilities to run them. As a result, most of these facilities have adopted policies that restrict the number of experiments that can be run. Many of them have adopted the "user facility" approach where instrument time is allocated by a committee based on their evaluation of the technical merit of proposals submitted by those who want to use the facility. There are a number of drawbacks to this approach from the experimenter's point of view. The proposal review and time allocation process takes a long time, often several months. Since all proposals cannot be approved, there is a substantial probability that any individual proposal might not be

United States

- o Brookhaven National Laboratory (HFBR)
Upton, Long Island New York
- o Oak Ridge National Laboratory (HFIR)
Oak Ridge, Tennessee
- o National Institute of Standards (NIST)
Gaithersburg, Maryland
- o University of Missouri (MURR)
Columbia, Missouri

Australia

- o Australian Nuclear Science & Technology Organization (ANSTO)
Lucas Heights

France

- o Institut Laue Langevin (ILL)
Grenoble
- o Orphee Reactor Center (ORPHEE)
Saclay
- o SILOE, CENG (SILOE)
Grenoble

Germany

- o KFA Research Reactor (JULICH)
Julich
- o HMI Reactor Facility (HMI)
Berlin

Japan

- o JAERI III Reactor Facility (JAERI)

Table 3. Worldwide Reactor Based Neutron Scattering Facilities

accepted at all. Many proposals end up in an alternate position or in a queue. The time and budgetary constraints of the Phillips Laboratory LCP experimental program are such that it would be very difficult to do all of the proposed experiments at a user facility simply because of the process required to obtain instrument time.

From those facilities listed in Table 3. five candidate facilities at which the experimental program might reasonably be carried out in a timely manner were selected. Four of these are in the United States and one is in Australia. Next, detailed technical and user policy information was collected for each candidate facility. Literature references were reviewed and printed materials were obtained where these were available. Personal contacts were made by telephone at each candidate facility. A summary of the information is given in Table 4.

	<u>HFBR</u>	<u>HFIR</u>	<u>HIFAR</u>	<u>NIST</u>	<u>MURR</u>
Reactor Power (MW)	60	100	10	20	10
Peak Thermal Flux (E14)	5	11	1.6	4	1
Cold Moderator?	Yes	No	No	Yes	No
Number of Spectrometers	13	9	8	12	8
User Facility?	Yes	Yes	No	Yes	No

Table 4. Features and User Policy of Candidate Facilities

All of these candidate facilities are (or soon will be) physically capable of providing the adequate Q range, neutron flux and other capabilities required to carry out the Phillips Laboratory LCP experimental program. Only two of these facilities, however, are not user facilities and thus would be capable under present circumstances of meeting all of the current program requirements: HIFAR and MURR. Both of these facilities have user policies that allow and, in fact, encourage collaboration between their own scientists and those of the experimenter. Formal proposals are not required at either of them. The reactor power and peak flux are similar and the SANS spectrometers are nearly identical. Both SANS spectrometers are currently being built or upgraded. Present schedules call for the SANS spectrometer at HIFAR to be completed in mid to late 1992 while that at MURR is planned for operation in the first or second quarter of 1993. Based on all of the above factors, it is recommended that the HIFAR facility be selected as the primary facility and MURR as the first alternate.

CONCLUSIONS

Neutron scattering techniques, particularly small angle neutron scattering and neutron diffraction, are capable of providing significant insight into both the structure and the morphology of liquid crystal polymers in the solid state. These techniques should be uniquely useful in helping to understand the molecular structure, dynamics and mechanism of formation of the annealed state. There are, however, significant problems in actually applying these tools to LCPs. These problems lie in two primary areas: The first area is the lack of previous work using neutron scattering techniques specifically for investigating LCPs. Only a few publications are available and these address only a small part of the total picture. The theory is adequately presented in the literature but there is little guidance for the actual application of the techniques and the interpretation of the results. The second area is the difficulty of actually getting instrument time at one of the very few neutron scattering facilities in the world capable of doing the work.

The essential conclusions reached from this work, then, can be summarized as follows:

1. Neutron scattering techniques, particularly SANS and ND are inherently capable of answering many of the fundamental structural questions of interest to the Phillips Laboratory LCP Research Program.
2. A very considerable effort is required before the actual experimental program can begin. The primary things that need to be done are a complete literature search and detailed experiment design.
3. Considering all of the requirements of the Phillips Laboratory program, particularly temporal and budgetary constraints, the preferred neutron scattering facility at which to do the work is the HIFAR facility in Australia. A close second is the MURR facility in Missouri.

RECOMMENDATIONS

The following two recommendations are made based on the results the Summer Research Program and discussions with the Phillips Laboratory research scientists and others in the neutron scattering community:

1. Complete the SANS literature search and extend it to include ND. The essential objective of the literature search should be to locate and obtain copies of references that will provide or support the development of:
 - A. A thorough understanding of the theory of the various possible scattering interactions.
 - B. The ability to model the contemplated experiments and predict specific results based on knowledge of the experimental conditions and of the scattering medium.
 - C. A knowledge of the techniques used and the specific results obtained for polymer systems in general and LCPs in particular.
2. Complete the preliminary experiment designs done in the current work and extend them to include ND.

These recommendations are included in the objectives of the author's AFOSR Research Initiation Proposal.

REFERENCES

1. *Neutron Scattering--General Introduction* by G. Kostorz and S.W. Lovesey in *Treatise on Materials Science and Technology*, Volume 15, Neutron Scattering, Academic Press, New York, 1979
2. *Introduction to Neutron Scattering* by D.L. Price and K. Sköld in *Methods of Experimental Physics*, Volume 23, Neutron Scattering, Part A, Academic Press, New York, 1986
3. *Small-Angle Scattering and its Applications to Materials Science* by G. Kostorz in *Treatise on Materials Science and Technology*, Volume 15, Neutron Scattering, Academic Press, New York, 1979
4. *Neutron Scattering and Amorphous Polymers*, A. Maconnachie and R.W. Richards, *Polymer*, Vol 19, July, 1978
5. *Small-Angle Neutron Scattering Studies of Molecular Clustering in Mixtures of Polyethylene and Deuterated Polyethylene*, J.Schelten et al, *Polymer*, Vol 18, November, 1977
6. *Chain Conformation in Molten Polyethylene by Low Angle Neutron Scattering*, J. Schelten et al, *Letters in Polymer*, Vol 15, October, 1974
7. *Polymers* by J.S. Higgins and A. Maconnachie in *Methods of Experimental Physics*, Volume 23, Neutron Scattering, Part C, Academic Press, New York, NY, 1987
8. *Polymer Conformation and Dynamics* by J.S. Higgins in *Treatise on Materials Science and Technology*, Volume 15, Neutron Scattering, Academic Press, New York, NY, 1979
9. *Small-Angle Neutron Scattering Measurement of Block Copolymer Interphase Structure*, R.W. Richards and J.L. Thomason, *Polymer*, Vol 24, September, 1983
10. *Conformational Anisotropy of Liquid Crystalline Side Chain Polymers: A Small Angle Neutron Scattering Study*, F. Moussa et al, *Le Journal De Physique*, 48, 1987, pp 1079-1083

11. *Liquid Crystal Polymers: A Small Angle Neutron Scattering Study*, F. Hardouin et al, *Molecular Crystals and Liquid Crystals*, Vol 155, 1988, pp 389-397
12. *Side Chain Mesomorphic Polymers: Studies of Labelled Backbones by Neutron Scattering*, P. Keller et al, *J. Physique Letters*, 46, 1985, pp L-1065-L-1071
13. *Small Angle Neutron Scattering Study of Comb-Like Liquid Crystal Polysiloxane Macromolecule Conformation in Smectic Phase*, J. Kalus et al, *Molecular Crystals and Liquid Crystals*, Vol 155, 1988, pp 347-356
14. *Major Facilities for Materials Research and Related Disciplines*, National Research Council, PB85-108850, Washington, DC, July, 1984
15. *Liquid Crystals* by J.A. Janik and T. Riste in *Methods of Experimental Physics*, Volume 23, Neutron Scattering, Part B, Academic Press, New York, NY, 1987
16. *Neutron Properties and Production*, J.M. Rowe, Workshop on Neutron and Synchrotron Radiation Studies of Materials, Brookhaven National Laboratory, Upton, NY, May, 1992
17. *Neutron Probes Tackle Industrial Problems*, H.J. Prask, *Advanced Materials & Processes*, 9/91
18. *Industrial Applications* by M.T. Hutchings and C.G. Windsor in *Methods of Experimental Physics*, Volume 23, Neutron Scattering, Part C, Academic Press, New York, NY, 1987

**DEPARTMENT OF THE AIR FORCE**HEADQUARTERS SACRAMENTO AIR LOGISTICS CENTER (AFMC)
McCLELLAN AIR FORCE BASE, CALIFORNIA

17 Feb 93

FROM: SM-ALC/TIRO

SUBJ: Initial Irradiation of Liquid Crystal Polymers

TO: Dr.'s John Rusek and Kevin Chaffee
Astronautics Laboratory (AFSC)
AL/RKP
Edwards AFB, CA 93523-5000

1. On 16 Feb 93 ten 0.5-in. diameter liquid crystal polymer specimens were irradiated to an approximate thermal neutron fluence of 5.4×10^{16} n/cm².
2. The specimens consisted of five pairs of differing polymers wrapped in aluminum foil and placed in a titanium capsule for irradiation in the reactor's central thimble. Please refer to the attached sketch for clarification.
3. In addition to the specimens, three high range gamma TLD's were irradiated in the capsule. However, data from these TLD's cannot be made available until after they have been processed at a laboratory external to McClellan AFB.
4. As soon as radiation levels permit, our staff will open and remove the specimens from the titanium capsule. Chris Frank has requested to be present at this time. In addition, as soon as the specimens decay to releasable radioactivity levels, they may leave the facility. I will keep you and Chris informed of the specimen status.
5. For future irradiations, a design for an outer container was provided to Chris Frank that is similar to the titanium capsule used for this irradiation. The new capsule will be constructed of aluminum and be large enough to accommodate more than ten specimens.
6. We have enjoyed performing this initial irradiation and look forward to opening the capsule as soon as possible. Also, we are eagerly anticipating future irradiations as we are quite curious how the polymers will be affected by progressively larger fluences. Please call me if I or any member of our staff can be of assistance in the interim.

Angelia A. Weeks
ANGELIA A. WEEKS
Experimenter Coordinator
SNRS Reactor

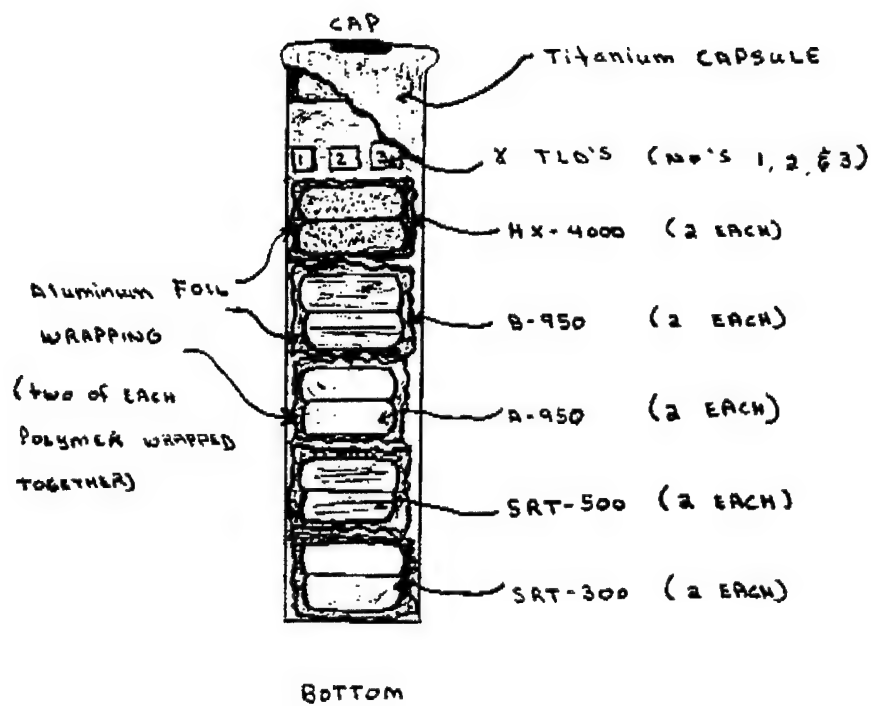
Attachment

cc: Chris Frank

LIQUID CRYSTAL POLYMER IRRADIATION

FEBRUARY 16, 1993

1.0 MW HT - CENTRAL THIMBLE





DEPARTMENT OF THE AIR FORCE

HEADQUARTERS SACRAMENTO AIR LOGISTICS CENTER (AFMC)
McCLELLAN AIR FORCE BASE, CALIFORNIA

09 Apr 93

FROM: SM-ALC/TIRO

SUBJ: Summary of Activity To Date

TO: Distribution
(Authorized Experimenters, Liquid Crystal Polymer Irradiations)

1. A summary description of the first liquid crystal polymer irradiation is provided below. In addition, a table showing the decreasing radioactivity of each sample over time follows.

- a. DATE OF IRRADIATION: 16 Feb 93
- b. NEUTRON FLUENCE: $10E+13$ n/cm²
- c. IN-CORE LOCATION: central thimble
- d. DATE POLYMERS REMOVED
FROM TITANIUM TUBE: 26 Feb 93

POLYMER RADIOACTIVITIES

Note: Readings are given in gross cpm and do not include background.

<u>Sample</u>	<u>03/05/93</u>	<u>03/09/93</u>	<u>03/19/93</u>	<u>03/26/93</u>	<u>04/02/93</u>	<u>04/08/93</u>
SRT-500	16,000	14,000	9,000	6,000	no data	3,200
SRT-300	14,000	12,000	8,000	5,500	no data	3,000
B-950	1,000	900	600	420	210	180
A-950	450	440	320	240	140	released
HX-4000	240	200	160	released	---	---
background	40	40	40	60	40	60

2. The HX-4000 and A-950 polymers are no longer radioactive and can be removed from our facility at any time. Also, the B-950 polymer should be releasable in the very near future.

3. The SRT-500 and 300 polymers may remain radioactive for some time yet. Space is available and radiation safety coverage would be provided if you would like to bring equipment to analyze these polymers within our facility.

4. Gamma spectroscopy has identified trace amounts of the following impurities within the polymers causing the radioactivity:

- a. ^{51}Cr (largest contributor)
- b. ^{58}Co
- c. ^{60}Co
- d. ^{113}Sn
- e. ^{122}Sb
- f. ^{123}Te (metastable)

5. Initially we were told that it was acceptable to wait until after several polymer irradiations had been completed before sending the gamma TLD's off base for analyses as a batch. However, because of the delays and the unexpected impurities, we are unsure which action to take. Should we send the TLD's to the external laboratory for extraction of high range gamma dosimetry, or wait for subsequent irradiations? Please let us know as soon as possible.

6. We look forward to performing future irradiations of the liquid crystal polymers. Please let us know if there is anything else we can do prior to that time.

Angelina H. Weeks
ANGELIA A. WEEKS
Reactor Experiment Coordinator

Distribution

- 1. Dr. John Rusek
Astronautics Laboratory (AFSC)
AL/RKP
Edwards AFB, CA 93523-5000
- 2. Dr. Kevin Chaffee
Astronautics Laboratory (AFSC)
AL/RKP
Edwards AFB, CA 93523-5000
- 3. Chris Frank
TIEC
243 E-Bay

cc: Jeff Ching
Chuck Heidel
Wade Richards

Hardness Test Results of Irradiated Plastic Samples

TO: TIEC/Mr. Chris Frank

J. Meininger

29 Jun 93

1. We were requested to perform Rockwell hardness tests on several plastic samples, some of which were irradiated. Photographs were also requested to document the change in appearance of some of the samples.

2. Irradiated and unirradiated samples of the A-950, B-950, and HX-4000 material were received. Figures 1, 2, and 3 show the visible differences between the irradiated and unirradiated samples. The unirradiated A-950 and B-950 samples were a very light tan color. The irradiated A-950 and B-950 samples exhibited a slightly darker tan color. The unirradiated HX-4000 samples were a medium gray color. The irradiated HX-4000 samples were a medium tan color.

3. The Rockwell hardness test results are listed in Table I. The Rockwell E scale was used in all cases so that the results for the different materials could be compared. Some of the results were negative numbers; in these cases better precision would have been obtained with a different scale. However, there was insufficient material available for more than one test per sample, and there were at most two samples for a given material and condition. This small number of samples made it impossible to determine if there was any significant difference in hardness between the irradiated and unirradiated samples. ASTM D785 specifies a minimum thickness of 0.25 inches unless it can be shown that the use of thinner samples does not affect the results. All of the samples tested were less than 0.25 inches in thickness and thus did not meet ASTM D785 requirements.


John Meininger
Materials Engineer

4 Atch

1. Fig 1, Photo
2. Fig 2, Photo
3. Fig 3, Photo
4. Table I

TABLE I
Rockwell E Hardness Test Results

<u>Material</u>	<u>Hardness</u>
<u>Unirradiated Samples</u>	
A-950 #1	4
A-950 #2	1
B-950 #1	50
B-950 #2	45
HX-4000 #1	32
HX-4000 #2	Specimen cracked during testing.
<u>Irradiated Samples</u>	
A-950 #1	-1
A-950 #2	14
B-950 #1	35
B-950 #2	17
HX-4000 #1	28
HX-4000 #2	39
=====	
SRT-300, 2-16-93, 93-80	-6
SRT-300, 93-80	-3
SRT-500, 2-16-93, 93-80	-5
SRT-500, 93-80	-5

Atch 4

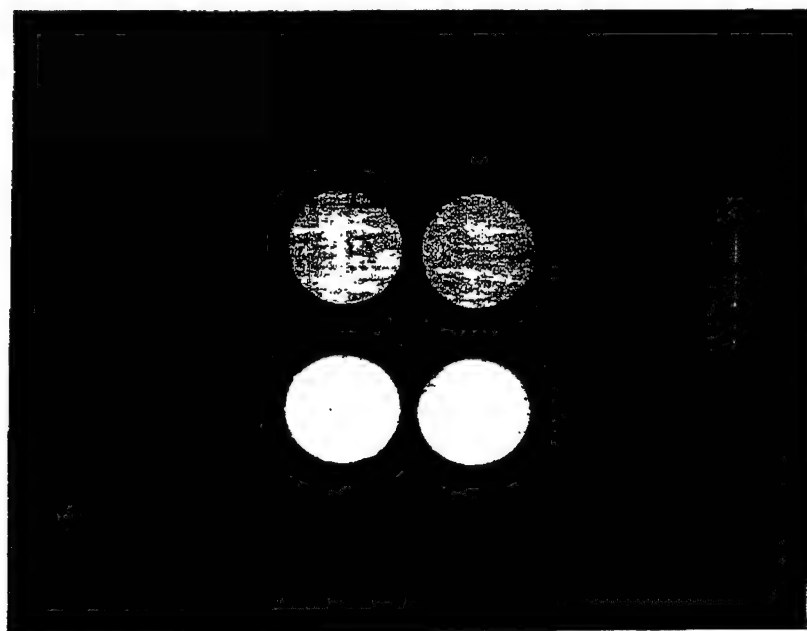


Figure 1. Irradiated samples of A-950 are slightly darker.

Atch 1

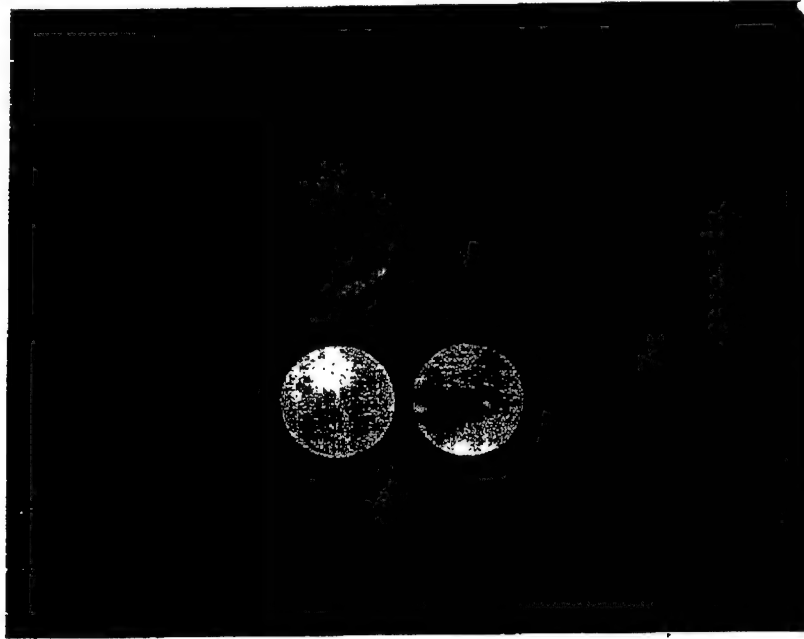


Figure 2. Irradiated samples of B-950 are slightly darker.

Atch 2



Figure 3. Unirradiated HX-4000 is gray, irradiated HX-4000 is tan.

Atch 3

The Investigation of Thermotropic
Liquid Crystalline Polymeric Fibers
at the Micromechanics Level

by

Professor Anthony N. Palazotto
Air Force Institute of Technology
Principal Investigator, AFIT/ENY,
WPAFB OH 45433

Associate Investigators

Professor Satish Kumar - Georgia Institute of Technology

Professor C.T. Tsai - Florida Atlantic University

Professor Fu-Gwo Yuan - North Carolina State University

October 1992

Approved for public release, distribution unlimited

Acknowledgment

The authors would like to thank Dr. John Rusek, chemical engineer of the Propulsion Laboratory, Edwards AFB, for his support. John was instrumental toward the research undertaking and financing. He made many constructive suggestions that led toward the eventual success of this work.

Table of Contents

	Page
Acknowledgement	i
Table of Contents	ii
List of Figures	iii
List of Tables	v
Summary	1
 Chapter I LCP Temperature Dependent Torsional Modulus	
1. Introduction	2
2. Vectra™	12
3. Experimental	16
4. Results & Discussion	21
References	25
 Chapter II LCP Fibers Under Tension Loading	
1. Introduction	30
2. Description of Proposed Research	31
2.1 Homogenization Method of Modeling	
LCP Fibers	31
2.2 Numerical Analysis	31
2.3 Analytical Study of Microfibril	
Stress Distribution	37
References	41
 Chapter III LCP Fibers Under Compressive Loading	
1. Introduction	43
2. Fiber Compressive Failure Modes	44
3. Compressive Test Methods	48
3.1 Bending Beam Test	48
3.2 Elastica Loop Test	52
4. Discussion	54
References	55
Appendix I Extensional and Shear Buckling	58

List of Figures

	Page
I-1 Schematic of the anisotropic and isotropic phases in liquid crystalline polymers.	3
I-2 (a) Viscosity as a function of polymer concentration in a solution indicating lyotropic behavior and (b) The DSC plot as a function of temperature indicating thermotropic behavior of the LCP.	4
I-3 Classification of the LCP based on chemical structure.	6
I-4 Physical arrangement of the molecules in the LCP.	7
I-5 Chemical structures of LCP.	9
I-5 (Cont.) Photographs of the chemical structural model of the LCP's.	10
I-6 Monomers of HBA and HNA which polymerize to give thermotropic copolyester Vectra™.	13
I-7 Morphology model of Vectra™.	14
I-8 Micrographs of the fracture deformation due to tensile test of VectranHS showing fibrillation.	15
I-9 (a) Schematic diagram of a torsional pendulum.	17
I-9 (b1) Experimental set-up of the torsional modulus apparatus.	18
I-9 (b2) Photographs of an experimental set-up to study torsional modulus of a fiber.	19
I-10 Behavior of torsional modulus of VectranHS with temperature.	22
I-11 Behavior of damping factor with temperature for the torsional modulus studies of the VectranHS.	23
I-12 Plot of torsional modulus vs tensile modulus of various LCP fibers.	24

II-1	LCP fibers under tension.	38
III-1	Schematic of ideal kink band.	45
III-2	Relationship between microfibrillar geometry and the buckling mode.	47
III-3	Schematic drawing of bending beam test apparatus and strain distribution in the fiber.	49
III-4	Schematic of fixture for elastica loop test.	51
III-5	Proposed model for compressive failure.	53
III-6	Packing geometry for a collection of interfacing and perfectly oriented link-hinge chains.	56
III-7	Coordinate for extension mode buckling deformation.	59
III-8	Coordinates for extension mode buckling deformation.	60
III-9	Coordinate for shear mode buckling deformation.	63

List of Tables

	Page
1. Mechanical and physical properties of VectranHS.	27
2. Experimental results of the temperature dependance study of torsional modulus and damping factor of VectranHS.	28
3. Mechanical Properties of High Performance Fibers.	29

Summary

This report is divided into three chapters. The first chapter reviews the categorization of the liquid crystalline polymers. It then discusses the characteristics of Vectra™. The shear modulus and mechanical damping of this fiber are determined experimentally at various temperatures, and the test set-up is discussed.

The second chapter presents a micromechanical model of the LCP fiber under tension. A proposed theory is suggested, for future research efforts, in which a crack imperfection is generated causing microfibril failure in the view towards better understading of the overall tensile strength of thermotropic LCPs. The theory not only provides a derivation of effective moduli in a fiber level but also details the interaction effects due to the defect in the microfibril level.

The third chapter suggests a model to characterize the compressive failure of the LCP fiber. Strong evidence appears in previous studies which suggests a nonlinear response of the fibril under compressive load.

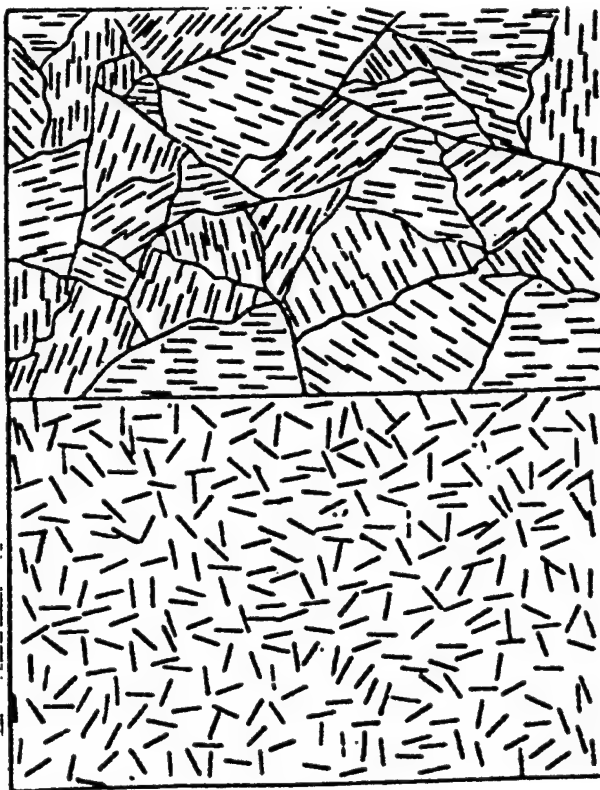
Chapter I LCP Temperature Dependent Torsional Modulus

I. INTRODUCTION

This chapter first presents some background in the characterization of liquid crystalline polymer fibers and then presents the experimentation and results leading to the torsional stiffness of VECTRA™ fibers.

The liquid crystalline behavior of polymers is a result of chain rigidity. A limited number of rod like chains can be accommodated in random arrangement in a solution. At higher polymer concentration, local order between the chain molecules will exist. Schematic diagrams of isotropic and anisotropic phases are given in Figure I-1. Polymers, which show the liquid crystalline phase as a function of temperature, are known as thermotropic liquid crystalline polymers. For a thermotropic LCP a turbid liquid phase may exist between the melting point of the crystalline phase and the isotropic, non-turbid liquid phase [1]. In contrast, some polymers exhibit mesomorphic behavior as a function of their concentration in solution; that is, if the number of rod like polymer chains exceed certain critical concentrations than a liquid crystalline phase forms; these are known as lyotropic liquid crystals. The characteristic features of lyotropic and thermotropic liquid crystalline polymers are shown in Figure I-2(a) and I-2(b). As shown in Figure I-2(a), in the lyotropic liquid crystals, the solution viscosity initially increases with increase in polymer concentration, and then it decreases. The concentration at which the viscosity begins to decrease, represents the concentration at which the polymer goes into the anisotropic phase. The typical

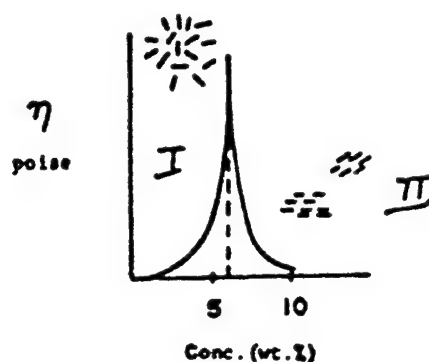
ANISOTROPIC PHASE



ISOTROPIC PHASE

FigI-1. Schematic diagrams of the anisotropic and isotropic phases in liquid crystalline polymers.

LYOTROPIC

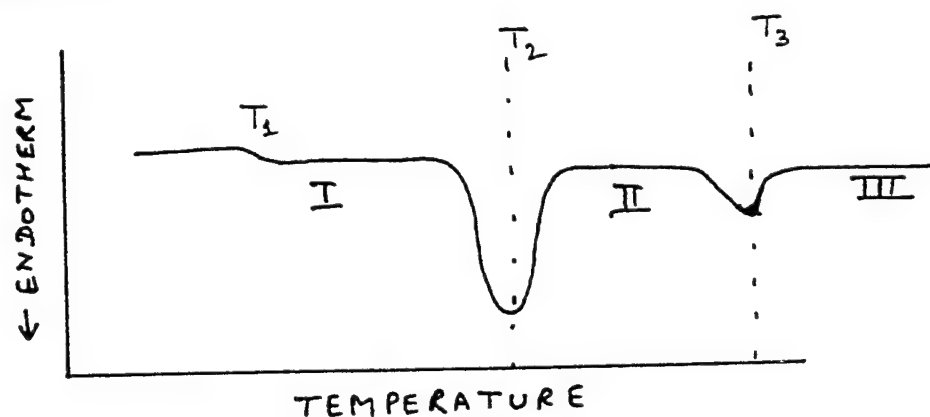


VISCOSITY AS A FUNCTION OF POLYMER CONCENTRATION IN SOLUTION

PHASE I: ISOTROPIC

PHASE II: ANISOTROPIC

THERMOTROPIC



DIFFERENTIAL SCANNING CALORIMETRY PLOT AS A FUNCTION OF TEMPERATURE

REGION I: SEMICRYSTALLINE

REGION II: LIQUID CRYSTALLINE

REGION III: LIQUID LIKE

FigI-2 (a). Viscosity as a function of polymer concentration in a solution indicating lyotropic behavior and (b) the DSC plot as a function of temperature indicating thermotropic behavior of the LCP.

behavior of thermotropic liquid crystalline polymer is shown by the Differential Scanning Calorimetry scan in Figure I-2(b). In this figure, T_g , represents the glass temperature, and T_m is the melt temperature. The region between T_g and T_m represent the liquid crystalline (anisotropic) phase. Above T_m , the system is in the isotropic amorphous melt state.

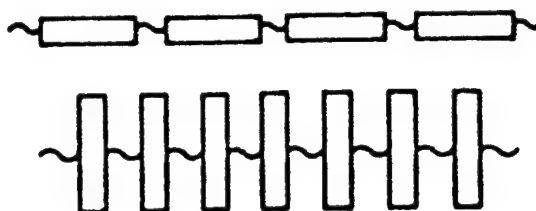
Based on chemical structure, liquid crystalline polymers (LCP) are categorized into two types (Fig I-3): a main chain LCP which involves a succession of rigid molecular structures in the main chain to give a stiff chain with high axial ratio (ratio of length of a molecule to its diameter), and a side chain LCP which involves rigid molecular structures on the side of the main chain [2].

Furthermore, in a liquid crystal, polymer molecules can be arranged in three different ways (Fig I-4).

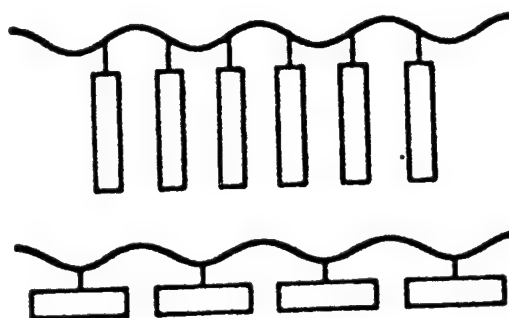
1. Nematic LCP in which molecules show parallel one dimensional order (chain ends are not aligned).
2. Smectic LCP in which molecules align parallel and stratified with two dimensional order in a coterminal manner.
3. Cholesteric LCP which consists of nematic layers arranged in helical structure [3].

A hierarchical fibrillar structure model has been developed by L.C. Sawyer and M. Jaffe for highly oriented liquid-crystalline polymers in the forms of fibers and films. This model was first developed for thermotropic copolyester Vectra™ and then extended for the lyotropic LCPs, such as Kevlar™ and poly(p-phenylene benzobisthiazole). The fibrillar morphology was conformed after extensive characterization using broad range microscopy techniques

MAIN CHAIN LIQUID CRYSTALLINE POLYMERS



SIDE CHAIN LIQUID CRYSTALLINE POLYMERS



FigI-3. Classification of the LCP based on chemical structure.



Nematic



Smectic



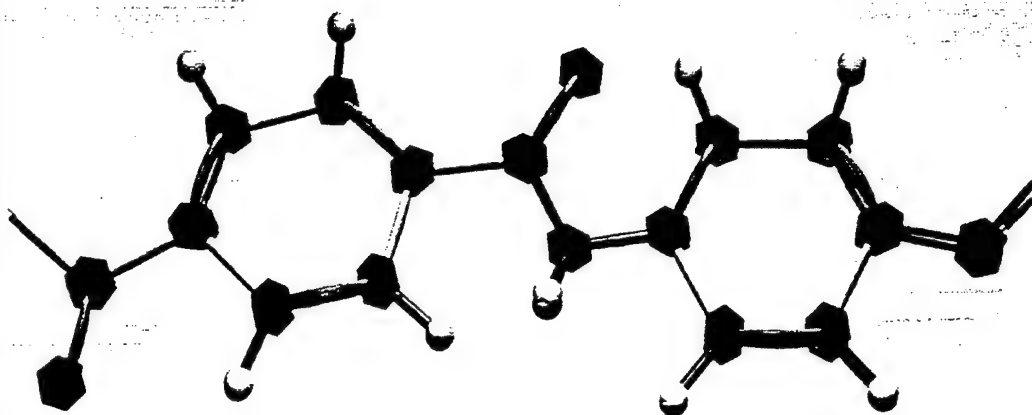
Cholesteric

FigI-4. Physical arrangement of the molecules in the LCP.

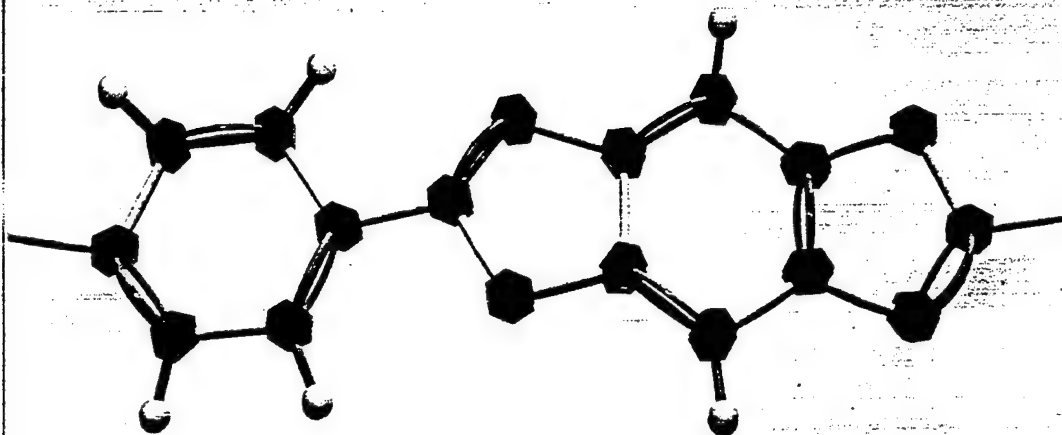
such as Light microscopy, TEM, and SEM. Furthermore, recent studies using Field Emission Scanning Electron Microscopy (FESEM) and Scanning Tunneling Microscopy (STM) delineates a microfibrillar structure within the fibrillar structure [11]. According to Sawyer et al, microfibril does not arise due to fracture deformation but rather exists as a unit of fibrillar structure of LCPs. Microfibril are composed of two to five molecules and thus can be termed macromolecular in nature. Microfibril exhibits a tap-like shape. Also, kink band results due to deformation of the microfibril [11]. The LCP structural model consisting of elongated well-known fibrils give rise to high anisotropy.

Owing to the aromatic nature of the structure (Fig I-5) both lyotropic and thermotropic liquid crystalline polymers generally possess combination of properties such as high heat distortion and service temperature, high chemical resistance, high tensile properties, flame retardancy without the need of additives; this enables LCP for Hi-Tech applications.

The theoretical development on the basis of the thermodynamics for the prediction of liquid crystalline behavior for a complete rigid chain was given in 1956 by P.J. Flory who used modified lattice theory and proposed a statistical theory of spontaneous ordering of rod like polymer molecules in concentrated solutions and melts. The theory specifically predicts that above a certain critical concentration, a rod like molecule that possess an axial ratio(x) greater than approximately 6.4, will spontaneously form two phases. At a lower axial ratio, the phase is isotropic in which the molecules are completely uncorrelated; at a higher axial ratio

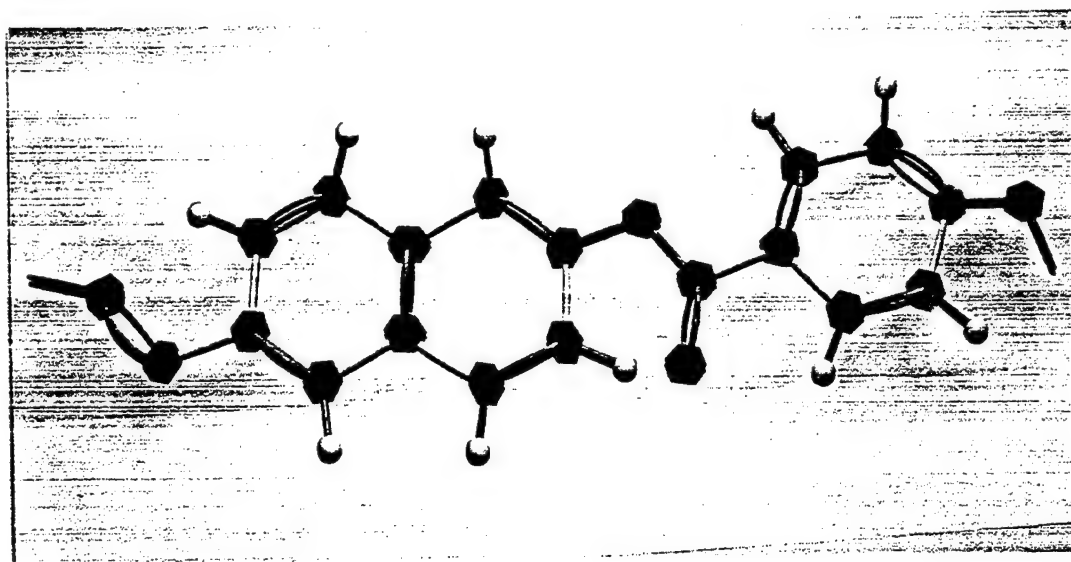


Kevlar™



PBZT

Fig 1-5. Chemical Structures of LCPs.



Vectra™

(cont.)
 Fig 15 Photographs of the chemical structural model of the LCPs.

the phase is anisotropic in which the molecules are highly correlated with respect to their long axis resulting in an appearance of a stable anisotropic phase.

For processing, a thermotropic system requires a melting temperature at which polymer degradation and decomposition does not occur [2]. This is a necessary condition for processing of the TLCP melt. Chemical structural modifications are sought for achieving the reduction in melt temperatures for such systems. For example, phenyl groups can be linked by ethylene linkage for increased flexibility. With the introduction of a more flexible group, the entropy change ΔS increases and hence melting temperature T decreases. The melt temperature of a number of liquid crystalline polyesters is in the range of 280 to 350°C [4].

Thermotropic LCP possesses several processing advantages. For example, because the melt being ordered and having lower heat of fusion, a very small amount of heat has to be removed when the mould is cooled and hence melt solidifies rapidly. This results in a short cycle time. Moreover, TLCPs possess low melt viscosity and hence long flow paths are achieved; therefore, the smallest mould can be filled [5]. The mechanical properties of thermotropic LCP are also influenced by processing parameters. Microfibrillar structures are formed within larger fibrillar structure during processing [11]. Fibrils forms a layered structure, with a long axis of the fibrils arranged along the extrusion direction due to shear and elongational flow arising during processing; this gives TLCP a wood-like, fibrous structure morphology. A range of exceptional properties, such as very good mechanical properties and

low coefficient of linear thermal expansion results from this special morphology.

Because of exceptional properties and processing advantages of TLCPs several corporations are engaged in the development of TLCPs and are exploring the possibilities of application of TLCP fiber in composites and for electronic circuit, fiberoptics, and aerospace industry. A family of Vectra™ products are made by Hoechst Celanese [7].

2. VECTRA™

Vectra is a high performance thermotropic Liquid Crystalline Polymer. The polymer is a thermotropic copolyester made from 4-hydroxybenzoic acid (HBA) and 2-hydroxy, 6-naphthoic acid (HNA)[6]. The chemical structure of the starting monomers and the repeat unit of Vectra are shown in Figure I-6.

Hoechst Celanese further developed Vectran™, a multifilament spun fiber. The FESEM and STM studies reveals that Vectran™ has fibrillar morphology, and the fibrils are not perfectly straight, neither are they perfectly aligned with the fiber or the tape axis but they wind in a serpentine fashion into and out of the longitudinal plane parallel to the fiber axis [11]. Figure I-7 shows a schematic of the Vectran™ fiber structural model. The SEM studies of the fracture deformation of Vectran™ due to tensile testing shows fibrillation (Fig I-8).

The typical properties of Vectran™HS fiber are given in Table 1. The fiber exhibits exceptional mechanical and physical properties: High strength and modulus, high abrasion resistance, low moisture absorption, excellent chemical resistance, negative

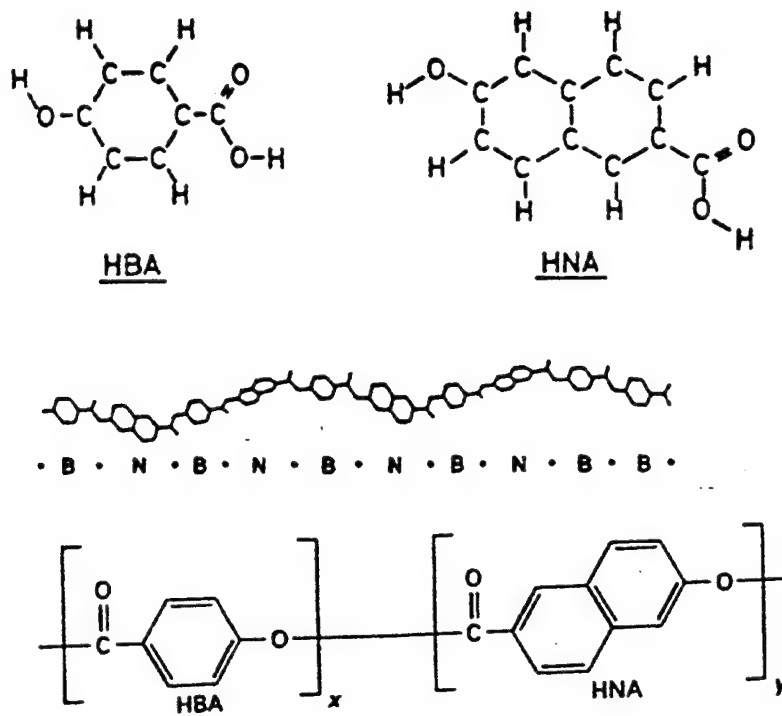
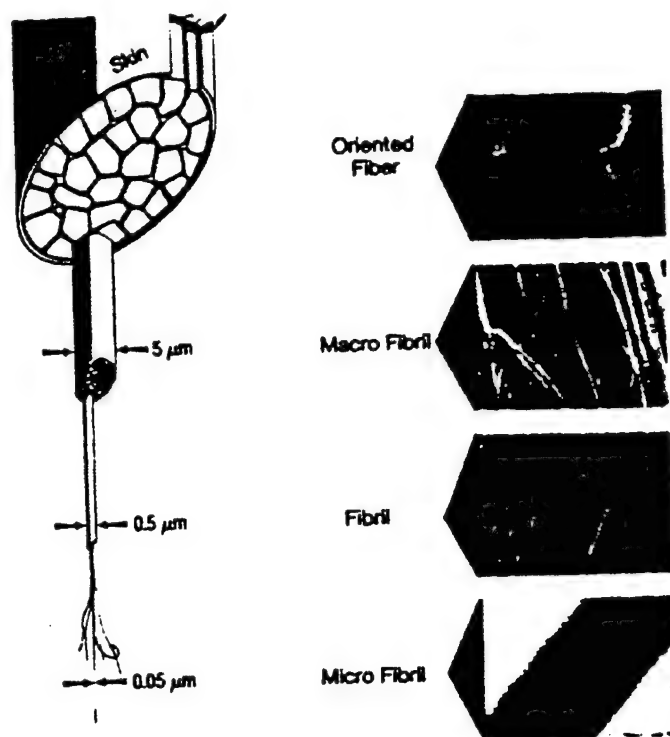


Fig16. Monomers of HBA and HNA which polymerize to give thermotropic copolyester Vectra™.



FigI-7. Morphology model of Vectran™.



Fig 8. Micrographs of the fracture deformation due to tensile test of VectranHS showing fibrillation.

CTE, high impact resistance, high temperature resistance, excellent flammability resistance, and high dielectric strength [7].

3. EXPERIMENTAL

A torsion pendulum is a simple method for measuring shear modulus and mechanical damping of a polymeric fiber. One end of the specimen is rigidly clamped and other is attached to a inertia disk, which is free to oscillate. The torsional pendulum arrangement is shown in Figure I-9(a) and I-9(b). The torsional modulus measurement were made on sample of VectranHS fiber. Four readings of each sample were taken. Measurements were made at 25°C, 60°C, 90°C, 120°C, and 150°C. The samples were mounted on the cardboard tabs of one inch gage length. Epoxy glue was used for mounting the fibers on the tab, and the glue was allowed to set for 24 hrs. The radius of the sample was measured at four places along the one inch gage length by a laser-beam diffraction method, using He-Ne laser. The radius of the fiber is given by the diffraction theory as

$$r = \mu S / \Delta$$

Where,

μ = wavelength of the laser (632.8 nm for the He-Ne laser)

S = distance between fiber and screen

Δ = distance of the first intensity minima from the main beam

The torsion pendulum was prepared using a cardboard disk. At the center of the disk a round head aluminum fastener was inserted for holding a bottom end of the paper tab containing the fibre sample. The top end of the paper sample was clamped on the stand. Both sides of the paper tab were cut carefully without

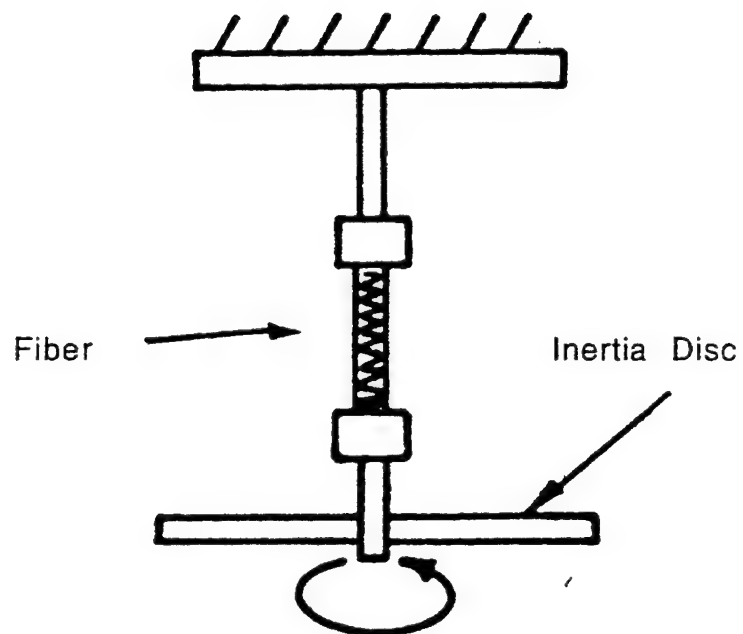


Fig 9(a). Schematic diagram of a torsional pendulum.

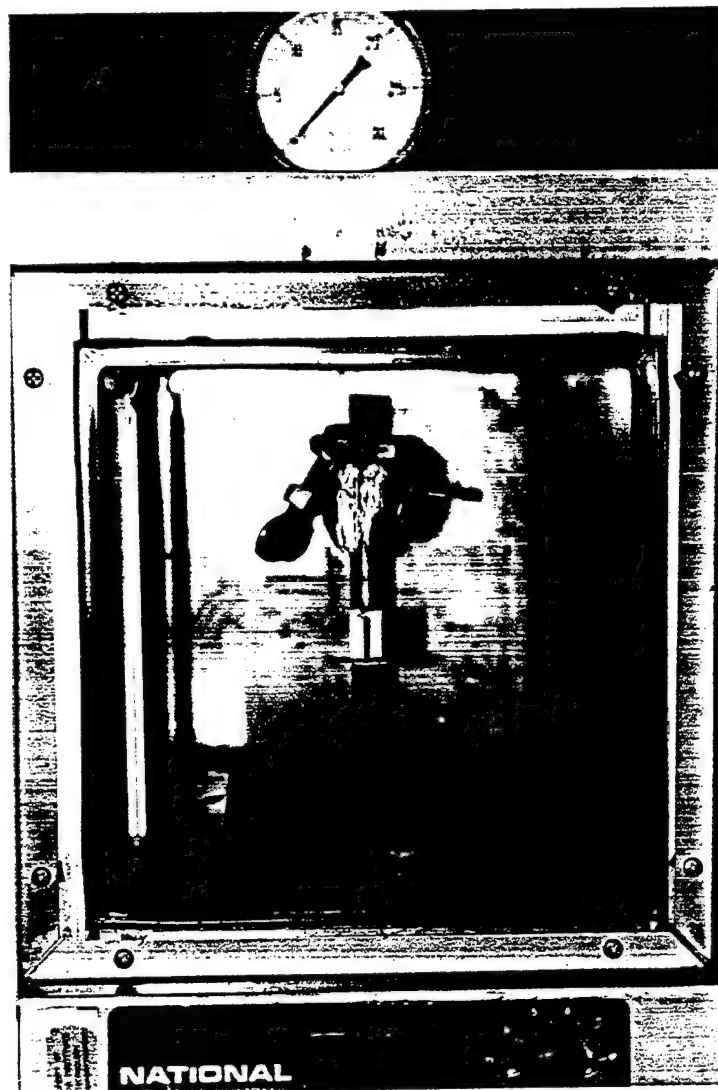


Fig. I-9(61). Experimental set-up of the torsional modulus apparatus.

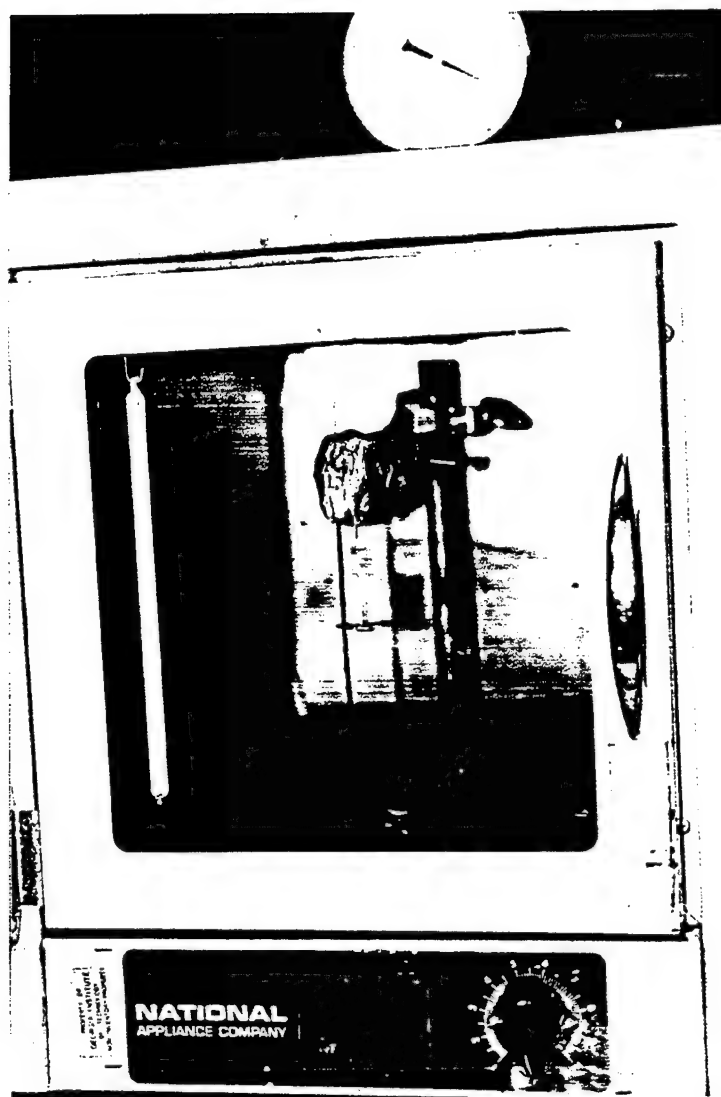


Fig1-9(b2). Photographs of an experimental set-up to study torsional modulus of a fiber.

straining the fiber so that the fiber can be freely attached to the torsion pendulum. The whole arrangement was placed in the vacuum oven, initially maintained at the room temperature. After mounting the specimen, the vacuum was pulled. The fiber was set to rotate by letting very small amounts of air in the oven chamber, and the displacement period was recorded. The temperature of the oven was then raised to 60°C to measure displacement period for the rotation of the fiber at that temperature. Similarly, measurements were taken at 90°C, 120°C, 150°C. The pendulum's moment of inertia was calculated by incorporating the contributions of cardboard disk, aluminum fastener and the lower portion of the paper tab. From the displacement-time data both the dynamic torsion modulus and logarithmic decrement Δ were calculated using the free-torsion pendulum equation [9]:

$$G = 8\pi^3 IL/A^2 T^2$$

where,

I = moment of inertia of the pendulum = 0.2204 g-cm²

L = length of the fiber in cm

A = cross sectional area of the fiber in cm² = πr^2

T = corrected oscillation period given by

$$T = T_0 / (1 + (\Delta/2\pi)^2)^{0.5}$$

Where,

T_0 = measured period of the oscillation in seconds

Δ = logarithmic decrement = $\ln (A_0/A)$

A_0 and A are amplitude in two successive oscillations.

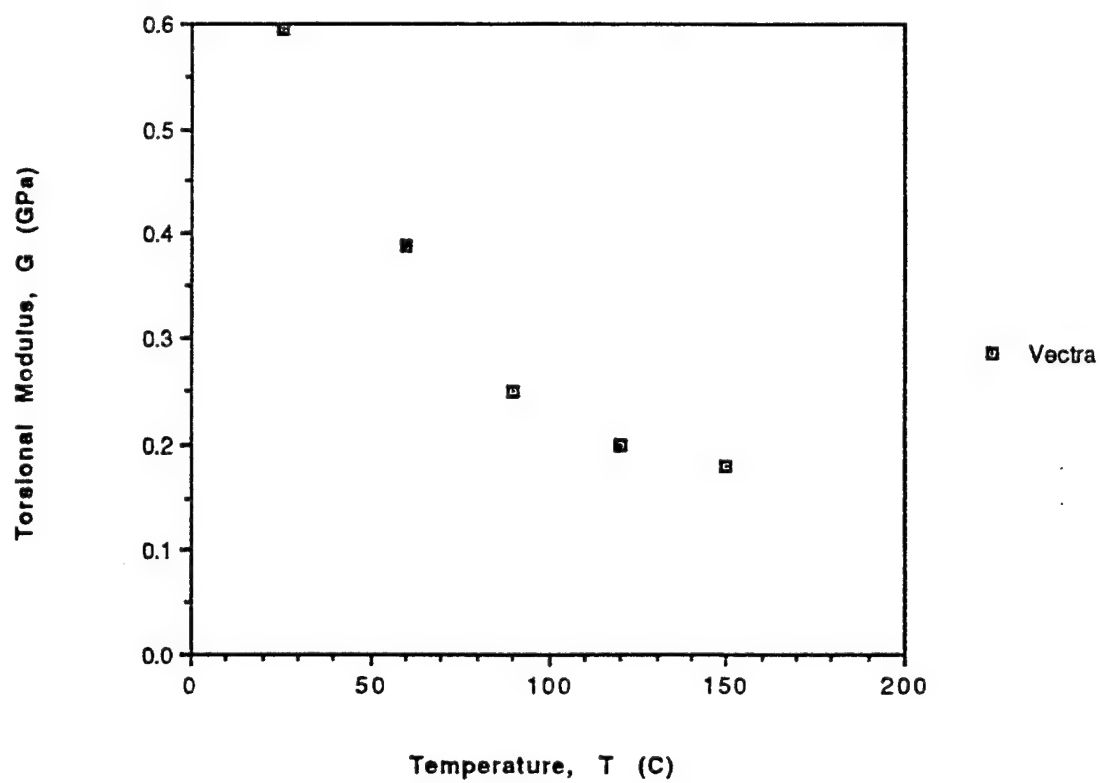
4. RESULTS & DISCUSSION

From the Results (Table 2), it is clear that as the temperature increases the torsional modulus of Vectran^{HS} decreases (Fig I-10). This can be explained by considering the chain and crystal structure, and orientation and the morphology of the fiber.

VectranTM has fibrillar morphology; the crystals are closely packed. Under the torsion at high temperature the crystals may get distorted; as a result, torsional modulus may decrease. Also, crystal lattice distortion may increase with increasing temperature; hence, there is greater amount of energy loss due to which damping increases (Fig I-11). Moreover, since Vectra has negative CTE, the chains may shrink axially on heating and hence random coil morphology may initiate resulting in a torsional modulus decrease. Breakage of the dipole-dipole interaction on heating may further contribute to decrease in the torsional modulus.

Other studies carried out indicate that, in the temperature range studied, the torsional modulus of all polymeric fibers decreases with increase in temperature, and the most significant decrease is observed in the torsional modulus of KevlarTM 49 and VectraTM. In the temperature range studied (room temperature to 150°C) no significant change in the torsional modulus of carbon fibers was observed. A comparison of the torsional moduli of the four polymeric fibers is given in Figure I-12. Of these four high performance polymeric fibers, VectraTM has the lowest torsional modulus and KevlarTM 49 has the highest, with the intermediate

Plot of Torsional Modulus Vs. Temperature of Vectra



FigI-10. Behavior of torsional modulus of VectranHS with temperature.

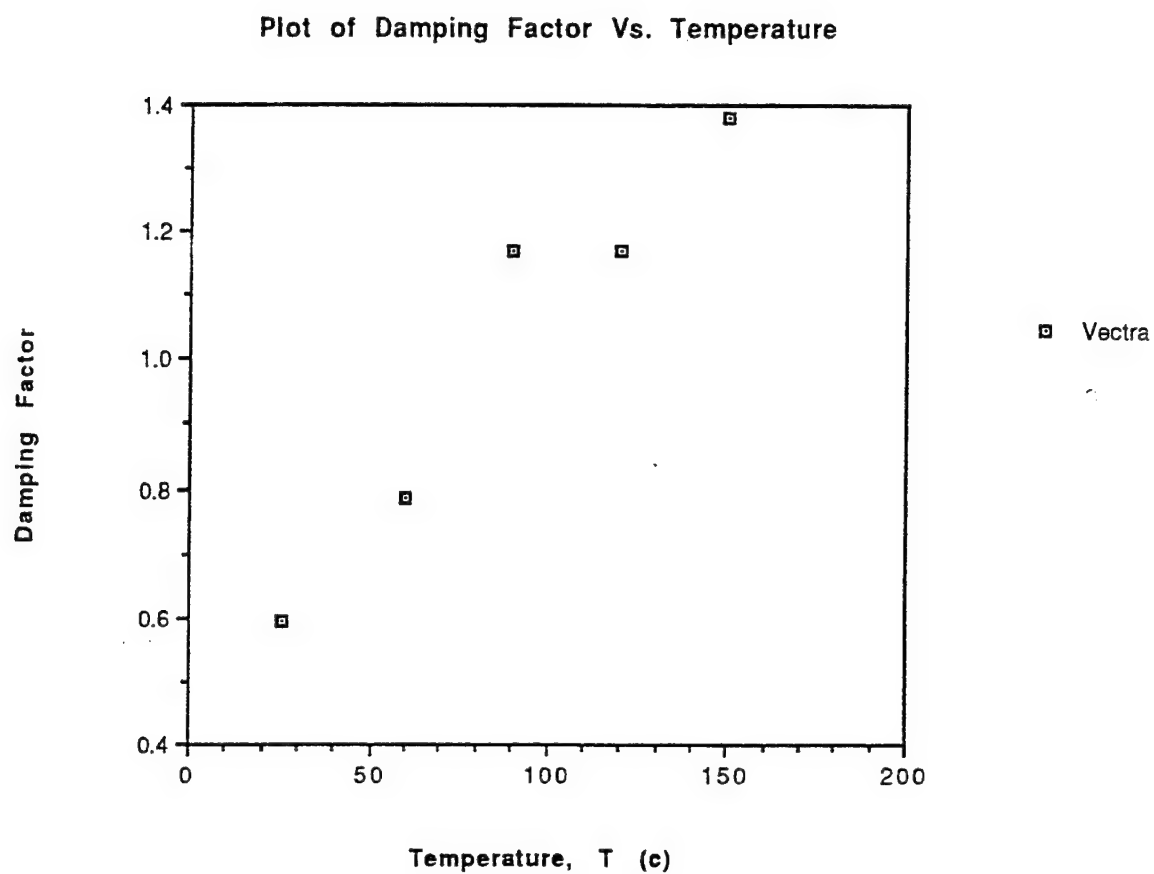
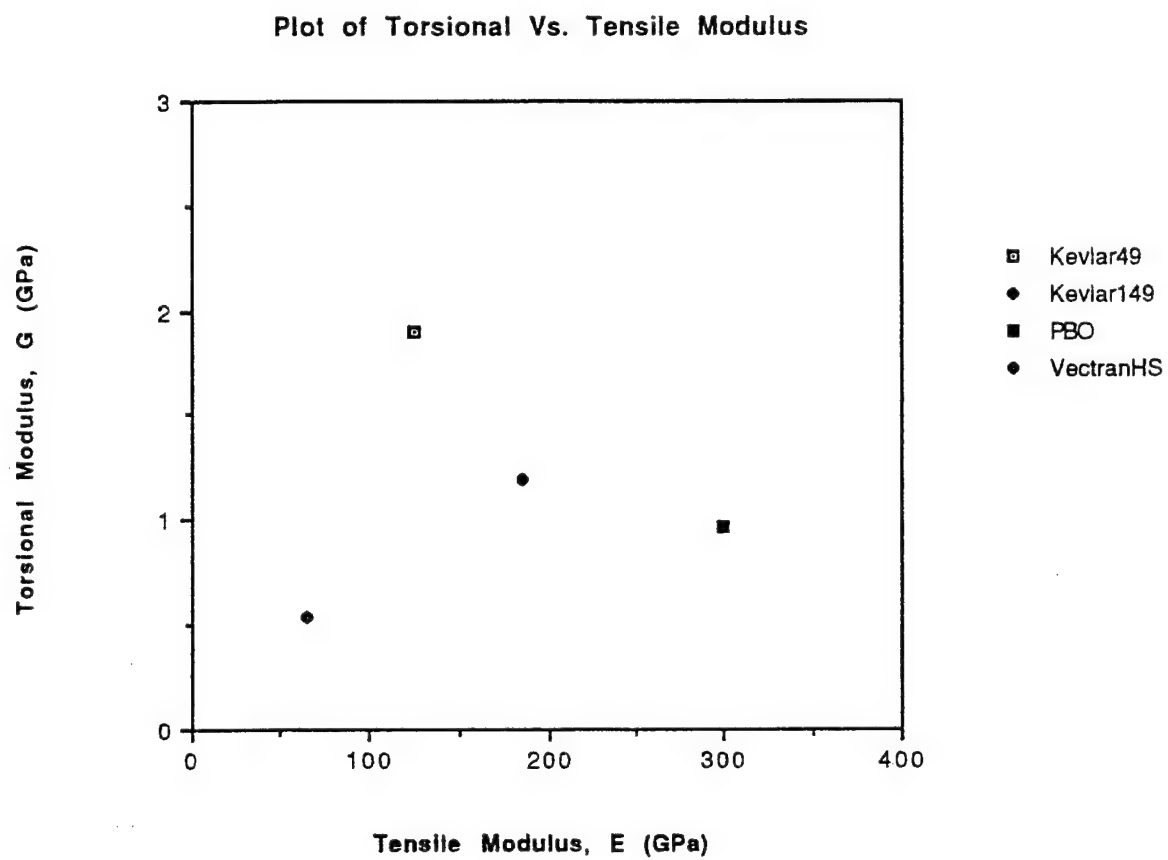


Fig I11. Behavior of damping factor with temperature for the torsional modulus studies of the VectranHS.



FigI-12. Plot of torsional modulus Vs. tensile modulus of various LCP fibers.

values for PBZT and PBO. The low torsional modulus of Vectra™ is likely a result of -COO- group, as the rotation about -C-, an -O- will encounter little resistance. In Kevlar™ easy rotation around -NH- and -CO- is presumably resisted by the hydrogen bonding between adjacent chains, thus yielding higher torsional modulus for this fiber.

The damping factor can also reveal some structural information about the fibers. However, in the case of fine fibers it must be ensured that the damping factor represents the true value for the fiber, and that it is not a result of aerodynamic effects. Towards this end, it was concluded in a study by Adams & Lloyd [12] that, in order to obtain true fiber damping it was necessary to use very high vacuum levels (10^{-6} torr). Adams & Lloyd further contend that at higher than 0.1 torr the damping is essentially due to aerodynamic effects, and that at these vacuum levels fiber damping makes negligible contribution. However our study seems to indicate that the damping factors reported are the true damping factors.

REFERENCES

1. Russell A. Gaudiana, "Polyesters, Mainchain Aromatic," in The Encyclopedia of Polymer Science and Engineering, John Wiley and Sons, New York, Index Volume, pp 264, (1990).
2. S.L. Kwolek, P.W. Morgan, J.R. Schaefgen, "Liquid Crystalline Polymers," in The Encyclopedia of Polymer Science and Engineering, John Wiley and Sons, New York, pp 547, (1990).
3. Michael Jaffe, Gordon Caludann, Myun-Nam Yoon, "Fibers

- from Naphthalene-based thermotropic liquid crystalline copolyester," in High Technology Fibers, Part B (M. Lewin and J. Preston, Eds.), Marcel Dekker, New York, 1985.
4. Maged A. Osman, *Polymer*, Vol. 28, No. 5, pp 713 - 715, (1987).
 5. G. Kirsch, H. Terwyn, *Kunststoffe-German Plastics* , Vol. 80, No. 10, pp 57-60, (1990).
 6. Geoffrey R. Davies, Ian M. Ward, "Structure and properties of oriented thermotropic liquid crystalline polymers in the solid state," in High Modulus Polymers (A.E. Zachariades, R.S. Porter, Eds.), Marcel Dekker, New York, 1988.
 7. D.E. Beers, J.E. Ramirez, *Journal of the Textile*, Vol. 81, No. 4, pp 561-574, (1990).
 8. T. Murayama, *Dynamic Mechanical Analysis of Polymeric Material*, Elsevier, Amsterdam, pp 43-44, 1978.
 9. Satish Kumar, Vinay R. Mehta, David P. Anderson, Allan S. Crasto, *Proc. 37th International SAMPE Symposium*, March 1992, pp 967-973.
 10. Charles E. McChesney, *Liquid Crystalline Polymers*, in the *Engineered Materials Handbook*, ASM International, Vol. 2, pp 179-182, (1988).
 11. L.C. Sawyer, R.T. Chen, M.G. Jamieson, I.H. Musselman, P.E. Russell, *Journal of Material Science Letters* , Vol. 11, No. 2, pp 69 - 72, (1992).
 12. R. D. Adams & D.H. Llioyd, *J. Phys. E. Scientific Instruments*, Vol. 8, pp 475, (1975).

Typical Properties of VectranHS

Tensile Strength	412 ksi (2.8 GPa)
Tensile Modulus	9.4 Msi (65 GPa)
Elongation at Break	3.3 %
Melting Point	625° F (330° C)
Moisture Regain	<0.1 %
Dielectric Constant @1 KHz	3.3
Density	1.4 g/cc (0.05 lbs/in ³)
Chemical Resistance	Hydrolytically stable
Resistance to organic solvents	

Table 1. Mechanical and physical properties of VectranHS.

Temperature (°C)		G (GPa)	Std. Deviation	Δ	Std. Deviation
1.	26	0.59	0.035	0.594	0.050
2.	60	0.39	0.030	0.785	0.113
3.	90	0.25	0.046	1.170	0.250
4.	120	0.20	0.050	1.170	0.390
5.	150	0.18	0.040	1.380	0.450

Table 2. Experimental results of the temperature dependence study of torsional modulus and damping factor of VectranHS.

Fiber	Tensile Strength (GPa)	Tensile Modulus (GPa)	Density (g/cc)	Torsional Modulus (GPa)	Compressive Strength (GPa)
Kevlar™ 49	3.5	125	1.44	1.9	0.39-0.48
Kevlar™ 149	3.4	185	1.47	1.2	0.32-0.46
Spectra™ 1000	3.0	170	0.97	-	0.17
PBO	3.5-5.7	280-360	1.58	0.97	0.20-0.40
Vectran™HS	2.9	65	1.41	0.54	-
Pitch based Carbon fibers					
P-100	2.2	725	2.15	4.7	0.48
P-25	1.4	160	1.90	-	1.15
PAN based Carbon fibers					
T-300	3.2	235	1.76	15	2.88
T-50	2.4	390	1.81	14	1.61
Inorganic fibers					
S-Glass	4.5	90	2.46	-	>1.1
Al ₂ O ₃	1.7	350-380	3.7	-	6.90
SiC	3.45	400	3.0	-	-

Table 3. Mechanical properties of High Performance Fibers.

Chapter II LCP Fibers Under Tension Loading

1. INTRODUCTION

Liquid Crystalline Polymers (LCPs) have attracted special attention since the last decade. This has arisen primarily because successful advances in processing of LCPs. For example, the fibers with very high stiffness and nearly perfect orientation can now be produced by spinning thermotropic solutions without further mechanical processing. These fibers with its very high microscopic anisotropy have remarkable properties greater than other currently available high performance fibers. Particularly nowadays, fiber-reinforced composites having high strength/weight and stiffness/weight ratios are becoming increasingly important. Extensive discussion of various LCPs as well as most of pertinent references, can be found in Ref. [1].

To exploit the fiber system in future structural applications, one critical concern in design is the mechanical response under tension loading. Based on SEM micrographs and the observation of fracture surfaces, Sawyer and Jaffe [2] revealed the thermotropic LCP fibers exhibit a hierarchical structure with three different scales of composition; fiber, macrofibrils and microfibrils. Since a fiber consists of numerous microfibrils that are separated by weak boundaries (interfibrillar region), it is crucial to determine the consequences of the weak region in the microscopic level. Under such circumstances, the understanding of the microscopic deformation behavior under tension can be useful in the selection of the mechanical

properties of the constituents which would minimize the potential internal damage in the fiber and thereby increase the fiber tensile strength.

The proposed research is to study and quantify microstructural fracture behavior of microfibril level with a view towards better understanding the microscale failure mode which degrade the overall tensile strength of thermotropic LCPs. In view of the complicated multi-scale geometry in the fiber, analytical and computational models of LCP fibers are constructed using a mathematical theory called homogenization [3-5]. The theory not only provides a derivation of effective moduli in a fiber level but also details the interaction effects due to the defect in the microfibril level. More importantly, the effect of microdamage on the moduli of the fiber under tension can be estimated in a systematic manner. A representative element in the microfibril level will be employed in the analysis. The modelling of weak adhesion between the microfibrils and interfibrillar domains will be simulated on the basis of axisymmetric elasticity. The stress concentration due to degree of weak adhesion and detailed microfibril arrangement will be examined and a strain criterion will be explored to represent fiber failure.

2. DESCRIPTION OF PROPOSED RESEARCH

2.1 Homogenization Method of Modeling LCP fibers

Consider the macrofibril and the microfibrils with two basic spatial scales, d and d' . The ratio of d/d' is within a small parameter. If the spatial variable x' is used to describe

the stress variations in the macrofibrils, then $x = x'/\varepsilon$ is adopted to investigate the corresponding stresses in the microfibrils. The governing equation of the macrofibrils are

$$\operatorname{div} \sigma = 0, \sigma = C \varepsilon \quad (1)$$

By using asymptotic expansion of stresses and displacements in terms of ε ,

$$\sigma = \sigma^{(0)}(x') + \varepsilon \sigma^{(1)}(x, x') + \varepsilon^2 \sigma^{(2)}(x, x') + \dots \quad (2)$$

$$u = u^{(0)}(x') + \varepsilon u^{(1)}(x, x') + \varepsilon^2 u^{(2)}(x, x') + \dots$$

Substitution of equations (2) into (1) leads to three sets of equations:

$$\operatorname{div} \sigma^0 = 0 \quad (3)$$

$$\sigma^0 = C \varepsilon_x(u^0)$$

$$\operatorname{div} \sigma^1 + \operatorname{div} \sigma^0 = 0 \quad (4)$$

$$\sigma^1 = C[\varepsilon_x(u^1) + \varepsilon_{x'}(u^0)]$$

$$\operatorname{div} \sigma^2 + \operatorname{div} \sigma^1 = 0 \quad (5)$$

$$\sigma^2 = C[\varepsilon_x(u^2) + \varepsilon_{x'}(u^1)]$$

The system of equations(3) provides a trivial solution:

$$\sigma^0 = 0, \quad u^0 = u^0(x) \quad (6)$$

A combination of equations(6) and equations(4) leads to

$$\operatorname{div} \sigma^1 = 0, \quad \sigma^1 = C[\varepsilon_x(u^1) + \varepsilon_{x'}(u^0)] \quad (7)$$

cylindrical coordinates.

$$\Delta = \partial_{rr} + (1/r)\partial_r + \partial_{zz} \quad (2)$$

With the Love's stress function, all stresses and displacements for each individual phase can be written in the following form

$$\begin{aligned} \sigma_r &= (v\Delta\Psi - \Psi_{,rr}),_r, & \sigma_\theta &= (v\Delta\Psi - (1/r)\Psi_{,r}),_z \\ \sigma_z &= \{(2-v)\Delta\Psi - \Psi_{,zz}\},_z, & \tau_{rz} &= \{(1-v)\Delta\Psi - \Psi_{,zz}\},_r \end{aligned} \quad (3)$$

$$u = -\{(1+v)/E\}\Psi_{,rz}, \quad w = \{(1+v)/E\}\{2(1-v)\Delta\Psi \Psi_{,zz}\}$$

To investigate the local behavior of the stresses near the crack tip, it is convenient to move the origin to the tip of the crack [7]. Consequently, all stress and displacement components will be expressed in terms of the new coordinate system. Let $(r, z) = (a, 0)$ be the origin of local coordinate, a new polar coordinate system (ρ, ϕ) is introduced in terms of (x, z) as follows

$$x = r - a = \rho \cos \phi, \quad z = \rho \sin \phi, \quad (4)$$

where the variable ρ is assumed as a small quantity less than radius a .

For convenience, the following operators transforming to local coordinates are listed and used to derive the second and the fourth order partial differential operators.

$$\partial_r = \partial_x = \cos \phi \partial_\rho - (\sin \phi / \rho) \partial_\phi, \quad \partial_z = \sin \phi \partial_\rho + (\cos \phi / \rho) \partial_\phi$$

$$(1/r)\partial_r = \{1/(a + \rho \cos \phi)\}\partial_r = \{1/(a + \rho \cos \phi)\} \{\cos \phi \partial_\rho - (\sin \phi / \rho) \partial_\phi\}$$

$$\partial_{rr} = \partial_{xx} = \cos^2 \phi \partial_\rho^2 - (2 \sin \phi \cos \phi / \rho) \partial_\rho \partial_\phi + (\sin^2 \phi / \rho^2) \partial_\phi^2$$

$$\begin{aligned}
& + (\sin^2 \phi / \rho) \partial_\rho = (2 \sin \phi \cos \phi / \rho^2) \partial_\phi \\
\partial_{zz} & = \sin^2 \phi \partial_\rho^2 + (2 \sin \phi \cos \phi / \rho) \partial_\rho^2 \partial_\phi + (\cos^2 \phi / \rho^2) + (\cos^2 \phi / \rho) \partial_\rho \\
& - (2 \sin \phi \cos \phi / \rho^2) \partial_\phi
\end{aligned} \tag{5}$$

The new second order operator in coordinate system is expressed as

$$\begin{aligned}
\Delta_{(\rho, \psi)} & = \partial_\rho^2 + (1/\rho^2) \partial_\phi^2 + (1/\rho) \partial_\rho + \{1/(a + \rho \cos \phi)\} \{\cos \phi \partial_\rho - (\sin \phi / \rho) \partial_\phi\} \\
& = \partial_\rho^2 + (1/\rho) \partial_\rho + (1/\rho^2) \partial_\phi^2 + (1/a) \sum_{m=0}^{\infty} \{(-\rho/a) \cos \phi\}^m \{\cos \phi \partial_\rho - (\sin \phi / \rho) \partial_\phi\}
\end{aligned} \tag{6}$$

For the second order partial differential equation, one seeks a solution in the form of series expansion for the equation (5) which is separable with respect to ρ and ϕ

$$\psi(\rho, \phi) = \sum_{n=0}^{\infty} \rho^{\kappa+n+3} \Psi_n(\phi) \tag{7}$$

where κ is a complex constant to be determined. Based on positive definiteness of the strain energy density function, the following condition must be satisfied.

$$\operatorname{Re}(\kappa) > -1 \tag{8}$$

Inserting the assumed series solution (7) into the equation (6), one obtains

$$\begin{aligned}
& \{(\kappa+n+3)(\kappa+n+2) + (\kappa+n+3)\} \rho^{\kappa+n+1} \Psi_n(\phi) + \rho^{\kappa+n+1} \Psi_n(\phi)_{,\phi\phi} \\
& + (1/a) \sum_{m=0}^{\infty} \{(-\rho/a) \cos \phi\}^m \rho^{\kappa+n+2} \{(\kappa+n+3) \cos \phi \Psi_n(\phi) - \sin \phi \Psi_n(\phi)_{,\phi}\}
\end{aligned} \tag{9}$$

The two relationships corresponding to each order are thus

given as

For $\rho^{\kappa+n+1}$,

$$\{(\kappa+n+3)(\kappa+n+2) + (\kappa+n+3)\} \Psi_n(\phi) + \Psi_n(\phi)_{,\phi\phi} = 0 \quad (10)$$

For $\rho^{(\kappa+n+2)}$ or higher order,

$$\sum_{m=0}^{\infty} \{(-\rho/a) \cos \phi\}^m \rho^{\kappa+n+2} \{(\kappa+n+3) \cos \phi \Psi_n(\phi) - \sin \phi \Psi_n(\phi)_{,\phi}\} = 0 \quad (11)$$

As far as the solution of the equation $\Delta_{\rho,\phi} \Psi = 0$ is concerned, the lowest order term is the most dominant one since it shows the singular behavior near the crack tip. Furthermore, one extends the previous concept to seek the solution of the equation

$$\Delta_{(\rho,\phi)} \Delta_{(\rho\phi)} \Psi = 0.$$

The following form can be obtained

$$\Psi_n(\phi) = e^{-i(\kappa+n+3)\phi} \quad \text{or} \quad e^{i(\kappa+n+3)\phi} \quad (12)$$

From equation (7) with $n = 0$, one has an asymptotic crack-tip solution

$$\psi_1(\rho, \phi) \sim \rho^{\kappa+3} \{A \cos (\kappa+3)\phi + B \sin (\kappa+3)\phi\} \quad (13)$$

Similarly, one has a solution for the fourth order partial differential equation

$$\psi_2(\rho, \phi) \sim \rho^{\kappa+3} \{C \cos (\kappa+1)\phi + D \sin (\kappa+1)\phi\} \quad (14)$$

Consequently, the general asymptotic solution can be written in the form

$$\psi(\rho, \phi) \sim \rho^{\kappa+3} \{A \cos (\kappa+3)\phi + B \sin (\kappa+3)\phi + C \cos (\kappa+1)\phi + D \sin (\kappa+1)\phi\} \quad (15)$$

It is proposed to continue this study to investigate the local stress and displacement fields near the tip region. Using

traction free boundary conditions at the two crack faces and frictional fiber interface modelled by a Coulomb friction law, the dominant stress singularity and associated eigenvalues κ will be solved. Particularly, the effect of stress singularity on various Coulomb friction coefficient will be investigated.

2.2 Numerical Analysis

The analytical difficulties in determining stress intensity factors are complicated in composite materials because of the material inhomogeneity involved. Only very few cases have been solved in closed form. Furthermore, for the composite with complicated geometric, and loading variables, elasticity solutions for these problems are not available in general. Numerical methods such as finite element methods are considered most attractive due to their versatility in handling mechanics problems with a variety of complexities. Singular hybrid element procedure for treating a general class of mechanics problems involving different failure modes behavior will be constructed and used to solve these fracture mechanics problems. In the finite element approach to singular elasticity problems, it is well recognized that the rate of solution convergence is generally independent of the order of polynomials used for interpolation functions in the element formulation [8]. That is, the use of higher-order elements does not necessarily improve the rate of convergence of the numerical solution. This phenomenon has been indeed observed in many singular computational mechanics problems. For example, in a linear elastic fracture mechanics

The solution of the above equation can be solved by considering $\epsilon_x(u^0)$ as an initial strain and invoking a linear superposition principle and

$$\text{div } C \epsilon_x(u^1) = -\text{div } C \epsilon_x(u^0) \quad (8)$$

The equation (8) will be solved numerically in section 2.3.

In order to derive the constitutive equation in the microfibril level, the volume average of deformation and stress over a representative element will be used.

$$\langle \sigma^1 \rangle = C \epsilon_x(u^0)$$

2.3 Analytical Study of Microfibril Stress Distribution

When cracks form a regular spacing perpendicular to the microfibril direction (Fig. II-1) under tensile loading, the stress states in each cylindrical unit cell are the same. Therefore the boundary conditions can be formulated based on the periodic conditions. The crack deflected over the microfibril surface can be modelled in a similar way. Consider the unit axisymmetric cell consisting of microfibril and interfibrillar region. The two phases are assumed to be homogeneous, isotropic, linear elastic solids with moduli E_1 , and ν_1 . The interfaces are allowed to slip according to a Coulomb friction law. A crack lies along $z = 0$, $a \leq r \leq b$. The problem is formulated with a Love's stress function [6] assuming axisymmetric behavior. The function $\psi(r, z)$ for each phase is satisfied with the biharmonic equation.

$$\Delta \Delta \Psi(r, z) = 0 \quad (1)$$

where the symbol Δ is defined as an Laplacian operator in

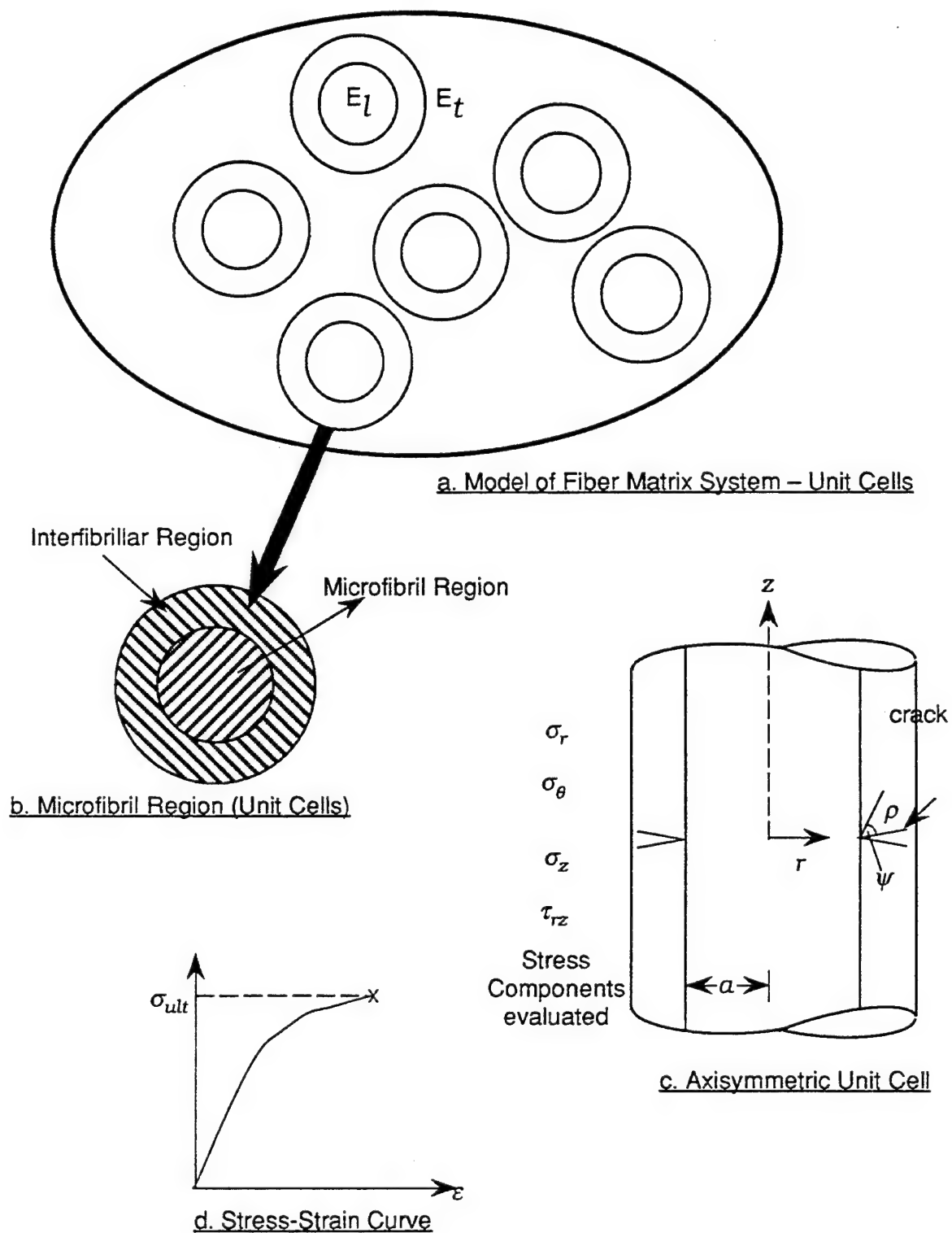


Fig II-1. LCP Fibers Under Tension

problem in which a $1/\sqrt{r}$ stress singularity is involved using conventional (nonsingular) elements of different orders results in similarly slow rates of solution convergence and hence, a very fine mesh with a large number of degrees of freedom is required to achieve numerical results of acceptable accuracy [9-11]. In fact, it has been shown [8] that for a singular elasticity problem the rate of convergence of the finite element solution is governed by the order of the singularity rather than the order of the polynomial for interpolation functions. For the present crack problems with stress singularities, the convergence of finite element solutions is also anticipated to be dominated by the order of stress singularity. Thus, to expedite the rate of solution convergence and to insure better accuracy, inclusion of proper singular terms in the formulation of improved finite elements to account for the stress singularity is essential in solving this class of problems. Among various models that incorporate local stress singularities in the recent development of finite element methods [12-15], the hybrid element approach pioneered by Pian, et al. [13] and later refined by Tong, et al. [14] is one of the most attractive methods and, therefore, is used here, because of its greater flexibility in the element formulation and demonstrated solution accuracy and convergence.

The element stiffness matrix is formulated on the basis of a hybrid variational functional $\pi_{mh}(\sigma, u, \bar{u})$ [12,14]

$$\pi_{mh}(\sigma, u, \bar{u}) = \iint_{A_m} (\sigma^T \epsilon - \frac{1}{2} \sigma^T S \sigma) dA - \int_{\partial A_m} T^T (u - \bar{u}) ds - \int_{S_{om}} T^* \bar{u} ds, \quad (16)$$

where A_m is the m th element; ∂A_m is the boundary of A_m ; S_{om} is the portion of element boundary where traction T^* is prescribed and

is the displacement vector defined over the element boundary. Standard matrix notations, S , σ , ϵ , u , and T , in the finite element analysis are used here for convenience to represent the compliance matrix, stresses, strains, and displacements in the interior of the element, and tractions along the element boundary, respectively, where

$$\sigma^T = \{\sigma_x, \sigma_\theta, \sigma_z, \tau_{xz}\}, \quad \epsilon^T = \{\epsilon_x, \epsilon_\theta, \epsilon_z, \gamma_{xz}\} \quad (17)$$

Within the crack-tip region, the stress field is completely governed by the singular term of the stress solution. For the case under consideration, the near-field stresses may be written as

$$\sigma_{xx} = K_I \rho^k, \quad \sigma_{xz} = K_{II} \rho^k \quad (18)$$

where K_I , K_{II} are mode I, II stress intensity factors, respectively.

These advanced singular elements in conjunction with adjacent nonsingular elements can not only deal with the detailed local singular behavior of each failure mechanism but also take into account various combinations of geometries and failure mode interactions. The initiation, stable and/or unstable progression of cracks deflected over the fiber interface or penetrated into the fiber will be analyzed based on appropriate criteria such as a critical fracture toughness K_{Ic}^{cr} and a maximum tensile stress criterion. The effect of geometric and material variables on the effective tensile moduli of the fiber will be studied. The microfibril level criterion will be extended to the fibril level using a rule of mixture technique also the homogenization method

indicated previously. Results will be compared to experimentation for a Vectra fiber.

REFERENCES

1. "Liquid Crystalline Polymers", National Materials Advisory Board, Commission on Engineering and Technical Systems, National Research Council, (1990).
2. L. C. Sawyer and M. Jaffe, "The Structure of Thermotropic Copolyesters", Journal of Materials Science, Vol. 21, No. 6, pp. 1897-1913, (1986).
3. A. Bensoussan and J. L. Lions, and G. Papanicolaou, Asymptotic Analysis for Periodic Structures, North Holland, (1978).
4. E. Sanchez-Palencia, Nonhomogeneous Media and Vibration Theory, Springer-Verlag, (1980).
5. N. Bakhvalov and G. Panasenko, Homogenization: Averaging Processes in Periodic Media, Kluwer Academic, 1990.
6. A.E.H. Love, A Treatise on the Mathematical Theory of Elasticity, Dover Publications Inc., (1944).
7. A. R. Zak, "Elastic Analysis of Cylindrical Configurations with Stress Singularities," Journal of Applied Mechanics, ASME, Vol. 39, No. 3, pp. 501-506, (1972).
8. P. Tong and T. H. H. Pian, " On the Convergence of the Finite Element Methods for Problems with Singularity," International Journal of Solids and Structures, Vol. 9, pp. 313-321, (1973).
9. S. K. Chan, I. S. Tuba, and W. K. Wilson, "On the Finite Element Method in Linear Elastic Fracture Mechanics,"

- Engineering Fracture Mechanics, Vol. 2, pp. 1-17, (1970).
10. G. P. Anderson, V. L. Ruggles, and G. S. Stibor, "Use of Finite Element Computer Programs in Fracture Mechanics," International Journal of Fracture Mechanics, Vol. 7, pp. 63-76, (1971).
 11. J. R. Rice and D. M. Tracey, "Computational Fracture Mechanics," Numerical and Computer Methods in Structural Mechanics, Fenvas, S., et al., eds., Academic Press, New York, pp.585-623, (1973).
 12. K. Y. Lin and J. W. Mar, "Finite Element Analysis of Stress Intensity Factors for Cracks at a Bi-Material Interface," International Journal of Fracture, Vol. 12, pp. 521- 531, (1976).
 13. T. H. H. Pian, P. Tong, and C. H. Luk, "Elastic Crack Analysis by a Finite Element Method, " in Proceedings of the Third Conference on Matrix Methods in Structural Mechanics, Wright-Patterson AFB, pp. 19-21, Oct. 1971.
 14. P. Tong, T. H. H. Pian, and S. J. Lasry, "A Hybrid-Element Approach to Crack Problems in Plane Elasticity," International Journal for Numerical Methods in Engineering, Vol. 7, pp. 297-308, (1973).
 15. S. S. Wang and F.-G. Yuan, "A Hybird Finite Element Approach to Composite Laminate Elasticity Problems with Singularities," Journal of Applied Mechanics, ASME, Vol. 50, No. 4, pp. 835-844, (1983).

Chapter III LCP Fibers Under Compressive Loading

1. Introduction

High performance polymeric fibers are main reinforcement for composite materials. Although these composites show excellent tensile properties, their behavior under compression is very poor. The kink band formation concept is very important because it is a compressive failure mode in polymer fibers. The kink bands were first described by Orowan as the deformation bands that result from the cooperative buckling of the easy shear slip planes. Orowan's theory was later used by DeTeresa to form a concept of kink band formation mechanism in polymeric fibers [1]. He stated that the critical compressive stress that initiates local buckling instabilities which subsequently lead to kink band formation in anisotropic materials is the compressive strength of these materials. Dobb et al. studied the compression deformation of Kevlar fibers by using the elastic loop test [2]. They proposed a structural mechanism describing the mode of deformation based on the initial formation of kink bands. Zwaag et al. studied kink band formation in aramid fibers [3]. They measured the kink band formation in single aramid filaments as a function of the applied compressive strain. Allen studied bending and compressive behavior of PBZT and PPTA (poly paraphenylene terephthalamide) fibers by using the elastica loop test [4]. He observed that the onset of kinking due to compressive stresses precludes the attainment of a tensile failure in the loop which is more common for brittle materials. However, there are other factors (i.e., glass transition temperature, fiber morphology/

microstructure, and intermolecular interaction) which might affect the compressive strength of polymer fibers.

The objectives of this study is to propose a theoretical model for predicting compressive strength of Vectra and the experimental methods for obtaining the compressive strength of Vectra along with its corresponding failure mode.

2. Fiber Compressive Failure Modes

Fiber compressive failure modes can be classified into three group: shear failure which is dominant in high modulus carbon fibers; kink band formation which is mostly seen in polymer fibers and the bending failure of brittle fibers, such as glass fibers. Although the bending failure starts on the tension side, kink band formation starts at the compressive side due to the local buckling of the fiber. Since this work studies polymeric fibers, kink band formation will be discussed next.

If we consider uniaxial compressive failure for isotropic and anisotropic materials; we see that although isotropic materials slip plastically or fracture along the plane at 45 degrees to the load direction, the mechanism of compressive failure in anisotropic planes depends on material symmetry (orientation of easy shear slip planes, see Fig. III-1) and direction of compressive load with respect to this symmetry. DeTerasa [1] stated that the compressive stress, which is just enough for the initiation of local elastic instabilities, subsequently leads to critical kink band formation in anisotropic polymeric fibers.

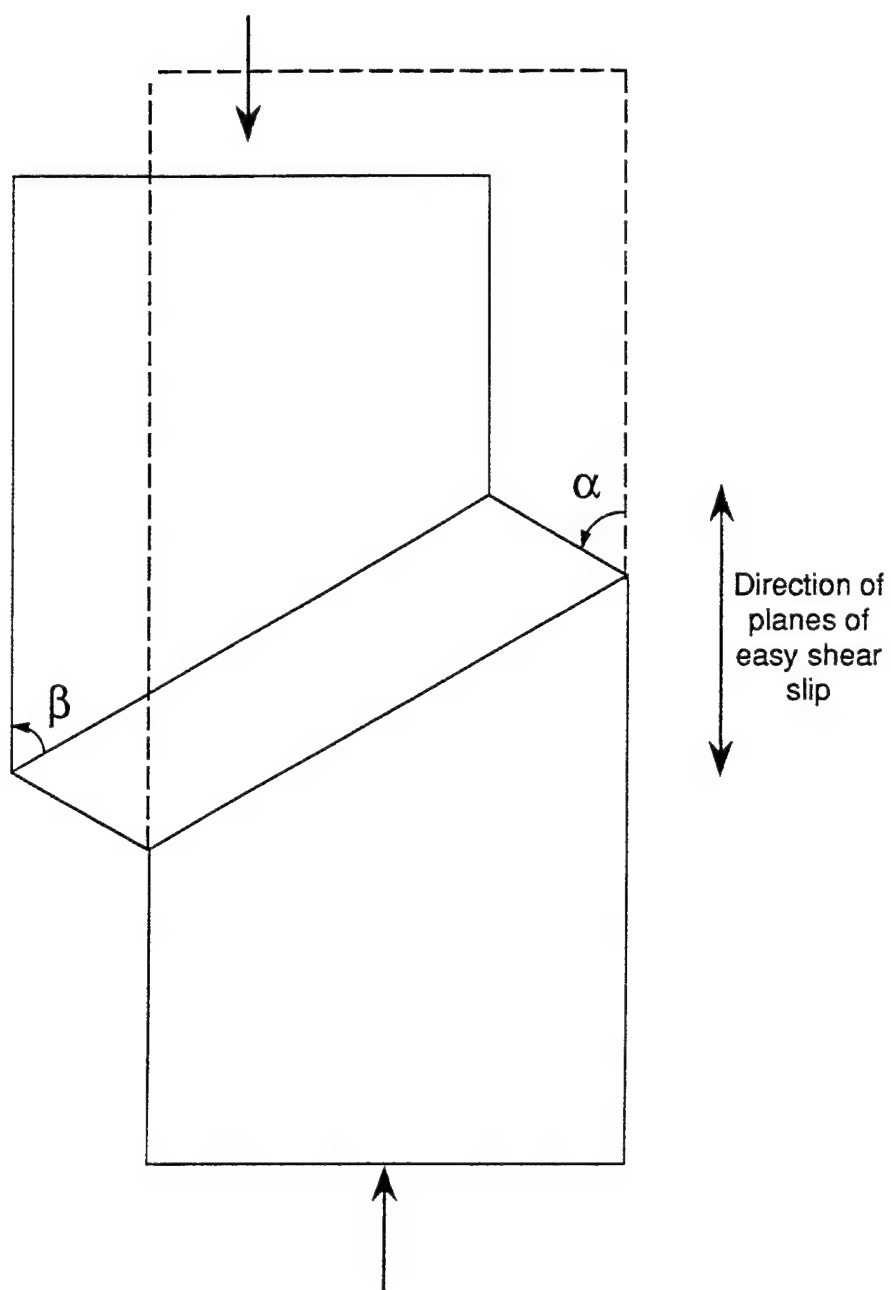


Fig III.1 Schematic of ideal kink band.

The equations describing three possible buckling modes (see Fig. III-2) of a fiber is

$$P_c = \frac{\pi^3 E_1 D^4}{64 L^2}, \quad (\text{Column Buckling}) \quad (1)$$

$$P_c = \frac{\sqrt{\pi^3}}{8} \sqrt{E_1 E_t} D^2, \quad (\text{Extensional Mode}) \quad (2)$$

$$P_c = \frac{\pi^4 E_1 X^2 D^4}{256 L^2} + \frac{\pi G D^2}{4}, \quad (\text{Shear Mode with equivalent interlaminar shear effect}) \quad (3)$$

where $X = d/D$, E_1 is longitudinal modulus of the material of the fiber, E_t is the transverse modulus of the fiber, G is the shear interaction between neighboring fibers, and D and d are diameters of the fiber and sub-fibers (i.e., microfibrils or molecular chains) respectively. The detail description of the extensional and shear buckling is shown in Appendix I. The material parameters E_1 , E_t , and G need to be measured from experiments.

Comparing Eqs. (1) and (2) it can shown that if

$$E_t > \frac{\pi^3}{64} \left(\frac{D}{L}\right)^4 E_1, \quad (4)$$

the fiber will buckle as a column instead of the extensional buckling of the microfibril. Similarly if

$$G > \frac{\pi^2}{16} \left(\frac{D}{L}\right)^2 E_1, \quad (5)$$

then the shear buckling of the microfibril will not take place. Hence, the compressive failure due to buckling of single fiber, or shear or extensional buckling of the microfibril depends on the values of D , L , d , E_1 , E_t and G .

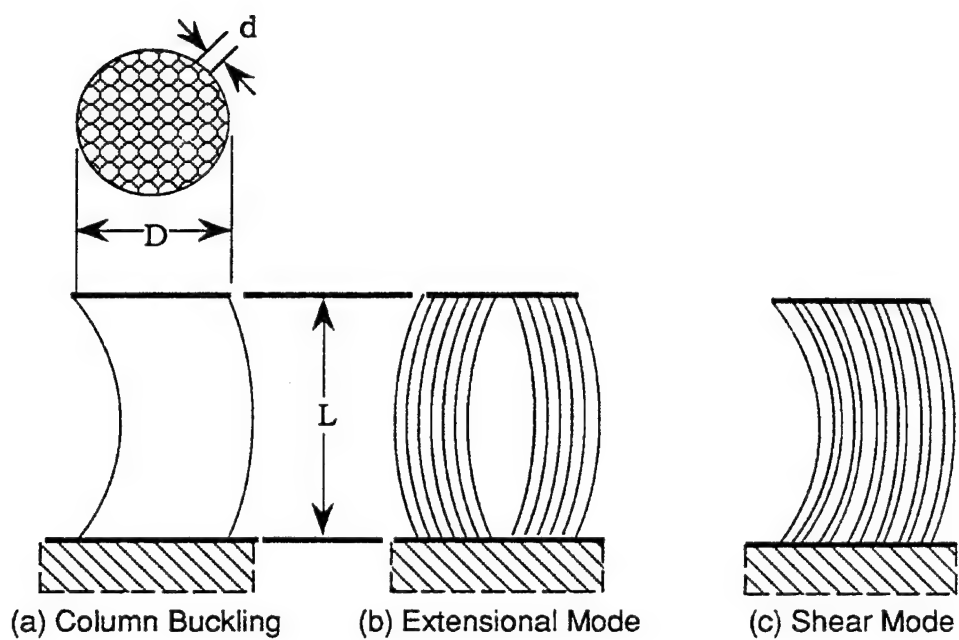


Fig III-2. Buckling Modes of a Fiber with a Microfibrillar Morphology

Based on the theoretical model described by Eqs. (1-3), Fig. III-3, shows the relationship between the microfibrillar nature of the fiber (D/d), the aspect ratio of the fibrils (L/d) and the different buckling failure modes. Hence, experimental methods are proposed next in order to verify this theoretical model.

3. Compressive Test Methods

Many techniques have been used to apply uniform axial compressive stresses to single fibers to obtain their compressive properties. Since the fiber diameter is very small, it is difficult to apply axial compression stresses to fiber itself. Hence, most of the techniques use a matrix material to support the fiber against buckling and to transmit uniform axial compressive stresses to the fiber such as bending beam test and embedding fibers in the matrix. Also there are two other distinct indirect techniques in the literature for measuring the compressive properties of single fibers: elastica loop test and recoil test. The bending beam and elastica loop tests which are proposed for future compressive test of Vectra fibers will be discussed below.

3.1 Bending Beam Test

This test was first used by DeTeresa [1] to investigate the modes of compressive failure and to predict the compressive strengths of high performance polymer fibers. In this technique, the fibers are bounded under a certain tension onto a surface of a clear elastic plexiglass (see Fig. III-4), parallel to the length of the beam (6 mm x 25.7 mm x 152 mm). Tension is

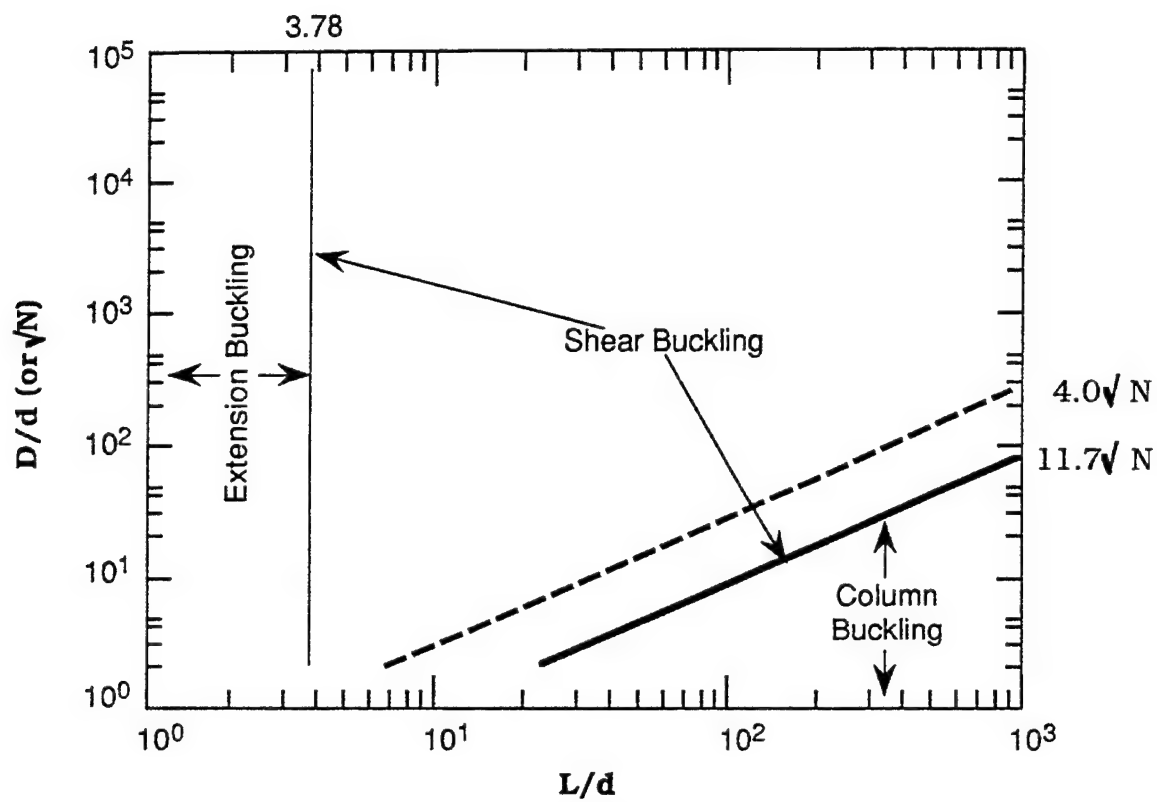


Fig III-3. Relationship Between Microfibrillar Geometry and the Buckling Mode

calculated for each fiber to give them a tensile strength of 0.03%. Then the beam is bent by clamping one end and deflecting the other. Assuming a perfect bonding of the fibers to the beam, the strain in the fiber at any point would be equal to the strain at the surface of the beam at the same location. Kink band formation, which is a compressive failure mode, is observed in-situ under the optical microscope by holding the beam in the bent position. The last kink band along the fiber, called the critical kink band, is recorded to calculate the strain $e(x)$ at this point (see Fig. III-4). This strain is called the critical compressive strain of the fiber, and used to calculate compressive strength of the fiber by multiplying it by the tensile elastic modulus of fiber, or in case of KevlarTM fibers, by fiber compressive modulus from composite data, assuming that the fiber is linear elastic.

The bending beam test is a simple test in nature and easy to take measurements. In-situ observation of fiber deformation, while loading the beam, is very useful in examining the fiber compressive behavior. The axial stress gradient created along the fiber is very advantageous in observing the fiber compressive behavior at different stress levels. This axial stress gradient can be changed easily by varying the wedge size or by removing the wedge close to clamped end. It was reported [5] that, in matrix-fiber combination, matrix shrinkage is a problem in testing fiber compressive properties. Bending beam test eliminates this drawback by applying a very thin coating relative to the beam thickness.

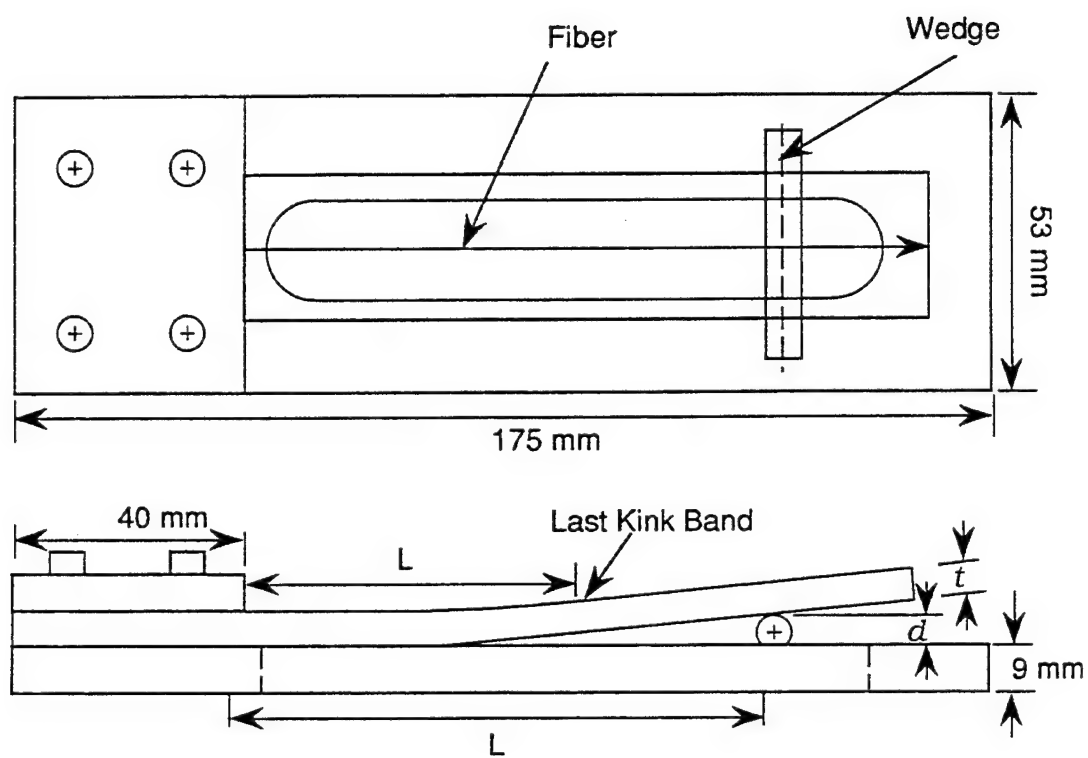


Fig III-4. Schematic Drawing of Bending Beam Test Apparatus and Strain Distribution in the Fiber

The disadvantages of the bending beam test are: Some fiber surface imperfections make it impossible to observe critical kink bends in the fiber by optical microscope. For instance, as PBZT had such surface irregularities so that it was not possible to distinguish the critical kink bands with surface imperfections; Kink band formation in fibers could not be observed even if the beam was deflected beyond small deflection concept. This indicates that these fibers take large compressive strains for failure.

3.2. Elastica Loop Test

Elastica loop test was first performed for glass fibers by Sinclair [6] to measure their tensile strength. Later, Jones et al. [7] used it to determine the intrinsic strength of carbon fibers. Allen [4] conducted the elastica loop test to observe the compressive behaviors of PBZT and PPTA fibers.

Basically, a loop in a fiber is twisted and the loop size is reduced gradually by pulling on the loop ends until the first kink band is observed at the bottom of the loop where the critical bending stresses are developed. At the same time, the fiber deformation was observed by optical microscope method. For very small fiber surface deformation, scanning electron microscopy method was used. The schematic of fixture for elastica loop test is shown in Fig. III-5. As mentioned before, kink band formation in the compressive side of the fiber is assumed to occur just before elastic instability of fiber material. At this stage, the loop size is recorded from photographs. The critical compressive strain, e_{cr} , in the fiber can be calculated by where r is fiber radius and R_m is minimum radius of curvature

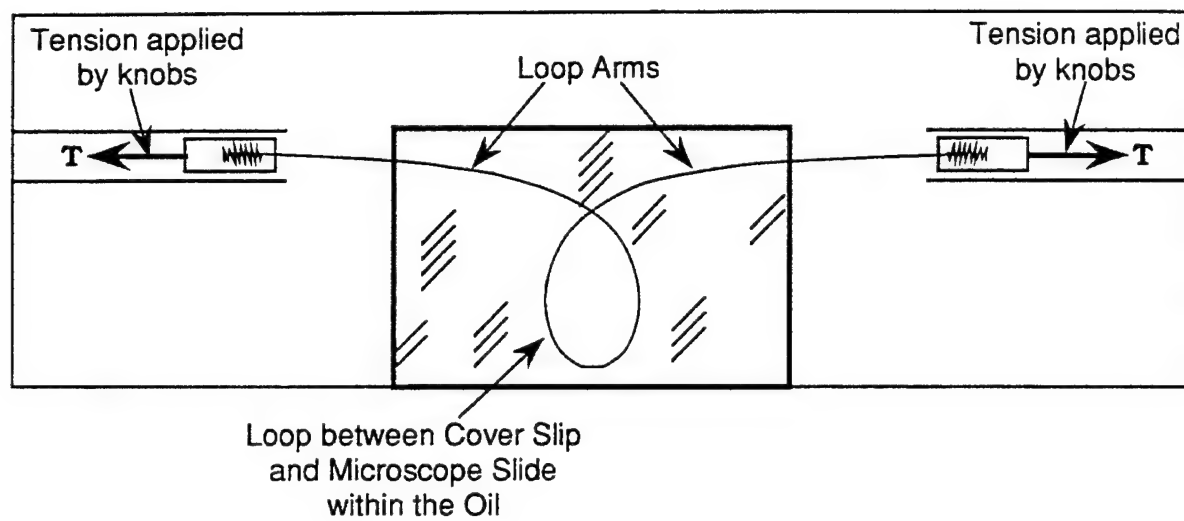


Fig III-5. Schematic of Fixture for Elastica Loop Test

$$e_{cr} = \frac{r}{R_m}, \quad (6)$$

at the location where the last kink band is seen. R_m can be calculated either from equations of elastica [8] or from radius of the circle drawn into the loop.

The elastica loop test is a simple test in nature and easy to take measurements. Surface irregularities are not a problem, because the compressive deformation is observed on the compressed side of the fiber. More information about fiber compressive behavior can be obtained from in-situ observation of the fiber deformation. The disadvantages is that special care must be taken to apply the in-plane forces.

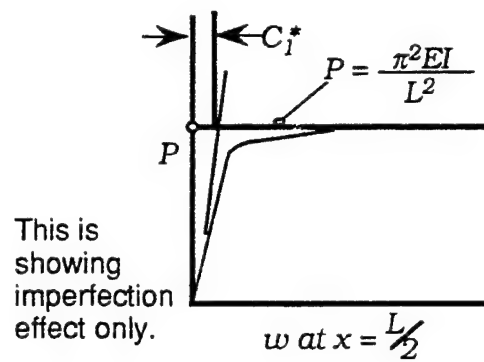
4. Discussion

Based on the proposed theoretical model, it suggests that improvement in compressive strength of polymeric fibers require stabilizing these structures either by improving the inter-microfibrillar interactions (G and E_t) or eliminating these microfibrillar structures through processing. Observing the past results from both experiments and theoretical model for Kevlar fiber, it indicates that the predicted compressive strength is usually larger than the experimental one. It suggests that some important features affecting compressive strength of fibers may be missed from the current theoretical model. For examples, the residual stresses, the defects and damages in the fiber can reduce the compressive strength of fibers. The eigenstrains developed in the weakest slip systems in sub-fiber level (from the microfibril down to individual molecular chains) may have to

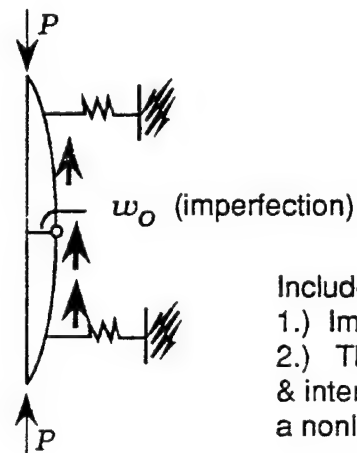
be considered in the theoretical model from the micromechanics point of view if the fiber is not a homogeneous isotropic material. However, the micromechanics aspect of theoretical model for compressive strength of fibers is not a easy task and needs further and intensive study. One of the new concepts in predicting the compressive strength will be a microbuckling model taking the microfibril imperfection into consideration (see Fig. III-6) in which the imperfection is assumed to be an off-set dimension W_0 . Transverse elastic supports and through-the-line thickness shear will be included within the model. One can observe from the figure that the problem is nonlinear geometrically. Once microfibular buckling is found it will be extended to the fiber level by the rule of mixture technique.

Reference

1. S.J. DeTerasa, The axial compressive strength of high performance polymer fibers, Ph.D Dissertation, University of Massachusetts (1985).
2. M.G. Dobb, D.J. Johnson and B.P. Saville, Compressional behavior of carbon fibers, *Polymer*, Vol. 22, pp. 960-965 (1981).
3. S. van der Zwaag and G. Kampschoer, Compressive failure in the high modulus polymeric fibers, *Proceedings of the Second International Meeting on Polymer Science and Technology*, edited by P.J. Lemstra and L.A. Kleintjens, Elsevier Applied Science (1987).
4. S.R. Allen, Mechanical and morphological correlations in poly(p-Phenylenebenzobibthiazole) fibers, Ph.D



$$w = \frac{PC_1^* \sin \frac{\pi x}{L}}{\frac{\pi^2 EI}{L^2} - P} + \frac{PC_2^* \sin \frac{2\pi x}{L}}{\frac{4\pi^2 EI}{L^2} - P} + \frac{PC_3^* \sin \frac{3\pi x}{L}}{\frac{9\pi^2 EI}{L^2} - P} + \dots$$



Include:

- 1.) Imperfection
- 2.) Thru the thickness shear & inter. lamina shear, this is a nonlinear problem.

Fig III-6. Proposed Model for Compression Failure

- Dissertation, University of Massachusetts (1983).
5. R.L. Keller, A.N. Palazotto, and S.J. Bai, The consideration of compressive deformation in polymer fiber, 28th Structures, structural Dynamics and Materials Conference, AIAA/ASME/ASCE/AHS, pp. 245-251, (1987).
 6. D. Sinclair, A bending method for measurement of the tensile strength and Young's modulus of glass fibers, J. appl. Phys., Vol. 21, pp. 380-386, (1950).
 7. W.R. Jones and J.W. Johnson, Intrinsic strength and Non-Hookean behavior of carbon fibers, Carbon, Vol. 9, pp. 645-655, (1971).
 8. S. Fidan, Experimentation and analysis of compression test methods for single filament high performance fibers, M.S, Thesis, Air Force Institute of Technology, AFIT/GAE/AA/88D-14 (1988)

Appendix I. Extensional and Shear Buckling

The chains are assumed to be packed in the cross-section of the fiber on a cubic lattice as shown in Fig. III-7, where b is a lattice dimension, L is the length of the lattice of perfectly oriented link-hinge chains.

(a) Extension Buckling:

For buckling within a plane, the extension mode configuration is shown in Fig. III-8. The lateral deflection of a chain is

$$v(x) = \sum a_n \sin\left(\frac{n\pi x}{L}\right), \quad (7)$$

where n can be chosen from 1 to infinite. Based on the variation in work due to compressive load p acting on a chain that buckles into a shape described by Eq. (7) and the variation in strain energy of a chain that has a bending rigidity kl and variation in energy due to the deformation of foundation, a energy balance equation can be described as

$$\frac{p\pi^2}{4L} \sum n^2 a_n^2 = \frac{\pi^4 kl}{4L^3} \sum n^4 a_n^2 + E_t L \sum a_n^2. \quad (8)$$

Eq. (8) gives the critical buckling load as

$$p_{cr} = \frac{\pi^2 kl}{L^2} \frac{\sum n^4 a_n^2}{\sum n^2 a_n^2} + \frac{4E_t L^2}{\pi^2} \frac{\sum a_n^2}{\sum n^2 a_n^2}. \quad (9)$$

The ratio of the summation is minimized when only arbitrary coefficient a_n is used. Hence,

$$p_{cr} = \frac{\pi^2 kl}{L^2} (m^2) + \frac{4E_t L^2}{\pi^2} \left(\frac{1}{m^2}\right), \quad (10)$$

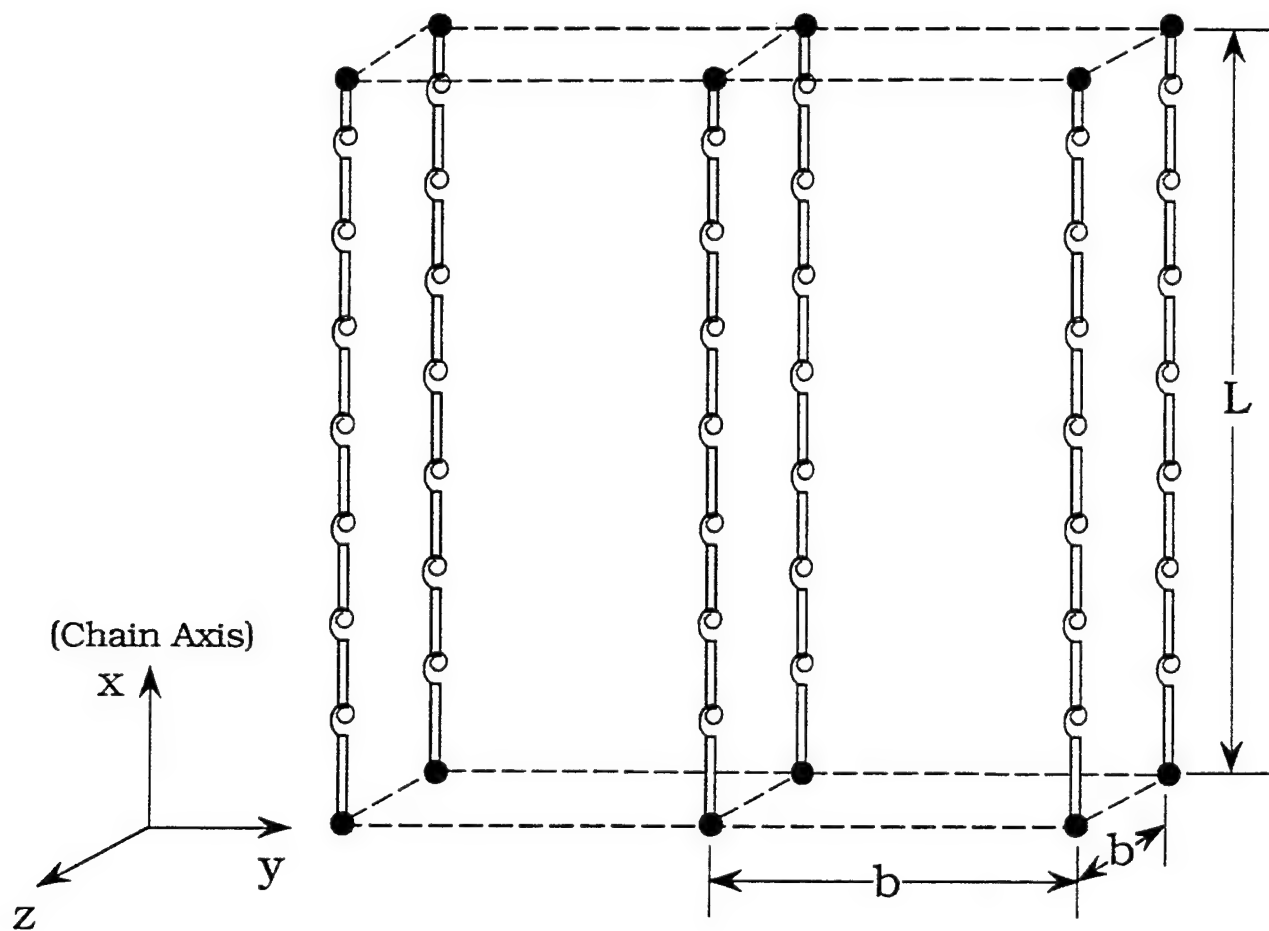


Fig III-7. Packing geometry for a collection of interfacing and perfectly oriented link-hinge chains.

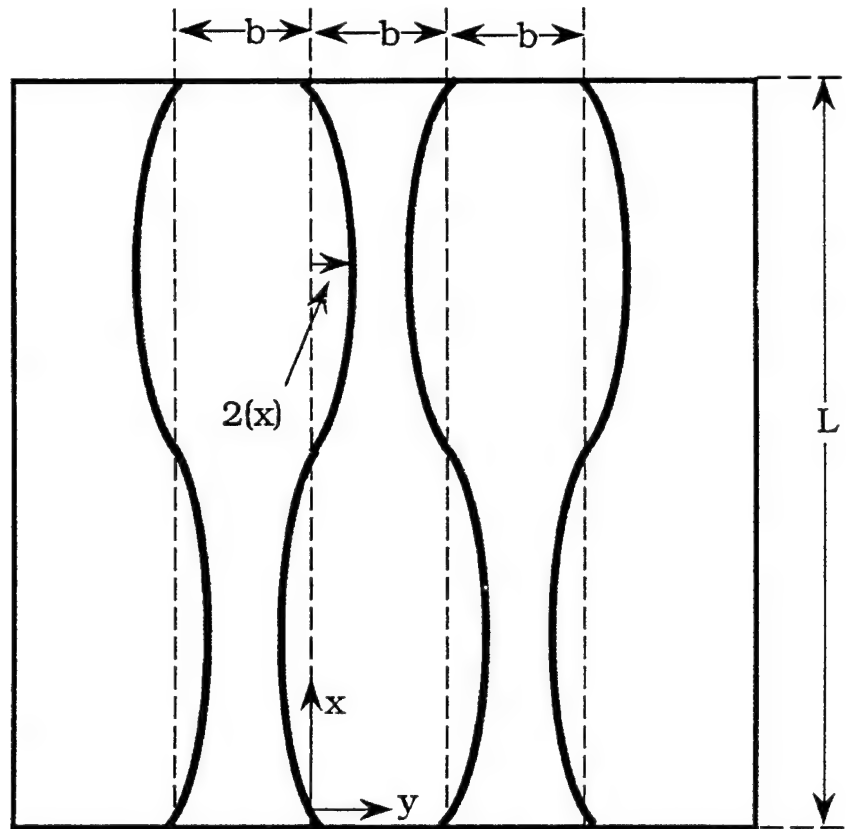


Fig III-8. Coordinates for Extension Mode Buckling Deformation

where $m = 1, 2, 3, \dots$

The minimum value of p_{cr} depends on the relative value of kl and E_t . If the bending rigidity kl is replaced by the column bending rigidity $E_1 I$, the foundation is stiff relative to the bending rigidity of the chain (i.e., $E_t \gg E_1$), and the chain is long, then the second term in Eq. (10) will dominate and large values of m will be required to minimum p_{cr} , which is

$$p_{cr} = 4\sqrt{E_t E_1 I}, \quad (11)$$

where I is the moment of inertia which is a function of diameter of microfibrils or molecular chains. For a fiber being split into finer structures (see Fig. III-2) without loss of volume, the buckling load of the bundle of N finer structures will be

$$P_{cr} = N p_{cr} = \frac{\sqrt{\pi^3}}{8} \sqrt{E_1 E_t} D^2. \quad (12)$$

(b) Shear Buckling:

The shear mode of buckling within a plane is represented in Fig. III-9. Substituting the variation in work due to compressive load p acting on a chain that buckles into a shape described by Eq. (7) and the variation in strain energy of a chain that has a bending rigidity kl and variation in energy due to the shear deformation of foundation into a energy balance equation and minimizing the ratios of the summation as before leaves

$$p_{cr} = \frac{\pi^2 k l}{L^2} + G b^2, \quad (13)$$

where p_{cr} is the critical buckling load of each individual sub-

element. The buckling load of the bundle of N fibrils will be

$$P_{cr} = NP_{cr} = \frac{\pi^4 E_1 D^2 d^2}{256 L^2} + \frac{\pi G D^2}{4}. \quad (14)$$

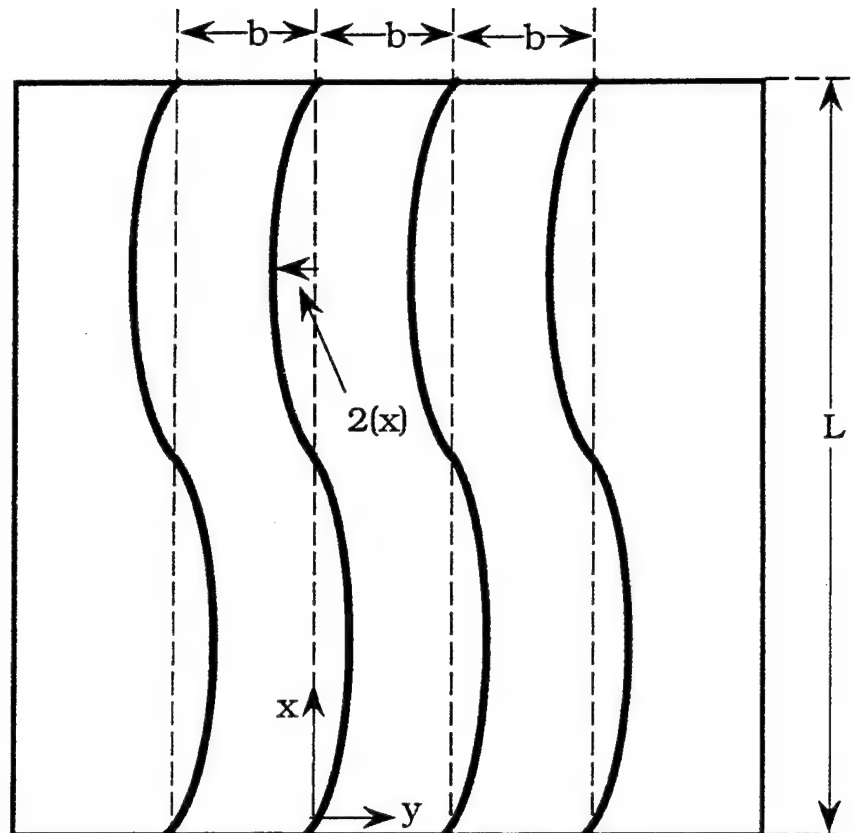


Fig III-9. Coordinates for Shear Mode Buckling Deformation

Advanced Materials for Liquid Rocket Engines
Technical Memo #1
Liquid Crystal Polymer's
Suitability for MMH and NTO Turbopump Applications

Thomas R. Hill
AL/RKLC

30 August 1990

Abstract

This investigation was designed to determine the usability of Liquid Crystal Polymers (LCP's) in the storable propellant turbopump environment, as part of the Advanced Materials for Liquid Rocket Engines Program. The investigation centered around two main areas - material's compatibility with the propellants, and the material's ability to be formed using injection molding. Chemical compatibility testing has been carried out on most of the LCP's that are available, and the majority have experienced changes in their physical properties which will make their application to turbopump components difficult. Some materials that experienced little change in the propellant environment are not injection moldable - making them difficult to work with. Measures which would protect the LCP's from the propellants are being investigated, and they may prove to be useful. More research is required into the effects of storable propellants on polymers before any conclusions can be drawn.

Materials Being Tested

Liquid Crystal Polymers (LCP's) are a relatively new form of plastic which have both high strength and ease of molding. Considered polyesters, LCP's have found their way into a variety of uses within industrial and commercial markets. They may be filled with other materials (glass, graphite, etc) to increase their strength, melt resistance, or other physical properties. LCP's have exhibited high chemical resistance in the past, and were considered to be likely candidates for turbopump component replacement.

Compatibility Testing

When a new material is considered for a job, it must be able to stand up to the necessary environment. In order to determine the LCP's suitability, simple compatibility testing was used. While not exposing candidate materials to all the conditions they would face in a turbopump, the tests would eliminate materials from consideration due to any chemical incompatibility.

Testing Method

Testing was designed to determine if any chemical reactions would take place between the candidate LCP and the propellants (MMH or NTO). The following procedure was followed:

1. Samples were placed into an oven and heated to 50 degrees Celsius (122 degrees Fahrenheit) for a period of 3 hours, then allowed to cool. This procedure was to remove any moisture from the samples.
2. Samples were weighed and, if possible, measured. In some cases, size measurement of samples was impossible due to odd geometries.
3. The LCP's were immersed in MMH and NTO for 24 hours. The exposure took place at room temperature and ambient pressure.
4. After removal from the propellants, the samples were dried again, reweighed and remeasured.

Descriminating Results

Once the samples were dried, they were examined. Most samples lost weight, changed chemical composition, gained weight, or significantly discolored, showing that there was some form of chemical reaction with the propellants. Research is being conducted to determine what level of reactivity will disqualify a material from further consideration.

Results

After 24-hour exposures, the following data were recorded for the liquid crystal polymers tested:

Table 1
MMH and NTO
Compatibility Test Results

Material	Dimension MMH	Change NTO	Weight MMH	Change NTO	Color MMH	Change NTO
Vectra A950	X	X	+7.5%	+0.45%	NONE	Lightened
Vectra C950	X	X	-4.08%	+0.04%	NONE	NONE
Vectra A625	-1.2%	NEG	-3.2%	NEG	NONE	NONE
Vectra A130	+0.8%	+0.016%	-16.4%	+0.02%	Yellowed	Yellowed
Ryton	+0.4%	+0.8%	NEG	+4.7%	NONE	1
HX-4000 (Beads)	X	X	-53%	+14.2%	NONE	NONE
HX-4000	-3.5%	+0.1%	-61.3%	+2.33%	2	2
PBO +/-22 (3)	X	X	-13.1%	+8.4%	NONE	Darkened
PBZT +/-22 (3)	X	X	-22.7%	+30.9%	NONE	Purpled
Vectra +/-45 (3)	X	X	-13.4%	+0.05%	Yellowed	Browned

NEG - Negligible (less than $\pm .01\%$)

1 - Sample turned brown and decomposed. Surface changed significantly

2 - MMH - Center of the sample eaten away, surface cracked

NTO - Surface lightened and blistered.

3 - Numbers after material name (+/-22,etc) indicate alignment of polymer chains.

X - Unmeasurable quantity

Most materials tested have proven to react with one or both of the propellants. Materials such as HX4000 and Vectra A130 lost a considerable amount of weight, leading to the theory that the propellant actually dissolved the materials. Some materials such as Vectra A950 gained weight, suggesting that they absorbed propellant.

Other materials, such as Vectra A625 and Ryton experienced small weight losses and no discoloration. They may prove to be likely candidates for further consideration.

Theory of MMH and NTO Failures

Working through the AL Chemistry Lab, a theory for the liquid crystal polymers incompatibility has been developed. The theory centers around the "ester" linkage which is common to all the LCP's tested. In the ester bond, there is a weak carbon link which is vulnerable to the MMH molecule. The breakdown theory is pictured in figure 1.

The NTO reactions are less critical than the reactions which take place between MMH and the LCP's. In nearly all reactions, the LCP being tested gained weight. This has been theorized to be due to a "radical" electron which exists on the NO₂ molecule. The NO₂ molecule then attaches on to the polymer chain, but does not break it. This attachment accounts for the weight gain. A chemical analysis which will test this theory has yet to be devised, but work continues.

Conclusions and Recommendations

Liquid crystal polymers have survived exposure to storable propellants with varying success. A decision as to which materials can be used in the turbopump environment has not been made yet, and will not be made until the materials can be tested mechanically after exposure to the propellants. Testing to date has revealed that some LCP's, such as HX-4000 and Vectra A130, can be removed from consideration.

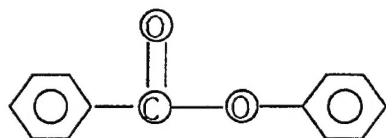
Testing will continue on LCP's which have not been exposed to the MMH and NTO environments. It is hoped that the new materials will do as well or better than those already tested. Meanwhile, LCP's already exposed to storable propellants will be tested more extensively.

Other research will be directed towards discovering why the polymers change their chemical makeup when exposed to MMH and NTO. This will allow future polymers to be engineered to prevent reactivity in the storable propellant environment.

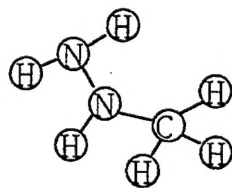
The main test which will be used to determine the reaction products of the polymer-MMH exposure will be a carbon-13 test. The test will examine the MMH which remains after reacting with the polymer, looking for impurities. The impurities will be materials left over from the MMH-polymer reaction, and should indicate which bonds in the polymer chain the MMH is breaking.

Further research will also be conducted into methods of protecting the polymers from the effects of the MMH and NTO. Possible alternatives would include coating the material with a metal, or, exposing the polymer to a chemical which will react to form a "shell" of altered polymer.

**Ester-Link Breakdown Due to
MMH Exposure
(A Preliminary Theory)**



Undisturbed Ester Bond



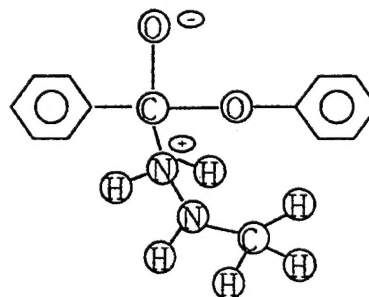
Mono-Methyl Hydrazine Molecule

1. MMH molecule attaches to the exposed side of the carbon atom. This makes the Oxygen and the Nitrogen atoms ions.

2. The Hydrogen atom jumps across the Carbon atom join with the Oxygen atom. Either the C-OH, the C-O or the C-N bond must break at this point. (The C-O is the most likely)

3. After the C-O bond breaks, it may re-combine, however, the recombination rate is much lower than that of destruction.

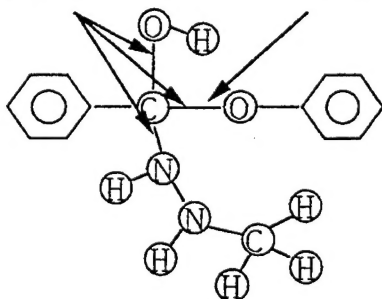
1



One of these bonds
must break

This C-O bond is
the most likely

2



3

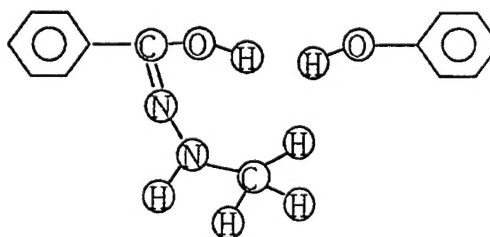


Figure 1 - Description of breakdown theory - all LCP's tested to date contain the ester bond.